

Sborník příspěvků studentské konference

Blansko **2016**
29. - 31. 8.

Název: Sborník příspěvků studentské konference Blansko 2016
Editor: Ondřej Zach
Vydavatel: Vysoké učení technické v Brně
Fakulta elektrotechniky a komunikačních technologií
Rok vydání: 2016
Vydání: první

Organizační výbor konference:

Miroslav Cupal
Martin Hrabina
Roman Mego
Ondřej Zach

Tato publikace neprošla jazykovou úpravou.
Za obsah, původnost a literární citace odpovídají autoři jednotlivých příspěvků.

ISBN 978-80-214-5389-0

Konferenci podpořili

Zlatý sponzor



Bronzový sponzor



Další partneři



Úvodní slovo

Drazí přátelé,

dovolte mi, abych Vás krátkým slovem přivítal na stránkách sborníku již tradiční konference Blansko 2016, pořádané studentskou sekci IEEE při VUT v Brně. Jsme rádi, že se můžeme i tento rok setkat v přátelské atmosféře a navázat nová přátelství, ať již osobní nebo profesní.

Tento ročník konference se koná v rekreačním zařízení Vyhlídka v obci Češkovice u Blanska na hranici chráněné krajinné oblasti Moravský kras. Letošního ročníku konference se účastní velké množství studentů z několika českých i slovenských technických univerzit. Pevně věříme, že účast studentů z různých vědních oborů pomůže rozšířit obzory všech účastníků a navázat dobré profesionální a přátelské vztahy.

Rád bych poděkoval našim partnerům a sponzorům za podporu, bez které by naše konference nemohla proběhnout. Velké díky patří československé sekci IEEE a také partnerům z řad firem, kterými jsou Rohde and Schwarz jako zlatý sponzor, a firmy ESI group a H test jako bronzový sponzor.

Na závěr bychom Vám chtěli poděkovat za účast na konferenci a tím podporu myšlenky IEEE. Přejeme Vám příjemně strávený čas s kolegy a přáteli na konferenci Blansko 2016.

Za studentskou sekci IEEE v Brně

Miroslav Cupal

Obsah

Arm Jakub, Zdeněk Bradáč	
Real-time Virtual Machine Simulator with Collision Detection	4
Báňa Josef	
Parallel computing on graphics cards and possible contemporary solutions	8
Miroslav Cupal	
3D Textile Integrated TIW Horn Antenna for UWB Wirelles Link	13
Dvořák Jan, Gajdoš Adam, Jeřábek Jan	
Electronically Reconfigurable Universal Frequency Filter with Controllability of its Pole Frequency	17
Dvořák Vojtěch	
High Precision Motor Control in FPGA for Space Applications	21
Havlíček Jaroslav	
Arrangements of capacitively loaded dipoles for 20 bit chipless RFID tag	25
Hubka Patrik	
Textile Linearly Polarized HMSIW U-Slot antenna for Off-Body Communication	28
Kotol Martin, Raida Zbyněk	
The Neural models for differrent training algorithms	31
Krejčí Lukáš, Novák Jiří	
Model-Based Testing Framework with Automatic Testing Priority Assignment for Automotive Distributed Systems	35
Krutílek David	
Design and Limitations of the Metal – Composite Hybrid Joint Structures	39
Kufa Jan, Stavěk Marek, Kratochvíl Tomáš	
High Frame Rate Video: Is It Always Better?	43
Kupková Kristýna, Sedlář Karel, Provazník Ivo	
Correlated Mutation Analysis Improvement by Proteomic Signal Processing	47
Liberdová Ivana, Kolář Radim	
Video Quality Assessment in experimental retinal imaging	51
Maršánová Lucie	
Detection of P, QRS and T Components of ECG Using Phasor Transform	55
Mego Roman	
Implementation of retargetable configurable CORDIC algorithm for FPGA devices	59
Mrnka Michal	
Low Temperature Co-Fired Ceramics for High Radiation Efficiency Antenna Design	63
Němcová Andrea, Vítek Martin	
Compression of ECG signals using SPIHT – alternatives to wavelet transform	67
Novák Marek, Cingel Marian	
Lockless Shared Memory Based Multicore Communication Protocol	71
Polak Josef, Jeřábek Jan, Langhammer Lukáš	
Automated measuring system used to measure input and output impedances of current amplifiers	74

Schneider Ján, Novák Daniel, Gamec Ján

Using UWB impulse radar system for measuring of wideband antenna parameters and its comparison **78**

Smíšek Radovan, Vítek Martin

Detection of QRS Notching Using Continuous Wavelet Transform **83**

Starý Vadim, Křivánek Václav

UAS Model Using WEBOTS Robot Simulator **87**

Vašina Petr, Jakubíček Marek

Study of wearable antenna for 2.4 GHz ISM frequency band **91**

Vélim Jan

Analysis of Microstrip Line Relative Permittivity Measurement **95**

Vychodil Josef

System Impulse Response Measurement Using M-sequences in the Presence of Non-linearities **98**

Ondřej Zach, Eva Klejmová

When the Numbers Speak - Hidden Statistics of a Crowdsourced QoE Study **102**

Real-time Virtual Machine Simulator with Collision Detection

Jakub Arm

Department of Control and Instrumentation
Brno University of Technology
Brno, Czech Republic
Email: xarmja00@stud.feec.vutbr.cz

Zdenek Bradac

Department of Control and Instrumentation
Brno University of Technology
Brno, Czech Republic
Email: bradac@feec.vutbr.cz

Abstract—This paper deals with real-time simulation of a machine using virtual reality. This project uses directly OpenGL API, ODE engine and X3D format for machine representation. Collision detection methods, their principle and features are presented. The core of this work is the created machine simulator which uses the appropriate collision method. This simulator is controlled using Modbus TCP and acts as a Modbus slave device. Simulation process and some drawbacks are described. Simulating of box carrying on the belt is discussed and the simplest method is implemented while believable behaviour is achieved. Using ODE physics, the gravity and moving box dynamics are also simulated. The created virtual machine simulating a model of a trunk sorting machine is presented.

I. INTRODUCTION

In the area of manufacturing, the current demand to reduce costs and increase efficiency is bigger. Therefore, companies look for new powerful technologies and they integrate them into production system and developing process. One of the used technology is virtual reality. Virtual reality allows creating virtual machine in the three-dimensional (3D) world which can be seen on the computer screen or using modern VR equipment.

When a virtual machine model can be controlled via any input, it can be called simulator. Positions of each parts can be defined by user. Virtual machine can be also updated according to a real machine. A camera gets position of machine tool and the virtual model is updated according to this data. This is called augmented reality. Aim of this project is to control a model via Modbus TCP which is the free industrial protocol. So the input/output is implemented using Modbus TCP slave. The simulator can be connected to a real PLC (see Fig. 1) or simulated PLC on computer. The simulator does not recognize it.

According to the result requirements, detail depth has to be stated before creating a model. The detail depth improves result quality and can reveal hidden problems. On the other hand, computational power demand is growing even using optimized algorithms. After all, machine simulation saves hardware costs caused by software bugs and even developer costs because the software debug phase can be faster and more comfortable. Appreciable effect is stress reducing during development phase and simpler hardware changes.

There are many commercial tools that simulate machines. The sophisticated are Matlab with Virtual Reality toolbox,

Witness, LabView or CAD-like software which can directly control position of each part of a model. Simulators of CNC machines have in-built a CNC motion controller which interprets CNC commands to simulated tool motion and a simulated final product. This tool serves also to CNC program debugging. Also PLC HMI system with in-built connectors can be used as a simulator. The majority of software draws only a machine in virtual reality environment with the specific degree of details. The features like physics and collision detection are implemented only in some specialized software like Siemens Tecnomatix or other professional tools.

Physics applies physical laws to objects in virtual reality like gravity, rigid body dynamics, collision detection, etc. An object can be specified by material moreover. There are two ways how to implement physics. Firstly, high precision engines are used mostly by scientists to compute precise realistic physics which is more computationally demanding. Moreover, when count and complexity of objects is growing. Secondly, real-time engines are used mostly by game developers to compute physics simpler and fast to achieve high frame rate to be considered as real-time behaviour. There are some sophisticated commercial physics engines which are used by commercial software and also open-source engines like Bullet or Open Dynamics Engine (ODE).

Collision detection is a feature to detect overlapping of objects which is unwanted and signalled. Methods, how to achieve this functionality, are described in Chapter II. Collision detection is computed for all objects already by physics engine, but this is for simulation of object material and boundaries. The signalled collision detection has to be stated explicitly.

This project provides online simulation which is sufficient to project aims. All is about simulation speed and model complexity to achieve an average frame rate of 30 *fps* at least to be pleasant for human. Real-time means that all execution time are bounded and guaranteed. But, in this area, term represents fast executing of the simulation loop to achieve fast response. This loop uses fast and less accurate algorithms and model representation in comparison to exact offline simulation.

The whole application is written in Python using appropriate open-source libraries. This project is inspired by [1] and [2], where a model is defined using VRML, and by [3], where Matlab with Virtual Reality toolbox is used and control is interfaced by specialized PCI cards. The basic purpose of created application is to simulate an laboratory equipment

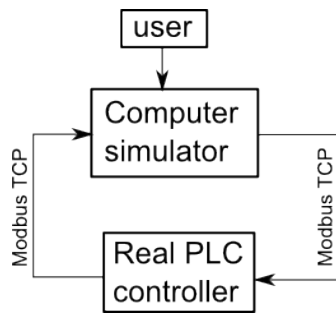


Fig. 1. Overall diagram of the system

as a simulator controlled by PLC system for educational purpose.

II. COLLISION DETECTION

The collision detection is implemented basically by a physics engine. Developer has to declare which collision will be signalled. Also, a reaction to this unwanted collision has to be declared. So objects can be grouped by their collision domain.

This article aims to collision detection algorithms used for real-time purposes. So the complexity of objects is usually simplified to basic shapes like box, cylinder or sphere, or some approximations are done mostly when computational costly triangular mesh to mesh collision is being detected. Mesh to mesh collision detection is powerful because any object can be decomposed [4]. Some real-time algorithms how to detect collisions are :

- bounding box - any object or mesh is represented by bounding box which is faster to calculate. The simpler option is AABB (Axis-Aligned Bounding Box) where bounding boxes are orthogonal to axis. This method can be combined also with hierarchical method to achieve less computational demands (see hierarchical method). The more accurate option is OBB (Oriented Bounding Box) tree that is based on decomposing an object to oriented boxes where each box is placed such that it is almost minimal [5].
- separating planes - this algorithm is usable for convex objects. When a separating line or plane between vertices of each object is founded out using algorithm similar to perceptron, objects do not collide [5].
- hierarchical - this method reduces computational demands using grouping objects into hierarchical BV (Bounding Volume) tree. First, bounding boxes at the top level are checked. In case of collision, object volumes at lower levels are checked down to basic objects. The computation time reducing arises from non-checking of all objects together but checking together only if their volume box collide [5].
- points and voxels - one object is represented by voxels and another is represented by equidistant contour points. In case of intersection, voxel bits are set which is detected. Voxel representation is on the other hand memory-inefficient [5].

- space indexing data structures - many data structures to checking collision using space decomposing has been developed. Cell subdivision method is based on definition that if a space cell is occupied by more objects, they collide [5].
- image space method - this method represents an object as a image with minimal and maximal depth. If pixel exists where depths are intersected, objects collide. This method is usable for convex objects [6].

The physics engine has a problem when the refresh cycle frequency is smaller than frame rate. This can be caused by high frame rate, high count of objects, complexity of objects, precision of physics or non-optimized algorithm. As a consequence, some high speed object can move through another object without collision detection. This effect can be caught using direction vector method that considers also the previous position of an object.

III. CREATED SIMULATOR

In this chapter, the created simulator is described. Firstly, used tools are presented, then control of the simulation is described, then the core of the simulator is drawn as a diagram, then real-time capabilities are discussed and in the end, simulator response is measured and some workaround approaches are proposed.

A. Graphics and physics engine

In this project, the scene is drawn directly using OpenGL API. A model is created in X3D (Extensible 3D) format that is the successor of VRML (Virtual Reality Modelling Language) format that is used in industrial virtual reality [2]. X3D is based on XML (Extensible Markup Language) and it is a standard of virtual reality languages. X3D language supports creating of textured objects like sphere, box, or cone, and indexed face-set. It is even implemented in HTML5 technology. A model file is then parsed using specialized parser and processed by OpenGL driver. Using raw OpenGL functions is therefore necessary. There are two ways how to pass objects to OpenGL. Array based model is faster and more difficult to work with. On the other hand, display list can be optimized to achieve nearly the same speed as array based model.

As a physics engine, ODE is used. It provides rigid body dynamics, joints, friction simulation and basic collision detection which is sufficient to the project needs. It is open-source BSD licensed and belongs to real-time physics. The gravity and dynamics are simulated and applied only on the moving box representing material because everything else should be static. This reduces computational demands and the simulation loop can be more frequent.

For collision detection, it uses fast spaces method described in Chapter II. Signalled collision detection is provided by declaration of object collision domain. When the signalization is performed, the simulation is stopped. Then it has to be reset. Non-signalled collision are used to simulate physics and sensor reaction like object in front of photoelectric sensor.

There are a lot of methods how to implement physics like Lagrange multipliers, reduced coordinate, Jakobsens or impulse dynamics. It is good to implement something between

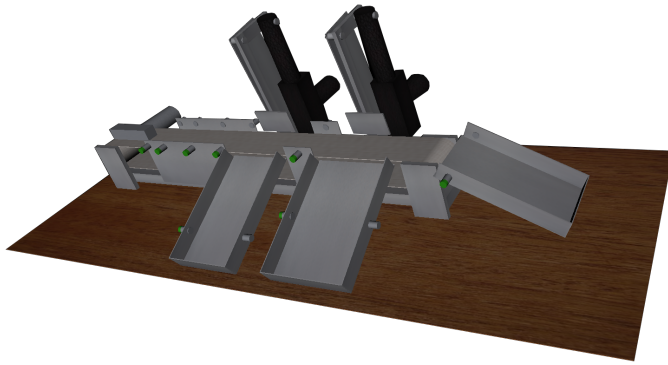


Fig. 2. Created virtual machine using X3D

slower and more flexible Lagrange multipliers, and faster reduced coordinate method. ODE state of art method which also includes a direct method that is based on Lemke's algorithm, which is an extension of Dantzig's algorithm. Even the integration method is important because of speed and numerical stability. Explicit integrator type is faster, on the other hand, implicit type is more numerical stable. ODEs integrator is more stable and particularly less accurate. Contact and friction simulation can be implemented according to the old way using springs and dampers. But ODE uses non-penetration constraints methods that leads to solve the linear complementarity problem. Collision detection can be implemented using various methods (see Chapter II). ODE uses basic shapes collision detection like box, sphere, cylinder or triangle mesh using spaces method.

The problem of carrying a box on the belt is more complex. Because of standing belt object, the force to a box has to be simulated if the belt is running. Or, a virtual object which is connected to the box by a virtual joint of spring and damper can be connected. The problem is when a paddle throws the box out. The box has to react to the paddle and then its momentum is applied, friction and moving down the inclined plane. This collision is caught and force is evaluated. Then the box is moving from this force using ODE algorithms. ODE uses friction models that are approximations to standard model using a friction cone. ODE computes first the normal forces frictionless if exist, and then computes the maximum limits for the friction forces.

The virtual machine can be various and in this project, a model of a trunk sorting machine is simulated. This model is one to one copy of real model. The virtual machine can be seen on Fig. 2.

B. Control of the model

The virtual machines becomes a simulator when some input is implemented to control the machine. Many commercial and also free software provide some user interface to create a motion. But this project uses Modbus server acting as a slave device on a bus to control the motion. This is the key aspect of this project because this transforms the simulator to the PLC controlled simulator of the virtual machine.

Modbus has been chosen for its free license, standard and widening. Another choice can be e.g. Profibus DP or Profinet. Modbus protocol specifies also the presentation

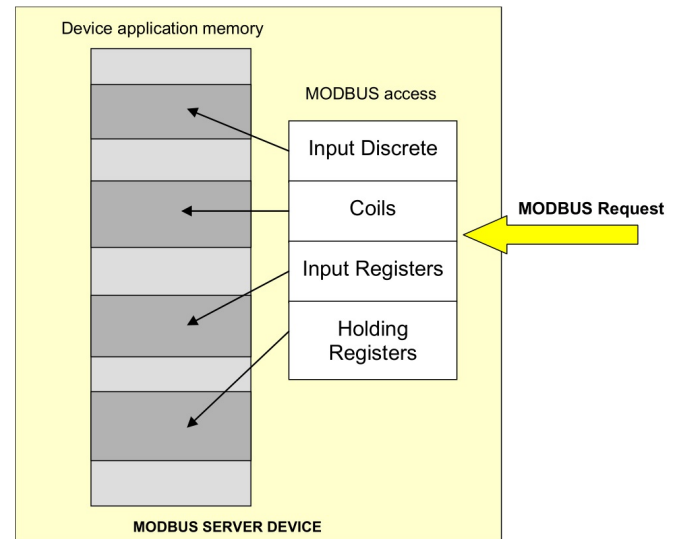


Fig. 3. Separated Modbus data model [7]

of data. It defines analogous to digital/analog input/output areas like coils, discrete inputs, holding registers and input registers. A slave acting as a server has to process a request as soon as possible. The slow response of the server can lead to some problems. The request processing consists of request function decoding which determines an memory area on the server to work with (see Fig. 3). When a value changes, the simulator has to be updated. The first option is to update the values immediately asynchronous right after request arrived which leads to short response. The second option is to refresh the simulator periodically which adds other non-determinism to simulator response.

Modbus area (coils, etc.) is then mapped to model parameters like position or velocity. This simulates real machine equipment like motors, servomotors, pneumatic valves, etc. connected to a process station communicating via Modbus TCP. Now the mapping is performed only at the development phase. So changing virtual wires from process station to virtual machine is not possible.

The model can be controlled also by user through GUI. But this is permitted only to defined objects that acts as a material for the virtual machine. This inputs are processed right after Modbus server inputs processing so physics is not applied in this update cycle (see Chapter III-C).

C. Simulation process

The simulation process consists of initialization when models are parsed and loaded, physics is initialized, Modbus server is established, and OpenGL is prepared. Then the endless control routine process Modbus server outputs and updates the model. Then physics is applied. At the same time, collisions are detected. In the end, Modbus server inputs are updated according to the model. Simultaneously, GUI modification of the model are performed (material objects). The initialization process consists of the following steps :

- Parse X3D machine model, create objects, joints and scene.

- Set the initial state (position etc.) of all objects.
- Create joints in the dynamics world.
- Attach the joints to the objects.
- Set the parameters of all joints.
- Create a collision world and collision geometry objects, as necessary.
- Create collision domains to get collisions signalled.
- Initialize Modbus server.
- Create mapping from Modbus area to parameters of objects.

The simulation loop consists of the following steps :

- Get Modbus server outputs as model inputs.
- Apply outputs to objects as parameters or forces as necessary.
- Apply user requests like new material insertion, etc.
- Adjust the joint parameters as necessary.
- Call collision detection and signal collisions across collision domains.
- Create a contact joint for every collision point and put it in the contact joint group.
- Calculate forces coming from collisions and joints.
- Take a simulation step calling ODE physics.
- Remove all joints in the contact joint group.
- Determines Modbus inputs according to model parameters using non-signalled sensor-object collisions.

In the end, destroying of dynamics, collision world, joints and Modbus server is called.

D. Further work

In our further work, we plan to test the created simulator among students as an educational equipment. Some physics problem solutions and simplifications are going to be made. Then new connector will be created to simulate a Profibus DP slave process station. Some parameters and mappings are going to be changeable using settings. The biggest challenge will be connecting the simulator virtually on PLC inputs/outputs using Siemens S7 protocol to avoid Modbus client in PLC and using IO addresses directly.

IV. CONCLUSION

This project aims to online simulating of a machine using virtual reality. This is done using standard and nearly industrial technology X3D. Graphics is painted using fast OpenGL which is able to use GPU and on the other hand, it provides only raw API. To this model, physics engine ODE is implemented providing collision detection and simulation of physics laws. Some other collision detection methods are presented. A Modbus TCP server is implemented to control the model using standard industrial communication protocol to be controllable using PLC. The simulation loop is described. The whole

simulator is written from scratch in Python language using OpenGL wrapper, ODE physics wrapper and Modbus TCP server library. The simulator is intended to use for educational purposes and will be tested among students as a real model simulator for their PLC control application.

ACKNOWLEDGMENT

The research was financially supported by Brno University of Technology. This work was supported also by the project “TA04021653 - Automatic Lift Inspection” granted by Technology Agency of the Czech Republic (TA CR). Part of the work was carried out with the support of core facilities of CEITEC – Central European Institute of Technology. Part of this paper was made possible by grant No. FEKT-S-14-2429 - “The research of new control methods, measurement procedures and intelligent instruments in automation”, which was funded by the Internal Grant Agency of Brno University of Technology. The above-mentioned grants and institutions facilitated efficient performance of the presented research and associated tasks.

REFERENCES

- [1] S. Qin, R. Harrison, A. West, and D. Wright, “Development of a novel 3d simulation modelling system for distributed manufacturing,” *Computers in Industry*, vol. 54, no. 1, pp. 69 – 81, 2004. [Online]. Available: <http://www.sciencedirect.com/science/article/pii/S0166361503001878>
- [2] S. Ressler, A. Godil, Q. Wang, and G. Seidman, “A vrml integration methodology for manufacturing applications,” in *Proceedings of the Fourth Symposium on Virtual Reality Modeling Language*, ser. VRML '99. New York, NY, USA: ACM, 1999, pp. 167–172. [Online]. Available: <http://doi.acm.org/10.1145/299246.299291>
- [3] J. Bathelt and A. Jönsson, “How to implement the virtual machine concept using xpc target,” *Nordic MATLAB Conference 2003*, 2003.
- [4] R. Tesic and P. Banerjee, “Exact collision detection using virtual objects in virtual reality modeling of a manufacturing process,” *Journal of Manufacturing Systems*, vol. 18, no. 5, pp. 367 – 376, 1999. [Online]. Available: <http://www.sciencedirect.com/science/article/pii/S0278612500876396>
- [5] T. Mujber, T. Szecsi, and M. Hashmi, “Virtual reality applications in manufacturing process simulation,” *Journal of Materials Processing Technology*, vol. 155–156, pp. 1834 – 1838, 2004, proceedings of the International Conference on Advances in Materials and Processing Technologies: Part 2. [Online]. Available: <http://www.sciencedirect.com/science/article/pii/S0924013604005618>
- [6] H. Aiqing, *The Research on Collision Detection in Virtual Reality*. Berlin, Heidelberg: Springer Berlin Heidelberg, 2012, pp. 71–76.
- [7] Modbus, “Modbus application protocol specification v1.1b3,” Modbus Organization, Tech. Rep., 2012.

Parallel computing on graphics cards and possible contemporary solutions

Josef Báňa

Department of Radio Electronics
Brno University of Technology
Brno, Czech Republic
banaj@feec.vutbr.cz

Abstract — This paper deals with parallel computing on graphics cards compared with conventional solutions to contemporary architecture x86. The main objective is to emphasize the benefits and pitfalls of possible solutions. It also deals with the possibilities of potential programming approaches, especially for languages such as C / C++.

Keywords—Parallel computing, FLOPS, performance, NVIDIA CUDA, Intel Xeon Phi, AMD stream, OpenCL, C / C++ parallel programming.

I. INTRODUCTION

An increasing amount of information entails the need to process huge amounts of data. Joining the performance of multiple computers across the network means a large slowdown. Acceleration of problem solving through parallelization and distribution to multiple threads (or kernels) and processing with multi-core processors is already quite common today.

In the long used computer architecture, serial data processing has been used or with various data has been processed as multiplexed, which entails a certain way of thinking of programmers accustomed to the established concept. However, with parallel processing of multiple programmes at once, programming in low-level languages, led to significantly increased demands on the programmer and his thinking.

On the other hand, the concept of graphics cards has been designed from the beginning for parallel processing of large amounts of elemental data. The efforts of manufacturers to optimize subsections (shaders) specialized for a particular purpose, so that none would be idle led to new solutions. Thus a Unified Shader Model was formed, which with its versatility is in some ways closer to a conventional CPU. Gradually, shaders processors developed into stream processors, which are even closer to a classic CPU. Hence the possibility to process data other than graphics on graphics cards came about. CPUs now generally have 2-16 core processors. In contrast, graphics cards now commonly contain 96-2880. High-end class of graphics cards, designed exclusively for the calculations and created by NVIDIA, carries the name Tesla. We can see on Fig. 2. NVIDIA Tesla K40, without graphical outputs.

Due to their different original concept, graphics cards (compared to CPU) gradually bring new microarchitecture already designed for parallel processing of different types of data. In order to really take advantage of the huge potential of graphics cards, new concepts of parallel programming are being developed together with the hardware.

The main purpose of this article is to provide an overview of the most common hardware architectures suitable for parallel processing and also present the diversity of possible programming approaches.

II. GRAPHICS CARDS



Fig. 1. NVIDIA Tesla K40 graphics card.
<http://www.NVIDIA.com/object/tesla-workstations.html>

Source:

A. Basic concepts in graphics cards

- Shader – Generally, a shader in a GPU is a PC programme, which controls programmable parts of the GPU. Special programming languages are used for producing such programme.
- Pixel shader (fragment) – 2D, colour compute and other attributes of each pixel. It is used for rendering

advanced graphical features such as bump mapping and shadows.

- Vertex shader – 3D, it is oriented on scene geometry, it transforms each vertex's 3D position in virtual space to the 2D coordinates in which it appears on the screen. [1]
- Geometry shader – it can generate new graphics primitives (points, lines, triangles, etc.) and can perform calculations on it. [2]
- Compute shader – possible use for non-graphics applications. [3]
- Unified Shader Model (USM known as Shader Model 4.0 in Direct3D 10) – where all of the shader stages in the rendering pipeline (geometry, vertex, pixel, etc.) have the same capabilities. They can all read textures and buffers, and they use instruction sets that are almost identical. Before USM the system was less flexible, sometimes leaving one set of shaders idle if the workload used one more than the other. [4]
- GPGPU (General-Purpose computing on graphics processing unit). GPGPU is a technique using parallelization of the graphics card for computing common algorithms, which are usually performed by CPU. These are a few adjustments for increased GPU calculation accuracy and simplify programming, with support for accessible programming interfaces and industry-standard languages. [5]
- Single Precision floating-point – computer format of real number that can use 32 bits of memory.
- Double Precision floating-point - computer format of real number that can use 64 bits of memory.
- SIMD (Single Instruction Multiple Data) - all parallel units share the same instruction, but they carry it out on different data elements. They perform the same operation on multiple data points simultaneously. SIMD threads are used in GPU to minimize thread management.
- Stream Processing – Given a (typically large) set of data (“stream”). Runs the same series of operations (“kernel” or “shader”) on all of the data (SIMD). GPUs use various optimizations to improve throughput. PUs are designed to solve problems that tolerate high latencies. High latency tolerance has lower cache requirements - less transistor area for cache - more area for computing units, how we can see on Fig. 2. [6]

B. CPU versus GPU Transistor Allocation

GPUs can have more ALUs for the same sized chip and therefore run many more threads of computation. How we can see on Fig. 2.

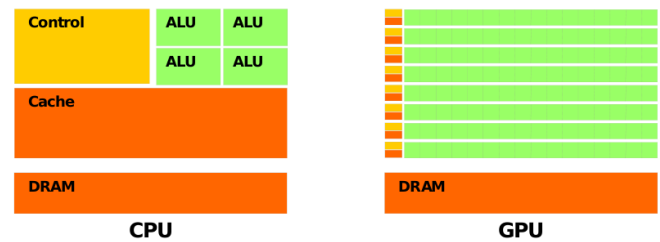


Fig. 2. CPU vs GPU on chip comparison.

Source:

ftp://download.NVIDIA.com/developer/cuda/seminar/TDCI_Arch.pdf

III. NVIDIA CUDA

CUDA (Compute Unified Device Architecture) is an extension of standard stream processors by mathematical functions that are necessary for mathematical computations. CUDA is a multiplatform (MS Windows, Linux and Mac OS) product developed and made by NVIDIA. [7]

CUDA is not a programming language. It is a microarchitecture with hardware modifications of graphics processors and also a few software libraries and extensions for possible programming into most used programming languages – probably the most commonly used is C / C++ for CUDA. [8]

Supported programming languages include C, C++, C#, Fortran, Java, Python, Matlab. Also, CUDA supports programming frameworks such as OpenACC and OpenCL. [9]

A. CUDA-toolkit

The CUDA Toolkit is software “package” that provides a comprehensive development environment for C and C++ developers building GPU-accelerated applications. The CUDA Toolkit includes a compiler for NVIDIA GPUs, math libraries, and tools for debugging and optimizing the applications’ performance. [10]

Its architecture enables threads to cooperate in solving each sub-problem, and allows automatic scalability at the same time. It means that each block of threads can be scheduled on any of the available multiprocessors within a GPU, in any order, concurrently or sequentially, so that a compiled CUDA programme can work on any number of multiprocessors as illustrated by Fig. 3, and only the runtime system needs to know the physical multiprocessor count.

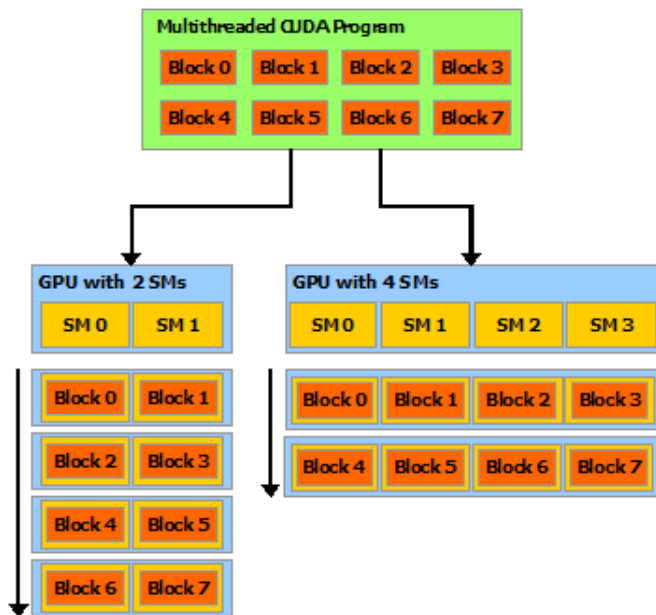


Fig. 3. Representation of CUDA Automatic Scalability.
<http://docs.NVIDIA.com/cuda/cuda-c-programming-guide>

Source:

B. Inside a Stream Multiprocessor (SM)

Is the part of the GPU. Perform the actual computations. Composed by 8, 16 or 32 CUDA cores (depend on architecture). On Fig. 4, we can see block representation of Stream Multiprocessor. [6]

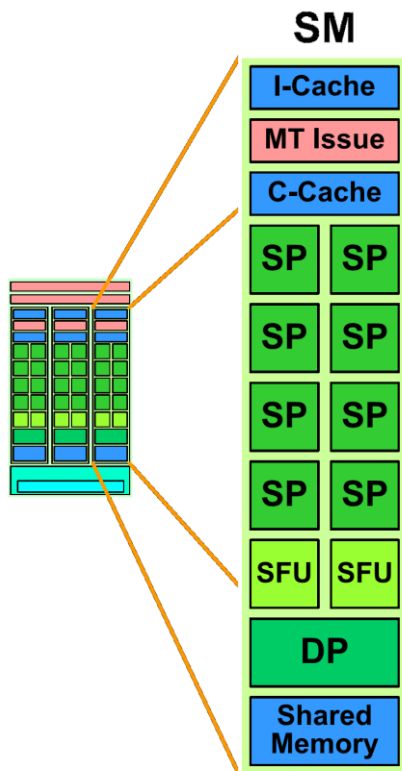


Fig. 4. Stream Multiprocessor (SM) block representation
ftp://download.NVIDIA.com/developer/cuda/seminar/TDCI_Arch.pdf

Source:

- Scalar register-based ISA
- Multithreaded Instruction Unit - Up to 1024 concurrent threads, hardware thread scheduling, in-order issue.
- 8 SP: Stream Processors (CUDA Cores) - Integer Arithmetic Logic Unit (ALU): Supports full 32-bit precision for all instructions, consistent with standard programming language requirements. It is also optimized to efficiently support 64-bit and extended precision operations. IEEE 754 32-bit floating point, 32-bit and 64-bit integer, 16K 32-bit registers.
- 2 SFU: Special Function Units - sin, cos, log, exp.
- Double Precision Unit - IEEE 754 64-bit floating point.
- 16KB Shared Memory

C. CUDA Programming Interface

CUDA C provides a simple path for users familiar with the C programming language to easily write programmes for execution by the device. It consists of a minimal set of extensions to the C language and a runtime library.

Any source file that contains some of these extensions must be compiled with nvcc as outlined in Compilation with NVCC. Most applications do not use the driver API as they do not need this additional level of control and when using the runtime, context and module management are implicit, resulting in more concise code.

When programing using CUDA, kernels must be compiled into binary code by nvcc to execute on the device.

Nvcc is a compiler driver that simplifies the process of compiling code: It provides simple and familiar command line options and executes them by invoking the collection of tools that implement the different compilation stages. This section gives an overview of nvcc workflow and command options. [11]

Benefits – lower costs compared to CPU. Energy efficient. A scalable parallel programming model and software environment for parallel computing. Extreme speed of mathematics calculations thanks to many parallel units working on high frequencies. Minimal extensions to familiar C/C++ environment. Heterogeneous serial-parallel programming model. Threads are managed by hardware; you needn't care about writing code for each thread. [6]

Disadvantages – not all algorithms can have theoretical speedup. CUDA's main disadvantage is that it is only meant for NVIDIA products.

IV. OPENCL

OpenCL (Open Computing Language) is a framework for writing programmes that execute across heterogeneous platforms consisting of central processing units (CPUs), graphics processing units (GPUs), digital signal processors (DSPs), field-programmable gate arrays (FPGAs) and other processors or hardware accelerators. OpenCL specifies a programming language (based on C99) for programming these

devices and application programming interfaces (APIs) to control the platform and execute programmes on the computing devices. OpenCL provides a standard interface for parallel computing using task-based and data-based parallelism. The first initiator of OpenCL is Apple Inc. [12]

OpenCL is an extension to existing languages. OpenCL is a low-level API for heterogeneous computing that runs on CUDA-powered GPUs. Using the OpenCL API, developers can launch written compute kernels using a limited subset of the C programming language on a GPU. [13]

The OpenCL standard defines host APIs for C and C++; third-party APIs exist for other programming languages and platforms such as Python, Java and .NET.

OpenCL version 2.2 library functions can take advantage of the C++ language to provide increased safety and reduced undefined behaviour while accessing features such as atomics, iterators, images, samplers, pipes, and device queue built-in types and address spaces. [14]

Benefits – universal programming usable for different hardware. Highly portable to another hardware architectures. It is planned to add support for other hardware architectures e.g. DSPs (digital signal processors). In version OpenCL 2.2 was more implemented support for FPGAs (field-programmable gate arrays)

Disadvantages – more knowledge is necessary, a more difficult programme compared to the standard approach. It is necessary to rewrite lot of code.

V. DEVICE PERFORMANCE COMPARISON

A. NVIDIA graphics cards with CUDA

Fir high level programming, you need add only a few CUDA headers to your C / C++ code. But parallel programing on graphics cards needs current code rewriting.

Graphics cards have lower performance than the competition at double precision computing. It is due to the fact that every third stream processor also has a support double. In newer cards intended primarily for the gaming segment (GeForce and Quadro series), double precision performance is even worse. [6]

NVIDIA Maxwell architecture (3th)

- 512 – 3584 CUDA cores,
- 2 – 16 GB DDR5.

Benefits – (there is no need to learn a new programming language. Only the techniques of parallel processing. Using ready-optimized libraries. Already programmed codes can be used, which do not require parallel processing. Detailed documentation. Own CUDA repository for many Linux distributions).

Disadvantages – Elements of calculations must not be dependent per se, thus it can not be used for addressing all issues – for example it is totally inefficient for the finite element method. Parallel programing on graphics cards needs

code rewriting. In many models of graphics cards there is lower performance when working with double numbers - double precision.

B. AMD stream graphics cards with OpenCL

AMD lags in benchmark tests behind competing NVIDIA products. Lower throughput and fewer operations per second This is probably primarily due to the fact that in recent years, AMD focused on inventing new architecture GCN (Graphics Core Next) suitable for parallel computing and easier programming, whereas NVIDIA expanded the existing graphics cards concept.

AMD Volcanic Architecture (3rd)

- 1792 – 4096 stream processors,
- 2 – 8 GB DDR5.

Benefits – lower price (about 2/3) with a similar absolute output (absolute performance) of the competing NVIDIA.

Disadvantages – AMD lags in benchmark tests behind competing NVIDIA latest products. Lower throughput and fewer operations per second. Only OpenCL support.

C. Intel Xeon Phi

This is not a graphics card, its philosophy is based largely on the x86 multi-core CPU concept. Design is derived from Atom, but they hat Hyper-Treading support. Knights Landing has 4 thread per core.

Programmes designed for today's Xeon processors in supercomputers will thus operate almost without any problems, yet optimization will be necessary for making use of ultimate performance. It is not necessary however to completely overwrite programmes and thus programmers can focus only on optimizing. A more universal application for computations of a wider range of problems. [15] [16]

Intel Knights Landing Architecture (2rd)

- 50 – 72 cores,
- 8 – 16 GB DDR4.

Benefits - Programs designed for contemporary Xeon server processors will operate almost without any problems, but it will be necessary code optimization for ultimate performance. There is no need to rewrite existing programs and programmers can focus only on optimizing. Universal application for computations, wider spectrum of problems. Newer “nanometres technology”. [17]

Disadvantages – At the moment they do not achieve so much FLOPS, compared to competitive solutions. Intel is the youngest in the field of parallel computing cards. Neither the hiring many top engineers it fails to catch up with the years of experience of competing brands.

D. Contemporary hardware - absolute performance comparison

The TABLE I below is a comparison of competing products with similar date of the sale - about 2013. The contractions were to compare competing products of similar categories and generations. Data were obtained from manufacturer pages, especially from [18], [19]. FLOPS (FLoating-point Operations Per Second).

For an idea is presented in TABLE I performance of processor Intel i7 6700K, based on Skylake architecture. It belongs to the highest class of desktop processors (in year 2016).

TABLE I. COMPARED DEVICE FROM SIMILAR CLASS ^a.

Feature	NVIDIA Tesla K40	NVIDIA GTX Titan	AMD Radeon R9 285	Intel Phi 5110P	CPU i7 6700K
Peak double precision floating point performance	1.43 Tflops	1.17 Tflops	0.21 Tflops	1.02 Tflops	0.08 Tflops
Peak single precision floating point performance	4.29 Tflops	3.52 Tflops	3.29 Tflops	2.06 Tflops	0.21 Tflops
Memory bandwidth (ECC off)	288 GB/s	208 GB/s	176 GB/s	320 GB/s	34.1 GB/s
Memory size (GDDR5)	12 GB	5 GB	2 GB	8 GB	-
Cores or stream processors	2880	2496	1792	60 (240)	4 (8)

^a. FLOPS (FLoating-point Operations Per Second)

VI. CONCLUSION

Xeon Phi is based more on standard CPU architecture. NVIDIA CUDA and AMD STREAM use different graphics card architecture, which requires significant changes in the original programme codes.

Effectivity of card depends on base unit clock, but more on architecture. AMD stream processors, CUDA cores and Intel cores, are basic compute units, but with so different performance per core. This is due to the various architectures. The performance is relatively comparable by FLOPS. Performance depends not only on the hardware, but also depends on the optimization of API.

NVIDIA is long-term winner thanks great performance tests, but also it is already widespread among programmers. During this year, NVIDIA placed on the market products on a completely redesigned architecture with name Pascal, which promises ten times bigger performance in comparison with current products on the Maxwell architecture.

New programming language and API - OpenCL, can by new long-term multi-platform solutions. Still not enough yet

developed, and it may be necessary large optimization after migration to new hardware.

REFERENCES

- [1] "Vertex Shader", OpenGL, 2015. [Online]. Available: https://www.opengl.org/wiki/Vertex_Shader. [Accessed: 09-Aug.-2016].
- [2] "Geometry Shader", OpenGL, 2015. [Online]. Available: https://www.opengl.org/wiki/Geometry_Shader. [Accessed: 09-Aug.-2016].
- [3] "Compute Shader", OpenGL, 2015. [Online]. Available: https://www.opengl.org/wiki/Compute_Shader.
- [4] "HLSL: Common-Shader Core", *Microsoft Developer Network*, 2016. [Online]. Available: [https://msdn.microsoft.com/en-us/library/bb509580\(VS.85\).aspx](https://msdn.microsoft.com/en-us/library/bb509580(VS.85).aspx). [Accessed: 22-Aug.-2016].
- [5] "About GPGPU", *GPGPU*, 2016. [Online]. Available: <http://gpgpu.org/about>. [Accessed: 09-Aug.-2016].
- [6] A. Rege, "An Introduction to Modern GPU Architecture", in *NVIDIA DEVELOPER: NVIDIA SDK*, 2008. [Online]. Available: http://http.download.NVIDIA.com/developer/cuda/seminar/TDCI_Arch.pdf [Accessed: 09-Aug.-2016].
- [7] "CUDA COMPILER DRIVER NVCC: Reference Guide", *NVIDIA Developer Zone: CUDA Toolkit Documentation*, 2015. [Online]. Available: http://docs.NVIDIA.com/cuda/pdf/CUDA_Compiler_Driver_NVCC.pdf. [Accessed: 09-Aug.-2016].
- [8] O. Morský, *Základy zpracování signálů na GPU*, vol. 12, no. 2. Brno: Elektrověda, 2010.
- [9] "About CUDA", *NVIDIA Accelerated computing: CUDA ZONE*, 2016. [Online]. Available: <https://developer.NVIDIA.com/about-cuda>. [Accessed: 09-Aug.-2016].
- [10] "CUDA Toolkit Documentation" .", in *NVIDIA Developer zone: CUDA Toolkit Documentation*, 2015. [Online]. Available: <https://developer.NVIDIA.com/cuda-toolkit>. [Accessed: 09-Aug.-2016].
- [11] "CUDA C PROGRAMMING GUIDE: Design Guide", in *NVIDIA Developer zone: CUDA Toolkit Documentation*, 2015. [Online]. Available: <http://docs.NVIDIA.com/cuda>. [Accessed: 09-Aug.-2016].
- [12] "OpenCL", in *Wikipedia: the free encyclopedia*, 2001-. [Online]. Available: <https://en.wikipedia.org/wiki/OpenCL>.
- [13] "OpenCL", *NVIDIA Accelerated computing: CUDA ZONE*, 2016. [Online]. Available: <https://developer.NVIDIA.com/opencl>. [Accessed: 09-Aug.-2016].
- [14] "The open standard for parallel programming of heterogeneous systems", *KHRONOS GROUP*. [Online]. Available: <https://www.khronos.org/opencl>. [Accessed: 09-Aug.-2016].
- [15] "Intel Many Integrated Core Architecture - Advanced", *Intel: Architecture and technology*. [Online]. Available: <http://www.intel.com/content/www/us/en/architecture-and-technology/many-integrated-core/intel-many-integrated-core-architecture.html>. [Accessed: 09-Aug.-2016].
- [16] J. Hruska, "Intel's next-generation Xeon Phi, Knights Landing, now shipping to developers", in *EXTREMETECH*, 2016.
- [17] "Powerful Performance for Deeper Insights", *Intel: Xeon processors*, 2016. [Online]. Available: <http://www.intel.com/content/www/us/en/processors/xeon/xeon-phi-detail.html>. [Accessed: 09-Aug.-2016].
- [18] "NVIDIA TESLA GPU ACCELERATORS", *NVIDIA Tesla*, 2013. [Online]. Available: <http://www.nvidia.com/content/tesla/pdf/NVIDIA-Tesla-Kepler-Family-Datasheet.pdf>. [Accessed: 09-Aug.-2016].
- [19] V. Hindriksen, "Intel's answer to AMD and NVIDIA: the XEON Phi 5110P", *STREAM COMPUTING: Performance Engineers*, 2012. [Online]. Available: <https://streamcomputing.eu/blog/2012-11-12/intels-answer-to-amd-and-NVIDIA-the-xeon-phi-5110p/>. [Accessed: 09-Aug.-2016].

3D Textile Integrated TIW Horn Antenna for UWB Wirelles Link

Miroslav Cupal

Department of Radio Electronics
Brno University of Technology
Technická 12, 61600, Brno, Czech Republic
cupalm@phd.feec.vutbr.cz

Abstract—This paper deals with textile integrated H-plane horn antenna for in-car communication. The antenna is designed on 3D textile material produced by SINTEX Company. The antenna is placed close to conductive plate which simulates roof of a car or small planes and buses. Results for different distances between the antenna and the metal plate are presented as well.

Keywords—horn antenna; 3D textile; TIW; car; UWB;

I. INTRODUCTION

Most of automobile manufacturers produce automobiles with large number of sensors. These sensors improve quality of traveling, safety and they help with driving. There are first examples of full autonomy cars that can drive without driver's assistance. Small wire networks are used for connection small modules like parking cameras, radars, air-condition sensors etc. The weight of the wires is approximately 35 kg for one car. The part of the wires would be replaced with wireless system.

UWB system could be very good solution for in-car communication between central unit and sensors, safety systems or between central unit and audio-video equipment. The theoretical bandwidth of UWB system is more than 500 MHz or 20% of fractional bandwidth [1].

The spectrum for UWB has been defined up 3.1-10.6 GHz. The WiMedia alliance has defined fourteen 528 MHz bands in 2002. The band group 6 is very interesting because it is the only band where all countries agree. The division of the UWB is shown in Fig. 1 [1].

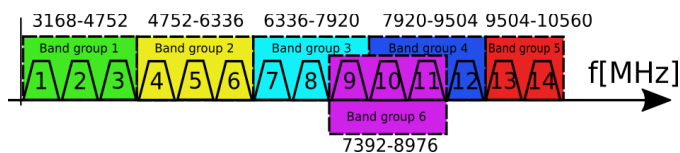


Fig. 1. Ultra-wide band frequency map

II. 3D TEXTILE H-PLANE HORN ANTENNA

A. 3D textile parameters

The 3D textile material consists of two firm textile layers with fine fibers in between. Fine fibers ensure a constant distance of firm layers. The top and bottom layers of the 3D textile could be developed from different textile material than the middle layer. For example, top and bottom layer could be conductive (conductive textile) and middle could be dielectric

(nilon). This structure is very advantageous for antennas and microwaves application because 3D textile do not need any additional layers and adjustments.

The height of the 3D textile produced by SINTEX, www.sintex.cz is $h = 3.4$ mm and the dielectric constant is $\epsilon_r = 1.4$. The top and bottom layers are developed from cotton and middle layer is nilon. The 3D textile can have different thickness, different materials and colors. For example, the top and bottom layers could be conductive and middle layer could be dielectric but in this paper is used only all dielectric 3D textile.

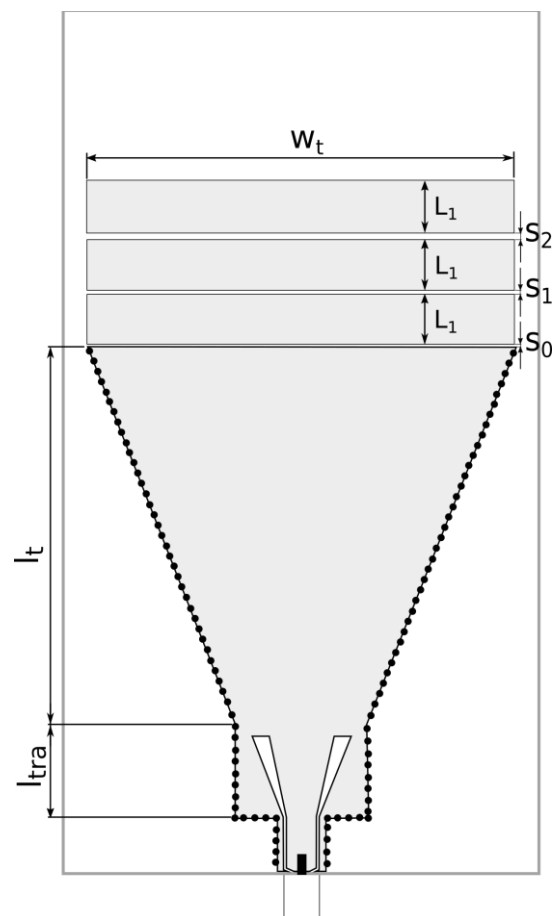


Fig. 2. Designed antenna, TOP view

B. H-plane horn antenna design

The design of an H-plane TIW horn antenna is very similar of a conventional pyramidal horn antenna. The antenna is fed with textile integrated waveguide. I have to respect basic design rules for a single mode excitation resulting in the condition 1[2].

$$\lambda_0 \sqrt{2\varepsilon_r} < a < \frac{\lambda_0}{\varepsilon_r}, \quad (1)$$

,where λ_0 is wavelength in free space, ε_r dielectric constant, a is width of waveguide.

The excitation of the TIW is realized with GCPW (grounded coplanar waveguide). There is a small problem because the width of the GCPW is large than the diameter of the SMA connector. Therefore, I need to use the edited GCPW close to SMA connector [2] and [3,7-9].

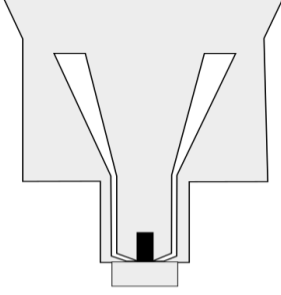


Fig. 3. Antenna feeding structure

I use planar resonators front of the horn to improve bandwidth and radiation patterns of the antenna. There are three planar resonators front of the horn with the same dimensions. Gaps between resonators are different to improve frequency bandwidth and radiation patterns. The resonance frequency of one resonator is

$$f_{r1} = \frac{c}{2l_{eq}\sqrt{\varepsilon_r}}, \quad (2)$$

where f_{r1} is resonant frequency, c is speed of light, l_{eq} is equivalent length of the resonator and ε_r is the dielectric constant of the substrate. There are capacitive couples between resonators. The resonant frequency of the coupled resonator can be calculated with:

$$f_{r2\pm} = \frac{f_{r1}}{\sqrt{1 \pm k_2}}, \quad (3)$$

where k_2 is the coupling factor [4-6].

C. Designed antenna

Feeding of the textile integrated waveguide is realized with SMA connector connected to grounded coplanar waveguide. You can see the detail of the feeding structure at the Fig. 3. The feeding structure is designed for minimal radiation into surrounding space. The designed antenna is depicted in Fig. 1 and the numerical values are shown in Table 1.

Simulations and experiments in laboratories of the SIX Center were financed by the project LO1401 INWITE of the National Sustainability Program. Research is a part of the COST Action IC 1301 WiPE supported by the grant LD14057 of the Czech Ministry of Education.

TABLE I. PARAMETERS OF DESIGNED ANTENNA

Dimension	w_t	l_{tra}	l_t	L_1	S_0
Value [mm]	90	18.85	80	10.05	0.25
Dimension	S_1	S_2			
Value [mm]	0.88	1.77			

III. SIMULATION RESULTS

The antenna was simulated in the CST Microwave Studio. The antenna was simulated in free space and close to conductive plate. The conductive plate was covered with 3D textile material and the gap between metal plate and the 3D textile material was 0 mm.

A. Antenna 0 millimeters of metal plate

Frequency response of the reflection coefficient of the designed antenna operating close to metal plate is depicted in Fig. 4. The impedance bandwidth for $S_{11} < -10$ dB is BW = 4.86 GHz (55 %). The antenna covers 100 % of UWB band-group 6 (7.392 to 8.976 GHz).

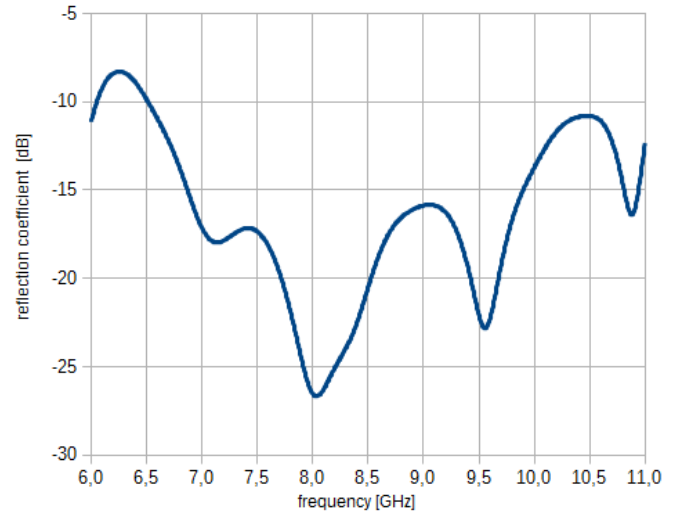


Fig. 4. Frequency response of reflection coefficient antenna close to metal plate

In **Chyba! Nenalezen zdroj odkazů.** and **Chyba! Nenalezen zdroj odkazů.** are radiation patterns of the antenna in planes E and H for nine frequencies. The simulated maximal gain of the antenna close to metal plate is 13.23 dBi in the main lobe direction at 8 GHz. The elevation angle in E-plane is 20°. In H-plane, the simulated gain is 11.87 dBi. At a frequency 8 GHz, the antenna radiates perpendicularly to the plane of the substrate. A high level of side lobes is the disadvantage of the antenna. The average side lobe level is 12 dBi in E-plane.

B. Antenna in different distances of metal plate

H-plane horn antenna was simulated in different distances between antenna and metal plate. The attention was paid to

frequency response of reflection coefficient and radiation patterns in E and H plane. The distances between antenna and metal plate are 0, 1, 2.5, 5, 10 and 20 millimeters. Antenna was simulated in free space to.

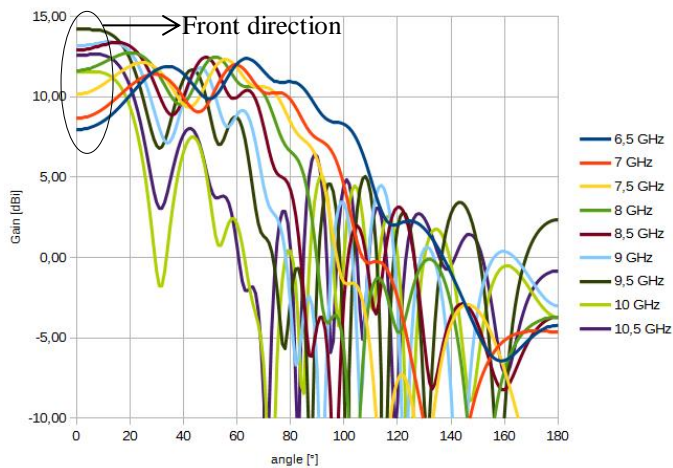


Fig. 5. Radiation patterns of antenna 0 mm close to metal surface E-plane

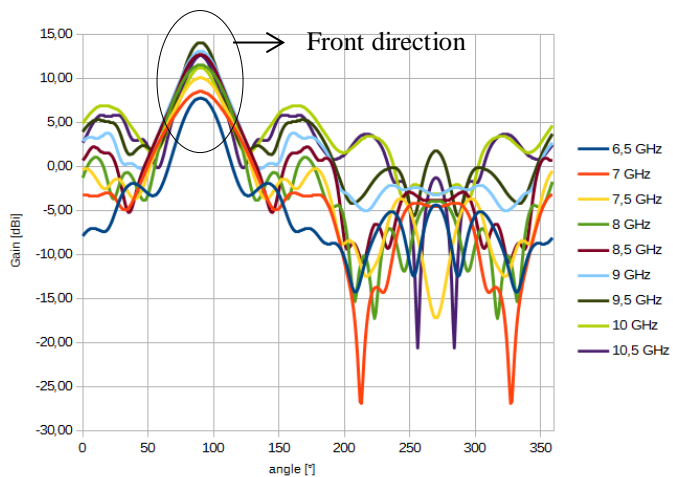


Fig. 6. Radiation patterns of antenna 0 mm close to metal surface H-plane

In Fig. 7 are reflections coefficients of the antenna close to metal plate, but in different distances. The metal surface affects the capacity couple between resonators. For case where the distance between metal plate and the antenna is one millimeter, the resonators are coupled very strongly. In other cases the effect of metal surface decreases and reflection coefficient is similar to antenna in free space.

In Fig. 8 and Fig. 9 are radiations patterns of the antenna close to metal plate, but in different distances. The gain is bigger for bigger distances between antenna and metal surface, but level of side lobes and back lobe is bigger too. Antenna radiates into space (elevation angle of mine lobe bigger than 60°) if the metal plate is far from antenna.

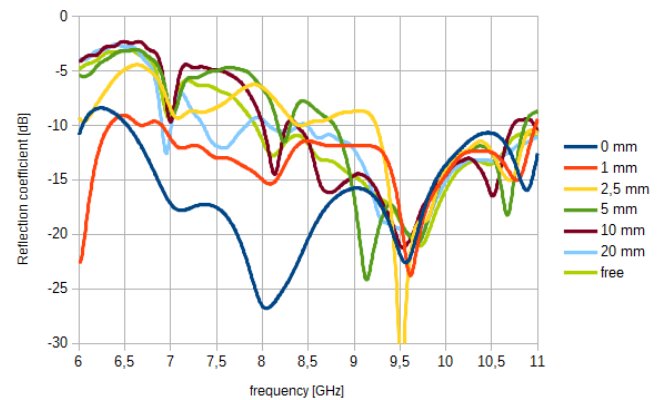


Fig. 7. Frequency response of reflection coefficient antenna for different distances between antenna and metal plate

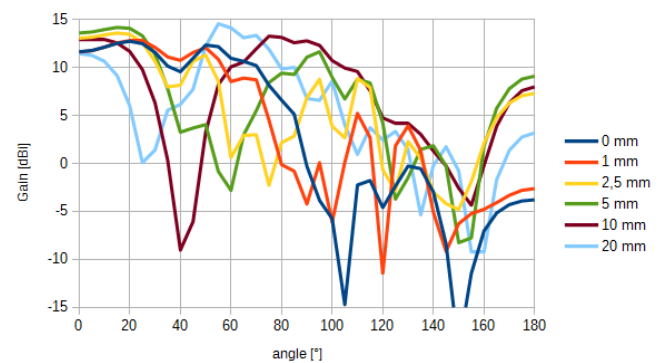


Fig. 8. Radiation patterns of antenna close to metal surface E plane at 8 GHz

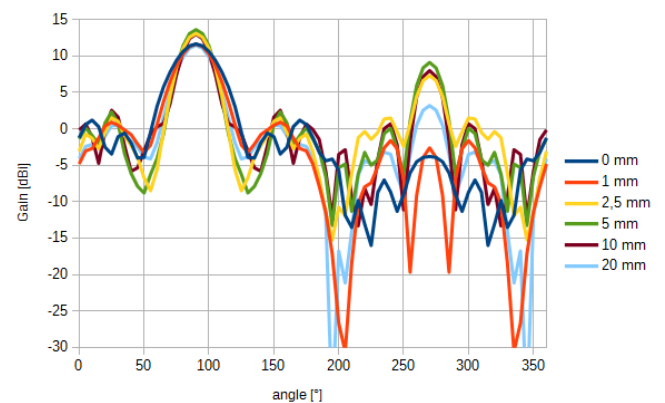


Fig. 9. Radiation patterns of antenna close to metal surface H plane at 8 GHz

CONCLUSION

The H-plane TIW horn antenna was designed for the operation close to conductive surfaces in the UWB band-group 6. The antenna is fed with grounded coplanar waveguide for minimize radiation of the transition between GCPW and textile integrated waveguide. The antenna covers 100 % of this band. The bandwidth of the antenna is 55 % for antenna close to

metal surface as is possible. The antenna shows an elevation 20° in proximity of a conductive plate.

Antenna was simulated in different distances of metal plate. Metal plate affects planar resonators front of the horn and properties of the antenna. To use the antenna in different distances have to be edited length of the resonators and the gaps between them.

REFERENCES

- [1] I. Oppermann, M. Hämäläinen and J. Iinatti. UWB theory and applications. Chichester: Wiley, 2004.
- [2] X. Chen, W. Hong, T. Cui, J. Chen, and K. Wu. "Substrate integrated waveguide (SIW) linear phase filter," IEEE Microwave and Wireless Components Letters, vol. 15, issue 11, pp.
- [3] F. Giuppi, A. Georgiadis, A. Collado, M. Bozzi, and L. Perregrini. "Tunable SIW cavity backed active antenna oscillator," Electronics Letters, vol. 46, issue 15, pp. 1053-, 2010.
- [4] C. I. Yeh, D. H. Yang, T. H. Liu, Jeffrey S. Fu, K. S. Chin, J. C. Cheng, Chiu, and C. P. Kao. "MMIC compatibility study of SIW H-plane horn antenna," 2010 International Conference on Microwave and Millimeter Wave Technology, pp. 933-936, 2010.
- [5] M. Esquiús-Morote, B. Fuchs, Jean-Francois Zurcher, and J. R. Mosig. "A Printed Transition for Matching Improvement of SIW Horn Antennas," IEEE Transactions on Antennas and Propagation, vol. 61, issue 4, pp. 1923-1930, 2013.
- [6] M. Esquiús-Morote, B. Fuchs, Jean-Francois Zurcher, and J. R. Mosig. "Novel Thin and Compact H-Plane SIW Horn Antenna," IEEE Transactions on Antennas and Propagation, vol. 61, issue 6, pp. 2911-2920, 2013.
- [7] C. A. Balanis. Antenna theory: analysis and design, 3rd ed. Hoboken: Wiley-Interscience, 2005. ISBN 978-0-471-66782-7.
- [8] T. Mikulasek, A. Georgiadis, A. Collado, and J. Lacik. Microstrip Patch Antenna Array Fed by Substrate Integrated Waveguide for Radar Applications," IEEE Antennas and Wireless Propagation Letters, vol. 12, pp. 1287-1290, 2013.
- [9] J. Lacik and T. Mikulasek, "Circular ring-slot antenna fed by SIW for WBAN applications," in Proc. 7th Eur. Conf. on Antennas and Propagation (EuCAP), Gothenburg, Sweden, Apr. 2013, pp. 213-216

Electronically Reconfigurable Universal Frequency Filter with Controllability of its Pole Frequency

Jan Dvorak

Faculty of Electrical Engineering and
Communication

Brno University of Technology

Brno 616 00, Technicka 12

Email: dvorakjan@phd.feec.vutbr.cz

Adam Gajdos

Faculty of Electrical Engineering and
Communication

Brno University of Technology

Brno 616 00, Technicka 12

Email: adamgajdos@phd.feec.vutbr.cz

Jan Jerabek

Faculty of Electrical Engineering and
Communication

Brno University of Technology

Brno 616 00, Technicka 12

Email: jerabekj@feec.vutbr.cz

Abstract—This paper deals with electronically reconfigurable current-mode filter with controllable pole frequency. The proposed filter contains these active elements: Current Conveyor Transconductance Amplifier (CCTA), Operational Transconductance Amplifier (OTA) and Adjustable Current Amplifier (ACA). The filter contains only single input and output (SISO). The filtering functions of the circuit can be electronically switched by current gain of the ACA elements without any reconnection in topology. The reconfigurable filter provides the ability to control pole frequency without disturbing quality factor. The PSpice simulator was used for verifying function of the proposed filter using available models of the active elements.

I. INTRODUCTION

The digital signal processing is the highly interested topic nowadays. However, there are still many scientific teams, who are interest about analogue frequency filters [1] – [15]. The great area of interest are filtering structures, which can realize various filtering functions or it is possible to control some of its parameters (pole frequency, quality factor, pass-band gain, bandwidth or the order of the filter).

Most of the papers describe the filtering structures, which allow to obtain all types of the transfer functions (low-pass, band-pass, high-pass, band-reject or all-pass) with adjustable parameters [1] – [11]. The transfer functions are usually obtained by manual reconnection of an output or input of the filter. The frequency filters can be divided according to number of inputs and outputs: single input-multiple output (SIMO) [1], [2], [4], [6] – [8], multiple input-single output (MISO) [3] or single input-single output (SISO) [9] – [14] filtering structures.

Reconfigurable filtering circuits represent one of the newer topic, which is attractive to many scientific teams [9] – [15]. These circuits contain only one input and output (SISO type of filtering structure). Nevertheless, the various types of transfer functions can be obtained from single output of the structure using electronically controlling of parameters of active elements. It is thus a filter which provides more types of transfer functions without manual reconnection of its input or output. Except reconfiguration of the type of transfer function, controllability of the pole frequency or quality factor is possible depending to selected types of the active elements of a proposed filter. The wide variety of active elements can be used for the design of a reconfigurable filter. For example, Operational Transconductance Amplifier (OTA) [6], [16], Current Conveyor Transconductance Amplifier (CCTA) [8], [16],

[17], Voltage Differencing Current Conveyor (VDCC) [16], Modified Current Differencing Unit (MCDU) [9] or Adjustable Current Amplifier (ACA) [18].

This paper deals with proposal of the universal reconfigurable frequency filter that operates in current mode. The circuit consists of CCTA, OTA and ACA active elements as described in section II. The proposed filter provides electronic switching of the various types of transfer functions and tuning of the pole frequency using adjustable parameters of the used active elements. The filter features were verified by PSpice simulations.

II. USED ACTIVE ELEMENTS

This section present the description of active elements, which are used for proposal of the filter. The filter structure contains three types of the used active elements.

The first type of the used active element is Operational Transconductance Amplifier (OTA), Balanced Output Operational Transconductance Amplifier (BOTA) respectively [6], [16]. The schematic symbol of this element is illustrated in Fig. 1. The OTA can be described by following relation: $i_{OUT+} = -i_{OUT-} = g_m \cdot (u_{IN+} - u_{IN-})$, where g_m is electronically controllable transconductance.

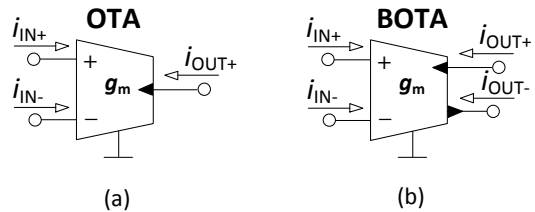


Fig. 1. Schematic symbol: (a) Operational Transconductance Amplifier (OTA), (b) Balanced Operational Transconductance Amplifier (BOTA)

Second used active element is Current Conveyor Transconductance Amplifier (CCTA) [8], [16], [17]. The CCTA consists of second-generation Current Conveyor with two outputs (CCII+/-) [19] that is followed by OTA element. For purposes of increasing the number of the outputs of the CCTA the BOTA can be used instead of OTA. The schematic symbol

is shown in Fig. 2, together with internal block structure. The basic adjustable parameter of this element is transconductance g_m . This element can be described by the following matrix:

$$\begin{bmatrix} i_Y \\ u_X \\ i_Z \\ i_{OUT} \end{bmatrix} = \begin{bmatrix} 0 & 0 & 0 \\ 1 & 0 & 0 \\ 0 & 1 & 0 \\ 0 & 0 & g_m \end{bmatrix} \cdot \begin{bmatrix} u_Y \\ i_X \\ u_Z \end{bmatrix}. \quad (1)$$

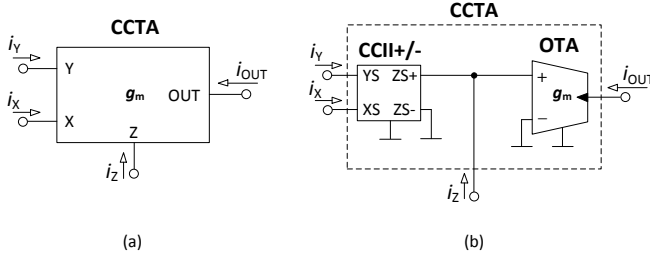


Fig. 2. Current Conveyor Transconductance Amplifier (CCTA): (a) Schematic symbol, (b) internal block structure

The last used active element is Adjustable Current Amplifier (ACA) [18]. The schematic symbol is shown in Fig. 3. Function of this active element is described by the following equation: $i_{OUT} = B \cdot i_{IN}$, where B is current gain.

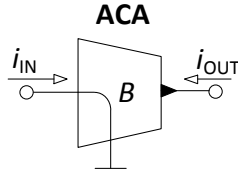


Fig. 3. Schematic symbol of Adjustable Current Amplifier (ACA)

III. DESIGNED FILTER

The universal reconfigurable frequency filter provides electronic switching of the filter functions and also ability to control the pole frequency of the filter. The filter structure is shown in Fig. 4. It consists of three ACAs, one CCTA, one OTA, two capacitors and one resistor.

Transfer function of this filter is described by the following equation:

$$K(s) = \frac{I_{OUT}}{I_{IN}} = \frac{s^2 C_1 C_2 B_1 - s C_1 g_{m1} B_2 + G g_{m2} B_3}{D}, \quad (2)$$

where

$$D(s) = s^2 C_1 C_2 + s C_1 g_{m1} + G g_{m2}. \quad (3)$$

The equations of the pole frequency and quality factor are described as follows:

$$f_0 = \frac{1}{2\pi} \sqrt{\frac{g_{m2} G}{C_1 C_2}}, \quad (4)$$

$$Q = \sqrt{\frac{C_2 g_{m2} G}{C_1 g_{m1}^2}}. \quad (5)$$

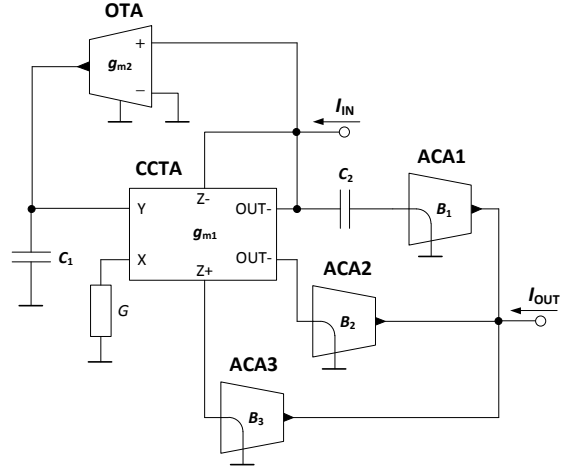


Fig. 4. Structure of the electronically reconfigurable filter

For possibility to control of the pole frequency (f_p) of the filter, without disturbing quality factor (Q), is used condition: $g_m = g_{m1} = g_{m2} = G$.

The each transfer function of the filter is obtained from equation 1 by controlling of the B_1 , B_2 and B_3 current gains. The transfer functions are as follows:

- HP response: $B_1 \neq 0$, $B_2 = 0$ and $B_3 = 0$. Pass-band gain can be controlled by B_1 , while $B_1 = 1$ provides theoretically zero pass-band attenuation.
- iBP response: $B_1 = 0$, $B_2 \neq 0$ and $B_3 = 0$. Pass-band gain can be tuned by current gain B_2 , while $B_2 = 1$ provides theoretically zero pass-band attenuation.
- LP response: $B_1 = 0$, $B_2 = 0$ and $B_3 \neq 0$. Pass-band gain can be tuned by B_3 parameter, while $B_3 = 1$ provides theoretically zero pass-band attenuation.
- BR response: $B_1 \neq 0$, $B_2 = 0$ and $B_3 \neq 0$. Pass-band gain can be controlled by B_1 and B_3 . If $B_1 = 1$ and $B_3 = 1$, theoretically zero pass-band attenuation is obtained.
- AP response: $B_1 \neq 0$, $B_2 \neq 0$ and $B_3 \neq 0$. Pass-band gain can be adjusted by B_1 , B_2 and B_3 . Configuration $B_1 = 1$, $B_2 = 1$, $B_3 = 1$ provides theoretically zero pass-band attenuation.

IV. SIMULATION RESULTS

The function of the filter, which is demonstrated in Fig. 4, was verified in PSpice simulator. OTA and CCTA elements were simulated using 3rd-level model of the UCC (Universal Current Conveyor) and CCII+/- [19]. For simulation of the ACA element was used current multiplier EL2082 [20]. Basic

parameters of the proposed filter are: starting value of the pole frequency $f_p = 1$ MHz, quality factor $Q = 0.707$ and starting value of the $g_m = G = 2$ mS. The capacitors, which are calculated from equations 4 and 5, are: $C_1 = 450$ pF and $C_2 = 225$ pF. The pole frequency $f_p = \{250; 500; 1000; 2000\}$ kHz is controlled by $g_m = G = \{0.5; 1; 2; 4\}$ mS.

The simulation (solid lines) and theoretical (dashed lines) results of the LP ($B_1 = 0, B_2 = 0, B_3 = 1$), BP ($B_1 = 0, B_2 = 1, B_3 = 0$), HP ($B_1 = 1, B_2 = 0, B_3 = 0$) and BR ($B_1 = 1, B_2 = 0, B_3 = 1$) responses are illustrated in Fig. 5. The functions are obtained by adjusting of the B_1, B_2 and B_3 parameters. From obtained characteristics can be seen that simulations results are very close to the theoretical results. The differences at higher frequencies are caused by limited frequency range of the used simulation models of the active elements. This applies to all results in this paper.

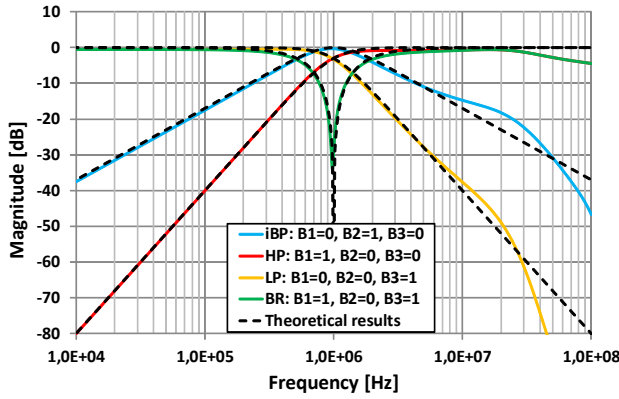


Fig. 5. Simulation results (solid lines) of the filter transfer functions in comparison with theoretical results (dashed lines) when $f_p = 1$ MHz and $g_m = G = 2$ mS

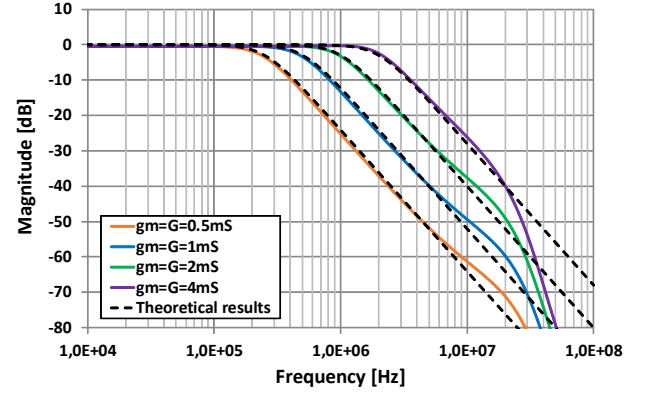
The LP, BR and AP ($B_1 = 1, B_2 = 1, B_3 = 1$) responses for four different pole frequencies are shown in Fig. 6 (a), Fig. 6 (b) and Fig. 6 (c). The pole frequency is tuned by $g_m = G$. Obtained values of the pole frequencies of the LP response are summarized in Tab. I. At frequencies above 20 MHz are also distinct differences between simulation and theoretical results.

TABLE I. VALUES OF THE THEORETICAL AND SIMULATED POLE FREQUENCIES FOR LP RESPONSE WHEN ADJUSTING f_p BY $g_m = G$

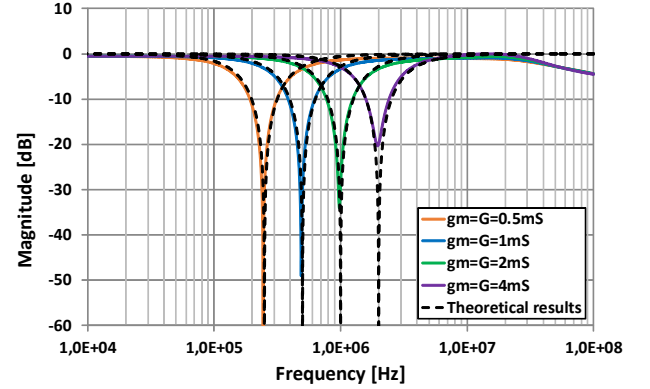
$g_m = G$ [mS]	Theoretical f_0 [kHz]	Simulated f_0 [kHz]
0.5	250	249
1	500	505
2	1000	1021
4	2000	2221

Fig. 7 (a) demonstrate electronic reconfiguration from AP to BR response by tuning B_2 current gain when $B_1 = 1, B_3 = 1, f_p = 1$ MHz and $g_m = G = 2$ mS. The simulation results are shown as solid lines and theoretical results are illustrated by dashed lines. Values of B_2 current gains have been set to 1, 0.75, 0.5, 0.25 and 0. From graph it obvious, that when B_2 is controlled from 1 to 0, the AP transfer function changes to BR. The reconfiguration from BR to HP response for five values of the B_3 current gain is depicted in Fig. 7 (b). Other parameters

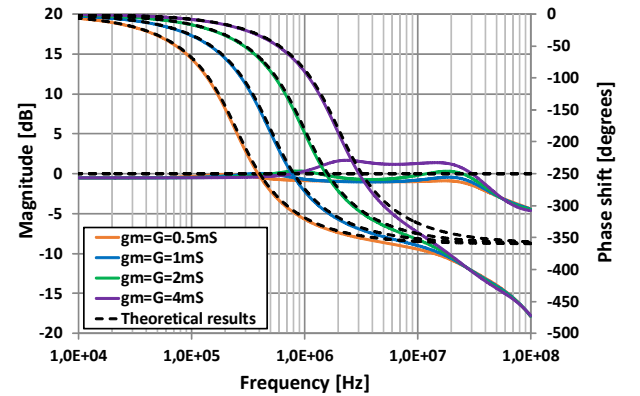
are: $B_1 = 1, B_2 = 0, f_p = 1$ MHz and $g_m = G = 2$ mS. From Fig. 7 (b) can be seen that if B_3 is controlled in range from 1 to 0, the BR function changes to HP function. From both graphs it obvious that simulation results are not so much different from theoretical results.



(a)



(b)



(c)

Fig. 6. Demonstration of the pole frequency controlling by g_m . Simulation results - solid lines, theoretical results - dashed lines. (a) LP responses (b) BR responses (c) AP responses (magnitude and phase responses)

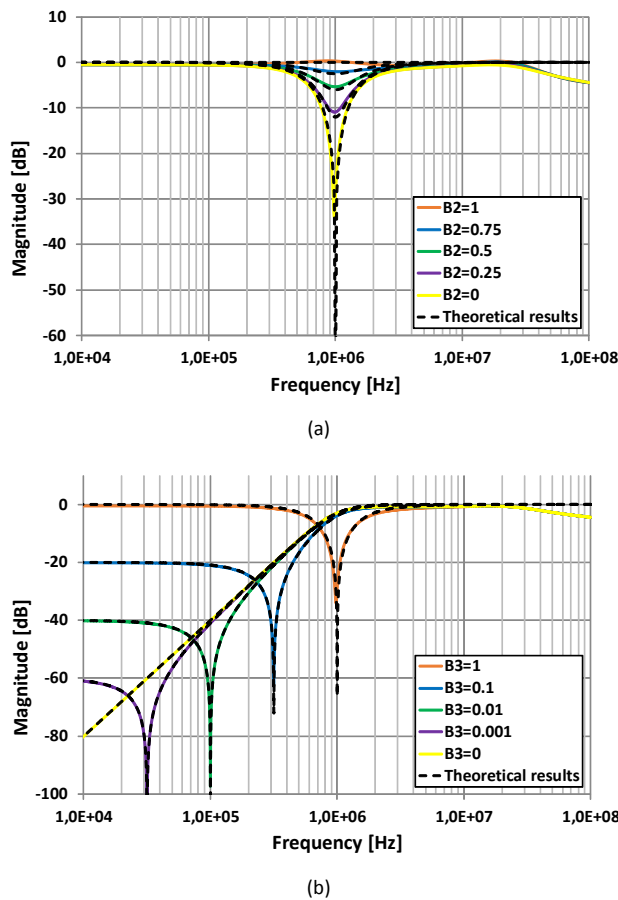


Fig. 7. Simulation results of the reconfigurable filter. Solid lines are simulation results and dashed lines are theoretical results. (a) Controlling AP response by B_2 gain while B_1 and B_3 were set to unity gain (b) Tuning stop-band gain of the HP response by B_3 gain while $B_1 = 1$ and $B_2 = 0$

V. CONCLUSION

Proposal and simulations of the reconfigurable universal filter are mentioned in this paper. This filter provides LP, BP, HP, BR and AP transfer functions. The transfer functions are obtained from single output by adjusting of the individual current gains of the ACA elements. Control of the frequency without disturbing quality factor is also demonstrated in this paper. The function of the proposed filter has been verified by simulations in PSpice simulator. From obtained results can be stated that simulations are in good agreement with theoretical results. Nevertheless, the proposed filter would be preferable to implement and measure for obtaining real results of this filter.

REFERENCES

- [1] C. Wang, J. Xu, A. Keskin, S. Du, and Q. Zhang, "A new current-mode current-controlled SIMO-type universal filter", *AEU - International Journal of Electronics and Communications*, vol. 65, no. 3, pp. 231-234, 2011.
- [2] H. -P. Chen, "Tunable versatile current-mode universal filter based on plus-type DVCCs", *AEU - International Journal of Electronics and Communications*, vol. 66, no. 4, pp. 332-339, 2012.
- [3] W. Jaikla, S. Siripongdee, and P. Suwanjan, "MISO Current-mode Biquad Filter with Independent Control of Pole Frequency and Quality Factor", *Radioengineering*, vol. 21, no. 3, pp. 886-891, 2012.
- [4] E. Yuce and S. Minaei, "Universal current-mode filters and parasitic impedance effects on the filter performances", *International Journal of Circuit Theory and Applications*, vol. 36, no. 2, pp. 161-171, 2008.
- [5] L. Langhammer, J. Jerabek, J. Polak, and P. Cika, "Single-Ended and Fully-Differential Current-Input Current-Output Universal Frequency Filter with Transconductance and Transresistance Amplifiers", *WSEAS Transactions on Circuits and Systems*, vol. 14, pp. 56-67, 2015.
- [6] J. Jerabek and K. Vrba, "Current-mode tunable and adjustable filter with digitally adjustable current amplifier and transconductance amplifiers", in *Proceedings of the European Conference of Circuits Technology and Devices (ECCTD'10)*, 2010.
- [7] J. Jerabek, R. Sotner, and K. Vrba, "Tunable Universal Filter with Current Follower and Transconductance Amplifiers and Study of Parasitic Influences", *Journal of Electrical Engineering*, vol. 62, no. 6, pp. 317-326, 2011.
- [8] R. S. Tomar, S. V. Singh, and D. S. Chauhan, "Current Processing Current Tunable Universal Biquad Filter Employing Two CCTAs and Two Grounded Capacitors", *Circuits and Systems*, vol. 04, no. 06, pp. 443-450, 2013.
- [9] R. Sotner, J. Jerbek, N. Herencsar, T. Zak, W. Jaikla, and K. Vrba, "Modified Current Differencing Unit and its Application for Electronically Reconfigurable Simple First-order Transfer Function", *Advances in Electrical and Computer Engineering*, vol. 15, no. 1, pp. 3-10, 2015.
- [10] R. Sotner, J. Jerabek, N. Herencsar, R. Prokop, K. Vrba, and T. Dostal, "First-order reconfigurable reconnection-less filters using modified current differencing unit", *2015 25th International Conference Radioelektronika (RADIOELEKTRONIKA)*, pp. 46-50, 2015.
- [11] S. Minaei, E. Yuce, and O. Cicekoglu, "Electronically tunable multi-input single-output voltage-mode filter", *Proceedings of the 2005 European Conference on Circuit Theory and Design*, 2005, pp. 401-404, 2005.
- [12] R. Sotner, J. Jerabek, N. Herencsar, R. Prokop, K. Vrba, and T. Dostal, "First-order reconfigurable reconnection-less filters using modified current differencing unit", *2015 25th International Conference Radioelektronika (RADIOELEKTRONIKA)*, pp. 46-50, 2015.
- [13] R. Sotner, J. Jerabek, R. Prokop, V. Kledrowetz, L. Fajcik, and T. Dostal, "Reconfigurable 1 st order filters based on differential voltage input and a single current output transconductance multiplier", *IEEE EUROCON 2015 - International Conference on Computer as a Tool (EUROCON)*, pp. 1-4, 2015.
- [14] R. Sotner, J. Petrzela, J. Jerabek, K. Vrba, and T. Dostal, "Solutions of reconnection-less OTA-based biquads with electronical transfer response reconfiguration", *2015 25th International Conference Radioelektronika (RADIOELEKTRONIKA)*, pp. 40-45, 2015.
- [15] E. J. Naglich, J. Lee, D. Peroulis, and W. J. Chappell, "Switchless Tunable Bandstop-to-All-Pass Reconfigurable Filter", *IEEE Transactions on Microwave Theory and Techniques*, vol. 60, no. 5, pp. 1258-1265, 2012.
- [16] D. Biolek, R. Senani, V. Biolkova, and Z. Kolka, "Active Elements for Analog Signal Processing: Classification, Review, and New Proposals", *Radioengineering*, vol. 17, no. 4, pp. 15-32, 2008.
- [17] R. Prokop and V. Musil, "New modern circuit block CCTA and some its applications", *The Fourteenth International Scientific and Applied Science Conference Electronics ET'2005*, no. 5, pp. 93-98, 2005.
- [18] J. Jerabek, J. Koton, R. Sotner, and K. Vrba, "Adjustable band-pass filter with current active elements: two fully-differential and single-ended solutions", *Analog Integrated Circuits and Signal Processing*, vol. 74, no. 1, pp. 129-139, 2013.
- [19] R. Sponar and K. Vrba, "Measurements and Behavioral Modeling of Modern Conveyors", *IJCSNS International Journal of Computer Science and Network Security*, vol. 6, no. 3A, 2006.
- [20] *EL2082 (Elantec) Current-mode multiplier (datasheet)*. 1996.

High Precision Motor Control in FPGA for Space Applications

Vojtech Dvorak

Department of Microelectronics
Brno University of Technology
Technická 10, 616 00, Brno, Czech Republic
dvorak@phd.feec.vutbr.cz

Abstract—This paper describes an architecture of a motor controller implemented in FPGA. The proposed controller is designed to drive a permanent magnet synchronous motor. The intended application of the proposed motor controller is in space applications to rotate the motor with high accuracy and slow speed according incoming synchronization signals. The presented architecture is optimized in order to achieve acceptable resource utilization of a target space qualified FPGA.

Keywords—Clarke Transform, FPGA, Motor Control, Park Transform, Permanent Magnet Synchronous Motor, Vector Control

I. INTRODUCTION

A motor driving is a common task in many space applications. Almost all satellites contain some mechanical part that is changing its position. A typical example can be a panel with array of solar cells that should be set towards the Sun to maximize efficiency of electrical power generation. Another example is an array of optical filters that are placed in front of a wide-spectrum camera and rotated to provide images in different spectrums. The motor controller described in this paper is intended to drive a permanent magnet 3-phase synchronous motor that rotates such disk with a set of optical filters with a constant speed, approx. 1 revolution per 5 sec.

The common approach to implement a motor controller is to utilize microcontroller due to low cost and well understood implementation of the motor controller there. However, this solution is not preferred for space applications because the verification of the software for the processor becomes bottleneck of the whole design flow.

Another approach is to use a dedicated hardware for the motor control task such as in [1]. This hardware is a multi-chip module in a single package containing complete circuitry to acquire signals, to process them and to generate PWM signals for the driven motor. The main advantage of such solution is a small weight of the module and a small area on the PCB. Unfortunately, such module cannot be used for final flight hardware because it is not implemented in any rad-hard technology.

Utilizing an FPGA is in general preferred solution for the motor control tasks in the space industry. The main advantage of FPGAs is a heritage in many space missions and a high

reliability of FPGAs qualified for space flight [2]. Another important advantage is possibility to implement additional monitoring and control functions that are often required beside the motor controller itself. The implementation of all monitoring and control functions in one single FPGA brings the advantage of smaller weight and smaller place on PCB and also higher reliability because less components are used.

There are available commercial solutions in form of IP cores for FPGA, i.e. [3] or [4], but these IP cores are not able to fulfil requirements on the control algorithm that are rather strict in terms of accuracy of control. Another reason to implement our own solution was due to the regulators described in these IP cores are intended to drive motor that is rotated with a higher speed than the speed required for this application and the resource utilization of the target FPGA is not the main concern here.

The rest of the paper is organized as follows: Section 2 brings short overview of the whole Motor Controller with concern to the structure of the cascaded regulation loop, Section 3 describes architecture of the Motor Controller in an FPGA and Section 4 contains details about a logic synthesis setup and implementation results in the target FPGA.

II. MOTOR CONTROL LOOP

The structure of the motor controller in FPGA (in Figure 1) was developed to fulfill requirements to rotate motor with constant speed and reach commanded position with high precision in time.

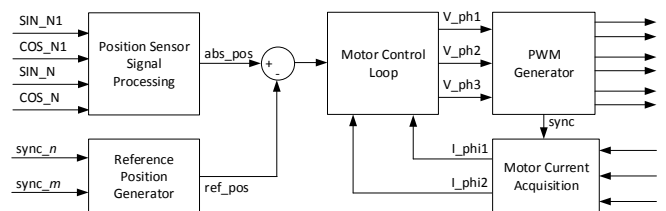


Fig. 1. Block Schema of Motor Controller in FPGA

The current position of the motor is computed in the Position Sensor Signal Processing (PSSP algorithm) from a position sensor with two tracks with different number of sinewaves per one revolution (nonius scale). Each of these

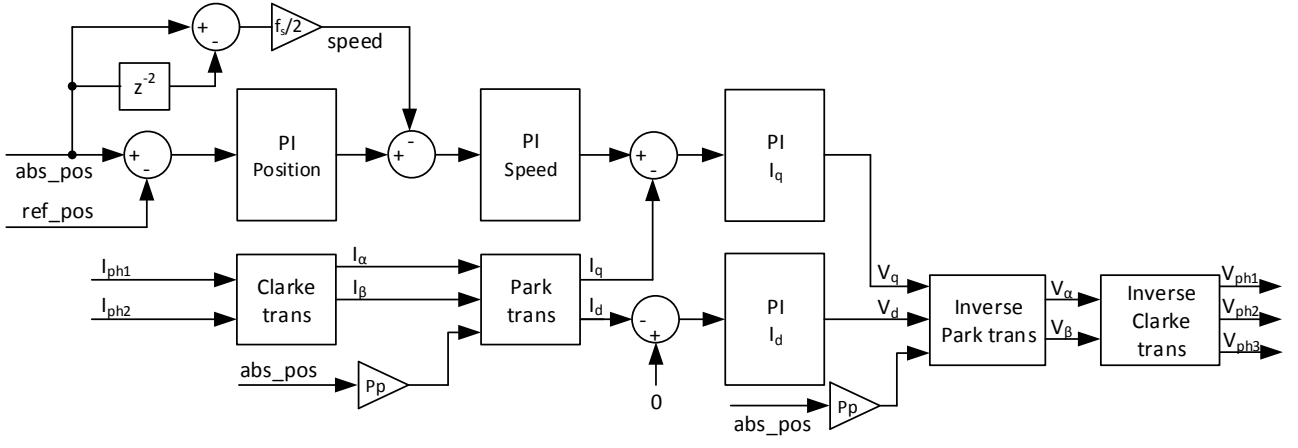


Fig. 2. Motor Control Loop Schema

tracks provides two signals shifted by 90° , i.e. sine and cosine. There are many approaches how to compute position from these set of signals including dedicated hardware [5], [6]. The common approach is to utilize goniometric functions such as arctan and perform computation with floating point numbers. This is not an efficient approach to implement in FPGA and we decided to follow a different approach where the set of input signals is compared with internally generated set of signals and the smallest difference between these sets is searched.

The computation of the reference position is performed by the Reference Position Generator. In this case, the reference position is a ramp generated from periodic pulses that are generated by a superior system. The period of these pulses can vary and the Reference Position Generator has to be able to adapt to different frequencies of synchronization signals with a high accuracy of the generated reference position. To fulfil the requirements on tunability and high accuracy, the architecture of the Reference Position Generator described in [7] was developed.

The Motor Control Loop (MCL) implements vector control of the permanent magnet synchronous motor. The MCL is composed of a cascaded structure of PI regulators regulating position, speed and current, and transformations from balanced three-phase system into rotating orthogonal reference frame and vice versa. The schema of the regulation loop is in Fig. 2.

All PI regulator have the same internal structure shown in Fig. 3. Input data are multiplied by a constant, summed with previous sample of data multiplied by a constant and added to integrator. The constants are different for each regulator and are derived according equation (1).

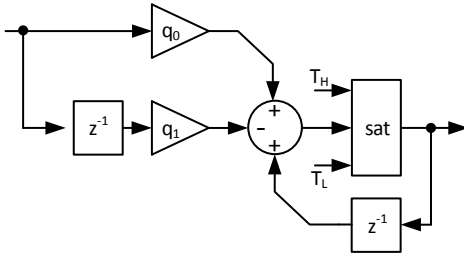


Fig. 3. PI Regulator Structure

$$\begin{aligned} q_0 &= K_p \\ q_1 &= K_p + K_p \cdot \frac{T_s}{T_i} \end{aligned} \quad (1)$$

The integrators in all PI regulators contains saturation of output. This feature allows to define some parameters of regulator, such as maximal and minimal speed of motor (output of the Position PI regulator), maximal torque of motor in both direction of rotation (output of Speed PI regulator) and maximum duty cycle of PWM Generator and thus maximum voltage (output of both I_q and I_d PI regulators).

The speed of rotation is computed from the current position of the motor and the position delayed by two samples. The resulting speed is actually speed of the previous sample. However, because rotation is quite slow, this delay has minimal impact on the speed regulation and on the other hand improves a resolution of the computed speed.

The Clarke Transformation (equation 2) and the Park Transformation (equation 3) are used to transform measured phase current from balanced three-phase system into rotating orthogonal reference frame.

$$I_\alpha = I_{ph1} \quad (2)$$

$$I_\beta = 1/\sqrt{3} * I_{ph1} + 2/\sqrt{3} * I_{ph2}$$

$$I_d = I_\alpha * \cos(\varphi) + I_\beta * \sin(\varphi) \quad (3)$$

$$I_q = I_\beta * \cos(\varphi) - I_\alpha * \sin(\varphi)$$

To transform the voltage to be applied on the motor from rotating orthogonal reference frame to balanced three-phase system, the Inverse Park Transformation (equation 4) and the Inverse Clarke Transformation (equation 5) are utilized.

$$V_\alpha = V_d * \cos(\varphi) - V_q * \sin(\varphi) \quad (4)$$

$$V_\beta = V_q * \cos(\varphi) + V_d * \sin(\varphi)$$

$$V_{ph1} = V_\alpha \quad (5)$$

$$V_{ph2} = 1/2 * (-V_\alpha + \sqrt{3} * V_\beta)$$

$$V_{ph3} = 1/2 * (-V_\alpha - \sqrt{3} * V_\beta)$$

Where angle φ is an electrical angle of the motor and is computed as the current position multiplied by the number of the motor pole pairs.

III. MOTOR CONTROLLER IMPLEMENTATION

The Motor Controller described in the previous section was implemented with concern to the efficient resource utilization rather than a latency of algorithm computation or a power consumption of the controller. A simplified schema of the Motor Controller is in Fig. 4. It is composed of a shared arithmetic unit, two controllers implementing computation algorithm (PSSP algorithm to compute position and Motor Control Loop algorithm to drive the motor), a control logic (Motor Control Block Controller) that drives access to the shared arithmetic unit and dedicated RAM blocks, one for each controller (RAM blocks are not part of the Fig. 4).

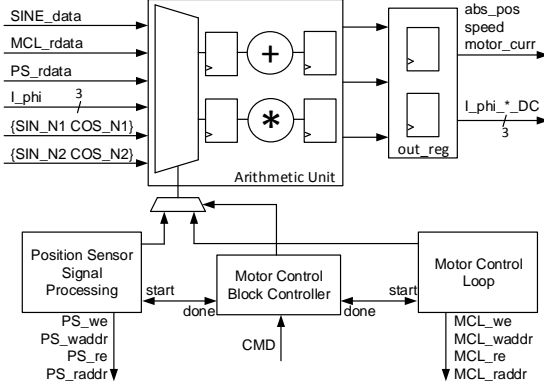


Fig. 4. Motor Controller Structure

The Motor Control Block Controller (MCBC) is implemented as a finite state machine that drives overall process of the motor driving. After appropriate command is received, MCBC periodically generates *start* signals to acquire sensor data, compute position with the PSSP algorithm and run motor driving with the MCL algorithm. The MCBC also control access to the control ports of the arithmetic unit and provides access to the PSSP controller or the MCL controller according to the state of the computation.

A. Arithmetic Unit

The proposed arithmetic unit is designed to be able to perform arithmetic operations for both, the PSSP algorithm and the MCL algorithm. It supports arithmetic operation addition and multiplication in 16-bit fixed point numbers. The schema of the shared arithmetic unit is in Fig. 5. It is composed of three main parts – fixed-point adder with saturation logic, fixed-point multiplier and a switching logic.

The fixed-point adder and the fixed-point multiplier have flip-flops with write enable ports on their inputs and outputs. The write enable ports of the inputs registers allow to save data into the registers in advance before they are used in the algorithm. The purpose of the registers on the output ports of the arithmetic unit is to hold results of the last valid operation.

The adder in the arithmetic unit contains a saturation logic that is required by the computation algorithm of the PI regulators. The threshold for saturation are saved in dedicated registers in the arithmetic unit and the saturation itself is activated by the enable signal. Values of the thresholds are loaded from the memory before the saturation is performed.

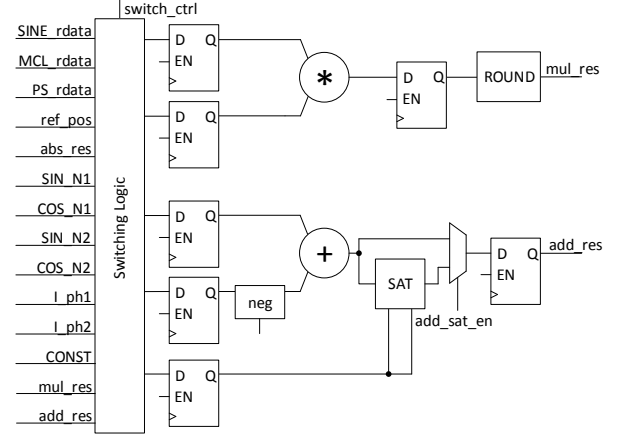


Fig. 5. Structure of the Shared Arithmetic Unit

The Switching Logic is arrays of multiplexers that are able to route all signals needed to perform arithmetic operations for PSSP algorithm and MCL algorithm. These arrays were carefully optimize to minimize the number of multiplexed signals and thus to minimize the number of utilized resources and the transport delay of the switching logic.

B. Motor Control Loop Logic

The Motor Control Loop of the Motor Controller implements the regulation algorithm described in the Section 2. The regulation algorithm was analyzed and optimized for implementation in a hardware. As a result, the computation of each PI regulator takes approximately 10 clock cycles and computation of the transformations (either forward or inverse) lasts 11 clock cycles. The computation of the MCL algorithm then lasts 62 clock periods and is performed in the following order: Position regulation → Speed regulation → Clarke & Park transformations → I_q regulation → I_d regulation → Inverse Park & Inverse Clarke transformations.

The Motor Control Loop drives the control signals of the arithmetic unit, a write port and a read port of the dedicated MCL memory. The MCL memory is implemented in one block RAM protected with EDAC (Error Detection And Correction) logic and its structure corresponds to the computation steps of the algorithm. That means that an address of data in the MCL memory is the same as a value of the computation step when these data shall be loaded into the registers in the arithmetic unit. This approach leads to a very efficient implementation. Only one counter to control the progress of the algorithm computation without any additional logic is needed to generate addresses for the write port of the MCL memory. The same progress counter is used to generate all control signals and only one small LUT for each control signal is needed.

A value of a sine/cosine of the motor electrical angle is needed in the Park transformation and in the Inverse Park transformation. The values of sine/cosine are read from a LUT table with saved sinewave samples. The address in the LUT is computed from the current position of the motor according to the equation (6).

$$addr = pos * \frac{2048 * Pp}{360} \quad (6)$$

The address computed in equation (6) can be greater than the size of the sine samples by factor Pp and a modular reduction is necessary to be used. However, the size of the LUT was chosen to be a power of 2 and the modular reduction is simple here, MSB bits are discarded.

To save additional resources, only the first quadrant of a sine period is saved in the LUT. The rest of the sine period and the cosine values are computed according to the TABLE I.

TABLE I. SINE LUT ADDRESSING SCHEMA

Address	Value	
	Sine	Cosine
addr < 512: addr[10:9] = 00	LUT(addr)	LUT(512-addr)
addr >= 512 ∧ addr < 1024: addr[10:9] = 01	LUT(512-addr)	-LUT(addr-512)
addr >= 1024 ∧ addr < 1536: addr[10:9] = 10	-LUT(addr-1024)	-LUT(1536-addr)
addr >= 1536 ∧ addr < 2048: addr[11:10] = 11	-LUT(2048-addr)	LUT(addr-2048)

IV. IMPLEMENTATION RESULTS

The Motor Controller implementing the proposed MCL algorithm was synthesized into the target FPGA Microsemi RTAX 2000S qualified for space flights. The logic synthesis was performed with the tool Synopsis Synplify Pro G-2012-09A. The synthesis results can be found in TABLE II.

TABLE II. FPGA RESOURCE UTILIZATION

Component	Resource Utilization		$f_{clk,max}$ [MHz]
	LUT [-]	FF [-]	
Arithmetic Unit	942	185	67.5
16-bit multiplier	632	108	67.5
16-bit adder	132	80	82.3
switching logic	151	-	-
MCL	79	27	204.4
total	1021	212	67.5

The frequency of the system clock in the target FPGA is 50 MHz. To have required 20% margin on the worst case path, the target frequency for the synthesis was set to 60 MHz. As can be seen in the synthesis results, the target frequency was reached after a retiming had been allowed. The FPGA RTAX 2000S does not contain any DSP blocks. The 16-bit multiplier is thus implemented into 632 4-input LUTs. This is the largest single combinational network in the whole FPGA design and it also creates the critical path that limits the frequency of the system clock.

V. CONCLUSION

The paper introduced an architecture of the motor controller suitable for implementation in an FPGA. The controller involves the PSSP algorithm to compute position from two pairs of harmonic signals (nonius scale), the Reference Position Generator and the Motor Control Loop.

The developed regulation loop is intended to be used with permanent magnet synchronous motor in space application. The most important property of the regulation loop is high accuracy of the regulation with slow speed of the motor rotation.

The paper is mostly focused on architecture of the Motor Control Loop. The proposed architecture contains an arithmetic unit shared with the PSSP algorithm and efficient implementation of regulation algorithm utilizing just one 6-bit counter and a few LUTs to generate control signals for the shared arithmetic unit and memory access.

The implementation into flight FPGA was performed and results of the synthesis were presented in the paper. The FPGA RTAX 2000S by Microsemi was chosen as the flight FPGA due to heritage in many space missions. These FPGAs are manufactured in 150 nm rad-hard technology and are rather large and slow compared with modern FPGAs. Moreover, this specific type of FPGA does not contain DSP blocks and the 16-bit multiplier in the arithmetic unit had to be implemented in the combinational network. However, the proposed architecture is designed to share the multiplier wherever it is needed and thus a lot of resources can be saved.

ACKNOWLEDGMENT

Research described in this paper was financed by the National Sustainability Program under Grant LO1401, by the Czech Science Foundation under Grant No. P102-14-07724S and by the project no. FEKT-S-14-2300 "A new types of electronic circuits and sensors for specific applications". For the research, infrastructure of the SIX Center was used. Cadence software was used with support through the Cadence Academic Network.

REFERENCES

- [1] G. C. Caprini, F. Innocenti, L. Fanucci, S. Ricci, G. Taraschi, P. Terreni, M. Tonarelli, L. Tosi, "Embedded system for brushless motor control in space application", 7th annual MAPLD International Conference, 2004
- [2] K. O'Neill "FPGAs for Space Applications", SEFUW: Space FPGA Users Workshop 1st edition, 2012
- [3] Microsemi: Dual-Axis Motor Control on a Single SoC FPGA, Microsemi, 2015
- [4] Altera: Motor Control IP Suite Components for Drive-on-Chip Reference Designs, Altera, 2014
- [5] iC Haus: High-Precision Sine/Cosine Interpolation, iC-House GmbH, 2014
- [6] GEMAC: 2-Channel Interpolation Circuit with Nonius Calculation, GEMAC, 2013
- [7] V. Dvorak, "High Precision Reference Position Generator for Motor Control in FPGA", Proceedings of the 22nd Conference STUDENT EEICT 2016, pp. 625-629, Vysoke Ucení Technické, 2016

Arrangements of Capacitively Loaded Dipoles for 20-bit Chipless RFID Tag

Jaroslav Havlíček

Department of Electromagnetic field
Czech Technical University in Prague
Prague, Czech Republic
havlij18@fel.cvut.cz

Abstract—This paper presents three arrangements of uniplanar capacitively loaded dipole scatterers used as a basic building element for a 20-bit chipless RFID tag with frequency domain information coding. Proposed simulation results of the arrangements demonstrate that strong mutual coupling between scatterers can negatively affect uniformity of tag radar cross-section response which is crucial for readability of the tag.

Keywords—chipless RFID, tag, scatterer, mutual coupling, radar cross-section, spectral response coding

I. INTRODUCTION

The radiofrequency identification (RFID) is a widespread technology, which is applied mainly in industry (production process monitoring), logistics (acceleration of storing procedures), commerce (antitheft feature), health care (elimination of patient confusions) and inventorying (e.g. books in libraries). RFID is expected to have an important role in the internet of things concept [1].

There is a perfect opportunity for further spreading in commerce, provided that the RFID transponders (tags) are suitable for optical barcode replacement [2]. The advantage of the tag consists in the possibility to be read without necessity of clear line of sight. Low price of the tag is essential for reaching this goal. Unfortunately conventional tags which consists a chip are about hundred times more expensive than barcode [3]. Perspective approach to reduce the tag cost is chipless RFID which provides different methods of storing information without chip.

Promising examples of the chipless RFID technology are tags based on spectral signature [4], [5], which in most cases consist of resonating scatterers. Presence or non-presence of each scatterer's peak in tag's spectral signature represents logic one or zero, respectively. This method of the chipless tag design is employed in this paper. Second part discusses required properties of the scatterer and describes capacitively loaded dipole. Third part presents three arrangements of the scatterers for 20-bit chipless RFID tag. First of them demonstrates negative effect of mutual coupling between scatterers on uniformity of tag radar cross-section response which is crucial for readability of the tag. Two other arrangements were design for mutual coupling reduction.

II. CAPACITIVELY LOADED DIPOLE

There are many different types of planar resonators which can be used as a scatterer for the chipless RFID tag. [6] Each of these resonators can be described via three important quantities. First of them is radar cross-section (RCS) which determines the reading range of the tag. The higher RCS results in the longer reading range.

Second quantity is bandwidth (BW) of resonance peak which depends on quality factor of resonance. It can be evaluated from frequency characteristic of the resonator as frequency range of three decibel resonance peak drop. This value is important from spectral bit capacity point of view. For example when bandwidth is 200 MHz there cannot be stored more than only five bits for each GHz in the spectrum.

Last quantity is product ka where k is wave number and a is radius of circle circumscribed the resonator. This quantity represents rate of electric reduction of the resonator. Resonators with ka below one are suitable candidates because small scale is essential for purposes of chipless RFID.

Theory of electrically small antennas says that resonance structures with small ka have high quality factor Q which implicates low bandwidth which is beneficial for high spectral bit capacity and low RCS which is inappropriate for reading range. Therefore there is always a trade-off between spectral bit capacity and reading range of the tag.

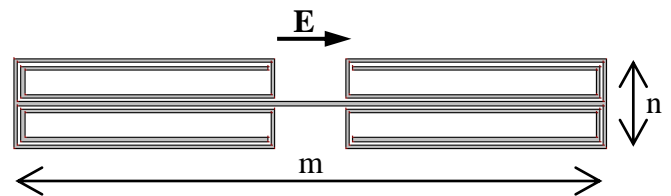


Fig. 1. Capacitively loaded dipole

Capacitively loaded dipole represents quite advantageous choice from the point of view of this trade-off [6]. Its width n is 2.5 mm, length m depends on resonant frequency ($m = 16.7$ mm is maximum). Dipole is loaded via four spiral (one turn and half) endings. Width of all lines as well as spacing between arms equals 0.1 mm. Its RCS is -33.5 dBsm, BW is 17.2 MHz and ka is 0.35.

III. PREPARE YOUR PAPER BEFORE STYLING

All three proposed arrangements are compared with theoretical diagonal arrangement (blue lines). Resonance peaks are highly uniform due to negligible mutual coupling between dipoles. Unfortunately size of this arrangement would be 164 mm by 583.2 mm, which makes it inapplicable. Basic arrangement is presented in the figure 2. Its size is 69 mm by 16.7 mm. Dipoles are simply sorted by size from longest to shortest. Spacing between dipoles is 1 mm. Characteristics in the figure 3 illustrate that this is not sufficient solution because of significant RCS differences between resonant peaks. More over some peaks are split.



Fig. 2. The layout of basic arrangement

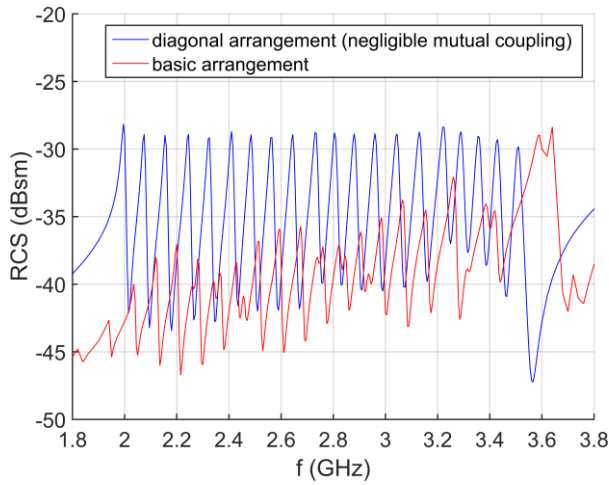


Fig. 3. Simulated performance of basic arrangement

Modified arrangement is presented in the figure 4 [7]. Each fourth dipole of basic arrangement was moved to the corresponding quarter of the array so that the original ascending order according to their resonant frequency '1 2 3 ... 20' is modified to '1 5 9 13 17 2 6 10 14 18 3 7 11 15 19 4 8 12 16 20'. In basic arrangement, the two neighboring dipoles differ by at least 0.2 mm in length, while in modified arrangement the difference is at least 0.8 mm. In figure 5 it can be observed that the greater distance between neighboring scatterers reduces mutual coupling between them which results in more uniform RCS response.

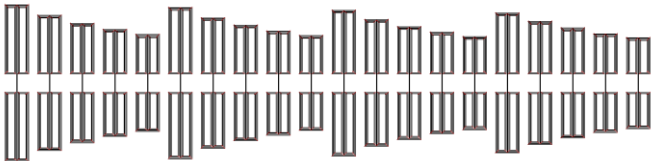


Fig. 4. The layout of modified arrangement

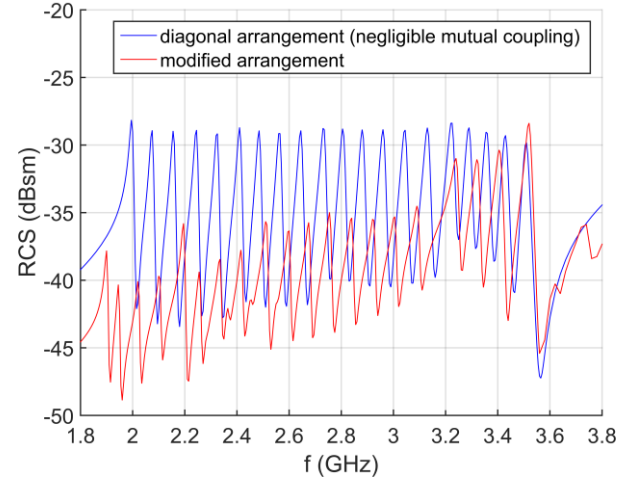


Fig. 5. Simulated performance of modified arrangement

Matrix arrangement is presented in the figure 6. Its size is 16.5 mm by 68.9 mm. All quarters of modified arrangement were relocated from horizontal ordering to vertical. Uniformity of resonance peaks is higher than in the case of modified arrangement (figure 7) due to further reduction of mutual coupling. Nevertheless matrix arrangement is not still sufficient for chipless RFID tag because of frequency shift of the peaks.

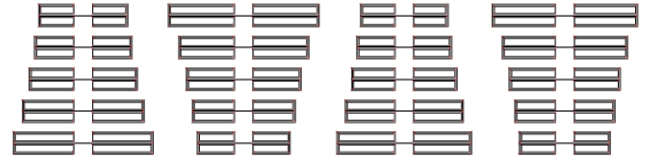


Fig. 6. The layout of matrix arrangement

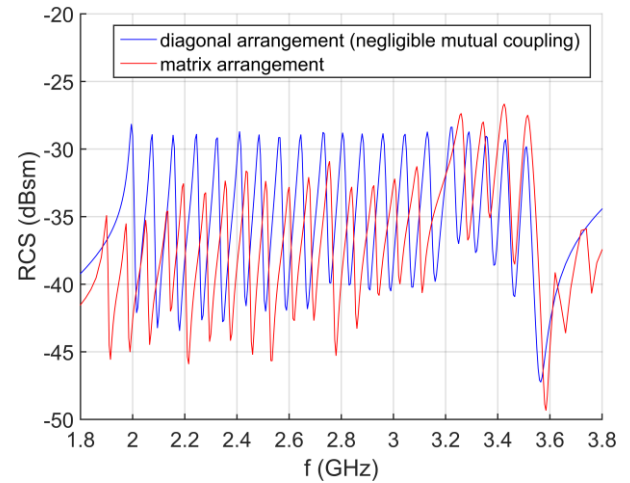


Fig. 7. Simulated performance of matrix arrangement

IV. CONCLUSION

The paper discusses behaviour of planar capacitively loaded dipole scatterer proposed as a basic building block of

the RFID chipless tag working in the frequency domain mode. Three presented arrangements illustrate how important is reduction of mutual coupling between scatterers for readability of the tag. It is essential to propose a new arrangement minimizing this mutual coupling for the design of high bit capacity tag. Further work on this project will be focused on describing mutual coupling in more exact way using equivalent circuit.

ACKNOWLEDGMENT

This work was supported by the Czech Technical University in Prague under the project SGS10/271/OHK3/3T/13.

REFERENCES

- [1] S. Dey, J. K. Saha and N. C. Karmakar, N. Smart Sensing: Chipless RFID Solutions for the Internet of Everything. *IEEE Microwave Magazine*, 2015, vol.16, no.10, pp.26-39. DOI: 10.1109/MMM.2015.2465711
- [2] P. Harrop, R.Das, *Printed and Chipless RFID Forecasts, Technologies & Players 2011-2021*. [Online] Cited 2016-04-25. Available at: <http://www.idtechex.com/research/reports/printed-and-chipless-rfid-forecasts-technologies-and-players-2011-2021-000254.asp>.
- [3] S. Preradovic, and N.C. Karmakar, "Chipless RFID: Bar Code of the Future," *IEEE Microw. Mag.*, vol. 11, no. 7, pp. 87-97, Dec. 2010.
- [4] R. Rezaiesarlak, and M. Manteghi, "Complex-Natural-Resonance-Based Design of Chipless RFID Tag for High-Density Data", *IEEE Transactions on Antennas and Propagation*, vol. 62, no. 2, pp. 898-904, 2014.
- [5] A. Vena, E. Perret, and S. Tedjini, "A Fully Printable Chipless RFID Tag With Detuning Correction Technique", *IEEE Microwave and Wireless Component Letters.*, vol. 22, no. 4, pp. 219-229, 2016.
- [6] J. Havlicek, M. Svanda, J. Machac, M. Polivka, "Improvement of Reading Performance of Frequency-Domain Chipless RFID Transponders", *Radioengineering*, vol. 25, no. 2, pp. 209-211, 2012.
- [7] M. Polivka, M. Svanda, J. Machac, Chipless RFID Tag with an Improved RCS Response, *Proc. of 44th European Microw. Conf. (EuMC)*, 2014, pp.770-773, ISBN: 9781479955985, DOI: 10.1109/EuMC.2014.6986548

[1] S. Dey, J. K. Saha and N. C. Karmakar, N. Smart Sensing: Chipless RFID Solutions for the Internet of Everything. *IEEE Microwave*

Textile Linearly Polarized HMSIW U-Slot Antenna for Off-Body Communication

Patrik Hubka

Department of Radio Electronics
Brno University of Technology
Brno, Czech Republic
xhubka00@stud.feec.vutbr.cz

Abstract—In this paper, a textile linearly polarized U-slot half-mode substrate integrated waveguide (HMSIW) antenna for off-body communication is presented. It is based on a combination of a U-shaped slot etched in the HMSIW top wall and two shorts placed in this slot. The antenna operates at 5.8 GHz. The antenna is designed on a textile dielectric substrate. In order to verify performance of the proposed antenna placed in the proximity of a human body, a three-layer phantom of the human body – a chest model – is used. The antenna placed in proximity of the phantom of the human body achieves simulated impedance bandwidth of 3.01 % and the gain of 7.62 dBi.

Keywords— *Half-mode substrate integrated waveguide, slot antenna, human body model*

I. INTRODUCTION

Many antennas have been developed at Industrial, Scientific and Medical (ISM) bands (2.4, 5.8 and 61 GHz). These antennas could be exploited for in-body, on-body or off-body communication [1]. Few antennas for off-body communication at 5.8 GHz were reported in [2] and [3]. In this case, a dielectric substrate needs to be substituted by a textile dielectric substrate. The HMSIW technology [4] could be successfully exploited for the antenna design. Very interesting dual-band diamond-shape HMSIW textile antenna was presented in [2]. The antenna fulfills standard antenna requirements, but feeding of the antenna is made by a coaxial probe, which, in general, is not suitable for body centric communications. In [3], the authors focus on crumbling of the antenna on a textile substrate. It was demonstrated, that heavy crumbling has negative influences on operating frequency, minimum of the reflection coefficient and radiation patterns. Other antennas for off-body communication at 2.45 GHz, 5.8 GHz and 60 GHz were reported in [5] - [10].

In this paper, a textile half-mode substrate integrated waveguide U-slot antenna radiating linearly polarized wave designed for the 5.8 GHz ISM band for off-body communication is proposed. The dielectric substrate of the antenna presented in [11] is substituted by a softshell textile dielectric substrate. The antenna is placed in proximity of human body model and its parameters are studied.

II. ANTENNA DESIGN

The antenna is depicted in Figure 1. The softshell textile dielectric substrate of the length L , the width W , and the height

The presented research was supported by the Czech Grant Agency project no. P102/12/1274, by the Czech Ministry of Education in frame of National Sustainability Program under grant LO1401, and by the Internal Grant Agency of Brno University of Technology project no. FEKT-S-14-2483. The research is the part of the COST Action IC1301 which is financially supported by the grant of the Czech Ministry of Education no. LD14057. For research, infrastructure of the SIX Center was used.

h with the relative permittivity ϵ_r , and the loss tangent $\tan(\delta)$ is on its both sides covered by conductive layers. Glue with ϵ_r , $\tan(\delta)$ and h_{glue} is used for gluing the conductive layers to the softshell textile substrate. The HMSIW is created by a row of vias and both its ends are shorted. It operates in the fundamental mode $\text{TE}_{0.5,0}$. The radiating U-slot is etched in the top wall of the HMSIW at the distance L_{viaX} from its short end in the x-direction, and from the row of vias at the distance L_{viaY} in the y-direction. The outer dimensions of the slot are $L_{\text{SLOT-X}}$ and $L_{\text{SLOT-Y}}$. The width of the slot is W_{SLOT} . The slot is shorted by the strips of the width W_{SHORT1} and W_{SHORT2} . The antenna is equipped by a HMSIW to GCPW (grounded coplanar waveguide) transition.

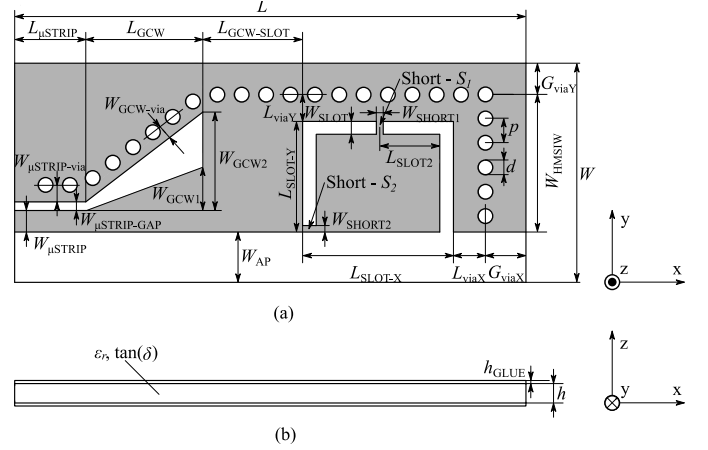


Fig. 1. Top (a) and side (b) view of HMSIW U-shape slot antenna (taken from [11]).

III. HUMAN BODY MODEL

The human body model used for simulations is composed from three layers – a skin, a fat, a muscle. From the viewpoint of the propagation of electromagnetic waves, all the described layers are lossy dielectrics of specific thicknesses and complex permittivity. The skin is a planar organ which plays the role of an external surface of organism and protects organism against surrounding environment. The thickness of the skin is between 0.4 mm and 4.0 mm. The fat is a reservoir of the energy and a heat insulator. The thickness of the fat layer is impossible to determine because everyone has unique anatomy. Muscles are

tissues with elastic properties. Muscles are able to contract and relax. The layer of muscle has various thicknesses which depend on the type of muscle and the location on the body.

The configuration of the multilayer model (the phantom) of a chest is shown in Figure 2. The parameters of the phantom are summarized in Table 1 [12]. The phantom is a block of base $200 \text{ mm} \times 200 \text{ mm}$. The height of the phantom is given by the thicknesses of the layers representing the skin, the fat and the muscle. The distance d between the human body model and the antenna is 1 mm.

TABLE I. PARAMETERS OF THE CHEST PHANTOM

	ϵ_r	$\tan(\delta)$	$\sigma \text{ (S/m)}$	thickness [mm]
Dry skin	35.114	0.32807	3.7170	2
Fat	4.955	0.18335	0.29313	10
Muscle	48.485	0.31715	4.9615	28

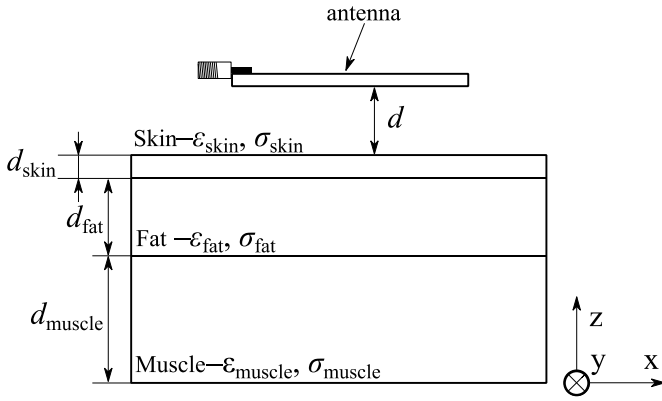


Fig. 2. The chest phantom (taken from [11]).

IV. ANTENNA DESIGN AND SIMULATED RESULTS

The softshell antenna was designed with the help of the time domain solver of CST Microwave Studio (CST MWS), where local optimization procedures Trust Region Framework were used, for the operating frequency of 5.8 GHz on the softshell textile dielectric substrate with relative permittivity $\epsilon_r = 1.32$, tangent loss $\tan(\delta) = 0.025$, and height $h = 1.32 \text{ mm}$. The glue is applied on the bottom and the top side of the softshell textile substrate with $\epsilon_r = 2.8$, $\tan(\delta) = 0.025$ and $h_{\text{glue}} = 0.0075 \text{ mm}$. The resultant dimensions of the antenna are summarized in Table 2.

TABLE II. DIMENSIONS OF DESIGNED ANTENNA (FIGURE 1)

	[mm]		[mm]		[mm]
L	64.66	W	21.28	W_{AP}	2.92
L_{uSTRIP}	8.87	W_{uSTRIP}	2.34	W_{HMSIW}	15.15
L_{GCW}	9.12	$W_{\text{uSTRIP-GAP}}$	1.00	G_{viaX}	3.29
$L_{\text{GCW-SLOT}}$	15.99	$W_{\text{uSTRIP-via}}$	1.15	G_{viaY}	3.21

$L_{\text{SLOT-X}}$	25.13	W_{GCW1}	2.98	h	1.32
$L_{\text{SLOT-Y}}$	12.64	W_{GCW2}	11.66	h_{GLUE}	0.0075
L_{SLOT2}	12.60	W_{SLOT}	1.10	p	0.75
L_{viaX}	2.26	W_{SHORT1}	0.47	d	0.45
L_{viaY}	2.51	W_{SHORT2}	0.47		

The distribution of the electric field in the substrate at the frequency 5.8 GHz is depicted in Figure 3. Thanks to the short S_1 , the electric field at the slot is cutted into two halves and the linearly horizontally polarized wave in the far field is obtained.

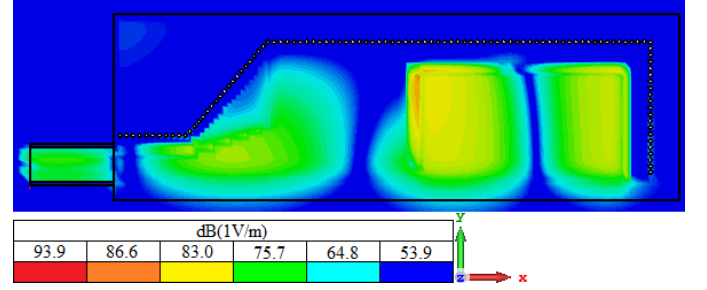


Fig. 3. Distribution of electric field intensity at 5.8 GHz in softshell textile substrate (magnitude).

The simulated reflection coefficient of the antenna in the free-space and in the proximity of the chest phantom is depicted in Figure 4. The simulated reflection coefficient of the antenna achieves impedance bandwidth about 3.23% and 3.01% for the antenna placed in the free-space and in the proximity of human body, respectively. The minimum of the reflection coefficient of the antenna placed in proximity on human body is slightly shifted about 30 MHz to lower frequencies due to the influence of the phantom.

The normalized simulated radiation patterns in two orthogonal cutting planes in the free-space and in the proximity of the phantom at the frequency 5.8 GHz are depicted in Figure 5. It can be observed that the co-polarizations are in good agreement at the boresight direction in E-plane. In H-plane, the co-polarization of the antenna near of the phantom of human body model has narrower radiation beam. The level of the cross-polarization at the boresight direction reaches higher level due to the influence of phantom in comparison to the cross-polarization of the antenna placed in the free-space. The simulated antenna peak gain is 6.28 dBi and 7.62 dBi for the antenna placed in the free-space and in the proximity of the phantom, respectively.

Simulated total efficiency at operating frequency $f = 5.8 \text{ GHz}$ of the antenna is 43% and 36% in the free-space and in proximity of the phantom of human body model, respectively. Total efficiency is lower thanks to the higher losses in the softshell textile dielectric substrate.

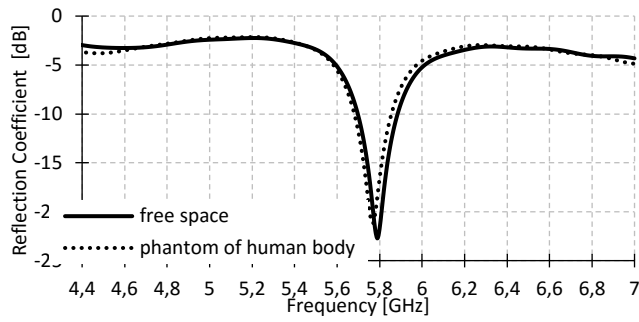


Fig. 4. Simulated reflection coefficient

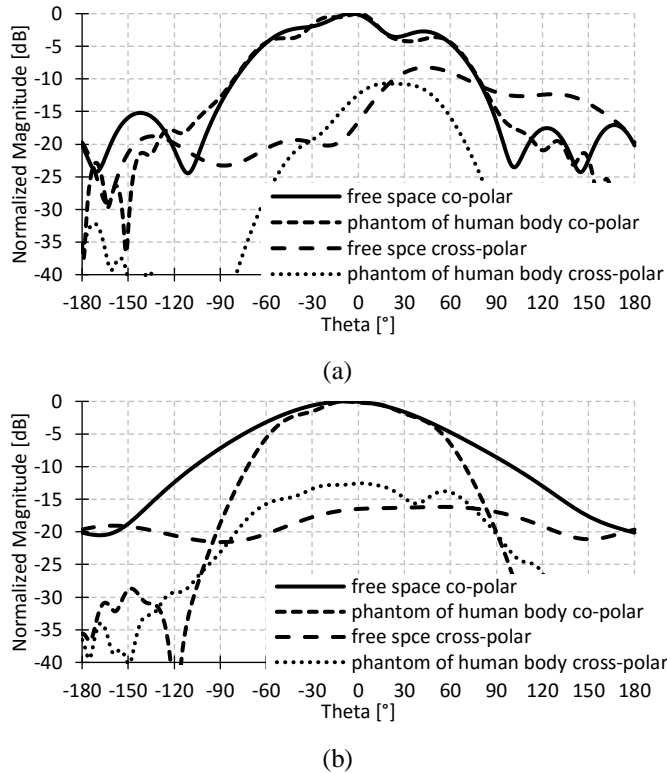


Fig. 5: Simulated radiation patterns of the antenna placed in free-space and in proximity of human body (phantom): (a) E-plane and (b) H-plane.

In comparison to antenna proposed in [2], the presented antenna has a higher gain and smaller size.

CONCLUSION

In this paper, a linearly polarized half-mode substrate integrated waveguide U-slot antenna operating at the frequency of 5.8 GHz in the proximity of a human body model (a chest phantom) has been proposed. The antenna is placed on the softshell textile dielectric substrate. The simulated results of the antenna placed in the proximity a human body achieves impedance bandwidth of 3.01% and gain of 7.62 dBi. The

antenna is suitable for off-body communication. The antenna will be experimentally verified and the results will be presented at the conference.

REFERENCES

- [1] P. S. Hall, "Antennas challenges for body centric communications," in *Proc. Int. Workshop Antenna Technol., Small Antennas Metamater. Appl.*, Mar. 2007, pp. 41–44.
- [2] S. Agneessens, and H. Rogier, "Compact Half Diamond Dual-Band Textile HMSIW On-Body Antenna," *IEEE Transactions on Antennas and Propagation*, 2014, vol. 62, no. 5, pp. 2374–2381.
- [3] Q. Bai, and R. Langley, "Crumpled textile antennas," *Electron. Lett.*, vol. 45, pp. 436–438, 2009.
- [4] W. Hong, B. Liu, Y. Wang, Q. Lai, H. Tang, X. X. Yin, YIN, Y. D. Dong, Y. Zhang, and K. Wu, "Half Mode Substrate Integrated Waveguide: A New Guided Wave Structure for Microwave and Millimeter Wave Application," *Joint 31st International Conference on Infrared Millimeter Waves and 14th International Conference on Terahertz Electronics*, 2006, pp. 219.
- [5] P. Salonen, and L. Humre, "A novel fabric WLAN antenna for wearable applications," in *Proceedings of the IEEE Antennas and Propagation Society International Symposium*, Jun. 2003, vol. 2, pp. 700–703.
- [6] L. Panzin, and Y. Leviatan, "A compact 60-GHz tapered slot antenna printed on LCP substrate for WPAN applications," *IEEE Antennas and Wireless Propagation Letters*, vol. 9, pp. 272–275, 2010.
- [7] I. Kahn, L. Yu, Y. I. Nechayev, and P. S. Hall, "Space and pattern diversity for on-body communication channels in an indoor environment at 2.45GHz," in *Proceedings of The Second European Conference on Antenna and Propagation (EUCAP 2007)*, Nov. 2007, pp. 1–6.
- [8] I. Khan, and P.S. Hall, "Multiple Antenna Reception at 5.8 and 10 GHz for Body-Centric Wireless Communication Channels," *IEEE Transactions on Antennas and Propagation*, Vol. 57. No. 1, January 2009.
- [9] S. S. Hsu, K. C. Wei, C. Y. Hsu, and H. R. Chuang, "A 60-GHz millimeter-wave CPW-fed Yagi antenna fabricated by using 0.18- μ m CMOS technology," *IEEE Electron Devices Letters*, vol. 29, no. 6, pp. 625–627, Jun. 2008.
- [10] A. R. Chandran, and W. G. Scanlon, "Dual-band low profile antennas for body-centric communications," *International Workshop on Antenna Technology (iWAT)*, pp. 1–4, 2010.
- [11] P. Hubka, "Linearly Polarized HMSIW U-Slot Antenna for Off-Body Communication," in *Proceedings of Conference of Electrical Engineering and Communication (EEICT)*, Brno (Czech Republic), April 2016, pp 318–322.
- [12] C. Gabriel, "Calculation of the Dielectric Properties of Body Tissues in the frequency range 10 Hz – 100 GHz. IFAC. [online]. 1997 [cit. 2016-06-03], Available at: http://niremf.ifac.cnr.it/tissprop/htmlclie/htmlclie.php.

The Neural models for different training algorithms

Martin Kotol

Brno University of Technology, Technická 12, 616 00

Brno, Czech republic

kotol.martin@phd.feec.vutbr.cz

Abstract—This paper is aimed on artificial neural networks that are used for modeling of a transmission channel. The neural networks were trained with different training algorithms and results of estimation were compared. The paper describes the procedure of measurement and the further processing of results.

Keywords—Artificial neural networks, Feed-forward neural networks, training algorithms, measurement, transmission function

I. INTRODUCTION

This paper is aimed on the Feed-forward (FF) artificial neural networks (ANN). The NNs accuracy approximation will be compared for particular training algorithm. At first a general NN is introduced; later the principle of the FF ANN will be introduced. Training algorithms of the FF neural networks will be described in the following part of text. Modeling the properties of a transmission channel can be computationally and time demanding. Parallel structure of the ANN can be used for modeling of the transmission channel.

For the accuracy verification of experimental measurement results the channel transfer function (CTF) is used. This experimental measurement is described in detail (a specification of used antennas type, localization antennas, setting measuring instrument, etc.).

The following text describes the measured values processing and pattern training and verification for ANN. The results will be compared for several training algorithms.

II. GENERAL ARTIFICIAL NEURAL NETWORK

This chapter is aimed on general description of neurons and their implementation into the ANN.

ANN is a universal computational tool which is composed of simple units called neurons. Neurons are organized into layers which are interconnected and form a network. Input of each neuron in the layer M is connected to the outputs of all neurons in the previous layer $M-1$. Output of the neuron in the layer M is connected to inputs of all the neurons in the next layer $M+1$. Interconnections between neurons are associated with different weights. Weights are set randomly during the initialization. During the training of the network, weights are adjusted in order to minimize the error at the output of the ANN (the difference between the expected response and the actual one) [1].

Figure 1 shows a general ANN containing the input layer, the hidden layer and the output layer. Here, x_1 to x_n are signals at the input of input neurons, w_{11} to w_{mn} denote weights between neurons and f_1 to f_n are signals at the output of output neurons. The input layer distributes input signals among hidden neurons [2]. Neurons in the hidden layer transform signals using a specific activation function. The output layer forms output signals of ANN.

For the comparison of the accuracy approximation the FF ANN was used and it depends on the training algorithm used. In the FF ANN the information flows from inputs directly to outputs without any feedback. During the training weights between neurons are set to minimize the difference between expected and actual outputs. After training the network is ready to estimate an appropriate output target from an arbitrary input pattern.

The FF ANN contains three layers of neurons; the input layer, the hidden layer and the output layer [2]. Each of these layers has a specific task:

- The input layer consists of input neurons which are described by the linear activation function. Input neurons distribute input signal to hidden neurons.
- The hidden layer consists of neurons with a specific activation function (sigma function, sigmoid function, ...). The sigma function is shown in equation 1. All neurons in the hidden layer have a parameter vector.

$$a_{jm} = \frac{1}{(1 + e^{-S_{jm}})} \quad (1)$$

$$\text{where } S_{jm} = \sum_{x=0}^n w_{ijx} a_{ix}$$

Where a_{jm} is activation function for m^{th} neuron in j^{th} layer, S_j is the sum of the products the activations nodes by their respective weights; the member w_{ij} is the set of all weights between layers i and j which are associated with neurons that feed into neuron m of layer j .

- The output layer forms output targets as a linear combination of signals from outputs of hidden neurons.

The Figure 2 shows the general structure of a FF network. Here, x_1 to x_n are inputs, w_{11} to w_{mn} are weights between neurons, and f_1 to f_n are outputs. During the training weights are

adaptively changed so that given input patterns are associated with respective output targets.

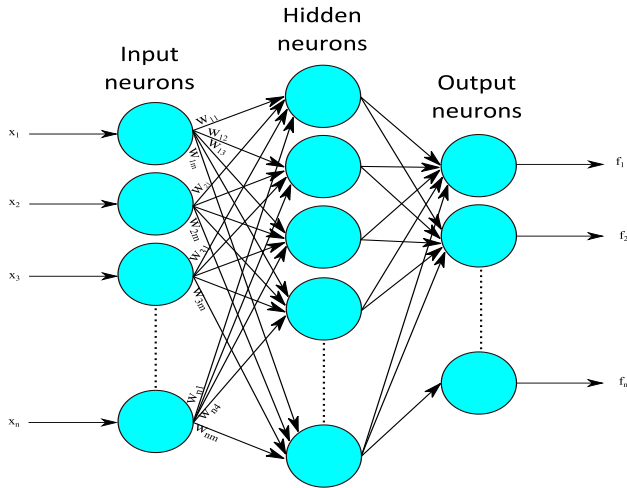


Fig. 1. General architecture artificial neural network.

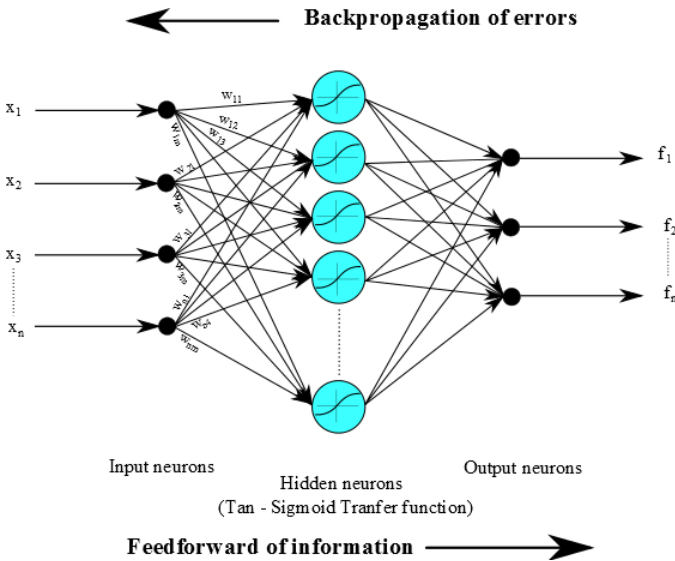


Fig. 2. Structure of general feed forward neural network

III. USED TRAINING ALGORITHMS

The following training algorithms were used: Bayesian regularization, Levenberg-Marquardt algorithm, quasi Newton method and scaled conjugate gradient algorithm.

Bayesian regularization is a mathematical process that converts a nonlinear regression into a "well-posed" statistical problem in the manner of a ridge regression. The advantage of Bayesian regularization is that the models are robust and the validation process, which scales as in normal regression methods, such as back propagation, is unnecessary. [3]

Regularization is a traditional way to eliminate negative effect of strong weight and additionally favours small values of weights; this decreases the tendency of model to overfit.

Mackay introduces a technique of automatically setting the parameter function to achieve the best generalization functions described. Regularization requires a computation of the Hessian matrix with the minimum points. This matrix is used in the Gauss-Newton approximation which is used to compute local minimum point with Levenberg-Marquardt optimization algorithms.[4]

The Levenberg-Marquardt algorithm combines advantages of the steepest descent method (i.e. minimization along the direction of the gradient) with the Newton method (i.e. using a quadratic model to speed up the process of finding the minimum of a function). This algorithm obtains its operating stability from the steepest descent method and adopts its accelerated convergence in the minimum vicinity from the Newton method. Standard implementation of the Levenberg-Marquardt algorithm is on solving nonlinear least squares problem.[5]

Quasi-Newton method divides into three types. DFP is the first quasi-Newton method, named after Davidson, Fletcher and Powell. The advantage of this method is that to computation of the exact Hessian is not necessary to compute at each point of approximation. DFG method computes Hessian and use it for approximation based on the change in gradient between iterations. Second quasi-Newton method is BFGS (Broyden, Fletcher, Goldfarb and Shanno). This method is very similar to DFP it approximates the inverse Hessian. Advantage of the BFGS method is that it is not necessary to solve a linear system to get the search direction. Only matrix or vector multiply is needed. It is more numerically stable and more effective; for these reasons the BFGS method will be used. The third method is L-BFGS; this algorithm does not require computation of the exact Hessian or inverse Hessian but it is not possible to use it on problems with very high number of variables. L-BFGS ("limited-memory" BFGS) solves problem by storing the approximate Hessian in a compressed form and requires storing only a constant multiple of vectors with length n . [6]

The last training algorithm is the scale conjugate gradient (SCG) algorithm. SCG belongs to the class of Conjugate gradient methods which can apply on the most of problems. SCG can be faster than other algorithms by using a step size scaling mechanism; because each step has a variable length and is able to achieve better results. On the other hand this algorithm is extremely demanding on the memory.[7]

IV. DESCRIPTION OF MEASUREMENT

The channel transmission function (CTF) was measured along the inner surface of the car roof between antennas in different positions. CTF were measured for all combinations of the transmit antenna (TX) positions Tx1 to Tx3, and the receive antenna (RX) positions Rx1 to Rx3 (see Figure 3).

In the ISM band (55 GHz to 65 GHz), an open-ended waveguide WR15 played the role of antennas (see Figure 3).

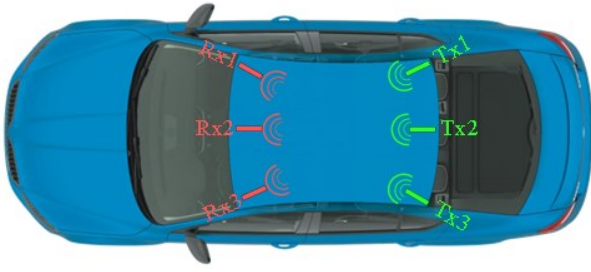


Fig. 3. Location TX and RX antennas

The CTF (frequency response of the magnitude of the transmission coefficient S_{21}) was measured by the four-port vector network analyzer (VNA) Rohde & Schwarz ZVA 67. The output power was set to 5 dBm and the resolution bandwidth used for all measurements was 100 Hz. The frequency band of measurements was sampled using the frequency step 10 MHz (CTF was measured in 1001 points).



Fig. 4. Waveguide WR 15,

Antennas were connected to the VNA by phase stable coaxial cables. The measurements were carried out in Skoda Octavia III limousine.

V. PROCESSING OF MEASUREMENT

Figure 5 shows measured values of the transmission between the transmit antenna Tx3 and the receive antenna Rx1 (red points). Measured values were processed in Matlab and NN was created using Matlab Neural Network Toolbox. The measured values were approximated by a polynomial function to partially smooth data for training neural networks (blue line). Smoothing of the measured data is equivalent to a low-pass filtering.

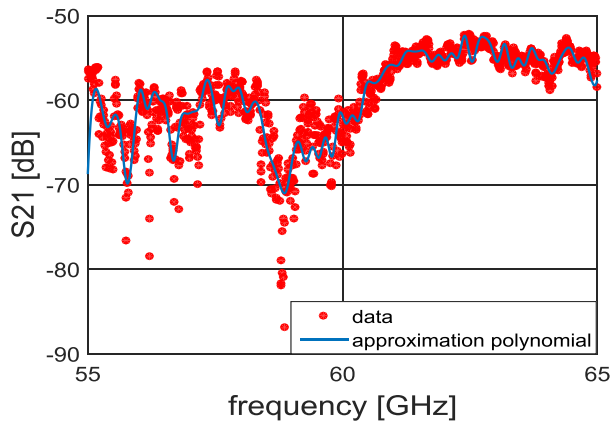


Fig. 5. Measured frequency response of the transmission between the antennas (red). Polynomial approximation of frequency response (blue).

As an input training pattern a matrix of operational frequencies and corresponding transmission coefficients was created; for all the measured configurations of antennas.

The transmission between antennas was measured from 55 GHz to 65 GHz with the frequency step 10 MHz. From measured values training patterns were created by selecting each 15th value. Therefore training patterns were created by values with the frequency step 150 MHz. This approach was used for all the configurations.

As an output training pattern a matrix of transmission coefficients corresponding with input matrix of frequencies was created. The training process was stopped at the moment the relative training error lower than 10^{-6} was reached.

For the verification of the trained ANN a new input matrix was created. From the values which were measured in the band defined above the starting sample was randomly selected between 2 and 14 (1 was used for training and 15 starts the following period). The rest of the sequence was formed from each 15th sample from the starting one. That way, the verification matrix with the frequency step 150 MHz (different from the training one) was created.

The new input pattern (created by the described way) was introduced to the input of the trained ANN and the neural network estimated the CTF in the car. This estimation was compared with real measured values.

In figures 6 – 9 the difference between ANN estimated and measured values is shown; ANN was trained using different training algorithm. In figure 10 shows the error of neural model for transmission channel in the car for different training algorithm (Bayesian regularization, Levenberg-Marquardt algorithm, quasi Newton method and scaled conjugate gradient algorithm). The biggest errors has achieved the ANN with training algorithm using the quasi Newton method because this algorithm does not provide a good adaptation on the big dynamic signals.

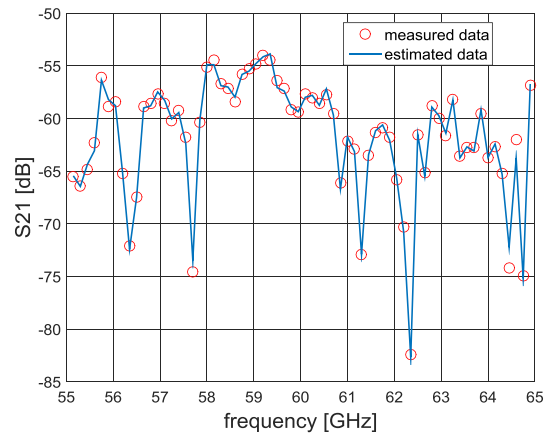


Fig. 6. Frequency response of transmission between antennas Tx3 and Rx1. Measured values (red points) versus estimated values by FF ANN (blue line) with used Bayesian regularization training algorithm.

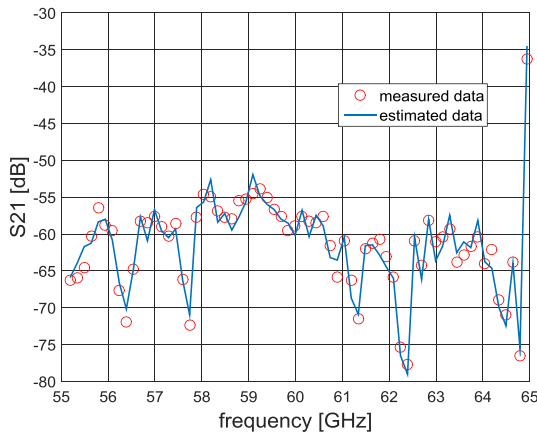


Fig. 7. Frequency response of transmission between antennas Tx3 and Rx1. Measured values (red points) versus estimated values by FF ANN (blue line) with used Levenberg-Marquardt training algorithm.

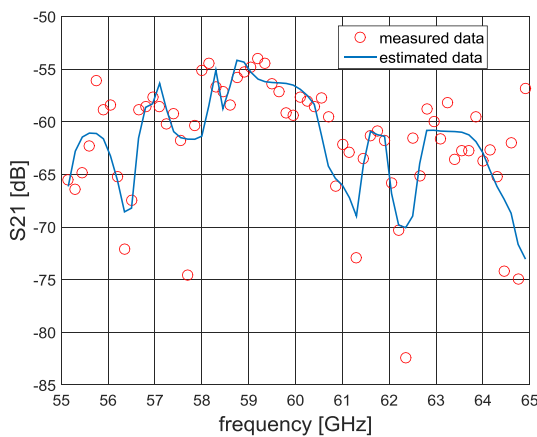


Fig. 8. Frequency response of transmission between antennas Tx3 and Rx1. Measured values (red points) versus estimated values by FF ANN (blue line) with used quasi Newton method training algorithm.

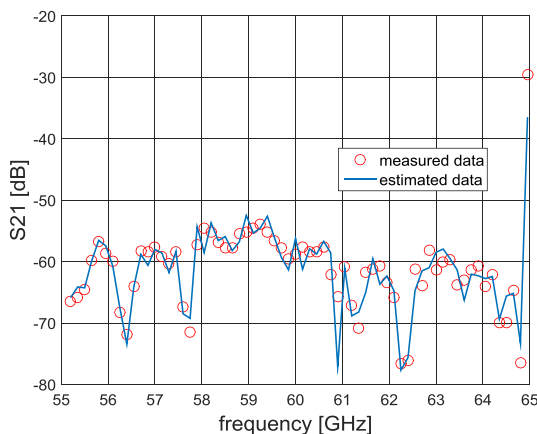


Fig. 9. Frequency response of transmission between antennas Tx3 and Rx1. Measured values (red points) versus estimated values by FF ANN (blue line) with used scaled conjugate gradient training algorithm.

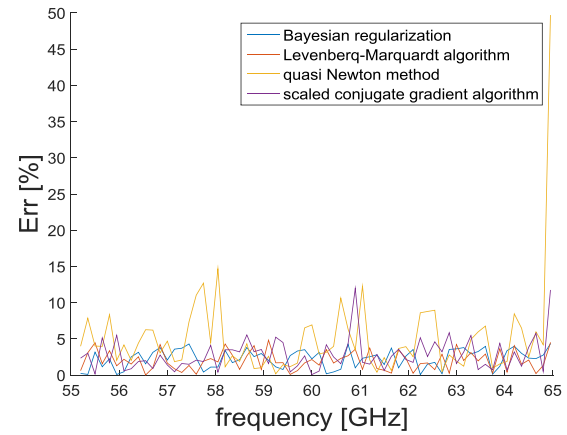


Fig. 10. Error of neural models for transmission channel in the car.

VI. CONCLUSION

This paper describes the application of FF ANN on modeling of the transmission channel along the car roof. General structure ANN is described in first part of this text. The function of FF ANN is introduced. The training algorithms (Bayesian regularization, Levenberg-Marquardt algorithm, quasi Newton method and scaled conjugate gradient algorithm) used for training the NN are briefly described. The procedure of measurement in the car is defined in part IV. The results show that the Bayesian regularization training algorithm, Levenberg-Marquardt algorithm and scaled conjugate gradient algorithm are similar but quasi Newton method is not exactly in estimation because it is not suitable for dynamic functions.

ACKNOWLEDGMENT

The presented research was supported by the Czech Grant Agency project no. P102/12/1274, by the Czech Ministry of Education in frame of National Sustainability Program under grant LO1401, and by the Internal Grant Agency of Brno University of Technology project no. FEKT-S-14-2483. The research is the part of the COST Action IC1301 which is financially supported by the grant of the Czech Ministry of Education no. LD14057. For research, infrastructure of the SIX Center was used.

REFERENCES

- [1] D. Kriesel, A Brief Introduction o Neural Networks, University of Born in Germany, 2005.
- [2] Š. Jiří and N. Roman, Teoretické otázky neuronových sítí, pp.389.
- [3] <http://www.ncbi.nlm.nih.gov/pubmed/19065804>
- [4] Wen Wang, Pieter H.A.J.M. van Gelder and J.K. Vrijling, "Comparison Bayesian regularization and cross-validated early-stopping for streamflow forecasting with ANN models" Methodology in Hydrology. IAHS Publ 311, 2007
- [5] Henri P. Gavin, "The Levenberg-Marquardt method for nonlinear least squares curve-fitting problems", Department of Civil and Environmental Engineering Duke University May 4, 2016
- [6] Andrew Galen, "Overview of Quasi-Newton optimization methods", available on : <https://homes.cs.washington.edu/~galen/files/quasi-newton-notes.pdf>
- [7] José Orozco, Carlos A. Reyes García, "Detecting Pathologies from Infant Cry Applying Scaled Conjugate Gradient Neural Networks", ESANN'2003 proceedings - European Symposium on Artificial Neural Networks Bruges (Belgium), 23-25 April 2003, d-side publi., ISBN 2-930307-03-X, pp. 349-354

Model-Based Testing Framework with Automatic Testing Priority Assignment for Automotive Distributed Systems

Lukáš Krejčí, Jiří Novák

Czech Technical University in Prague, Faculty of Electrical Engineering, Technická 2, 166 27 Prague 6, Czech Republic
krejclu6@fel.cvut.cz

Abstract—The paper presents an optimized framework for model-based testing of automotive distributed system and a method of automatic assignment of testing priorities used within the framework. The proposed method, envisioned for integration into existing, currently developed model-based testing tool, utilizes classifiers in order to assign testing priorities automatically to specific parts of the tested system. The paper also introduces a set of supplemental data enriching the modeling language that are exploited by the proposed method during the classification process. It is shown, that the presented approach's advantages, such as low requirements for the testing operators' insight, are valuable for the automotive distributed systems testing process.

Keywords—*Model-Based; Testing; Automotive; Classification; Classifiers; Artificial Neural Networks*

I. INTRODUCTION

The Aim of this paper is to propose a new, optimized framework for Model-Based Testing (MBT) of automotive distributed systems and particularly present its automated testing priority assignment procedure.

The MBT is a popular approach of automated testing, which utilizes an abstract model of a System-Under-Test (SUT) in order to generate a testing sequence or drive the testing procedure in real time. The MBT can be applied even on complex software or hardware SUTs, such as automotive distributed systems.

Typically, the automotive industry uses a testing process composed of three distinct parts: the mandatory standard assessments, the specific test cases, and integration testing. The mandatory standard assessments are given by various international, national or organization safety standards and are thus unavoidable. The prearranged specific test cases are often based on the organization know-how and are therefore desirable, as they can uncover specific corner-case faults. The purpose of integration testing is to evaluate the automotive system as a whole since such testing can discover possible failures caused by distributed systems interconnection. Such failures characteristically originate from the inconsistent interpretation of the system specification among the subsystems suppliers, which may result in incorrect implementation and consequently in malfunction of multiple subsystems. Presently, the integration testing is usually performed manually by testing operators and thus can be automated using the MBT principles. However, as

the automotive distributed systems are reactive, real-time and parallel, it was necessary to develop the appropriate testing tool.

II. BACKGROUND

The developed testing tool, called Taster, is based on diploma thesis [1] and described in paper [2]. Since automotive systems are real-time and reactive, a modeling language used by this tool is based on the theory of timed automata, developed by UPPAAL team [3]. This modeling language allows describing modeled system as a network of Timed Safely Automata (each is referred as a template) bound by a set of variables.

Due to significant complexity of a typical SUT, it is impossible to execute its complete evaluation, and only some parts of its state space can be tested. Therefore, the test sequence generation can be driven by various strategies. The Taster tool currently utilizes a generation of pseudorandom test sequences according to priorities manually inscribed in the model. Since the correct assignment of priorities is affected by multiple parameters, this approach requires significant insight from testing operators. Furthermore, pseudorandom sequences can be suboptimal in several cases. Consequently, a new optimized testing framework for this tool was designed to reduce the mean time required for the failure detection and to lower the amount of insight required from testing operators. Fig. 1 shows its structure.

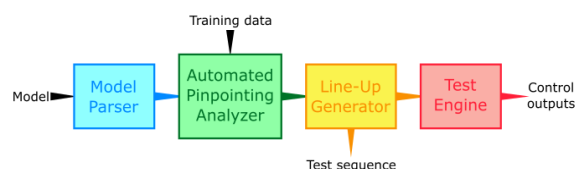


Fig. 1. Framework structure

The framework is defined as a pipeline chain consisting of following parts:

- The Model Parser, which loads a model from its XML-formatted file.
- The Automated Pinpointing Analyzer, which encases the procedure of labeling the model with testing priorities.
- The Line-Up Generator responsible for generating the testing sequences. This block takes an enriched

model as an input and generates the control outputs for the Test Engine.

- The Test Engine, which directly executes given operations on the SUT using supported testing backend.

This paper focuses on the presentation of the labeling encased in the Automated Pinpointing Analyzer block. This procedure, called Automated Pinpointing, utilizes classification of extra data stored in the model and is described in section IV.

III. RELATED WORK

The MBT and test generation are still active research topics [4]. Currently, a variety of different approaches exist. The Model-Based Statistical Testing (MBST) is an MBT approach utilizing the empirically obtained behavioral models. Authors of [5] describe the usage of MBST principles on embedded systems. Due to the purpose of integration testing, the MBST approach does not seem to be viable. However, the MBST usage could be reconsidered in future, e.g. to discover failures caused by unexpected user behavior.

As the presented approach uses a testing priorities for driving the test sequence generation process, it can be interpreted as the Risk-Based Testing (RBT). The paper [6] describe usage of the MBST and RBT principles for testing of railway control system. Authors focus on the feasible method of test sequences generation and the problem of marking the critical parts of the system is left to the future research.

Authors of [7] investigate utilization of MBT principles on the testing of graphical user interface and usage of classifiers for identification of infeasible test cases. Method presented in this paper utilize classifiers as well, however, for different purpose.

In all papers described above (and even in commercial tools, such as [8]), the critical parts of SUT have to be manually marked in the model. As stated in section II, manual assignment can be dubious, since it depends on various factors. Consequently, in order to avoid this potentially dubious process, this paper proposes a method for automatic assignment of testing priorities.

IV. AUTOMATED PINPOINTING PROCEDURE

As revealed in section II, the purpose of Automated Pinpointing procedure is to enrich the provided system model with testing priorities. Because the functionalities of an SUT are bound to the transitions and templates in the model, these priorities are assigned to them as well. Therefore, the procedure iterates through all transitions and templates in the model and assigns a priority to each of them. Nevertheless, in order to allocate the priorities in a viable manner, additional extra data providing further insight to the SUT are required.

The proper allocation of testing priority depends on various objective and subjective factors. Since the automotive systems consist of several safety-critical subsystems, the safety-impairment factor of particular functionality should be taken into account. Certainly, if some particular functionality is safety-critical, it should have higher testing priority than a non-critical one. Similarly, it is vital to allocate higher testing priority

to systems that are not necessarily safety-critical, but highly impact overall car user experience. Moreover, if a particular functionality of the SUT is expected to be a source of a failure, it is desirable to assign a high testing priority to it. Failure in a certain SUT functionality can be predicted using several objective factors that reflect the amount and severity of changes recently made to this functionality, as well as the reliability of its back-end. The safety importance and user experience impairment aspects are vastly subjective, as they depend on an individual manufacturer or user. From the other hand, factors that can be used for failure prediction are objective.

The Automated Pinpointing procedure utilizes two categories of extra data inscribed into a model on the transition and template level. The fault indicators are used for prediction of particular transition or template failure. This prediction is afterwards combined with the experience aspects in order to obtain transition or template testing priority, which is interpreted as an integer in range from 1 to 10. This is depicted on Fig. 2.

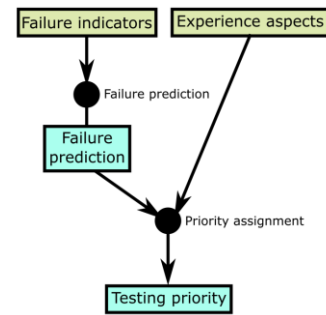


Fig. 2. Transition / template priority assignment workflow

Details about failure prediction and priority assignment procedures follows in sections IV.A and IV.B.

A. Failure Prediction

As the section IV declares, assignment of testing priority depends on failure prediction. In order to enable prediction of failure of particular functionality, the following failure indicators have been introduced as additional transition and template extra data:

- The *Modification Amount* ratio (real number in the range from 0 to 1) representing the amount of changes made to the particular functionality since the last evaluation.
- The *Modification Severity* index (integer in the range from 1 to 10) representing the severity of changes made to the particular functionality since the last evaluation.
- The *Back-End Reliability* ratio (real number in range from 0 to 1) representing the reliability of a back-end (i.e. hardware and lower software layers) of particular functionality obtained from the testing of low-level parts of the SUT.

Clearly, the failure prediction can be taken as a classification problem, where the input vector consists of the failure indicators and output is a real number between 0 (meaning failure is not predicted) and 1 (meaning failure is predicted). The Artificial Neural Network (ANN; described in [9]) approach has been chosen as a classification method suitable for this task.

Since the actual values of input vectors strongly depend on a particular manufacturer, programmer or tool used for the functionality modification or utilized back-end, the feature space may not be linearly separable, so a simple solution with a single perceptron neuron is infeasible [11]. Therefore, two neural networks have been proposed for this task.

The structure of first proposed ANN is shown in Fig. 3.

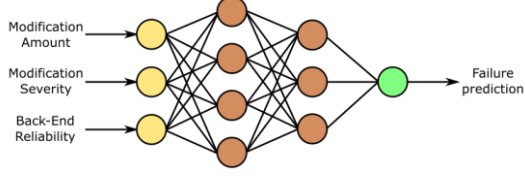


Fig. 3. Structure of multilayer perceptron feedforward network

The first proposed ANN is a multilayer perceptron feedforward network composed of two hidden layers; the first layer consists of four neurons and second layer consists of three neurons. All neurons use the sigmoid function as an activation function. The input weights of all neurons are initialized randomly. The ANN is learned using standard backward propagation procedure using the provided input vector and the actual test result as expected output. The inference is realized by forward propagation.

The structure of second proposed ANN is depicted in Fig. 4.

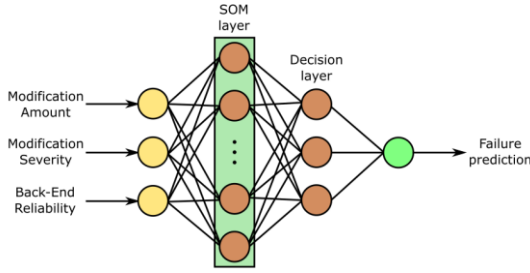


Fig. 4. Structure of SOM-based network

The second ANN is, similarly to the first proposed ANN, composed of two hidden layers. However, this ANN utilizes a Self-Organizing Map (SOM; described in [10]) as the first layer and a single-layer perceptron feedforward network as the second layer. The SOM layer is used for quantization of input vector and thus contains 216 neurons initially uniformly distributed among feature space as a 3-D mesh. Each neuron of SOM layer uses the Euclidian distance as an output function. The decision layer is designed as a single-layered ANN composed from 3 neurons with sigmoid activation function and randomly initialized weights. During the learning process, the weights of SOM and decision layer are adjusted using standard approaches, i.e. supervised learning of the decision layer by backward propagation and unsupervised learning of the SOM layer. Usage of the SOM layer allows this ANN to adapt more smoothly to the specific SUT development patterns applied by particular automotive systems manufacturer.

Both proposed ANN structures have to be evaluated on training and test data obtained from real automotive systems in order to select the most optimal structure. However, such data are not currently available and hence the evaluation, as well as

optimization of selected structure, will be a part of future research.

B. Priority Assignment

As mentioned in section IV, proper assignment of testing priority also depends on several experience factors. Therefore, following experience aspects have been introduced into transition and template extra data:

- The *Safety Impairment* index (integer in the range from 1 to 10) representing the impact of particular functionality failure on the vehicle safety.
- The *User-Comfort Infringement* index (integer in range from 1 to 10) representing impact of particular functionality on the comfort of the vehicle users.

The rationale behind these aspects is intuitive. The higher index means more severe effect of the failure on the vehicle safety or users comfort. Therefore, the higher index together with the potential prediction of failure implies higher testing priority.

The process of priority assignment can be interpreted as a process of classification, where the classifier assigns a priority according to the input feature vector composed of the *Safety Impairment* and *User-Comfort Infringement* indexes and the failure prediction. Clearly, from the perspective of a single priority, such feature space is linearly separable and thus simple perceptron classifiers can be utilized for this task [11]. Fig. 5 shows a feature space linearly separated by hyperplanes into diagonal zones corresponding to priorities.

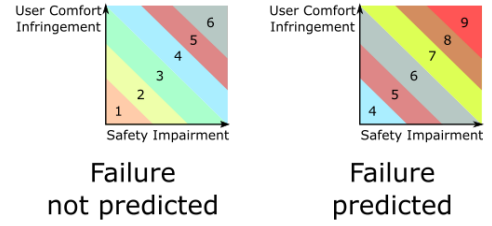


Fig. 5. Priority assignment feature space separation

Since there are ten possible testing priorities, nine different perceptron classifiers are utilized, each having a fixed hyperplane associated with it. Fig. 6 depicts schema of the classification structure.

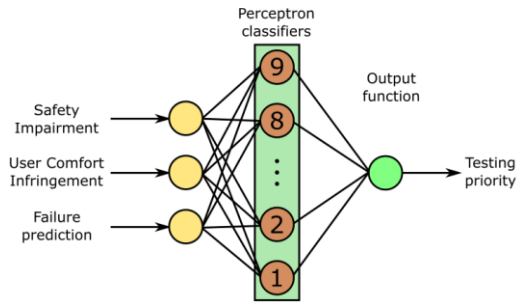


Fig. 6. Priority assignment classification structure

The classification function of each perceptron returns 1, if the input vector lies below its associated hyperplane, and returns

0 otherwise. The output function of classification structure, defined as $f_{out}(x_1, \dots, x_9) = 10 - \sum_{i=1}^9 x_i$, counts the outputs of separate perceptron classifiers and subtracts this sum from 10, which is then used as testing priority for given transition or template.

Since the testing priority is not objectively measurable, the priority assignment procedure does not use learning and utilizes a fixed configuration instead.

V. CONCLUSIONS AND FUTURE WORK

In this paper, a part of new framework for the model-based testing of an automotive distributed systems is presented. The presented framework part, called Automated Pinpointing procedure, exploits the SUT model supplemented with the extra data in order to automatically assign testing priorities to model's transitions and templates. This is useful for automatic pinpointing of the SUT parts that are most worthwhile to be tested.

Additionally, an appropriate set of extra data was introduced. The proposed system of transition and template extra data includes both subjective factors (i.e. experience aspects), as well as objective factors (i.e. fault indicators). As supplemental data take into account various factors influencing the testing priority, the proposed method significantly lowers overall testing operators' insight requirements, as most of the required model parameters can be obtained repetitively by automatic procedures (the objective factors) or once by empirical research (the subjective factors).

Presently, the framework is being implemented into developed tool Taster that currently utilizes pseudorandom test sequence generation. Since this tool uses a modeling language based on timed automata, the presented framework, Automated Pinpointing procedure and proposed extra data utilize it as well.

Future research will be focused on the optimization of the classification structures used within the procedure. Since the priority assignment procedure makes use of strongly subjective *User-Comfort Infringement* index extra data, proper values of this parameter will be acquired by empirical research. Also, it is necessary to gather training data to optimize the ANN structure for failure prediction. Furthermore, other classifiers than ANN will be evaluated, so the most optimal approach could be found. For example, the rule-based methods seem to be promising for this purpose.

Additional research will be focused on the methods for prediction of possible regression in particular functionality caused by influences originating in other, possibly similar, SUT functionality. Such information can be obtained using the static analysis principles from the SUT source code or can be provided by the system modeler. Afterward, such information can be exploited by the context-sensitive classifiers for more precise prediction of functionalities failures.

Finally, since the developed tool currently generates testing sequences pseudo-randomly, more optimal approaches will be explored.

The proposed procedure and complete Taster tool will be evaluated, thanks to the co-operation with Škoda Auto a. s., on the real automotive systems developed and manufactured by this company. Moreover, Škoda Auto a. s. will supply data from real automotive systems that are necessary for the procedure optimization.

ACKNOWLEDGMENT

Research described in the paper was supported by the Grant Agency of the Czech Technical University in Prague, project Model-Based Testing methods for automotive electronics systems (grant No. SGS16/171/OHK3/2T/13) and by the support of EU Regional Development Fund in OP R&D for Innovations (OP VaVpI) and The Ministry of Education, Youth and Sports, Czech Republic, project # CZ.1.05/2.1.00/03.0125 Acquisition of Technology for Vehicle Center of Sustainable Mobility.

REFERENCES

- [1] Tomáš Grus, "Implementation of Integration Testing Test Cases Generation Tool," *Master's Thesis*, CTU in Prague, 2014.
- [2] Sobotka, J. and Novák, J., "Testing Automotive Reactive Systems using Timed Automata," *In BEC 2016 - 2016 15th Biennial Baltic Electronics Conference*. Tallin: Tallin University of Technology, 2016, [under review].
- [3] Behrmann, G., David and A., Larsen, K. G., "A tutorial on UPPAAL," *In proceedings of the 4th International School on Formal Methods for the Design of Computer, Communication, and Software Systems (SFMR'04)*.
- [4] S. Rösch, S. Ulewicz, J. Provost, and B. Vogel-Heuser, "Review of Model-Based Testing Approaches in Production Automation and Adjacent Domains—Current Challenges and Research Gaps," *J. Softw. Eng. Appl.*, vol. 08, no. 09, pp. 499–519, 2015.
- [5] F. Böhr, "Model Based Statistical Testing of Embedded Systems," *2011 IEEE Fourth Int. Conf. Softw. Testing, Verif. Valid. Work.*, pp. 18–25, 2011.
- [6] Zimmermann, F., Eschbach, R., Kloos, J. and Bauer, T., "Risk-based Statistical Testing: A Refinement-based Approach to the Reliability Analysis of Safety-Critical Systems," *12th European Workshop on Dependable Computing, EWDC 2009*, Toulouse, France, 2009.
- [7] Gove, R., Faytong, J., "Chapter 4 – Machine Learning and Event-Based Software Testing: Classifiers for Identifying Infeasible GUI Event Sequences," *Advances in Computers*, vol. 86, pp. 109–135, 2012.
- [8] MaTeLo, <http://www.all4tec.net/MaTeLo/homemateLo.html>.
- [9] Aleksander, I. and Morton, H., "An introduction to neural computing," *International Thomson Computer Press*, 2nd edition, 1995.
- [10] Kohonen, T., "Self-Organizing Maps," *New York : Springer-Verlag*, 1997.
- [11] Minsky, M. and Papert, S., "Perceptrons: An Introduction to Computational Geometry," *M.I.T. Press*, 1969.

Design and Limitations of the Metal – Composite Hybrid Joint Structures

David Krutílek

Department of Radio Electronic
Brno University of Technology
Brno, Czech Republic
xkruti01@stud-feec.vutbr.cz

Abstract—This paper provides an overview of design aspects and limitations of joints in metal-composite hybrid structures and identifies limitations and recommendations regarding electromagnetic properties of the joints. Besides the design recommendations, the most frequently used ways of modelling the joints during the design stage is provided.

Keywords—joint; transfer impedance Z_t ; Discrete circuit elements; Shielding efficiency; lightning damage rating

I. INTRODUCTION

The materials used in aircraft industry are being permanently improved and developed to reduce weight, increase flexibility and strength, and decrease the price. Conventional metal materials are therefore replaced by different composite materials. Composite materials are also advantageous due to their easy shaping ability.

From the EMC point of view, one of the most important aspects of metal-composite joints is to safely conduct possible currents flowing through the joint and, if necessary, protect electromagnetically sensitive equipment against external electromagnetic fields leaking into the internal parts of the aircraft. Ideally, to achieve such a goal, the whole joint area would need to be completely sealed by a highly conductive material with good conductive contact to both adjacent surfaces (contact area between composite and metallic parts). Unfortunately, similar goals are usually not achievable or they represent significant increase of the joint's cost from both time and financial point of view.

In case of riveted metal-composite joints, the main design problems consist of preventing the joint from excessive heating and sparking that can result in damaging of the joint. This is followed by decrease of the shielding effectiveness (SE), degradation of mechanical/strength properties of the composite material near the joint and shortening of its service lifespan.

II. DESCRIPTION OF THE JOINTS USING TRANSMISSIONS CHARACTERISTICS

Transmission characteristic of a joint describes a joint behavior depending on the frequency. Transmission characteristic of a joint are as follows:

- Transfer impedance Z_t
- Discrete circuit elements

- Shielding efficiency (SE evaluation)

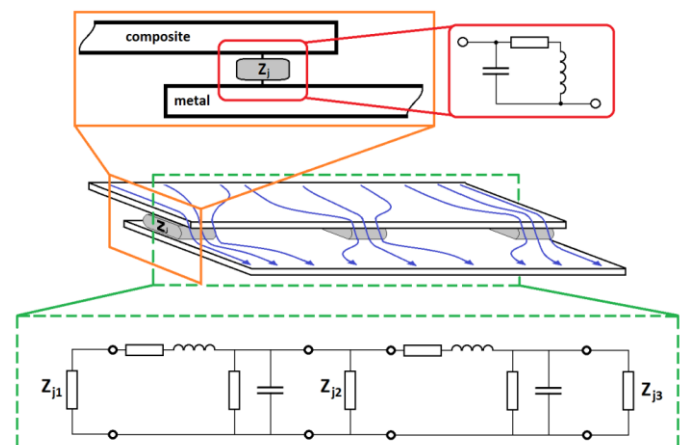


Fig. 1 Illustrative characterization of impedance behavior of a riveted joint (sketch)

For low frequency (maximum sample dimension is $\lambda/10$) it is appropriate to use description based on discrete element circuit. Shielding efficiency (SE evaluation) is used for high frequency description.

A. Discrete circuit elements

Fig. 1 shows behavior impedance (Z_j) of the joint. The path should be subsequently designed with the view of the following aspects:

1) Resistive behavior

The total contact area of all rivets in the considered area, which should be large enough to carry the expected amount of electric current and the conductivity of the path through the joint and should be sufficiently high (e.g. below $2.5 \text{ m}\Omega$ [1]). If the conductivity is poor, overheat of the joint is possible. Resistivity of the joint is a very important aspect especially when designing lightning strike protection or evaluating paths for current return (e.g. [2]).

2) Capacitive behavior

Between the adjacent parts of the joint there should not be any significant accumulation of electric charges, because the formation of spark is possible. When dealing with electro-static discharge (ESD) measures or sparking issues, the property of

the joint is important, especially capacitance. Moreover, in combination with inductance it defines a resonant behavior of the joint.

3) Inductive behavior

Inductance of the joint is increasing with increasing the length of the conductive path through the joint. For this reason, the path should be as short and straight as possible. There should not be a significant problem in case of riveted joint. High inductance of the joint successfully prevents quickly changing currents (high di/dt) to easily pass through the joint despite its low DC resistivity. It is very important to design the conductive path with significantly lower inductance.

B. Shielding efficiency (SE evaluation)

A device made of conductive and / or magnetic material which isolates two regions or space, one with some electromagnetic sources and the other without any source. A way to measure the efficiency of an electromagnetic shield. It is given by formula:

$$SE_{db} = 20 \times \log_{10} \frac{Field_{without_shield}}{Field_{with_shield}} \quad (1)$$

A positive SE corresponds to attenuation. A negative value is also possible, it corresponds to resonances. Shielding effectiveness can be affected by different factors:

- The type of material used for the screen
- Presence of slots, seams, gaskets
- Holes, wires

Shielding effectiveness is evaluated in the context of the considered system (like as panel with cover). It is therefore the global assessment of the whole connection, which consists of more joints on the sample. Poor construction and design of joints may affect on the shielding effectiveness of the materials on high frequency band (especially cover, panels, inspect doors etc.)

A distance between the neighboring rivets (which are creating the conductive paths through the joint) should be small enough (ca. $\lambda/10$ for a maximal considered frequency) to prevent the penetration / re-radiation of electromagnetic fields / currents through the joint (remark: Despite very low DC resistance of riveted joints, an approximate SE of riveted aluminum panels with nonconductive sealants can be expected on the order of 20 dB. In case of a metal-composite riveted joint, it is reasonable to count with the SE below this threshold.[3], [4])

III. SUMMARY OF PROPOSED TESTS

The main purpose of this project is to describe the electrical properties of joints using RLC parameters, and the verification of their hardness against lightning. Since the tests and measurements are principally different, for each test method, it is necessary to produce various samples. Moreover, once the tests for resistance to lightning strikes are finished, it is likely that the sample is permanently damaged.

To determine the RLC parameters, maximum size of the sample is recommended. The maximum dimensions (L_{max}) can be determined with the aid of simple formula:

$$L_{max} = \lambda/10 \quad (2)$$

The test sample, which length is approximately 50 mm, can be measured on maximum frequency $f_{max} = 300$ MHz. Testing the lightning strike is performed on samples of dimensions 500 x 500 mm (550 x 550 mm). These tests can permanently damage and devalue the samples.

A. Impedance measurement method

Electromagnetic properties of a riveted joint can be described via its impedance behavior. The simplest way to describe impedance in both the frequency and the time domain is in a form of an equivalent electric circuit (R, L, C, and G).

However, prior to making any equivalent circuit model of a junction, it is necessary to find out the junction's transfer impedance. Depending on circumstances, it can be done by one of the following measurement setups [5]:

1) Bridge method

The value of the unknown impedance (Z_x) can be obtained by the relationship of the other bridge elements. When no current flows through the detector (D), the bridge is balanced. Various types of bridge circuits, employing combinations of R, L and C components as the bridge elements, are used for various applications. Applicable frequency range is from DC to 300 MHz.

Advantages

- High accuracy (0.1% typ.)
- Wide frequency coverage by using by different types of bridges
- Low cost

Disadvantages

- Needs to be manually balanced
- Narrow frequency coverage with a single instrument

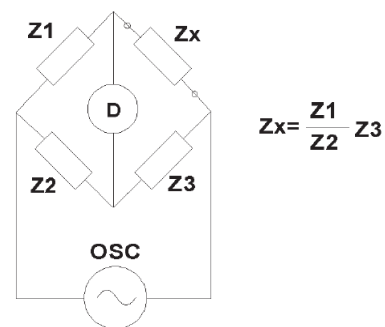


Fig. 2 Principle of bridge method.[5]

2) Auto-balancing bridge method

The current I_x balances with the current I_r which flows through the range resistor (R_r), by operation of the I-V converter. A "virtual ground" is maintained at zero volts the potential at the Low point. Using the voltage measured at the High terminal (V_x) and across R_r (V_r) is calculated the impedance of the DUT.

Advantages

- High accuracy over a wide impedance range
- Wide frequency coverage from LF to HF
- Grounded device measurement

Disadvantages

- Higher frequency range is not available

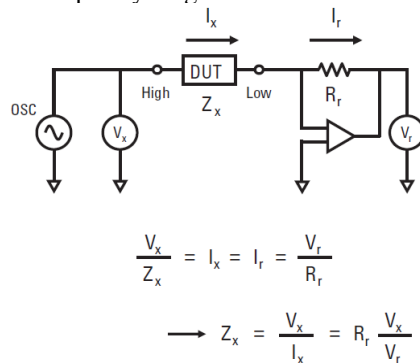


Fig. 3b Principle of auto-balancing bridge method [5].

3) Network analysis method

By measuring the ratio of an incident signal to the reflected signal the reflection coefficient is obtained. To detect the reflected signal is used a bridge or directional coupler. The network analyzer is used to supply and measure the signals. Since this method measures reflection at the Z_x , it is usable in the higher frequency range from 300MHz and above.

Advantages

- Good accuracy when the unknown impedance is close to the characteristic impedance
- High frequency ranges

Disadvantages

- Recalibration required when the measurement frequency range is changed
- Narrow impedance measurement range

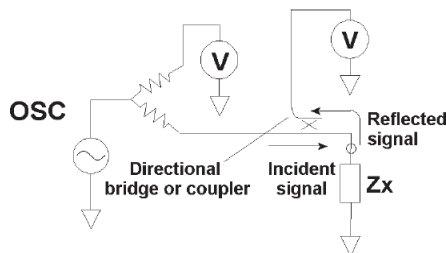


Fig. 4 Principle of network analysis method [5].

B. Shielding effectiveness testing method

When electromagnetic wave of certain frequency impinges on a shielding barrier, electric current is induced into the barrier. This current is reduced by the barrier's skin effect as the wave penetrates the barrier. The ratio of the wave that penetrates the barrier and the incident wave on the barrier is the Shielding Effectiveness of the barrier. Fig. 5 illustrates a chamber with a removable shielding plate. The plate divides

the chamber into two smaller chambers: receiving and transmitting chamber. A gasket (which is not shown) around the sample under the test holds it in place against the shielding plate. A transmitting antenna is inside the transmitting chamber, connected to signal generator. RF amplifier boosts the signal to levels per standards [6]. A receiving antenna is inside the receiving chamber is connected to a spectrum analyzer to measure the exited signal strength.

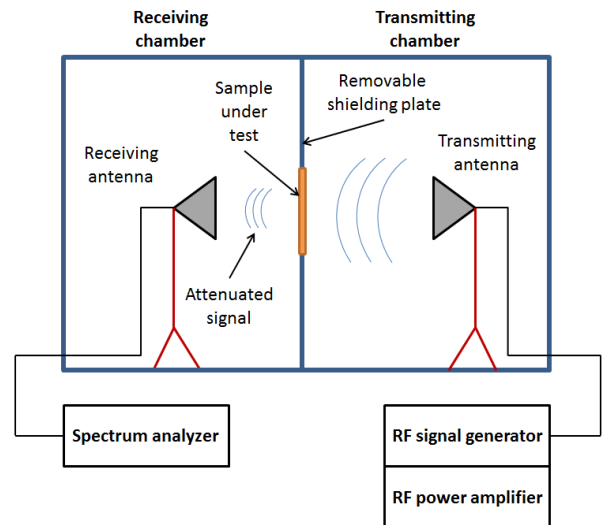


Fig. 5 Sketch of the shielding effectiveness testing method

C. Lightning protection testing method

The transition of high electrical currents may affect the integrity and functionality of the joints. The tests are performed in a high voltage laboratory. The purpose of the test is to determine the direct effects of lightning on the test structure and to predict the joints behavior. The test involves insertion of defined lightning pulse to the determined place of the sample. Once the test is finished, the sample parts are individually rated according to following criteria:

A – Rate of material damage

- Evaluation of the damage due to propagation of lightning current through the defined sample composite material.

B – Rate of part damage

- Evaluation of the damage due to propagation of lightning current through the complex sample.

C – Rate of joint damage

- Evaluation of the damage due to propagation of lightning current through the defined joint.

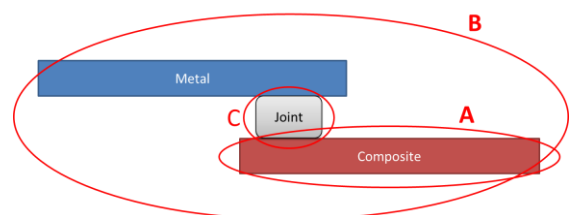


Fig. 6 Illustrative joint (sketch) – damage rating.

These experiments are realized in special laboratories. A variety of test rigs are available to accommodate different sizes of test panel and aircraft structural components. Many structural assessments can be performed on square panels (typically 500mm, or 550mm). For larger structural items or parts of flight control surfaces bespoke test rigs and return conductor paths are set up as required.

Figure 15 illustrates the principle of lightning protection testing. The sample is fixed in the grounded fixture. A thin copper wire is inserted between the electrode (sphere) and the top side of the sample (attachment point). The copper wire helps only to create lightning arc and is not involved in the current distribution. Lightning pulse generator boosts the current to levels per standard [6].

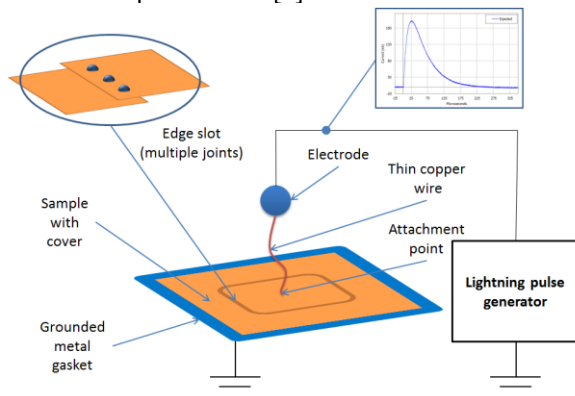


Fig. 7 Principle of lightning protection testing method

IV. ELECTROMAGNETIC MODELING

As mentioned in Chapter II, electromagnetic properties of a riveted joint can be described via its impedance behavior. The simplest way to describe impedance in both the frequency and the time domains, is in a form of an equivalent electric circuit (R, L, C, G; see Fig. 8).

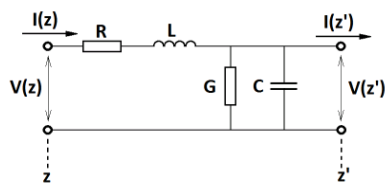


Fig. 8 General equivalent schematic representation of a transmission line element.

As can be seen in Fig. 1, geometrical character of a junction can be „easily“ described by those basic elements and formed into more complex nets, that could be solved by computational means (for example via transmission line matrix method (TLM), partial element equivalent circuit method (PEEC), etc.).

However, prior to making any equivalent circuit model of a junction, it is necessary to find out the junction's transfer impedance. Depending on circumstances, it can be done by one of the following ways:

- By measurement: this is the most common, straightforward, and usually the most exhaustive approach how to obtain real impedance behavior of a joint. Data is usually

obtained only in frequency domain at specific frequencies and has to be subsequently processed into an appropriate form used for time domain analyses.

- By analytical means: description of a junction is made via simple analytical formulas which are able take into account basic shapes and dimensions of its real composition / structure. It is one of the quickest, but not always accurate, ways how to describe the impedance behavior. It should be noted that impedance information obtained by this way is naturally defined by inherent limits of used analytical formulas.

- By computational means: impedance behavior of a junction is computed from its realistic CAD model representation (in 2D or 3D) with the help of computational electromagnetics (computationally efficient approximations to Maxwell's equations). Contrary to both previous ways, using of computational electromagnetics allows us to analyze junctions' impedance relatively quickly, precisely and in the whole necessary frequency spectrum that is of our interest from the EMC and design points of view (DC – 40GHz).

V. CONCLUSION

The measured RCL values of joint characteristics can be easily included in the EM-analyses. This can lead to more precise calculation and helps to define the requirements for the joint. The tests of resistance against lightning strike aim to obtain the information whether such a joint or set of joint is suitable for the area and concrete place on the airplane. In case that the original design is poor, the information obtained from EM-analyses can help to eliminate deficiencies before application on the real sample.

ACKNOWLEDGMENT

Research described in this paper was financed by Czech Ministry of Education in frame of National Sustainability Program under grant LO1401. This work also receives funding through specific research grant project FEKT-S-14-2281. Special thanks belong to EVEKTOR Company for providing the aircraft model data

REFERENCES

- [1] SAE ARP 1870A, Aerospace Systems Electrical Bonding and Grounding for Electromagnetic Compatibility and Safety, Stabilized: August 2012
- [2] MULAZIMOGLU, H., HAYLOCK, L. *Recent Developments in Techniques to Minimize Lightning Current Arcing Between Fasteners and Composite Structure*, Alcoa New Product Development, Aerospace Fasteners, 2011 < https://www.alcoa.com/fastening_systems_and_rings/aerospace/en/pdf/hasim_icosle_2011.pdf >
- [3] GOOCH, J. W., DAHER, J. K. *Electromagnetic Shielding and Corrosion Protection for Aerospace Vehicles*, Springer, March 2007, ISBN-10: 0471126993
- [4] [14] NASA-STD-P023 DRAFT, Electrical bonding for NASA launch vehicles, spacecraft, payloads, and flight equipment, 17th August 2001
- [5] AGILENT IMPEDANCE MEASUREMENT HANDBOOK: A GUIDE TO MEASUREMENT TECHNOLOGY AND TECHNIQUES 4TH EDITION, 2013, < <http://cp.literature.agilent.com/litweb/pdf/5950-3000.pdf> >
- [6] SAE ARP 5412B, Aircraft Lightning Environment and Related Test Waveform

High Frame Rate Video: Is It Always Better?

Jan Kufa, Marek Stavel, Tomas Kratochvil
 Department of Radio Electronics, SIX Research Center
 Brno University of Technology
 Brno, Czech Republic
 xkufaj00@stud.feec.vutbr.cz, kratot@feec.vutbr.cz

Abstract— Interest in multimedia content is rapidly increasing. In recent years there was extremely progress in improving Quality of Experience (QoE) in multimedia systems. This was mainly the stereoscopic video (3D) and High Definition video (HD). Nowadays a 3D video, as we know it is already on the retreat. With the upcoming Ultra HD resolution, we have already reached a stage where higher resolution does not have any more importance because the human eye is not enough sensitive to take benefit from an even higher resolution. Currently video content with a High Dynamic Range (HDR) is slowly expanding. In the future, we can expect expansion of video content with High Frame Rate (HFR). The aim of this paper is to examine if the viewers appreciate the Ultra HD video with a higher frame rate encoded by H.265.

Keywords— Ultra HD, HFR, subjective test, 60 fps.

I. INTRODUCTION

Contemporary trend is to deliver a higher quality of video content to customers. In recent years considerable attention was focus on the resolution and stereoscopic video. Now it is the time to focus on smooth and fluent video. This can be achieved by HFR. The frame rate is the frequency at which frame in a video sequence is displayed. The frame rate is usually expressed in frames per second (FPS). It is supposed that HFR is able to make fast action scenes looking smoother. Other techniques about frame rate and speed of playback are “Slow motion” and “Time-lapse”. Slow motion is achieved when each film frame is captured at a frame rate much faster than it will be played. When we replay this video at normal speed, moving looks more slowly. On the other hand, time-lapse is a technique whereby the speed, at which film frames are captured, is much lower than speed used to play the video.

Nowadays, there is no problem to find HFR videos. In 2014 the biggest video server YouTube already come with the ability to record and play video at frame rate 48 and 60 fps. In 2012 there was released the film “The Hobbit” which was filmed in Ultra HD resolution and 48 fps. This is double frame rate against the classic film standard.

In the article [1] there is evaluated subjective quality of HFR video but only in Full HD resolution and encoded by using H.264. The impact of frame rate on objective metrics is in the article [2]. Encoder and resolution of sequences is same as in article before. How to modeling HFR video transmission over wireless networks is described in [3].

This work was supported by the BUT project no. FEKT-S-14-2177 (PEKOS). The research described in this paper was financed by the Czech Ministry of Education in the frame of the National Sustainability Program under grant LO1401. For research, infrastructure of the SIX Center was used.

Can viewers appreciate the impact of higher frame rates on the usual Ultra HD TV? This is what we will focus on. How to transfer HFR Ultra HD video to TV is also part of this article. The research was carried out on three typical frame rates and two bit rates.

The rest of this paper is organized as following. Description of the used videos and encoder is described in Section II. Testing environment and subjective test are outlined in Section III. Obtained results are evaluated, compared and discussed in Section IV. At the end, Section V concludes this paper.

II. VIDEOS AND CODEC

A. Videos Used for the Comparison

Three videos were chosen for a set of tested sequences (see Fig. 2). Description of videos is in TABLE I. Calculated Spatial Activity (SA) and Temporal Activity (TA) of the video are in Fig. 1. As a source sequences, uncompressed video clips in RAW format were selected. Nowadays it is hard to find the source uncompressed video with Ultra HD resolution and 60 fps. Video database of sequences from Netflix [4] can be used as a good source. Currently, there is a boom of using action outdoor cameras. However, at present, does not exist action camera which can record in Ultra HD resolution at 60 fps. It is possible to select Ultra HD video at 30 fps or 60 fps video in Full HD.

TABLE I. PARAMETERS OF SEQUENCES USED IN TEST

Name	Time [s]	Description
Park joy	10	Moving footage of the people running in the park.
Aerial	10	View of the landscape by using a drone.
Toddler Fountain	10	A child running inside the fountain.

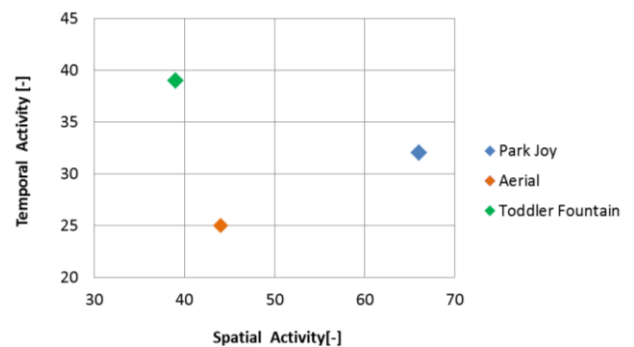


Fig. 1. Temporal and Spatial activity of used video sequences.

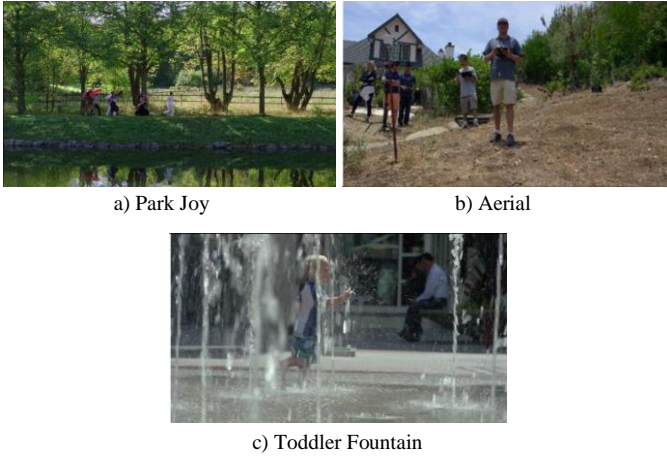


Fig. 2. Thumbnails of used videos.

B. Codec H.265/ HEVC

Source sequences were encoded by codec H.265 known as HEVC. This codec is able to encode video up to 8k resolution and frame rate 120 fps. The most widespread implementation of this codec, x265, was selected. Parameters for encoder are in the TABLE II. Level 5.1 was set in the encoder because Level 5.0 does not support frame rate 60 fps with Ultra HD video. The group of pictures (GOP) was set to 8. Other parameters of encoder were selected according to the recommendations in document [5].

TABLE II. PARAMETERS OF USED ENCODER HEVC

Implementation	x265
Built date	24.4.2016
Encoder version	1.9
Preset	Medium
Profile	Main

Two quality levels were chosen and each level is defined by its bit rate, see TABLE III. Low bit rate 5 Mb/s represents streaming with very limited bandwidth. On the other hand, bit rate 50 Mb/s represents almost limitless bandwidth, for example Ultra Blu-ray disk. We also focus on the fact if viewers appreciate the HFR video provided that are not limited by the bandwidth. What is the difference if they are very limited by the bandwidth? In the case where we have the same bit rate, then at a HFR, the size of one frame is smaller than the size of the frame at low frame rates. That means whether people appreciate more fluency than image quality.

TABLE III. USED FRAME RATES AND BIT RATES

Parameter	Value		
Frame rate [FPS]	24	30	60
Bit rate [Mb/s]	5	50	

Used frame rates are also in the table TABLE III. Frame rate 24 fps represents film standard, almost all films that can be downloaded from the internet have this frame rate. Generally mobile phones and other consumer electronics

record in frame rate 30 fps. Video with 60 fps represents HFR playback.

III. TESTING ENVIRONMENT AND SUBJECTIVE TEST SETUP

To ensure reproducibility of results, the subjective experiment was realized in a laboratory of video and multimedia technology. Laboratory conditions were set up according to ITU BT.500-13[6]. A workplace in a room with controlled lighting was created. Ultra HD television 49-inches LG 49UF8527 was used to display video sequences. The distance of the participants from the Ultra HD display was 1.5 meters.

The bit rate for decompressed Ultra HD video with 60 fps, color depth 8 bit and color model 4:2:0 is approximately 6 Gb/s. The TV was fed by a personal computer (PC), it was equipped with a fast SSD connected via PCI-Express with a read speed up 11 Gb/s. The reading speed of the disk must exceed the data stream of movies. The PC is equipped with NVIDIA GTX 960 that supports HDMI 2.0. Older version HDMI 1.4 is also capable of transmitting an image in Ultra HD resolution, however only in 30 fps. For the considered subjective test, it is necessary to use a newer version HDMI 2.0 which can handle image in Ultra HD resolution in 60 fps [7]. DisplayPort (DP) in version 1.2 is an additional interface, which is able to transfer the video in Ultra HD resolution in frame rate 60 fps to display. This interface, however it is not often used in television, is mainly used in monitors [8].

As a subjective method, Pair Comparison (PC) was chosen. This method was chosen because of its suitability to comparing two similar videos. The time to vote was 8 second. Sequences were played randomly and observers did not know what frame rate is currently presented. Total groups of 22 people were joined into the subjective test, half recruited from university students and second half from the public. An average age was 25 years.

IV. RESULTS AND EVALUATION

The impact of frame rate is more subjective aspect than evaluation of image quality. From this point of view, it is difficult to evaluate the exact perceptual improvement by switching from normal to the high frame rate. Participants compared a pair of two videos on a scale from -2 to +2. The limit value -2 means that the viewer conclusively prefers a smaller frame rate, while the value +2 indicates that viewer prefers video with higher frame rate. A detail description of the scale for comparison between 24 and 30 fps is in TABLE IV. The same meaning of scale is in the comparison between 30 and 60 fps.

TABLE IV. DESCRIPTION OF SCALE USED IN GRAPHS

Scale	Description
-2	Frame rate 24 fps definitely better than 30 fps
-1	Frame rate 24 fps slightly better than 30 fps
0	The same quality for both frame rate
+1	Frame rate 30 fps slightly better than 24 fps
+2	Frame rate 30 fps definitely better than 24 fps

Results are not represented by the average values for a better understanding of the measured data. In the graphs there are plotted cumulative boxplot for each value of QoE. In this representation of results is better seen how many viewers see differentness of QoE in various frame rates and how significant. The effect of video to QoE can be also better observed. Each video in the graph is represented by a different color, as can be seen in the TABLE V.

TABLE V. LEGEND OF USED VIDEOS IN GRAPHS

Color	Video
Blue	Park Joy
Orange	Aerial
Green	Toddler Fountain

From the result, in Fig. 3, it can be determined that viewers did not observe a significant difference between frame rate 24 and 30 fps if low bit rate 5 Mb/s is set. Insignificant dominance can be seen for sequences that have a frame rate 30 fps. About 95 % of respondents rated QoE for video “Park Joy” equal or better if the video has frame rate 30 fps.

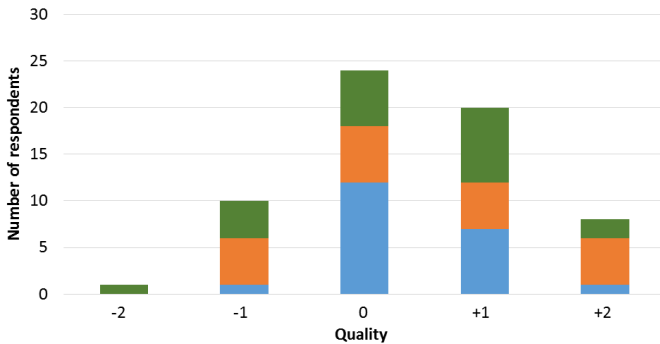


Fig. 3. Spread of QoE for frame rate 24 and 30 fps with bit rate 5 Mb/s.

In the case, which is shown in Fig. 4, participants predominantly rated higher frame rate as better. A quarter of respondents did not see the difference in QoE between a frame rate 30 and 24 fps.

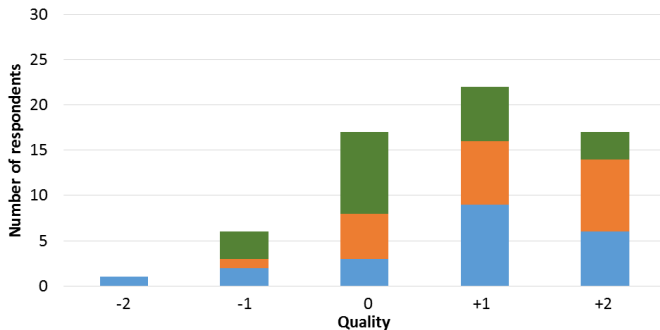


Fig. 4. Spread of QoE for frame rate 24 and 30 fps with bit rate 50 Mb/s.

The result of QoE for low bit rate 5Mb/s at a high frame rate of 60 fps is not unambiguous, see Fig. 5. The QoE highly

depends on the used video. In video “Aerial” viewers clearly preferred frame rate 60 fps. In contrast to this fact, the preferred frame rate in sequences “Park Joy” and “Toddler fountain” was 30 fps. Preference of video “Aerial” in HFR version can be caused by the properties of this sequence. The video is captured by flight drone and all scene is moving.

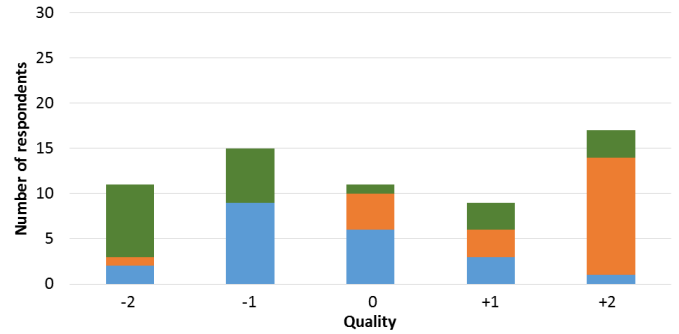


Fig. 5. Spread of QoE for frame rate 30 and 60 fps with bit rate 5 Mb/s.

Unambiguous results are for QoE for frame rate 60 fps and bit rate 50 Mb/s, as can be seen in Fig. 6. More than 75 % viewers prefer HFR video. This applies to all sequences. About 20 % of viewers do not see the difference between frame rate 30 and 60 fps.

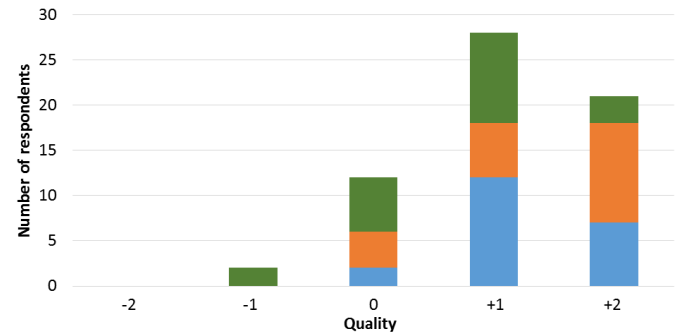


Fig. 6. Spread of QoE for frame rate 30 and 60 fps with bit rate 50 Mb/s.

V. CONCLUSION

If it is possible to have big data throughput, then viewers clearly prefer videos with higher frame rate. At lower bit rate results are not already conclusive. Observers almost did not see the difference in the QoE if frame rate 24 and 30 fps, with bit rates 5 Mb/s, was set. On the other hand, with the option of 30 and 60 fps, evaluation is extremely dependent on the type of sequence. Generally, it can be said that QoE strongly depends on the video sequence. In the optimal case, it would be perfect to have the option to switch the frame rate for each video. From the results, it is also clear that viewers can see the difference between the video with a classical frame rate and the HFR even though they have classic Ultra HDTV. Connecting TV to the source of HFR Ultra HD content is a complex task. Modern interface must be used, especially HDMI 2.0.

ACKNOWLEDGMENT

The authors acknowledge all the observers who took part in the subjective experiments.

REFERENCES

- [1] R. M. Nasiri, J. Wang, A. Rehman, S. Wang and Z. Wang, "Perceptual quality assessment of high frame rate video," in Proceedings of IEEE 17th International Workshop on Multimedia Signal Processing (MMSP), 2015, Xiame (PRC), pp. 1-6. doi: 10.1109/MMSP.2015.7340831
- [2] T. Zinner, O. Hohlfeld, O. Abboud and T. Hossfeld, "Impact of frame rate and resolution on objective QoE metrics," in Proceedings of Quality of Multimedia Experience (QoMEX) 2010, Trondheim, (Norway), pp. 29-34. doi: 10.1109/QOMEX.2010.5518277
- [3] J. Wu, C. Yuen, N. M. Cheung, J. Chen and C. W. Chen, "Modeling and Optimization of High Frame Rate Video Transmission Over Wireless Networks," in IEEE Transactions on Wireless Communications, vol. 15, no. 4, pp. 2713-2726, April 2016. doi: 10.1109/TWC.2015.2509063
- [4] Xiph.org::Dorf's Test Media Collection. Xiph.org Video Test Media. [online]. [cit. 2016-07-06]. Available from: <https://media.xiph.org/video/dorf>
- [5] x265 HEVC High Efficiency Video Coding H.265 Encoder. x265. [online]. [cit. 2016-07-06]. Available from: <http://x265.org/index.html>
- [6] ITU-R BT.500-13. "Methodology for the subjective assessment of the quality of television pictures." ITU, January 2012.
- [7] HDMI Forum's Technical Working Group. [cit. 2016-07-06]. Available from: http://www.hdmi.org/manufacture/hdmi_2_0/
- [8] C. Wiley, "DisplayPort Technical Overview" in Proceedings of IEEE International Conference on Consumer Electronics (ICCE), 2011, Las Vegas (USA). Available from: <http://www.vesa.org/wp-content/uploads/2011/01/ICCE-Presentation-on-VESA-DisplayPort.pdf>

Correlated Mutation Analysis Improvement by Proteomic Signal Processing

Kristyna Kupkova, Karel Sedlar, Ivo Provaznik

Department of Biomedical Engineering
Brno University of Technology
Brno, Czech Republic
xkupko00@stud.feec.vutbr.cz

Abstract— Correlated mutation analysis has become a powerful tool in protein contact prediction based on multiple sequence alignments of homologous proteins. Here, we introduce a novel method for the computation of correlated mutations based on prior transformation of protein sequences into their numerical form, which provides important biological properties about the amino acids. The method is then incorporated into a compact technique replacing the previously proposed Jaccard index. This results in the significant improvement of all of the statistical parameters used in this study.

Keywords— *correlated mutations; protein contact map; numerical representation*

I. INTRODUCTION

The function of a protein is fully determined by its spatial structure, which makes it a fundamental carrier of information in molecular biology. However, the current methodologies for protein structure assessment (such as X-ray crystallography or electron microscopy) are financially demanding and time consuming. Therefore, there is an incomplete protein structure database and it is not possible to follow the impact of fast mutational changes on molecular dynamics [1]. In order to overcome this barrier, there have been attempts since 1960s to devise a method for the determination of a 3D protein structure directly from its primary amino acid sequence [2]. One of the subproblems of this issue is the requirement for the construction of a protein contact map, which would indicate amino acid residues in close proximity to each other in the 3D model but distant from each other in the primary amino acid sequence. Correlated mutation analysis (CMA) which uses the multiple sequence alignment (MSA) of homologous proteins has become a popular approach to the construction of such a map. It is essential for a protein to maintain its structure intact in order to maintain its function. Therefore, negative point mutations at contact sites need to be compensated by other mutations. This mechanism, whereby pairs of residues in contact with each other need to co-evolve in synchrony, then results in a high correlation score for the pairs of positions in the MSA which are in contact with each other in the tertiary structure of homologous proteins [3].

Many CMA approaches have been tested over the past 30 years [3]-[8] with an achieved precision which is typically between 20% to 40%. These low precision values reflect a

large number of false positives in the predictions and are caused by additional phylogenetic residue correlation [9]. In order to reduce this background correlation, several CMA improvements have been introduced e.g. the application of specific filters [4], the combination of CMA results obtained from amino acid sequences with CMA results at codon level [5], or the combination of CMA results with neural networks [6]. Although these improvements reduce false positive detection, recall reflecting the number of correctly predicted contacts out of all existing contacts remains low. Recall enhancement has been introduced in [7], wherein several CMA methods were combined into a compact method, which leads to minimal precision impairment with significant recall improvement.

In this study, a novel approach to CMA, which uses a proteomic signal processing technique named proteomic signal correlation (PSC), is introduced. Numerical representation of the protein carrying information about important biological properties of amino acids has already proven useful in the prediction of the functional sites of proteins [10]. In this paper, we use a transformation method based on the hydrophobicity and hydrophathy of amino acids in combination with Pearson's correlation coefficient. The technique is then incorporated into the method introduced in [7], which results in further recall improvement with only low precision impairment.

II. MATERIALS AND METHODS

A. Data Preparation

The input for the CMA consists of the MSA of homologous proteins. These protein sequences can either be retrieved from suitable databases (such as Pfam or HSSP) or by performing a BLAST run against the protein database. Since the latter approach has provided better results [11], we used PSI-BLAST (Position-Specific Iterated BLAST) [12] on the non-redundant protein sequences database at NCBI (National Center for Biotechnology Information) [13]. Both orthologous and paralogous sequences were included in the dataset, for the exclusion of either seemed to be counter-productive [11]. Only sequences with a similarity between 70-90% with the reference sequence were selected and then aligned by using the Clustal Omega program [14]. Sequences with a similarity to each other which was higher than 90% were removed from the formed

MSA in order to reduce the phylogenetic background of closely related sequences. Completely conserved positions were excluded from the MSA, since these positions do not provide any relevant information for the CMA [11]. In addition, positions containing more than 20% of gaps and positions with a gap occurrence in a reference sequence were removed. The details of the final MSA dataset consisting of five protein sets are listed in TABLE I.

B. Proteomic Signal Correlation

The novel method introduced in this paper, proteomic signal correlation (PSC), involves two steps. First, each column of the constructed MSA is transformed into a suitable proteomic signal form. The second step involves the computation of the Pearson's correlation coefficient between all pairs of columns.

Many transformation techniques have been introduced over the past decade which convert the primary amino acid sequence into signal representation based on the biological properties of amino acids [10], [15], [16]. Finding the suitable transformation technique is crucial for the PSC outcome. In order to compute the Pearson's correlation coefficient, the final signal representation should ideally be 1D while carrying a sufficient amount of information about a given amino acid. For this reason, we chose the transformation technique introduced in [16]. The conversion of column x in the MSA is undertaken according to following equation:

$$x_i = \frac{Hp_t^1}{EH_t^1}, \quad (1)$$

where i is the index of the sequence in the MSA and Hp^1 and EH^1 are values derived from the hydropathy and hydrophobicity of amino acid t accordingly. The values for each amino acid t can be obtained from [16].

The final correlation coefficient r between the two positions x and y is computed as follows:

$$r(x, y) = \frac{1}{N-1} \sum_{i=1}^N \left(\frac{x_i - \mu_x}{\sigma_x} \right) \left(\frac{y_i - \mu_y}{\sigma_y} \right). \quad (2)$$

Here, i means the index of a sequence running from 1 to N and N is the number of sequences in the final MSA. Values μ_x and σ_x are the mean value and standard deviation of column x respectively.

C. Character-based Correlated Mutation Analysis

Compared to PSC, the CMA methods introduced in this section are purely character-based and work directly with the formed MSA.

1) Mutual Information

Mutual information (MI) as a measure of mutual dependence between two columns has been computed according to [3]. In order to reduce background MI caused by the finite sample effect and phylogenetic influence, the final values of MI were normalized by using MI/H_{xy} , where H_{xy} is the joint entropy of positions x and y .

TABLE I. DATASET DETAILS

PDB ID/ chain	Seq length ^a	MSA width ^b	MSA depth ^c
1A6K/A	151	142	61
1AFC/A	140	93	24
1HM6/A	346	313	51
3BCQ/A	143	137	88
4DT6/A	210	162	69

^a Original length of a reference sequence.

^b Length of sequences after preprocessing.

^c Number of sequences in MSA after preprocessing

2) Residue Correlation Analysis

The residue correlation analysis (RCA) has been computed according to [8]. We used the BLOSUM62 substitution matrix for obtaining the values of $s(x, k, l)$ at position x between the two sequences k and l since the dominance of the McLachlan substitution matrix has not been proven [17]. The final correlation score was normalized by using $RCA_{xy} = (RCA_{xy} - \min(RCA)) / (\max(RCA) - \min(RCA))$ in order for the values to fall into the 0 to 1 interval.

3) Jaccard Index

The Jaccard index (JI), representing the last measure of CMA used in this paper, has been computed by using the equation in [18].

D. Compact Correlated Mutation Analysis

The CMA approaches described above can be combined into a compact method by using the following equation:

$$\frac{MI_{xy}^2}{MI_{cut}^2} + \frac{RCA_{xy}^2}{RCA_{cut}^2} + \frac{JI_{xy}^2}{JI_{cut}^2} + \frac{PSC_{xy}^2}{PSC_{cut}^2} > 1. \quad (3)$$

In this equation, a numerator represents the squared value of the correlation coefficient between positions x and y computed by the given single CMA technique and the denominator refers to the squared cutoff value of the corresponding technique. A pair of protein amino acid residues is considered to be in contact if the condition of equation (3) is satisfied.

A compact method combining only two or three CMA techniques has been carried out by including only these desired techniques into equation (3) and omitting the rest.

E. Protein Contact Map Construction

In order to statistically evaluate the results of the different CMA methods, we have constructed a protein contact map for each protein set by using information about the reference protein structure from its Protein Databank (PDB) file. A protein contact map is a binary matrix, where 1 represents a pair of residues which are considered to be in contact. In this study, we have adopted the definition of contact of [19], where two residues are regarded as being in contact and, therefore, represent true positive values in the final statistical evaluation, if the distance between their Ca atoms is lower than 8Å.

All of the programs presented in this chapter were implemented in MATLAB.

III. RESULTS AND DISCUSSION

A. Cutoff Determination

The cutoff values from equation (3) for each CMA method have been specified by the computation of precision [precision = TP/(TP + FP)] and recall [recall = TP/(TP + FN)] for each possible correlation score value in the range of 0-1 with the step equal to 0.01. Since PSC provides both positive and negative correlation scores, the precision and recall for this method has been computed for values higher than the absolute value of a given correlation score. The results can be seen in Fig. 1. It is clear that recall drops rapidly with increasing precision. Therefore, a compromise was required to be made between recall and precision when specifying the cutoff values. This resulted in $PSC_{cut} = 0.69$, $MI_{cut} = 0.36$, $RCA_{cut} = 0.56$ and $JI_{cut} = 0.52$, where the precision curves intersect with the recall curves.

B. Method Evaluation

In order to compare the success of the different CMA methods in protein contact prediction, we have performed an analysis in the form of precision, recall, and improvement in precision relative to a random prediction for every protein set. The improvement in precision relative to a random prediction is the ratio between the precision of the given method and the precision of the random predictor [8]:

$$improvement = \frac{precision}{\frac{N_c}{N_p}}, \quad (4)$$

where N_c is the number of real contacts and N_p represents all of the possible contacts.

The final results evaluating the performance of both the individual CMA methods and their different possible combinations are listed in TABLE II. The combinations of the methods here are specified by the first letters of the given techniques separated by a hyphen. These results show that the

TABLE II. STATISTICAL EVALUATION OF THE METHODS

Method	Precision	Recall	Improvement
PSC	0.24	0.25	3.65
MI	0.25	0.25	3.88
RCA	0.22	0.22	3.24
JI	0.18	0.18	2.60
M-R	0.20	0.38	2.93
M-J	0.15	0.34	2.32
M-P	0.21	0.39	3.17
R-J	0.14	0.35	2.07
R-P	0.18	0.37	2.64
M-R-J	0.13	0.45	1.92
M-R-P	0.17	0.47	2.46

novel method introduced in this paper (PSC) seems to provide results which are comparable with MI, which seems to be the best of all of the individual CMA approaches. On the other hand, JI shows poor performance in terms of protein contact prediction in comparison with the other individual methods. Therefore, although any combination with JI leads to a recall improvement, it also rapidly decreases precision along with an improvement in precision relative to a random prediction.

If we examine all of the combined methods, it is clear that combination of MI with PSC seems to provide the best results in terms of minimal precision decrease with maximal recall gain. This combination even outperforms the M-R method, which showed the most promise in [7]. Although the precision and recall gain is only 1% when using M-P compared to M-R, the improvement increase is more than 20%.

When using the M-P method for contact prediction, the recall enhancement is rather significant, given that the achieved value is almost doubled compared with the resultant values when only an individual CMA technique is used. However,

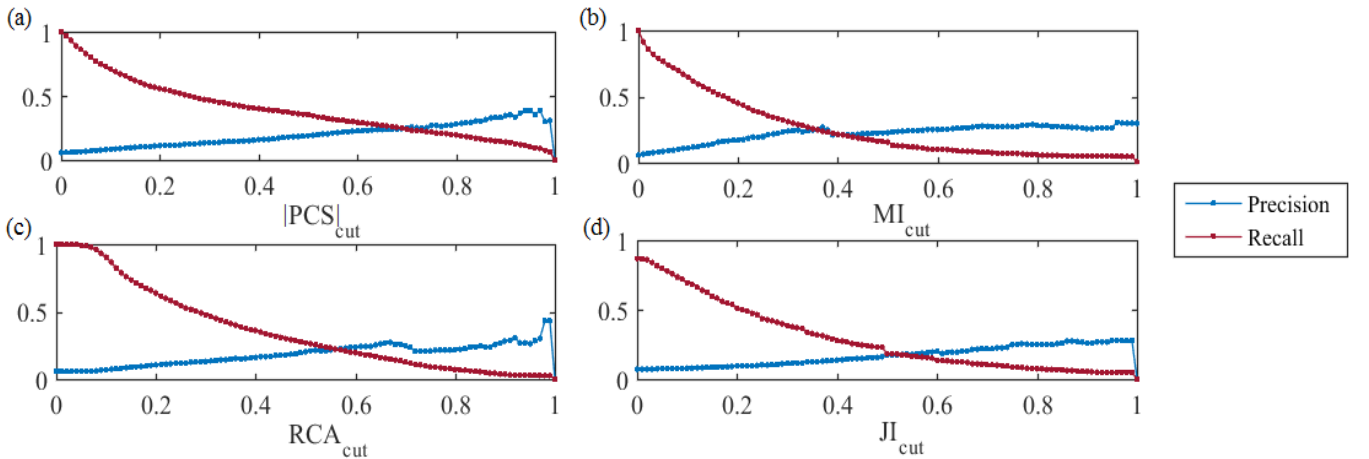


Fig. 1. Average precision (blue line) and recall (red line) values plotted against different cutoff values. Each point at a line represents precision or recall value when contacts are predicted as pairs of residues with higher correlation score than a given cutoff value on x-axis. Precision and recall are plotted against (a) absolute values of PSC correlation score cutoffs, (b) MI cutoff values, (c) RCA cutoff values, and (d) JI cutoff values.

when we are aiming for further recall gain, the best option would be a combination of M-R-P, by which the average recall achieved a value of 0.47 with only a 0.08 drop from the highest reached precision with the use of MI. This triple combination (M-R-P) also outperformed the triple combination with JI introduced earlier (M-R-J) [7] in all three statistical evaluations. Therefore, we can conclude that the use of PSC instead of JI can improve the performance of the compact method.

IV. CONCLUSION

Until this point, all CMA methods have been working with MSAs in their original character-based forms. Such form does not provide any additional information about an amino acid apart from its identity. Here, we presented an entirely new approach for the computation of CMA by using MSAs in the form in which each amino acid is represented by a number derived from its hydrophobicity and hydropathy. The correlation score is then obtained by a simple computation of Pearson's correlation coefficient. It is the simplicity and low computational requirement of the method which make it so unique compared to character-based techniques. At the same time PSC achieves statistical results which are comparable with the best approaches. Furthermore, the technique provides information about new contacts in comparison with other CMA techniques, which is proven by the rapid recall increase when the PSC is incorporated into the multidimensional CMA method formed by multiple techniques. It is clear that the results obtained by the PSC outmatch the statistical results obtained by the RCA, which has been, for so long, the "holy grail" of CMA. Since PSC is the first method of its kind to use protein sequences in a numerical form, we believe that, with further refinements and by the combination of the outcome with advanced machine learning techniques (such as neural networks or support vector machines), this approach provides great potential for advancement in the field of protein structure prediction.

REFERENCES

- [1] K. Hamacher, "Relating sequence evolution of HIV1-protease to its underlying molecular mechanics", *Gene*, vol. 422, no. 1-2, pp. 30-36, 2008.
- [2] Y. Xu, D. Xu and J. Liang, *Computational methods for protein structure prediction and modeling*. New York: Springer, 2007.
- [3] L. Martin, G. Gloor, S. Dunn and L. Wahl, "Using information theory to search for co-evolving residues in proteins", *Bioinformatics*, vol. 21, no. 22, pp. 4116-4124, 2005.
- [4] P. Kundrotas and E. Alexov, "Predicting residue contacts using pragmatic correlated mutations method: reducing the false positives", *BMC Bioinformatics*, vol. 7, no. 1, p. 503, 2006.
- [5] E. Jacob, R. Unger and A. Horovitz, "Codon-level information improves predictions of inter-residue contacts in proteins by correlated mutation analysis", *eLife*, vol. 4, 2015.
- [6] P. Fariselli, O. Olmea, A. Valencia and R. Casadio, "Prediction of contact maps with neural networks and correlated mutations", *Protein Engineering Design and Selection*, vol. 14, no. 11, pp. 835-843, 2001.
- [7] K. Kupkova, K. Sedlar and I. Provaznik, "Multidimensional Correlated Mutation Analysis for Protein Contact Map Prediction", *Advances in Intelligent Systems and Computing*, pp. 133-145, 2016.
- [8] U. Göbel, C. Sander, R. Schneider and A. Valencia, "Correlated mutations and residue contacts in proteins", *Proteins: Structure, Function, and Genetics*, vol. 18, no. 4, pp. 309-317, 1994.
- [9] D. Jones, D. Buchan, D. Cozzetto and M. Pontil, "PSICOV: precise structural contact prediction using sparse inverse covariance estimation on large multiple sequence alignments", *Bioinformatics*, vol. 28, no. 2, pp. 184-190, 2011.
- [10] A. Tamulewicz and E. Tkacz, "Human Fibroblast Growth Factor 2 Hot Spot Analysis by Means of Time-Frequency Transforms", *Advances in Intelligent Systems and Computing*, pp. 147-159, 2016.
- [11] H. Ashkenazy, R. Unger and Y. Kliger, "Optimal data collection for correlated mutation analysis", *Proteins*, vol. 74, no. 3, pp. 545-555, 2009.
- [12] S. Altschul, "Gapped BLAST and PSI-BLAST: a new generation of protein database search programs", *Nucleic Acids Research*, vol. 25, no. 17, pp. 3389-3402, 1997.
- [13] K. Pruitt, "NCBI Reference Sequence (RefSeq): a curated non-redundant sequence database of genomes, transcripts and proteins", *Nucleic Acids Research*, vol. 33, no., pp. D501-D504, 2004.
- [14] F. Sievers, A. Wilm, D. Dineen, T. Gibson, K. Karplus, W. Li, R. Lopez, H. McWilliam, M. Remmert, J. Soding, J. Thompson and D. Higgins, "Fast, scalable generation of high-quality protein multiple sequence alignments using Clustal Omega", *Molecular Systems Biology*, vol. 7, no. 1, pp. 539-539, 2014.
- [15] Z. Wu, X. Xiao and K. Chou, "2D-MH: A web-server for generating graphic representation of protein sequences based on the physicochemical properties of their constituent amino acids", *Journal of Theoretical Biology*, vol. 267, no. 1, pp. 29-34, 2010.
- [16] Y. Zhang, Y. Sheng, W. Zheng, P. He and J. Ruan, "Novel Numerical Characterization of Protein Sequences Based on Individual Amino Acid and Its Application", *BioMed Research International*, vol. 2015, pp. 1-8, 2015.
- [17] S. Salzberg and T. Warnow, *Algorithms in Bioinformatics*. Berlin, Heidelberg: Springer Berlin Heidelberg, 2009.
- [18] Z. Li, Y. Huang, Y. Ouyang, Y. Jiao, H. Xing, L. Liao, S. Jiang, Y. Shao and L. Ma, "CorMut: an R/Bioconductor package for computing correlated mutations based on selection pressure", *Bioinformatics*, vol. 30, no. 14, pp. 2073-2075, 2014.
- [19] A. Tegge, Z. Wang, J. Eickholt and J. Cheng, "NNcon: improved protein contact map prediction using 2D-recursive neural networks", *Nucleic Acids Research*, vol. 37, no., pp. W515-W518, 2009.

Video Quality Assessment in Experimental Retinal Imaging

Ivana Liberdová

Department of Biomedical engineering
Brno University of Technology
Brno, Czech Republic
xliber00@stud.feec.vutbr.cz

Radim Kolář

Department of Biomedical engineering
Brno University of Technology
Brno, Czech Republic

Abstract—This paper is focused on video quality assessment of experimental retinal video image sequences with two different approaches (automatic and expert analysis). Methods utilizing both video quality evaluations are presented and described within the paper. Evaluations consider the most frequent retinal imaging artefacts (contrast distortion, noise and blurriness). Automatic evaluating algorithm estimates the image quality based on three different parameters characterizing the image over time (signal to noise ratio - SNR, blurriness quality evaluation - BQE and contrast quality evaluation - CQE). Four different experts performed the evaluation with their subjective image perceiving and assess the degree of noise, blurriness and contrast in the images over time. The reliability of proposed algorithm for automatic retinal image video quality assessment seems to be correct for all three parameters. Medians of SNR as well as the medians of CQE are decreasing with decreasing image quality evaluated with 4 experts, and medians of BQE are increasing.

Keywords—retinal imaging, video quality assessment, cross correlation, noise

I. INTRODUCTION

This paper is focused on image quality assessment in experimental retinal imaging. The experimental retinal imaging lies in new approach of ophthalmoscopy measurements presented in [1], which provide long-term ophthalmoscopic video records. These records can give the information about the temporal changes of blood vessels and the hemodynamic analysis can be applied on recorded data. This new approach can clarify the process of glaucoma degenerative mechanism [1] or diseases connected with cardiovascular disease.

Shortly described, generally there exists only the one equipment providing the long-term video records of retina – mydriatic fundus camera (company Imedos Systems - Germany). In paper [1] were presented new approach – non-mydriatic videophthalmoscope (VO) which uses single LED light source of low illumination level to measure the long-term records of retina as well without any eye damage. Advantage of this approach is that there is no need to use any mydriasis which can cause the negative effects. On the other hand the records are noisier in comparison with the fundus camera. There are also other artefacts in video records caused by the eye movements (saccadic movements, blinking). These distortions in video sequences must be considered while the

evaluation or analysis is performed, because bad quality video records can skew the results.

II. VIDEO QUALITY ASSESSMENT

Before each analysis/study using the video, the video quality evaluation is needed to consider its appropriateness and usability. In extensive studies is very difficult and expensive to subjectively evaluate the large number of video records. That is why the objective video quality assessment (VQA) is needed.

VQA is common problem in the field of image quality processing. Generally there are many different approaches for video quality evaluation. Statistic error metrics (mathematical methods) as e.g. mean squared difference, average difference [2] [3], are computationally convenient but they ignore the human visual system (HVS).

Modern VQA approaches are classified into three groups – full-reference, reduced-reference, no-reference [2]. No reference methods are also called the “blind model” and have no access to original signal [2]. The example of the no-reference approach is e.g. BRISQUE metrics [4]. Reduced-reference methods use only certain features of the original image [3]. The most widespread are full-reference methods, which include methods based on HVS. Example of these methods can be SSIM method [2] and also method based on phase correlation presented below.

The mathematical methods are still very attractive mainly because of low computational complexity and because of independence on viewing conditions [5]. The image quality can be evaluated on base of many different viewing conditions which are not fixed in most cases. Considering N different viewing condition there will be N various results of quality measurements [5]. In [5] were presented and applied the new mathematical approach of universal image quality index which consider three viewing conditions – loss of correlation, luminance distortion and contrast distortion.

In this paper, the objective evaluation focused on retinal data is presented and compared with subjective evaluation. Due to retinal imaging and its artefacts, both objective and subjective image quality evaluation is based on three viewing conditions – contrast distortion, noise and blurriness.

III. METHODS

As mentioned, the methods in this paper are focused on contrast distortion, noise and blurriness. These three factors have the biggest influence on image quality perceiving in retinal video records (described in). The methods for evaluation of these factors for retinal imaging are described below.

A. Noise evaluation

The video record quality is affected by the Gaussian noise caused by acquisition parameters, camera temperature or also by sensor noise caused by poor illumination during the measurement of the ophthalmoscopic record.

Usually the peak signal-to-noise ratio (PSNR) [2] or signal-to-noise ratio (SNR) is used for noise evaluation in the image. For noise evaluation in retinal data, the SNR method is modified and used as the significant value for whole video record of M frames. The SNR for video record is computed as the ratio of the mean value of the averaged image (AI) of whole sequence and the mean value of the image noise (NI) throughout the sequence

$$SNR = \frac{\mu_{AI}}{NI} \quad (1)$$

$$NI = \frac{\sum_{m=1}^M \left(\frac{\sum_{p=1}^P \sum_{q=1}^Q (|image_m - AI|)_{p,q}}{P Q} \right)}{M} \quad (2)$$

where P, Q is number of pixels in image.

B. Blurriness evaluation

The retinal images in video record can suffer from blurriness caused by eye saccadic movements and due to imperfect focus. The blurriness extent depends on acquisition parameters and *speed* v of the motion. Example of the blurred frames in video records is shown in Fig. 1.

While simulating the blurred image $f_2(x, y)$ in one direction, the original image $f_1(x, y)$ is convoluted with the distortion function $h(x, y)$, where $h(x, y)$ is the imaging system response (according to [6]):

$$h(x, y) = \begin{cases} 1/v & \text{if } 0 \leq x \leq L \\ 0 & \text{else} \end{cases} \quad (3)$$

and its spectrum is $H(u, v)$ ([6]):

$$H(u, v) = e^{-j\pi Lu} \frac{\sin(\pi Lu)}{\pi u} \quad (4)$$

The blurriness estimation can be done as inverse Fourier transform (IFT) of normalized cross correlation (NCC) of original image and the blurred image afterwards

$$NCC = \frac{F_1(u, v) F_2^*(u, v) H(u, v)}{|F_1(u, v)| |F_2(u, v)| |H(u, v)|} = e^{-j\pi Lu} \quad (5)$$

$$IFT(NCC) = \frac{1}{4\pi^2} \int_{-\infty}^{\infty} \int_{-\infty}^{\infty} e^{2\pi jL(u x + \frac{v y}{L})} du dv \quad (6)$$

The blurriness analytical description for various directions is then

$$IFT(NCC) = \frac{1}{4\pi^2} \int_{-\infty}^{\infty} \int_{-\infty}^{\infty} e^{j2\pi KL(\frac{u}{K}x + \frac{v}{L}y)} du dv \quad (7)$$

In case of $K, L \rightarrow 0$ the resulted function leads to Dirac function and in other cases the function will have much more extensive distribution depending on specific blur kernel.

While the application in retinal imaging, the image translation (caused by eye movements) could be ignored, because data is already registered. The results of method application on retinal images can be seen in the image (Fig. 1) – the resulted function of the sharp image is close to Dirac function in comparison with the blurred one, where the distribution is spread and noisy without any visible maximum.

For quality evaluation, the quality criterion for result description is needed. Because of requirements for easy implementation and computational complexity, the sum of normalized intensities in resulted function of IFT of cross correlation is used as quality coefficient (QC), where C is the IFT of NCC .

$$QC = \frac{\sum_{m=1}^M \sum_{n=1}^N \left(\frac{C - \min(C)}{\max(C) - \min(C)} \right)_{m,n}}{NM} \quad (8)$$

This quality coefficient changes significantly with the resulted function distribution, as seen in Fig. 1.

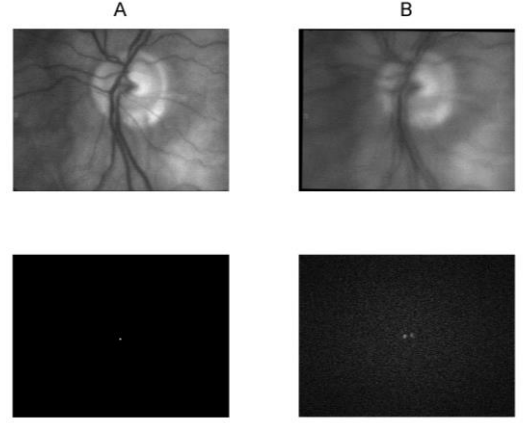


Fig. 1. Frames of video record with corresponding IFT of NCC A, sharp image with $QC = 2,2552 \cdot 10^{-6}$ B, blurred image with $QC = 0,10208$

As the quality coefficient is computed for all frames in sequence, the blurriness quality evaluation (BQE) for whole sequence can be evaluated as mean of QC of the frames, where M is number of frames in sequence

$$BQE = \frac{\sum_{m=1}^M QC_m}{M} \quad (9)$$

C. Contrast evaluation

Contrast in retinal data is very important for image perceiving and also for the following analysis e.g. hemodynamic analysis etc.

The method presented in [7] is used for contrast evaluation. The method is based on entropy metric applied on image histograms, where the histograms correspond to edge images of contrast enhanced images (computed by CLAHE method [8]). The edge images are computed on base of Sobel operator in both directions. The histogram of well contrasted image is relatively rich in comparison with histograms corresponding to

the images of bad contrast, which contains sharp peaks. The histogram changes can be evaluated then

$$E = - \sum_{i=1}^N p_i \log(p_i) \quad (10)$$

where p_i is probability of a density function [7].

The mean of E of whole sequence is taken for contrast quality evaluation (CQE).

D. Expert Analysis (Subjective assessment)

All video records were also evaluated subjectively by 4 people who evaluated the quality by the described viewing conditions – noise, contrast and blurriness. The observers assess the records by numbers 1-3 according to next rules: 1 – nice record, 2 – moderate record, 3 – bad record. For each parameter, the vectors of parameter quality were averaged over experts.

E. Comparison between the algorithm and expert analysis

Because of the expert analysis procedure, the quality output vector of each expert and the averaged vector can be considered as a discrete random variable. For that reason, the standard statistical tests for continuous random variables (e.g. t-test or Wilcox, etc.) cannot be used. Because of that we have arranged a simple way for the data comparison. The domain of subjective assessment was divided into 3 intervals of same length $1 \leq F \leq 1,5$, $1,5 < F < 2,5$, $2,5 \leq F \leq 3$. Then objective values of each sequence can be selected on corresponding positions of each interval and classified into 3 groups. The objective parameter's probability density function (p.d.f.) on corresponding interval is characterized then as a boxplot from selected parameter values.

IV. DATA

All three methods are applied on retinal data which were measured by experimental non-mydratic ophthalmoscope in Eye clinic, University Hospital in Erlangen in the framework of the Erlangen Glaucoma Registry (a clinical registry ClinicalTrials.gov identifier: NCT00494923).

There are 62 video records available for the VQA. The video records were measured on 21 both healthy and ill patients. Each video record includes 261 frames of 640 x 480 pixels. For recording was used CCD camera (iDS, UI-2210 SE-M-GL) and 1 pixel corresponds to 9,3 μm on retina. The records are with centered optic nerve.

Each video record was registered before applying the VQA methods.

V. RESULTS AND DISCUSSION

While applying described automatic methods on the retinal data, the three numbers – SNR, BQE, CQE were computed for each video sequence. The objective values for each video sequence are visualized in Fig. 2.

The averaged value of subjective evaluations for each viewing condition is visualized in Fig. 3.

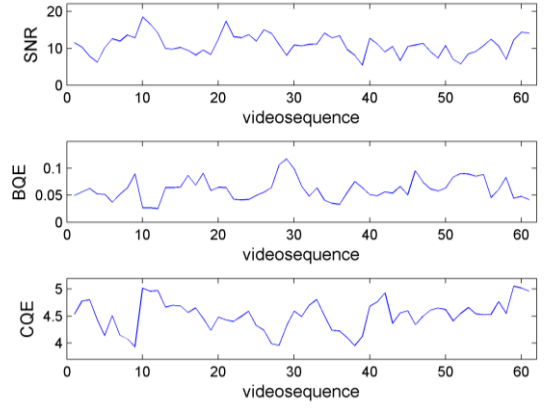


Fig. 2. Results of objective VQA methods for video sequences

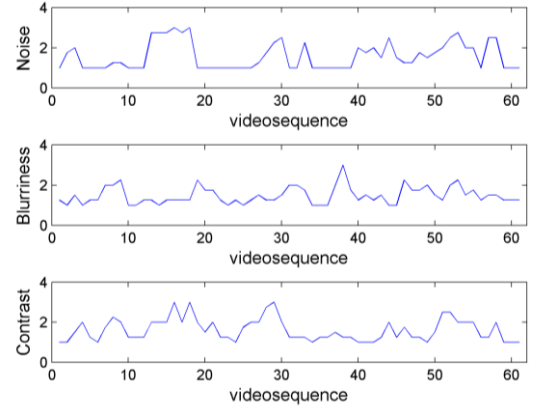


Fig. 3. Averaged subjective evaluation result for video sequences

The first boxplot graph (Fig. 4) describes the relation between subjective and the objective evaluation of noise. For the objective method apply that the quality increases with the SNR value. This verify the correctness of the objective method that rightly classify the bad video sequences.

The second boxplot graph (Fig. 5) describes the relation between the subjective and objective quality evaluation of blurriness. The quality increases with decreases BQE. According to the boxplot, the minimal values are rightly classified into the first group and the medians in the groups increase.

The third boxplot graph (Fig. 6) describes the last view condition, contrast. The contrast as the noise in the first boxplot is increasing with its quality coefficient CQE. That is why medians of CQE rightly decrease through the groups.

For better view on the values of coefficient the median values for three groups for each view condition are noted in the table below (TABLE I).

The median changes of objective quality coefficients agree with the subjective assessments. Mostly, the same trend is observable also for quartiles of p.d.f.-s. Although it seems that the median changes are not so significant, it must be considered the small ranges of coefficient values in measurements.

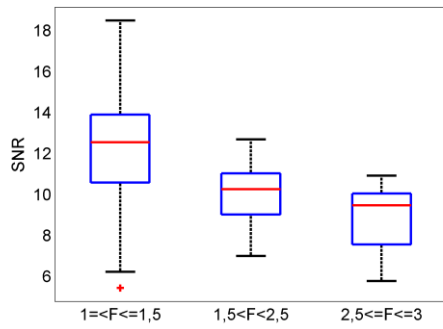


Fig. 4. Boxplot graph comparing the SNR and subjective quality evaluation of noise

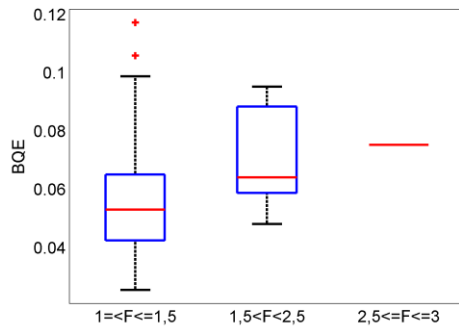


Fig. 5. Boxplot graph comparing the BQE and subjective quality evaluation of blurriness

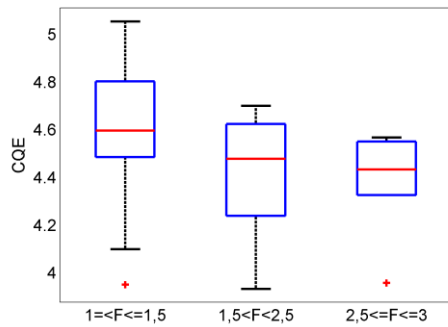


Fig. 6. Boxplot graph comparing the CQE and the subjective quality evaluation of contrast

TABLE I. THE MEDIAN VALUES OF OBJECTIVE QUALITY COEFFICIENTS SNR, BQE AND SNR IN GROUPS

	$1 \leq F \leq 1,5$	$1,5 < F < 2,5$	$2,5 \leq F \leq 3$
BQE	0,053	0,064	0,075
CQE	4,596	4,478	4,432
SNR	12,532	10,254	9,456

On the other hand, the values in boxplot throughout the groups are overlapping. This could be caused also by the differences in subjective evaluation. While comparing the

objective methods with the subjective ones, the subjectively measured data must be investigated. In the data, the human mistakes and also the differences in observer image perceiving must be considered. For data evaluation, the correlation coefficients between subjective measurement were computed (TABLE II). According to the values in the table, the blurriness view condition was variable throughout the evaluations. Also the evaluation of the fourth observer differs from the others.

TABLE II. CORRELATION COEFFICIENTS OF SUBJECTIVE MEASUREMENTS

	Correlation coefficient for observers					
	1-2	1-3	1-4	2-3	2-4	3-4
blurrines	0,575	0,102	0,519	0,538	0,374	0,019
contrast	0,8037	0,7036	0,3534	0,7604	0,5069	0,5155
noise	0,8622	0,7587	0,7507	0,8097	0,7653	0,7162

VI. CONCLUSION

In this electronic document the video quality assessment methods were introduced and modified for the experimental retinal data quality evaluation.

Both presented methods, automatic and expert analysis method evaluating the quality from different viewing conditions (contrast, blurriness and noise) were applied on 62 video sequences. Presented automatic methods agreed with the subjective expert evaluations as the median and quartiles of the objectively evaluated values rightly increased and decreased with the values of expert evaluation.

REFERENCES

- [1] TORNOW, Ralf-Peter, Radim KOLAR and Jan ODSTRČILIK. Ophthalmoscope measures fast temporal changes in the human retina. *SPIE Newsroom* [online]. 2015. DOI: 10.1117/2.1201509.006061. ISSN 18182259.
- [2] NISHA and Sunil KUMAR. Image Quality Assessment Techniques. *International Journal of Advanced Research in Computer Science and Software Engineering* [online]. 2013, 3(7), 636-640. ISSN 2277 128X.I.
- [3] ZHOU WANG, Alan C. Bovik. *Modern image quality assessment*. San Rafael, Calif: Morgan & Claypool Publishers, 2006. ISBN 1598290231.
- [4] MITTAL, A., A. K. MOORTHY a A. C. BOVIK. No-Reference Image Quality Assessment in the Spatial Domain. *IEEE Transactions on Image Processing* [online]. 2012, 21(12), 4695-4708. DOI: 10.1109/TIP.2012.2214050. ISSN 1057-7149.
- [5] ZHOU WANG and A.C. BOVIK. A universal image quality index. *IEEE Signal Processing Letters* [online]. 2002, 9(3), 81-84 [cit. 2016-08-10]. DOI: 10.1109/97.995823. ISSN 1070-9908.
- [6] Fourier Analysis and Image Processing. *Harvey Mudd College* [online]. Claremont, Los Angeles, 2007 [cit. 2016-08-17]. Dostupné z: http://fourier.eng.hmc.edu/e101/lectures/Image_Processing/Image_Processing.html
- [7] KOLAR, Radim, Ralf. P. TORNOW, Jan ODSTRČILIK and Ivana LIBERDOVA. Registration of retinal sequences from new video-ophthalmoscopic camera. *BioMedical Engineering OnLine* [online]. 2016, 15(1). DOI: 10.1186/s12938-016-0191-0. ISSN 1475-925x.
- [8] K. ZUIDERVELD, "Contrast limited adaptive histogram equalization," in *Graphics Gems IV*, 1994, pp. 474-485.

Detection of P, QRS and T Components of ECG Using Phasor Transform

Lucie Maršánová

Department of biomedical engineering
Brno University of Technology
Brno, Czech republic
xmarsa08@stud.feec.vutbr.cz

Abstract— This work introduces a new method of detection of P, QRS and T components of ECG based on phasor transform (PT). PT converts each ECG sample into a phasor and therefore enhances changes in the ECG signal. Waves with small voltage are then easily detectable. The method has been tested on standard ECG databases (MIT-BIH arrhythmia database, QT database and CSE database). The results of detection of P wave and QRS complex are better than results presented in previous works. The result of T wave detection is slightly worse than results of the most of previous works.

Keywords—*ecg, detection of P wave, detection of T wave, detection of QRS complex, phasor transform, ECG databases*

I. INTRODUCTION

Cardiovascular disorders are still the most common cause of death in Western countries. Due to the ease of use, non-invasiveness and cheapness, electrocardiogram (ECG) is nowadays still the most available and widely used method for the cardiovascular system examination [1]. The ECG reflects two heart activities: the atrial activity (represented by P wave) and ventricular activity (represented by QRS complex and T wave). Automatic analysis of ECG (especially detection of QRS, P and T wave) is fundamental task in cardiac monitoring and mainly in long-term ECG monitoring [2]. Due to the large volume of such data, it is not possible to do only manual evaluation, but it is also necessary to use automatic uter methods.

The automatic detection of QRS complex has been studied in many previous works. Most of them are mentioned in [3]. The results of these studies are sufficient and trusted, because they are evaluated on several ECG databases (usually around 100 000 beats). The automatic and reliable detection of P waves and T waves is more difficult task. The reasons are mentioned below. Moreover, the algorithms for P waves and T waves detection are tested at a much lower number of cycles (usually QTDB [4] from [5]).

P waves are difficult to detect primarily for these reasons: 1) P waves have a low voltage resulting in low signal-to-noise ratio (SNR), 2) P waves have no exclusive time and frequency characteristics, 3) P waves have high inter-patient variability, in case of AV dissociations, 4) P waves do not respect normal time sequence ordering and 5) P waves can be hidden within T wave. Reliable T waves detection is difficult (as well as in the case of

P waves) for their low voltage and mainly for their high morphology and amplitude variability.

Algorithms for P, QRS and T waves detection from previous works are based on very different approaches such as wavelet transform [6] and [7], moving average [8], phasor transform [9], quality-supported analysis of characteristic templates or by using marginalized particle filter [10]. However, none of them can achieve completely satisfactory results. This means, that there is still desirable further research.

In this paper, we introduce robust and mathematically simple methods for P, QRS and T wave detection based on phasor transform (PT). Phasor transform converts each ECG sample into a phasor, which can highlight P waves and T waves. These have lower amplitude than the QRS complex and are difficult to detect. Method based on phasor transform was presented also in [9], but approach presented in this paper is simplified and its realization and reproducibility is clearer and easier. The authors of work [9] do not fully explain the necessary preprocessing and postprocessing operations before and after applying the PT. In this paper is also pointed out to the insufficiency of standard databases, which contain mostly physiological records without pathology.

II. PROCESSING OF ECG

A. Preprocessing

For successful signal analysis is necessary to remove noise and artifacts from the ECG signal.

For QRS detection, signal is filtered by bandpass filter with cutoff frequencies 12 and 19 Hz. In this frequency range lies the most of QRS complex energy. Using this filter suppresses P and T waves and also high frequency artifacts. On the other hand, QRS complexes are highlighted.

For P wave detection is signal firstly filtered by lowpass filter with cutoff frequency 0.67 Hz. Then, smoothing signal by nonlinear median filter with 40 msec window size is performed. Smooth signal is necessary for accurate performing of PT.

B. Phasor transform

PT transforms each sample of the signal into a complex value preserving the signal information. It enhances ECG waves and makes the detection easier. Phasor transform for detection of ECG waves was firstly presented in [9].

Converting each ECG sample into a phasor enhances changes in the ECG signal (the waves). Thus, considering instantaneous

phase variation in consecutive samples of the transformed ECG, the slight variations provoked by P waves and T waves in the original signal are maximized. It can be observed in Fig. 1. Therefore, PT makes their detection and delineation notably easier [10].

The degree with which ECG waves are enhanced in phasor signal is determined by value R_V . The value of R_V is always within the interval 0-1. In case $R_V = 1$, the phasor signal is the same as the original signal. The only difference is normalization to the interval $0 - \frac{\pi}{2}$. In opposite case, when $R_V = 0$ the phasor signal contains only two values: 0 and $\frac{\pi}{2}$.

A constant value R_V is considered as a real part, whereas the imaginary component is the original value of the ECG sample: $y(n) = R_V + jx(n)$, (1)

where $y(n)$ is the phasorial signal and $x(n)$ is the original sample of signal. The magnitude $M(n)$ is computed as

$$M(n) = \sqrt{R_V^2 + x(n)^2}, \quad (2)$$

and phase (phasor) $\varphi(n)$ is computed as

$$\varphi(n) = \tan^{-1} \left(\frac{x(n)}{R_V} \right). \quad (3)$$

The example of phasor transform of ECG signal is shown in Fig. 1. In phasor signal $\varphi(n)$, the QRS complexes have in all cases higher amplitude than the other ECG components. This applies also in a case of original ECG signals with smaller amplitude of QRS complex than T. Due to this fact, the QRS complexes in phasor signal are easier detectable. P waves and T waves are in phasor signal highlighted as well.

III. DETECTION

A. QRS detection

The QRS complex consist of Q, R and S wave. In practice is usually detected R wave and it is considered as a position of QRS complex. In this work, we thus also searched for R wave. In the case of QRS detection, phasor transform of ECG signal with $R_V = 0.001$ is performed. In such preprocessed signal $\varphi(n)$, we search for maxima in sliding window with 300 ms size. The next step is a check, whereas the found maxima are higher than used adaptive threshold. The value of adaptive threshold is derived from standard deviation. Standard deviation is calculated in moving window with 2 sec size. Threshold is established as a double of standard deviation in given window. The positions of such maxima are considered as positions of QRS complex (R wave).

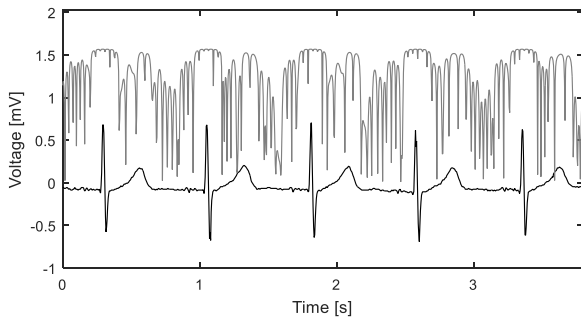


Fig. 1 The example of phasor transform (grey curve) of ECG signal (black curve) prepared for QRS detection.

At the end it is checked, whether the interval between two subsequent QRS complexes (RR interval) is 1.75x higher than previous one. If it is accomplished, backward searching is performed. In this case is searching for maximum in given segment in magnitude signal $M(n)$ with a new threshold established as 0.3 multiple of previously detected R wave size and the maximum is considered as position of QRS complex.

B. P wave detection

For P wave detection, the QRS complex as a reference is used. The area before QRS complex is demarcated with respect to the length of actual RR interval (RR_a). The area for searching P wave is demarcated from $0.25*RR_a$ to $0.08*RR_a$ before actual R wave and phasor transform with value of $R_V = 0.003$ is performed only for this segment. In phasor signal is found maximum and this is considered as a P wave. The example of phasor transform of ECG signal for detection of P wave is shown in Fig. 2. It is clear, that P waves (which are not visible in original signal) are in phasor signal significantly enhanced and therefore easier detectable.

After performing phasor transform is checked, whether the position of currently detected P wave is located after the position of T wave from previous heartbeat. If this is not met it means, that instead of P wave was detected T wave from previous heartbeat and P wave is not probably present in actual heartbeat or is hidden in previous T wave. In this case, the position of such P wave is deleted. Finally, the last condition is applied – voltage of P wave must be higher than value computed as $0.1 \times$ voltage of actual R wave. For specifying of P peak position is searched for maximum in $M(n)$ signal 15 ms around detected maximum of phasor signal.

C. T wave detection

As in the case of P waves, QRS complex as a reference is used for T waves detection. The area after QRS complex is demarcated from $0.1*RR_a$ to $0.57*RR_a$. In the next step, phasor transform with $R_V = 0.01$ is used. This value is used, because there is not necessary to highlight variations in signal as much as in case of P wave or QRS complex detection. The maximum of phase variation in demarcated segment is considered as a position of T wave. The example of phasor transform of ECG signal for T wave detection is shown in Fig. 3. As it can be seen, there is possible to detect also negative T waves by this approaches.

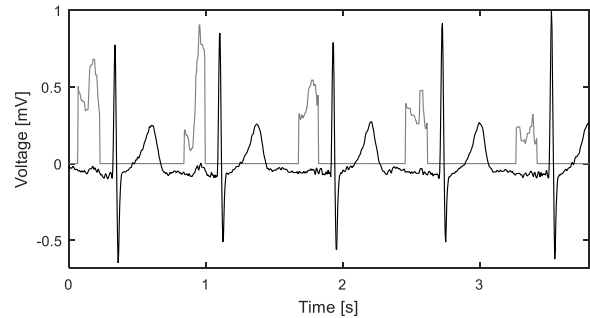


Fig. 2 The example of phasor transform (grey curve) of ECG signal (black curve) prepared for P waves detection.

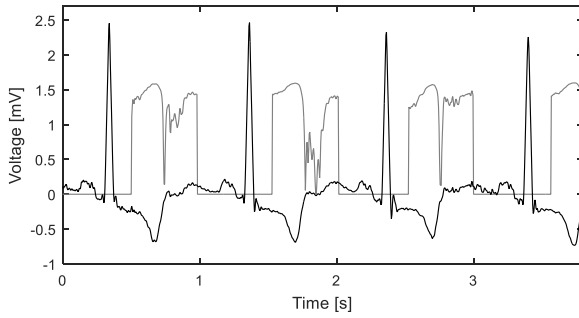


Fig. 3 The example of phasor transform (grey curve) of ECG signal (black curve) prepared for T waves detection.

IV. TESTING DATABASES

A. MIT-BIH Arrhythmia Database

The MIT-BIH Arrhythmia Database [12] is the most commonly used database for QRS detectors evaluation. The MIT-BIH Arrhythmia Database includes reference positions of QRS complexes. Database contains 48 half-hour two-channel ECG records. The sampling frequency is 360 Hz.

B. QT Database

The QT database (QTDB) [13] is the most commonly used database for heartbeat delineation and detection of P waves and T waves. Database contains 105 15 minutes two-channel ECG records. For all records are available reference positions of QRS complexes. Database includes manual annotations of P waves onset and offset positions, QRS complexes positions and positions of T waves offset. All these annotations are available for 79 out of 105 recording at least for 30 beats per record. The sampling frequency is 250 Hz.

C. CSE database

The CSE database [14] is the second most commonly used database for heartbeats delineation and detection of P waves and T waves. Database includes reference positions of onsets and offsets of P waves, QRS complexes and offsets of T waves. Reference positions of these ECG significant points are available only for one selected beat of each record. Database contains 125 10 second three-channel ECG records. The sampling frequency is 250 Hz.

D. Evaluation

Two standard benchmark parameters are calculated to evaluate designed detection algorithm (P, QRS and T) and compare it with previous works. The sensitivity (SE) and the positive predictivity (PP) of the algorithm are computed as: $SE = TP / (TP + FN)$ and $P+ = TP / (TP + FP)$. The sensitivity reports percentage of correct detection of given ECG component. The positive predictivity reports the percentage of detections, which were in reality true ECG components.

TABLE 1 THE RESULTS OF QRS DETECTION AND COMPARISON WITH PREVIOUS WORKS.

Methods	Database	Se [%]	P+ [%]
This work	QTDB	99.85	99.83
This work	MIT-BIH	99.62	99.65
This work	CSE	100	100
Correlation [15]	MIT-BIH	99.81	99.70
PT [12]	MIT-BIH	98.41	86.75
Power [16]	MIT-BIH	99.21	99.34
Power [16]	CSE	99.51	99.69

V. RESULTS

A. QRS detection

Performance of QRS detection algorithm was tested on the whole MIT-BIH arrhythmia database, QT database and CSE database. The achieved results are summarized in Table 1. In comparison with previous works, (see Table 1), the results of our method are comparable or even slightly better.

B. P wave and T wave detection

The performance of P wave and T wave detection algorithms was tested on manually annotated part of QT database (it contains around 3600 beats). The QRS detection was also tested on this part of QT database. The achieved results are summarised in Table 2. The results of P wave and QRS complex detection are better, than results presented in previous works. The result of T wave detection is slightly worse, than results of the most of previous works.

In Fig. 4 is shown example of detection algorithm results. P waves are marked by grey line with “*”, QRS complexes with “o” and T waves with “x”.

TABLE 2 THE RESULTS OF P WAVE AND T WAVE DETECTION IN QTDB AND COMPARISON WITH PERVIOUS WORKS.

Method	P wave		QRS complex		T wave	
	Se [%]	P+ [%]	Se [%]	P+ [%]	Se [%]	P+ [%]
This work	99.84	99.84	100	100	98.33	98.04
PT [9]	99.28	99.75	99.91	99.94	99.66	99.66
WT [7]	98.87	91.03	99.97	N/R	99.77	97.79
Correlation [10]	99.63	99.83	99.83	99.98	99.74	99.89

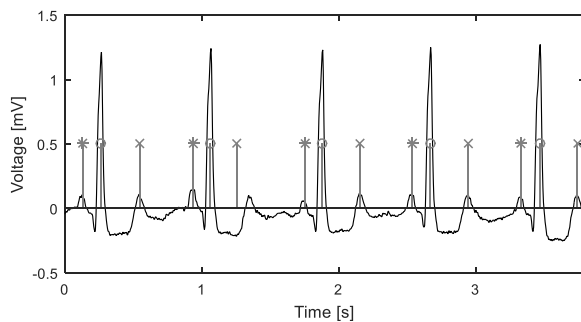


Fig. 4 The result of P wave marked by “*”, QRS complex “o” and T wave “x” detection in QTDB record sel840.

VI. DISCUSSION AND CONCLUSION

The results of automatic detection of QRS complexes, P waves and T waves using phasor transform presented in this paper are comparable with previous works and are sufficient.

It must be noted, that used databases contain only small amount of type of pathologies and precisely in these situations is detection of ECG components important and crucial for consequent diagnosis. Also number of heartbeats for testing of automatic detection algorithms is limited (only around 3600 heartbeats from QTDB and 125 from CSE). Without automatic detection of P waves and T waves, we are not able to automatically established diagnoses of pathologies such as 2nd and 3rd degree atrioventricular (AV) block, atrial fibrillation or flutter, supraventricular tachycardia, AV (nodal) reentrant tachycardia, junctional ectopic tachycardia, ventricular tachycardia, idioventricular rhythm, myocardial infarction, etc. The results of presented method and previous methods are sufficient, but what results would be reached in the case of pathological record is still the question.

It follows, that there is a high need for a database that will contain different types of pathologies and will include correctly annotated T waves and P waves. Only the algorithms which will pass testing on such database will have credible and practicable use in practice.

ACKNOWLEDGMENT

This work was supported by grant project GAČR P102/12/2034.

REFERENCES

- [1] World health Organization., *Global status report on noncommunicable diseases 2010*. Geneva, Switzerland: World Health Organization, 2011.
- [2] C. Fisch, “Centennial of the string galvanometer and the electrocardiogram”, *Journal of the American College of Cardiology*, vol. 36, no. 6, pp. 1737-1745, 2000.
- [3] B.-U. Kohler, C. Hennig, and R. Orglmeister, “The principles of software QRS detection”, *IEEE Engineering in Medicine and Biology Magazine*, vol. 21, no. 1, pp. 42-57, 2000.
- [4] P. Laguna, R. G. Mark, A. Goldberg, and G. B. Moody, “A database for evaluation of algorithms for measurement of QT and other waveform intervals in the ECG”, *Computers in Cardiology 1997*, pp. 673-676, 1997.
- [5] A. L. Goldberger, L. A. N. Amaral, L. Glass, J. M. Hausdorff, P. C. Ivanov, R. G. Mark, J. E. Mietus, G. B. Moody, C. -K. Peng, and H. E. Stanley, “PhysioBank, PhysioToolkit, and PhysioNet: Components of a New Research Resource for Complex Physiologic Signals”, *Circulation*, vol. 101, no. 23, pp. e215-e220, Jun. 2000.
- [6] M. Yochum, C. Renaud, S. Jacquir, J. M. Hausdorff, P. C. Ivanov, R. G. Mark, J. E. Mietus, G. B. Moody, C. -K. Peng, and H. E. Stanley, “Automatic detection of P, QRS and T patterns in 12 leads ECG signal based on CWT: Components of a New Research Resource for Complex Physiologic Signals”, *Biomedical Signal Processing and Control*, vol. 25, no. 23, pp. 46-52, 2016.
- [7] J. P. Martinez, R. Almeida, S. Olmos, A. P. Rocha, and P. Laguna, “A Wavelet-Based ECG Delineator: Evaluation on Standard Databases”, *IEEE Transactions on Biomedical Engineering*, vol. 51, no. 4, pp. 570-581, 2004.
- [8] M. Elgendi, B. Eskofier, D. Abbott, A. P. Rocha, and P. Laguna, “Fast T Wave Detection Calibrated by Clinical Knowledge with Annotation of P and T Waves: Evaluation on Standard Databases”, *Sensors*, vol. 15, no. 7, pp. 17693-17714, 2015.
- [9] J. P. Martinez, R. Almeida, S. Olmos, A. P. Rocha, P. Laguna, R. G. Mark, J. E. Mietus, G. B. Moody, C. -K. Peng, and H. E. Stanley, “A Wavelet-Based ECG Delineator: Evaluation on Standard Databases”, *IEEE Transactions on Biomedical Engineering*, vol. 51, no. 4, pp. 570-581, 2004.
- [10] A. Karimipour, M. R. Homaeinezhad, S. Olmos, A. P. Rocha, P. Laguna, R. G. Mark, J. E. Mietus, G. B. Moody, C. -K. Peng, and H. E. Stanley, “Real-time electrocardiogram P-QRS-T detection-delineation algorithm based on quality-supported analysis of characteristic templates: Evaluation on Standard Databases”, *Computers in Biology and Medicine*, vol. 52, no. 4, pp. 153-165, 2014.
- [11] J. G. Proakis, G. John and D. G. MANOLAKIS, “Digital Signal Processing: Principles, Algorithms & Applications”. USA, 1996.
- [12] G. B. Moody, R. G. Mark, D. Abbott, A. P. Rocha, and P. Laguna, “The impact of the MIT-BIH Arrhythmia Database: Evaluation on Standard Databases”, *IEEE Engineering in Medicine and Biology Magazine*, vol. 20, no. 3, pp. 45-50, 2015.
- [13] P. Laguna, R. G. Mark, A. Goldberg, and G. B. Moody, “A database for evaluation of algorithms for measurement of QT and other waveform intervals in the ECG: Evaluation on Standard Databases”, *Computers in Cardiology 1997*, vol. 20, no. 3, pp. 673-676, 1997.
- [14] J. L. Willems, “CSE Multilead Atlas: Measurement Results - Data Set 3”. Leuven, 1988.
- [15] M. R. Homaeinezhad, M. ErfanianMoshiri-Nejad, H. Naseri, G. B. Moody, and P. Laguna, “A correlation analysis-based detection and delineation of ECG characteristic events using template waveforms extracted by ensemble averaging of clustered heart cycles: Evaluation on Standard Databases”, *Computers in Biology and Medicine*, vol. 44, no. 3, pp. 66-75, 2014.
- [16] A. K. Dohare, V. Kumar, R. Kumar, G. B. Moody, and P. Laguna, “An efficient new method for the detection of QRS in electrocardiogram: Evaluation on Standard Databases”, *Computers*, vol. 40, no. 5, pp. 1717-1730, 2014.

Implementation of Retargetable Configurable CORDIC Algorithm for FPGA Devices

Roman Mego

Department of Radio Electronics
Brno University of Technology
Brno, Czech Republic
roman.mego@vutbr.cz

Abstract—This paper is dealing with the implementation of the CORDIC algorithm for FPGA. The implementation will be used in the high accuracy electric energy meter, so the main parameter of the implementation is focused on the result precision. The paper shows basics of the CORDIC algorithm principles, basic blocks of the implementation and its simulations.

Keywords—CORDIC; FPGA; implementation; simulation

I. INTRODUCTION

The CORDIC (coordinate rotation digital computer) [1][2] is simple and efficient algorithm originally used for the vector rotation, but it can be also used for computing of trigonometric functions. The algorithm itself uses only addition, subtraction, bit shifting and lookup table. This makes the algorithm suitable for use in digital systems without hardware multiplier, such as small microcontrollers or gate arrays.

This paper describes the implementation of CORDIC algorithm for high precision electricity energy measurement, which is used for computing active and reactive power. The FPGAs vendors such as Altera [3], Xilinx [4] and Lattice [5] provides CORDIC algorithm in form of the IP (intellectual property) cores that can be used on their devices. These IP cores are usually encrypted and can't be used with another development tools. In addition, these IP cores can't be edited and they can be modified only by the parameters given by the vendor, so they are sometimes insufficient in terms of precision, performance or data representation.

This paper is dealing with CORDIC algorithm implementation which is fully written in VHDL without special vendor dependent blocks. The inputs and outputs of the block can be parametrized for different data width and angle units. Second section is dealing with the CORDIC algorithm basics, which are used in the implementation. Third section shows CORDIC blocks in the implementation with the simulations. Last chapter concludes the paper results.

II. CORDIC DESCRIPTION

The algorithm for computing sine and cosine functions is iterative method which uses the idea of vector rotation with magnitude of one to approximate to the desired position, where

the Cartesian coordinates gives the sine and cosine of the given angle. The new position of the vector in each iteration will be

$$\begin{aligned} x_{i+1} &= x_i \cos(\alpha_i) - y_i \sin(\alpha_i) \\ y_{i+1} &= y_i \cos(\alpha_i) + x_i \sin(\alpha_i), \\ \Theta_{i+1} &= \Theta_i + \alpha_i \end{aligned} \quad (1)$$

where x_i and y_i are the coordinates of the original vector E_i . The new vector E_{i+1} after rotation will have coordinates x_{i+1} and y_{i+1} . The angle of the vector is changed from Θ_i to Θ_{i+1} . Because the rotation of the vector is non-trivial, CORDIC uses pseudo-rotations. The situation is shown on Fig. 1.

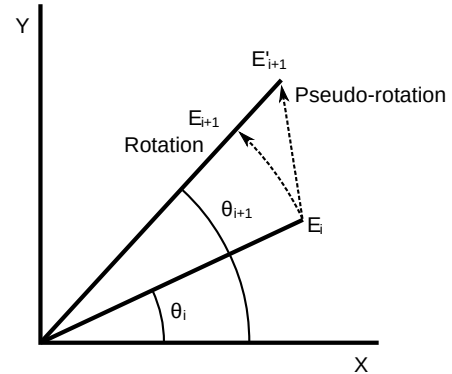


Fig. 1. Vector rotation and pseudo-rotation

The pseudo-rotation does not giving the correct result. It is only the approximation of the rotated vector. Its position is

$$\begin{aligned} x'_{i+1} &= x_i \pm 2^{-i} y_i \\ y'_{i+1} &= y_i \mp 2^{-i} x_i \end{aligned} \quad (2)$$

The relation between original and pseudo-rotated vector applies for both direction [1][2]. To achieve the effect of the cross addition in (2), the rotation angle needs to be

$$\alpha_i = \arctan(2^{-i}). \quad (3)$$

The increase of the magnitude (4) must be also considered for result correction.

$$|E'_{i+1}| = |E_i| \sqrt{1 + 2^{-2i}} \quad (4)$$

The final gain of the CORDIC will be

$$K = \prod_{i=0}^{N-1} \sqrt{1 + 2^{-2i}} \quad (5)$$

This gain depends only on the number of iterations. It can be precomputed in advance together with the rotation angles (3).

III. IMPLEMENTATION AND SIMULATION

The following section will describe basic blocks of the CORDIC implementation. The algorithm is written fully in VHDL language, with possibility of parametrization using the generic values. Generic parameters are used for setting

- input data width,
- output data width and
- angle unit.

The input and output data width can be set without any dependence on each other. The angle unit is given by the real number giving the full angle of the circle. For example, if the unit is in degrees, the generic value is 360.0. If it is in radians, the value can be MATH_2_PI from the standard math library.

Fig. 2. shows the CORDIC entity. It contains four inputs and three outputs, plus the generic parameters described above. The inputs are for clock signal, reset, angle to compute sine/cosine and strobe input. Output signals are sine and cosine of the input angle and strobe signal.

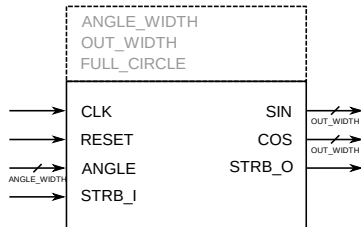


Fig. 2. CORDIC entity input/output

Relation between the signals is shown on Fig. 3. The input data representing angle is confirmed by the strobe input signal. After the end of process, the sine and cosine result is put on the output together with the active strobe signal. During the data processing, the input strobe signal should not be activated, because the internal process is not pipelined and the block resets its internal state and the previous results will be lost.

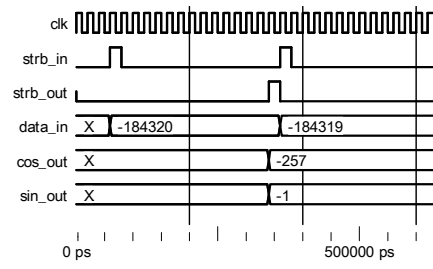


Fig. 3. Entity input/output simulation

The internal structure is divided into two main parts. First part computes the current angle position after the rotation and provides the direction of the rotation into the next block. The second block is the cross addition, which computes the Cartesian position of the rotated vector as in the original work [1].

A. Angle approximation

Fig. 4. shows the structure of the angle approximation block. At the start of the computing, the Z register is filled with the desired angle value from which will be computed the vector Cartesian position, or sine and cosine of the angle respectively. The counter giving the iteration number is also restored into its initial value. Block ATAN LUT it the look-up table with the angle differences with values according to (3).

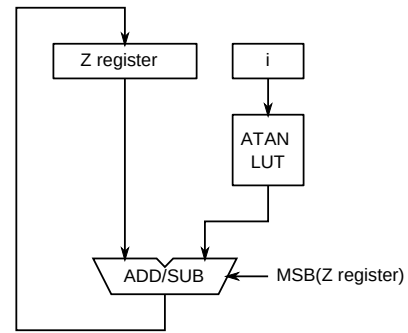


Fig. 4. Structure of the angle approximation

Z register is approaching to zero with every iteration. The rotation direction is given by the most significant bit of the Z register, because its value is represented by two's complement representation. The simulation is shown on Fig. 5.

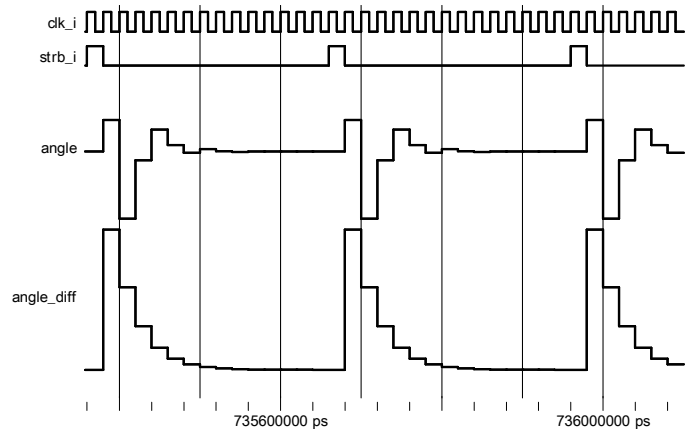


Fig. 5. Simulation of the angle approximation block

B. Cross adding

Fig. 6. shows the structure of the cross adding block. This block computes the position of the rotated vector according to (2). X register and Y register keeps the position of the rotated vector. At the start of the processing, these registers are filled with the initial position, which corresponds to the vector with angle equal to zero. To compensate the gain (5), the initial value of the X register is

$$x_0 = \frac{1}{K} \cos(0) \quad (6)$$

The direction of the vector movement is given by the MSB of the Z register like in the angle approximation block.

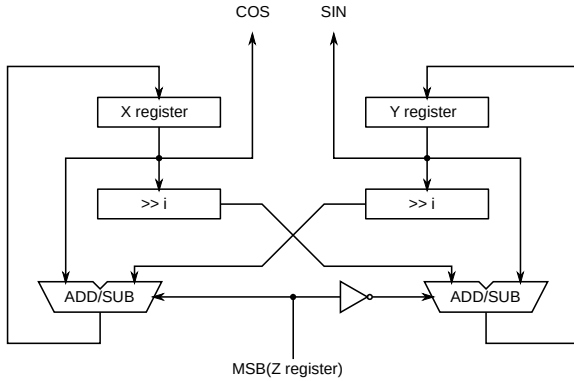


Fig. 6. Cross addition structure

Cross addition in the CORDIC consists of the addition/subtraction operation and the multiplication by the power of two. This multiplication can be substituted by shift operation. If this shift will be iterative, single vector rotation will take variable number of the clock cycles. Also the CORDIC speed will be rapidly slowed down. For that reason, the bit shift operation is realized by the barrel register. Fig. 7. shows the structure of 8-bit barrel shift register [6].

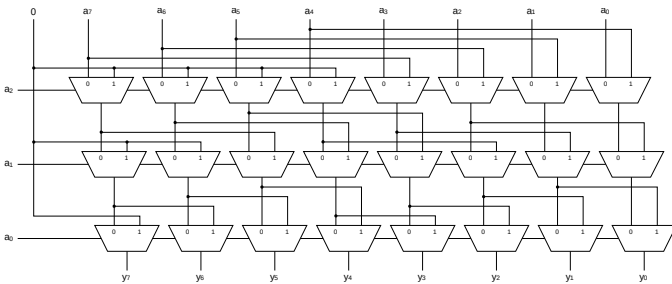


Fig. 7. 8-bit barrel shift register

Approximation simulation of the X and Y registers representing input angle sine and cosine is shown on Fig. 8. Because it is iterative method, it does not have infinite accuracy. It can be seen on the results, when the input value is 45°. In this case, the result should be 0.707 for both outputs, but it is not. The values are not even equal. For that reason the internal values of the X and Y registers were extended for additional

$$\lceil \log_2(\text{iterations}) \rceil \quad (7)$$

bits. The number of additional bits is given by the idea, that each iteration adds error in size of one least significant bit (LSB).

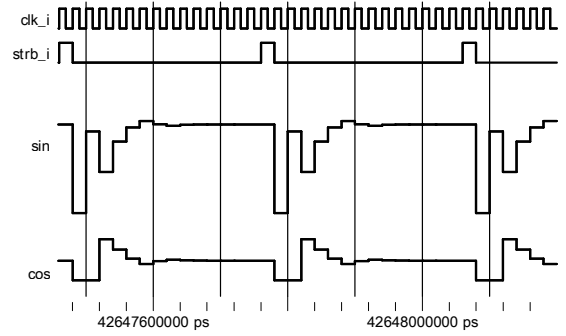


Fig. 8. Simulation of the cross addition block

C. Input range

The limitation of this structure is the range of the input angle which can be from 0° to 90°. To extend the operating range, the output value is computed from the range 0° to 90° and its sign is set according to the quadrant of the original angle (Fig. 9.). The conversion is shown in Table I.

TABLE I. QUADRANT RANGE AND OUTPUT SIGNS

Quadrant	Range	Angle conversion	Sine sign	Cosine sign
0	0° to 90°	Θ	+	+
1	90° to 180°	$180^\circ - \Theta$	+	-
2	-90° to -180°	$180^\circ + \Theta$	-	-
3	0° to -90°	$-\Theta$	-	+

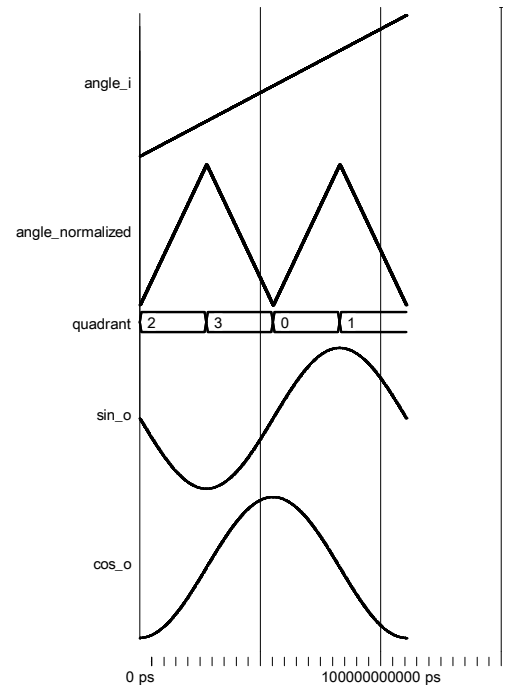


Fig. 9. Simulation of input angle conversion and sign assignment

Fig. 9. shows the simulation of the input data translation from full range $\pm 180^\circ$ to 0° - 90° with quadrant detection. The sine and cosine results are also shown to demonstrate correct assignment of the signs.

IV. CONCLUSION

This paper showed the implementation of the CORDIC algorithm for the FPGA devices. The algorithm is implemented in the VHDL without using any special vendor dependent blocks. This implementation was verified in ModelSim for the full range of the input angle with several widths of the fractional part of the fixed point number representation. The accuracy of the results is ideal for the high precision electric energy meter, for which was the algorithm originally implemented.

REFERENCES

- [1] Jack E. Volder, "The CORDIC Trigonometric Computing Technique," in *IRE Transactions on Electronic Computers*, 1959. doi: 10.1109/TEC.1959.5222693
- [2] Jack E. Volder, "The CORDIC Computing Technique," in *Proceedings of the Western Joint Computer Conference*, 1959. doi: 10.1145/1457838.1457886
- [3] Altera Corporation. (2016). *ALTERA_CORDIC IP user guide* [Online]. Available: https://www.altera.com/en_US/pdfs/literature/ug/ug_cordic.pdf
- [4] Xilinx. (2015). *CORDIC v6.0 LogiCORE IP Product Guide* [Online]. Available: http://www.xilinx.com/support/documentation/ip_documentation/cordic/v6_0/pg105-cordic.pdf
- [5] Lattice Semiconductor. (2012). *CORDIC IP Core User's Guide* [Online]. Available: http://www.latticesemi.com/view_document?document_id=33597
- [6] Matthew R. Pillmeier, Michael J. Schulte and E. George Walters III, "Design alternatives for barrel shifters," in *Proceedings of the SPIE*, 2002. doi: 10.1117/12.452034

Low Temperature Co-Fired Ceramics for High Radiation Efficiency Antenna Design

Michal Mrnka

Department of Radio Electronics
Brno University of Technology
Brno, Czech Republic
xmrnka01@stud.feec.vutbr.cz

Abstract— In the paper, we utilize Low Temperature Co-fired Ceramics (LTCC) as a dielectric material for design of a directive Dielectric Resonator Antenna (DRA). The antenna accomplishes its enhanced directivity by higher order modes excitation in relatively narrow frequency band. By using a slot in Substrate Integrated Waveguide (SIW) for feeding the resonator, the back radiation is significantly reduced as compared to microstrip feed line. The antenna produces broadside radiation pattern with linear polarization and radiation efficiency of about 87 %. The desired center frequency of the antenna is 25.5 GHz; however due to manufacturing tolerances, the resonant frequency of the fabricated antenna is shifted to 25.8 GHz.

Index Terms— Directive antennas, LTCC, millimetre-wave antennas, substrate integrated waveguide.

I. INTRODUCTION

Dielectric resonator antennas are very promising candidates for the deployment in millimeter-wave bands due to their inherently low conduction losses [2]. In majority of applications, the DRAs operate in one of their low-order modes producing radiation patterns comparable with a short magnetic dipole with gain about 5 dBi (very similar to the microstrip antennas). If more directive radiation pattern is needed, the antennas are mostly grouped into antenna array. In the last decade, different techniques were developed to increase the gain of a single element DRA. These include shaping of the ground plane [3], deployment of the electromagnetic band-gap structures [4] and superstrates [5], and finally, excitation of the higher order modes inside the simple shaped DRAs [6]. The last approach requires the least amount of additional features and does not significantly increase the complexity of the manufacturing process. A novel DRA element operating with higher order modes and achieving maximum gain of about 11.7 dBi has been proposed very recently [7].

The paper briefly describes development of a millimeter-wave LTCC based DRA utilizing the antenna concept described in [7], i.e. excitation of higher order modes, mainly HEM_{133} (hybrid electro-magnetic) mode in a cylindrical resonator at a center frequency of interest 25.5 GHz. This work should verify the suitability of the LTCC technology for building this type of antenna with high radiation efficiency at

lower millimeter wave bands. More elaborate description of the topic can be found in [10]. This technology is advantageous when it comes to the fabrication of more complex resonator shapes for very high frequency bands (millimeter waves), where it can be very difficult to meet the required tolerances with classical manufacturing methods. Resonator shapes with increased geometrical complexity and operating in higher modes might provide improved impedance bandwidth, similarly to the DRAs operating in lower modes. However, as in our case, the complex manufacturing process might cause slight errors in the dimensions of the final resonator (i.e. after firing) if the desired structure needs to be built from several layers of LTCC tape.

Green Tape 9K7 shows very low loss tangent at millimeter wave bands and according to the manufacturer it is suitable for applications up to approximately 100 GHz.

Moreover, to mitigate the losses and spurious radiation as much as possible the antenna is fed by a slot inside a substrate integrated waveguide (SIW). This solution decreases the losses when compared to the microstrip feed line on one hand and on the other hand decreases the back lobe radiation levels.

The paper is organized as follows. Section II briefly outlines the concept of the antenna and the properties of the materials used for design and fabrication. Design methodology utilized for obtaining the antenna dimensions is given in section III. Prototype of the antenna as well as the measurement setup are described in section IV. In addition, this section includes the final results, comparing simulation and measurement outcomes. Finally, we briefly conclude the paper in section V.

II. ANTENNA CONCEPT

The antenna is configured as a simple cylindrical dielectric resonator from LTCC material (Green Tape 9K7) with electrical properties $\epsilon_r = 7.1$ and $\tan \delta = 0.0009$ as defined at 10 GHz, placed above a conducting ground plane of square footprint. The properties of LTCC during field simulations at 25.5 GHz are extrapolated utilizing the 3rd order electric dispersion model by “Constant fit tangent delta” option in CST MWS.

The radiating element of the antenna is based on the higher order mode excitation inside a cylindrical dielectric resonator according to [7], providing relatively directive radiation

pattern with good radiation efficiency, if the ground plane size is accordingly adjusted. The directivity in the broadside direction is affected by the edge diffraction in the E-plane and thus the maximum gain of the antenna is a periodic function of ground plane size as showed in [9]. In this work, the resonator is fed by an aperture inside SIW in order to minimize the back radiation inherent to the microstrip line fed aperture. For the feeding structure, Arlon 25N microwave substrate with relative permittivity $\epsilon_r = 3.38$, loss tangent $\tan \delta = 0.0025$ and thickness 0.762 mm is used. The fields in the aperture determine the linear polarization of the radiation produced by the antenna.

In addition, the losses inside the SIW feed are reduced as compared to the microstrip line fed slot at such high frequency. However, further loss reduction (and increase of radiation efficiency) might be accomplished by using substrate with lower loss tangent as compared to Arlon 25N. The SIW is fed by a short section of a grounded coplanar waveguide (GCPW) line terminated with a linear taper connected to the SIW and efficiently transforming the quasi-transverse electromagnetic wave (QTEM) of the GCPW line into the transverse electric TE_{10} mode of the SIW. The electric and magnetic field distributions in cross-section of the resonator corresponding to the E-plane are visualized in Fig. 2.

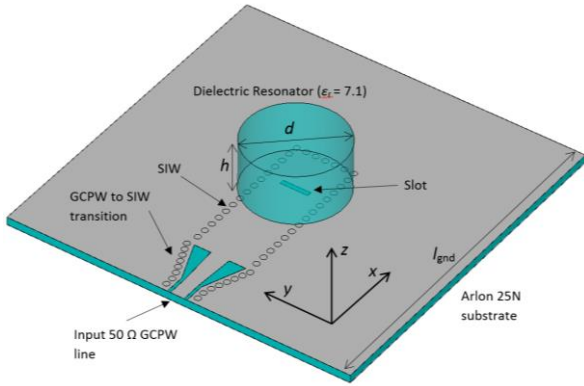


Fig. 1. Configuration of the proposed directive LTCC dielectric resonator antenna.

Plane, EM Field component	Top wall, E_x	A-A cut, H_y	B-B cut, H_y
Modal solution			
Designed DRA			

Fig. 1. E-field and H-field distributions of the HEM_{133} mode as obtained by the modal analysis and the same field components as excited in our DRA at 5.8 GHz. A-A cut corresponds to the E-plane of the resonator whereas B-B cut corresponds to the H-plane [7].

III. ANTENNA DESIGN

The antenna is initially designed for the 25.5 GHz center frequency and the relative impedance bandwidth (BW) is expected to be quite small as shown in [7]. The fact that a low relative permittivity material is used to build the resonator does not help to provide larger BW since larger Q factor is associated with higher order modes in general (compared to e.g. HEM_{118} mode). Achieving enhanced directivity while keeping high radiation efficiency and maintaining the impedance bandwidth is the main design goal.

The dimensions of the resonator (i.e. height h and diameter d) are first obtained by scaling down the DRA antenna published in [7] and subsequently followed by fine tuning. The magnetic wall model used for initial design, in which the dielectric-air interfaces are considered as perfect magnetic walls; gives only about 3 % shift in resonance frequency and therefore can be considered as good approximation for our purpose.

The width of the SIW feed is calculated to have a cut-off frequency about 18 GHz on a selected Arlon 25N substrate. In the first design steps, the SIW is modelled as a waveguide with full vertical walls instead of modeling individual vias and thus increasing the mesh complexity and eventually computation time. The SIW model with vias is included in simulations during tolerance analysis and the final tuning.

The coupling aperture length l , the width w and its distance from the shorted end of the substrate integrated waveguide s are determined for the resonator using

$$l = \frac{0.4\lambda_0}{\sqrt{\epsilon_e}} \quad (1)$$

$$w = 0.2l \quad (2)$$

$$s = \frac{\lambda_g}{4} \quad (3)$$

Here, $\epsilon_e = (\epsilon_r + \epsilon_s)/2$; ϵ_r and ϵ_s are relative permittivities of the DRA and the substrate, respectively and λ_g is the guided wavelength in the SIW. The length in (3) is selected, so that the half wave resonance of the slot is avoided.

The SIW is connected to the input 50 Ω GCPW line using linear taper with certain length and width at the SIW-GCPW connection, where the dimensions of the taper are obtained by simple optimization in CST.

The final design parameter is the size of the ground plane l_{gnd} , as it has been shown that the ground plane size has considerable impact on the gain value in the broadside direction [9] due to the edge diffraction. The size is therefore selected in order to provide maximum directivity whereas keeping the area as small as possible. Only the square footprint of the ground plane is considered despite the fact that the circular profile can further slightly increase the directivity.

All the simulation results are given in the following section as well as the results of the measurements.

IV. PROTOTYPE AND MEASUREMENTS

For manufacturing of the resonator, the 9K7 Green Tape from DuPont Microcircuit Materials [8] is used with electrical properties $\epsilon_r = 7.1$ and $\tan \delta = 0.0009$ at 10 GHz. For the resonator, 23 layers of the tape are needed. The final dimensions of the resonator, after lamination and firing, are: height $h = 5.03$ mm, $d \approx 9.80$ mm. Due to the considerable height of the resonator and its layered structure, the diameter varies between 9.77 – 9.82 mm. Since the difference between the dimensions of the designed and manufactured resonators cannot be neglected (almost 2 %), the simulations had to be carried out for the dimensions according to the manufactured samples in order to have valid comparison between simulation and measurement. The size of the resonator in simulations was therefore adjusted to correspond to the size of the manufactured resonator.

The resonator was attached to the ground plane using special type of double-sided duct tape with height about 50 μm and relative permittivity $\epsilon_r = 3$.

Due to the above mentioned facts, the resonance frequency was shifted to 25.8 GHz.

For interfacing, end launch connector from Southwest Microwave was attached to the GCPW at the edge of the board. The fabricated antenna with the attached connector can be seen in Fig. 4.

The reflection coefficient comparison between simulations and measurement is depicted in Fig. 5. Radiation patterns in the principal planes at the frequency 25.8 GHz are finally compared in Fig. 6 and Fig. 7. Very good agreement in the value of realized gain can be observed as well as in the shape of the main lobe. The differences in side lobes in the E-plane between simulation and measurements were caused by very inaccurate model of the connector which was part of the simulations. Due to the nature of our measurement range, only patterns for one hemisphere were measured (i.e. $\theta = -90^\circ$ to 90°).

The simulated radiation efficiency of the antenna in resonance is 87 %; however, the value can be further increased by using lower loss material for the feeding structure as compared to Arlon 25N which was used in our case. Based on very good agreement between simulation and measurements, we can predict that the real efficiency would not be far from the simulated value.

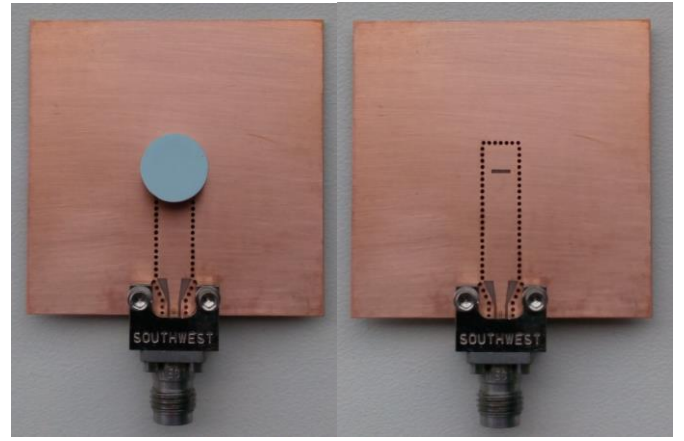


Fig. 3. Manufactured LTCC based DRA (on the left). Without attached dielectric resonator (on the right). The antenna parameters are: $h = 5.03$ mm, $d \approx 9.80$ mm, $\epsilon_r = 7.1$, $l_{\text{gnd}} = 34$ mm. And the feeding slot dimensions are $l = 2.75$ mm, $w = 0.46$ mm, $s = 4$ mm.

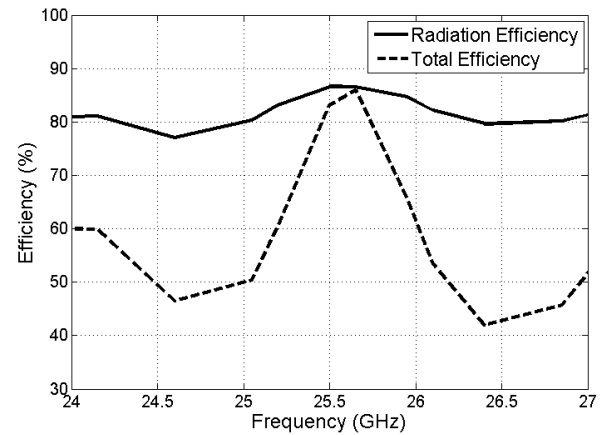


Fig. 4. Radiation and total efficiency of the designed antenna. Maximum radiation efficiency is about 87%. Total efficiency includes the radiation efficiency as well as the mismatch loss.

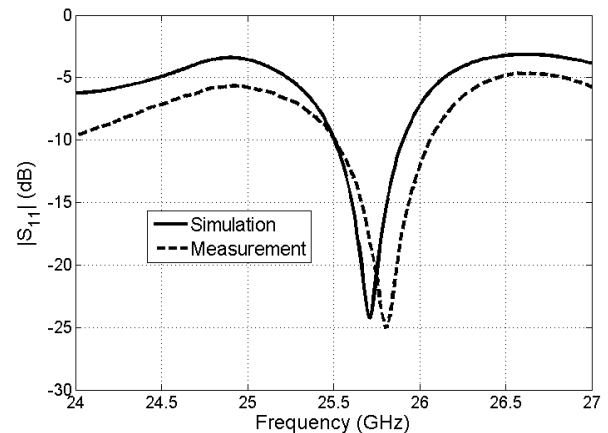


Fig. 5. Simulated and measured reflection coefficient magnitude as functions of frequency. The fractional bandwidth of the measured antenna is 2.15 % [10].

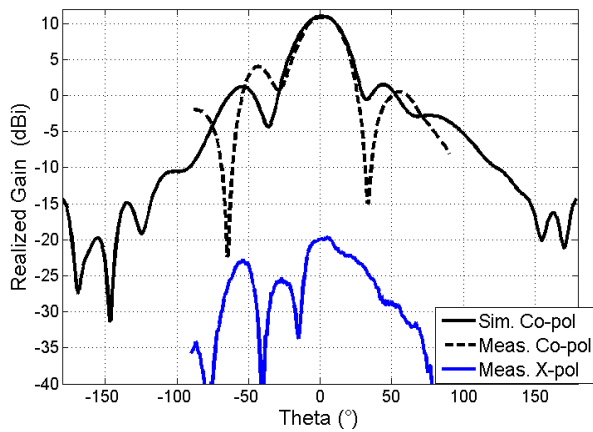


Fig. 6 Radiation patterns of the antenna in the E-plane, which corresponds to the xz plane according to the Fig.1. Measured gain in the broadside direction is 10.8 dBi (10.9 dBi in simulations). Very good agreement inside the main lobe can be observed between the simulated and measured results, the sidelobe level and in this plane was mostly influenced by the presence of the 2.4 mm connector which was modelled in simulations only as a simple brick with similar dimensions as the real connector [10].

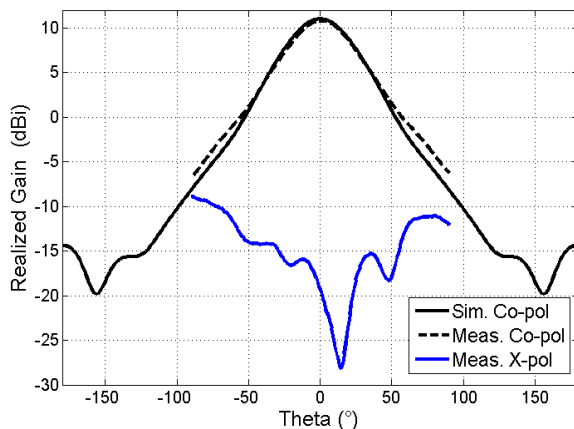


Fig. 7 H-plane radiation patterns (i.e. yz plane in Fig.1). Since the influence of the connector in this plane is minimal, we can see excellent agreement between simulation and measurements [10].

V. CONCLUSION

Design of a high performance millimeter-wave antenna with directive radiation pattern and high efficiency was described in the paper. The antenna was designed for central frequency 25.5 GHz and it operated mainly with the HEM₁₃₃ mode. Due to the manufacturing tolerances the resonant frequency of the fabricated prototype was 25.8 GHz and the simulations were redone with the dimensions of the actual prototype to have a valid comparison. The antenna provides 10.8 dBi gain with 2.15 % relative bandwidth. In simulations, 87 % radiation efficiency is achieved due to the low dielectric losses of LTCC.

ACKNOWLEDGEMENT

The author would like to thank prof. Alena Pietrikova from TU Kosice, Slovakia for fabrication of the resonators. The research described in this paper was kindly supported by the

grant LD 14057 provided by Czech Ministry of Education. Research is a part of the COST Action IC1301 WiPE Wireless Power Transmission for Sustainable Electronics. Numerical design and measurements were performed in laboratories of the SIX Research Centre thanks to the grant L0 1401 of the National Sustainability Program. The presented research was supported by the Internal Grant Agency of Brno University of Technology project no. FEKT-S-14-2483.

REFERENCES

- [1] Petosa, A.; Ittipiboon, A., "Dielectric Resonator Antennas: A Historical Review and the Current State of the Art," *Antennas and Propagation Magazine, IEEE*, vol.52, no.5, pp.91,116, Oct. 2010.
- [2] Qinghua Lai; Almpanis, G.; Fumeaux, C.; Benedickter, H.; Vahldieck, R., "Comparison of the Radiation Efficiency for the Dielectric Resonator Antenna and the Microstrip Antenna at Ka Band," *Antennas and Propagation, IEEE Transactions on*, vol.56, no.11, pp.3589,3592, Nov. 2008
- [3] Nasimuddin; Esselle, K.P., "Antennas with dielectric resonators and surface mounted short horns for high gain and large bandwidth," *Microwaves, Antennas & Propagation, IET*, vol.1, no.3, pp.723,728, June 2007
- [4] Denidni, T.A.; Coulibaly, Y.; Boutayeb, H., "Hybrid Dielectric Resonator Antenna With Circular Mushroom-Like Structure for Gain Improvement," *Antennas and Propagation, IEEE Transactions on*, vol.57, no.4, pp.1043,1049, April 2009
- [5] Coulibaly, Y.; Nedil, M.; Ben Mabrouk, I.; Talbi, L.; Denidni, T.A., "High gain rectangular dielectric resonator for broadband millimeter-waves underground communications," *Electrical and Computer Engineering (CCECE), 2011 24th Canadian Conference on*, vol., no., pp.001088,001091, 8-11 May 2011
- [6] Petosa, A.; Thirakoune, S., "Rectangular Dielectric Resonator Antennas With Enhanced Gain," *Antennas and Propagation, IEEE Transactions on*, vol.59, no.4, pp.1385,1389, April 2011
- [7] M. Mrnka and Z. Raida, "Enhanced-Gain Dielectric Resonator Antenna Based on the Combination of Higher-Order Modes," in *IEEE Antennas and Wireless Propagation Letters*, vol. 15, no. , pp. 710-713, 2016.
- [8] DuPont Green Tape datasheet, low temperature co-fired ceramic system. Available from:
- [9] M. Mrnka and Z. Raida, "Linearly polarized high gain rectangular dielectric resonator antenna," *2016 10th European Conference on Antennas and Propagation (EuCAP)*, Davos, Switzerland, 2016, pp. 1-4.
- [10] M. Mrnka and Z. Raida, "Millimeter-wave Directive Dielectric Resonator Antenna Based on LTCC," Accepted for publication in *2016 Loughborough Antennas & Propagation Conference*

Compression of ECG Signals Using SPIHT— Alternatives to Wavelet Transform

Andrea Němcová, Martin Vitek

Department of Biomedical Engineering

Brno University of Technology

Brno, Czech Republic

andrea.nemcova@phd.feec.vutbr.cz, vitek@feec.vutbr.cz

Abstract—One of the most effective methods for ECG signal compression is a combination of Wavelet Transform (WT) and Set Partitioning in Hierarchical Trees (SPIHT). WT transforms the signal into coefficients, which are arranged in a pyramidal structure. SPIHT is applied on these coefficients to compress the signal and create a bit stream. The article introduces alternative methods to WT – Pyramidal Median Transform (PMT) and Empirical Mode Decomposition (EMD). The combination of these methods with SPIHT has not been published yet. After SPIHT is applied, the output stream is further compressed by lossless methods (Burrows-Wheeler Transform, Move to Front, Run Length Encoding, and Huffman Encoding). WT, PMT and EMD in combination with SPIHT were tested and compared in terms of efficiency and quality of compression. Neither PMT nor EMD did not show to be as effective as WT.

Keywords—compression, ECG, wavelet transform, empirical mode decomposition, pyramidal median transform, SPIHT

I. INTRODUCTION

Nowadays, algorithms for ECG signal compression are very useful tools for reducing data amount. Compression of ECG signals is exploited especially in telemedicine, but it is suitable for archiving of data as well. Furthermore, the aim of ECG signal compression is to speed up the data transmission and to decrease the energy demands. For this purpose, lossy compression is used to reach higher efficiency. One of the most effective and popular compression method is Set Partitioning in Hierarchical Trees (SPIHT), which is usually used in combination with Wavelet Transform (WT) [1]. This article deals with WT and alternatives to WT, which are used in combination with SPIHT as well. There are described and tested three methods – WT, Pyramidal Median Transform (PMT) and Empirical Mode Decomposition (EMD). The combination of PMT or EMD with SPIHT as a method for ECG signal compression has not been published yet.

The algorithms were tested on the The Common Standards for Quantitative Electrocardiography (CSE) database [2]. The aim of ECG compression algorithms is to decrease the amount of data and to preserve diagnostic information. It is necessary to quantify the efficiency of compression and the quality of signal after compression (and reconstruction, which is an essential part of compression). For this purpose, Average Value Length (avL), Compression Factor (CF), Normalized Percentage Root Mean Square Difference (PRDN) and Wavelet Energy-based Diagnostic Distortion (WEDD) are used [3], [4].

II. METHODS

A. Wavelet Transform and Set Partitioning in Hierarchical Trees

Compression using WT in combination with SPIHT was firstly used in [5]. Later, the principle (shown in Fig. 1) was applied on ECG signal [6]. SPIHT is a progressive iterative algorithm. The output is a bit stream. The great advantage of SPIHT is the fact, that the compression efficiency and the output signal quality can be controlled. This algorithm can work in the lossless as well as the lossy mode.

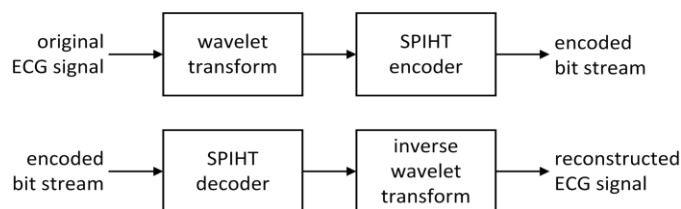


Fig. 1. Block diagram of the principle of compression and reconstruction using wavelet transform (or any alternative) and SPIHT [6].

As it can be seen in Fig. 2, SPIHT utilizes temporal orientation tree. One coefficient in lower frequency subband has zero (red color) or two (blue color) coefficients (descendants) in higher frequency subband. The most significant coefficients are stored preferably.

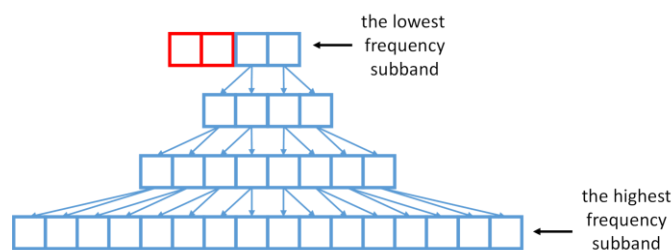


Fig. 2. Temporal orientation tree.

For the purpose of SPIHT application, it is necessary to have a pyramidal structure of coefficients. Therefore, the fast discrete time wavelet transform in dyadic form is used [6], [7]. According to [7], the ideal settings for WT are 6-level decomposition and filter bank bior4.4. In this work, SPIHT implemented in [8] was used.

B. Pyramidal Median Transform

The PMT is a nonlinear transform. It has been used especially for denoising [9], not much for compression [10]. It decomposes the signal into scales. Fig. 3 shows the block diagram of 2-level PMT. PMT consists of two parts – decomposition and reconstruction. At first, the original signal $x(n)$ is filtered by a median filter. The length of filter window is an adjustable parameter. Then, the filtered signal is downsampled with factor M (an adjustable parameter as well, for our purpose $M = 2$). The output is the input of branches 1 and 2. In the branch 1, the signal is upsampled and interpolation filter is applied (in our case, cubic interpolation was used). Interpolated signal is subtracted from the original signal and the residual signal $y_1(n)$ is obtained (the first and the finest scale). In the branch 2, the filtered and downsampled signal is filtered and downsampled again. In the branch 3, the output is upsampled, the interpolation filter is applied and it is subtracted. The residual signal $y_2(n)$ is the second, coarser scale. In the branch 4, the signal $y_3(n)$ is stored. The reconstruction is performed in the reverse order. PMT is a lossless transform; the signal can be reconstructed without an error.

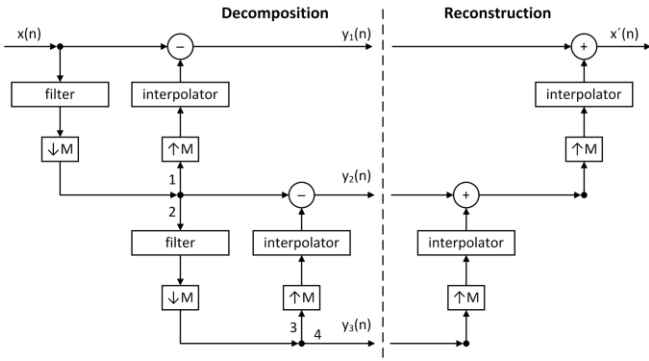


Fig. 3. Block diagram of 2-level Pyramidal Median Transform [9].

C. Empirical Mode Decomposition

EMD is a nonlinear method used for a nonstationary signal decomposition. It decomposes the signal into Intrinsic Mode Functions (IMF), which should met two criteria [11]:

- The number of extrema is equal or differ at most by one from the number of zero crossings.
- The mean value calculated from the local minima envelope and the local maxima envelope should be zero for every sample.

The algorithm works as follows. At first, a local minima and maxima are found. Then, they are interpolated and two envelopes are created. Later, the mean is calculated from these two envelopes and subtracted from the original signal. This process (called sifting) is iteratively repeated until the stop criterion is reached. The output of this process is the first IMF. Then, the first IMF is subtracted from the original signal and the second IMF is searched (using the sifting process). The EMD algorithm can be stopped after the trend of the signal is found or after the preset number of iterations (IMFs) is reached [11].

In this work, the fast EMD algorithm [12] was used. Different settings of this algorithm were tested – the number of

IMFs and the number of sifting iterations. Results are described in chapter III.

After EMD, the IMFs are gradually downsampled by the factor of 2 and its powers (similarly as in the dyadic WT).

D. Lossless Compression

After the compression of ECG signal using SPIHT, the output bit stream is further compressed using lossless compression methods and transforms. After SPIHT, Burrows-Wheeler Transform (BWT), Move to Front (MTF), Run Length Encoding (RLE) and Huffman Encoding (HE) are applied.

E. CSE Database

The compression algorithms were tested on the CSE database [2]. It contains original as well as artificial ECG signals. Data set 3 was used for this purpose. It includes 125 ECG records, each with 15 leads. In this work, only the first Frank's orthogonal lead (lead X) was used. Signals no. 60, 68, 76, 84, 92, 100, 108, and 124 were excluded from further analysis, because they are not considered as ECG signals. The original length of each record is 10 seconds, the sampling frequency is 500 Hz, the bit resolution is 16 bits/sample (bps).

F. Evaluation Algorithms

For evaluation of compression efficiency, avL (1) and CF (2) were used [3], [4].

$$avl(bps) = \frac{\text{size of the output stream}}{\text{original signal length}} \quad (1)$$

$$CF(-) = \frac{\text{size of the input stream}}{\text{size of the output stream}} \quad (2)$$

The quality of the signal after compression was evaluated using objective method without diagnostic information – PRDN (3):

$$PRDN(\%) = 100 \times \sqrt{\frac{\sum_{n=0}^{N-1} (X_s(n) - X_r(n))^2}{\sum_{n=0}^{N-1} (X_s(n) - \bar{X})^2}}, \quad (3)$$

where X_s is the original signal, X_r the signal after compression and reconstruction, and \bar{X} is the mean of the original signal [3]. PRDN is the most commonly used method. Signals with $PRDN \leq 5\%$ are acceptable for further analysis [13]. The second method for signal quality evaluation, which is used in this work is WEDD [14]. WEDD is an advanced objective method, which reflects diagnostic information. It is based on a wavelet transform. According to [15] the signal with very good quality has $WEDD \leq 2\%$. Calculation of WEDD is not trivial and more details can be found in [14].

III. RESULTS AND DISCUSSION

Combination of WT and SPIHT is considered as a reference. Only one ideal setting (according to [7]) was tested. For EMD and PMT, different settings were tested on the whole CSE database. The SPIHT algorithm is equally set for WT, PMT and EMD. For the testing of parameters of PMT and EMD, the SPIHT was set to have the maximum length of output bit stream equal to 10,000 samples. Criterion for selecting optimal parameters of the tested algorithms is the quality of ECG signal after reconstruction (values of PRDN and WEDD).

A. Pyramidal Median Transform

For PMT, the different level of decomposition and the length of the median filter window were tested. The results are shown in Table I. It is obvious from Table I, that the lowest (it means the best) PRDN and WEDD were reached with 4-level decomposition and window length of 3 (highlighted in red). According to the results, 2-level PMT is not appropriate for compression; it reaches very good avL and CF, but the signals are too much distorted (high PRDN and WEDD). With increasing window length of the median filter, the quality of the reconstructed signal is decreasing (increasing PRDN and WEDD).

TABLE I. RESULTS FOR PYRAMIDAL MEDIAN TRANSFORM

levels of decomposition	window length	avL [bps]	CF [-]	PRDN [%]	WEDD [%]
2	3	0.7862	22.4924	16.1133	14.9297
	5	0.7808	22.6807	17.3834	16.3283
	7	0.8167	21.5042	17.7888	16.8155
	9	0.8313	21.2318	19.1260	18.1573
3	3	1.5441	10.4540	7.0468	6.0187
	5	1.5852	10.1903	7.7924	6.6606
	7	1.5827	10.2050	8.8094	7.4756
	9	1.5539	10.3956	10.2821	8.6424
4	3	1.8539	8.6452	6.8170	5.8839
	5	1.8513	8.6599	7.6754	6.6491
	7	1.8451	8.6888	8.8823	7.6768
	9	1.8231	8.7951	10.4552	8.9767
5	3	1.9361	8.2701	7.5705	6.7592
	5	1.9389	8.2599	8.7292	7.8909
	7	1.9218	8.3333	9.7497	8.7762
	9	1.8951	8.4513	11.3935	10.2226

B. Empirical Mode Decomposition

EMD was tested in two steps. In the first step, the number of sifting iterations was set to 4 (based on the previous testing on 5 signals from the CSE database). The performance of the EMD and SPIHT algorithm with various levels of decomposition was tested. The results are shown in Table II. It is evident, that the best quality is reached with 5-level EMD (highlighted in red).

TABLE II. RESULTS FOR EMPIRICAL MODE DECOMPOSITION – CHANGING LEVEL OF DECOMPOSITION

level of decomposition	avL [bps]	CF [-]	PRDN [%]	WEDD [%]
2	0.6238	27.0537	45.7640	43.0589
3	1.4863	11.5463	16.1926	15.0036
4	2.2226	7.2977	8.4215	7.3493
5	2.4483	6.5542	7.7330	6.7411
6	2.5130	6.3726	7.9736	7.0522
7	2.5318	6.3233	8.4238	7.5284
8	2.5485	6.2817	8.8453	8.0748
9	2.5415	6.2988	8.9240	7.9950

In the second step, the 5-level EMD was used and the number of sifting iterations was changed. Table III shows the results. The lowest distortion of reconstructed signal is reached with the number of sifting iterations of 7 (according to PRDN) and 9 (according to WEDD). Because WEDD reflects the diagnostic information, number of sifting iterations of 9 was selected for further testing and comparison.

TABLE III. RESULTS FOR EMPIRICAL MODE DECOMPOSITION – CHANGING NUMBER OF SIFTING ITERATIONS

no. of sifting iterations	avL [bps]	CF [-]	PRDN [%]	WEDD [%]
1	2.2949	6.9942	13.6683	12.7562
2	2.4028	6.6785	9.2950	8.4083
3	2.4255	6.6140	8.2391	7.2942
4	2.4483	6.5542	7.7330	6.7411
5	2.4356	6.5845	7.5260	6.4903
6	2.4352	6.5826	7.4859	6.4337
7	2.4423	6.5638	7.4289	6.3538
8	2.4402	6.5728	7.4462	6.3289
9	2.4546	6.5350	7.4524	6.3094
10	2.4458	6.5575	7.5818	6.4274

C. Comparison of WT, PMT and EMD

All algorithms were tested for three levels of compression (maximum length of output bit stream was set to 10,000 samples, 15,000 samples, and 20,000 samples in the SPIHT algorithm). The final length was further influenced by lossless compression. PMT and EMD were tested with the best settings (described above). Results are shown in Table IV.

It is obvious from the table, that the combination of WT and SPIHT is the most effective one. The reconstructed signal is minimally distorted; average PRDN is 2.2550 % and WEDD is even smaller than PRDN, only 1.1714 % for the highest tested level of compression. The criteria mentioned in chapter II.F are met. This combination has the highest potential, because the efficiency of compression (avL and CF) can be further increased and it is highly probable, that the distortion will be still acceptable. EMD and PMT in the combination with SPIHT are not as effective as WT and SPIHT. The distortion is significantly higher and does not meet the criteria from II.F (except for PMT and maximum length of bit stream of 20,000 samples). On the other hand, PMT reaches lower avL and higher CF (higher efficiency) than WT. Table IV shows, that PMT is better than EMD in terms of both efficiency and quality. EMD works on different (empirical) principles than PMT and WT and its performance is highly dependent on the signal.

Fig. 4 and 5 show the examples of compressed signals. In Fig. 4, there is signal no. 117 compressed with the lowest distortion. In Fig. 5, there is shown signal no. 20, which was compressed with the highest distortion.

IV. CONCLUSION

The ECG signal was decomposed by three different algorithms – WT, PMT and EMD. Then the tree (pyramidal) structure was created for all algorithms using gradual downsampling. SPIHT algorithm was applied on the tree structures in order to compress the ECG signal. The output of this process was a bit stream, which was further compressed using lossless compression algorithms (BWT, MTF, RLE, and HE). PMT and EMD were optimized in terms of parameters settings. PMT performed the lowest distortion with 4-level decomposition and the median transform window length of 3. Using EMD, the lowest distortion was reached with 5-level decomposition and the number of sifting iterations of 9.

The comparison between WT, PMT, and EMD in the combination with SPIHT shows, that WT and SPIHT reaches the highest efficiency and the processed signal has the lowest

TABLE IV. COMPARISON BETWEEN WT, EMD AND PMT IN TERMS OF EFFICIENCY (avL AND CF) AND QUALITY (PRDN AND WEDD) OF COMPRESSION

type of decomposition	max length of bit stream	settings				avL [bps]	CF [-]	PRDN [%]	WEDD [%]
		level	wavelet	window length	no. of sifting iterations				
WT	10,000	6	bior4.4	-	-	2.0694	7.7333	2.2550	1.1714
EMD		5	-	-	9	2.4546	6.5350	7.4524	6.3094
PMT		4	-	3	-	1.8539	8.6452	6.8170	5.8839
WT	15,000	6	bior4.4	-	-	3.1038	5.1582	1.4276	0.7018
EMD		5	-	-	9	3.6873	4.3441	5.9039	4.4262
PMT		4	-	3	-	2.8410	5.6365	5.3837	4.4454
WT	20,000	6	bior4.4	-	-	4.2146	3.8042	0.8181	0.3700
EMD		5	-	-	9	5.0279	3.1893	5.3989	3.5797
PMT		4	-	3	-	3.8529	4.1553	4.4631	3.5221

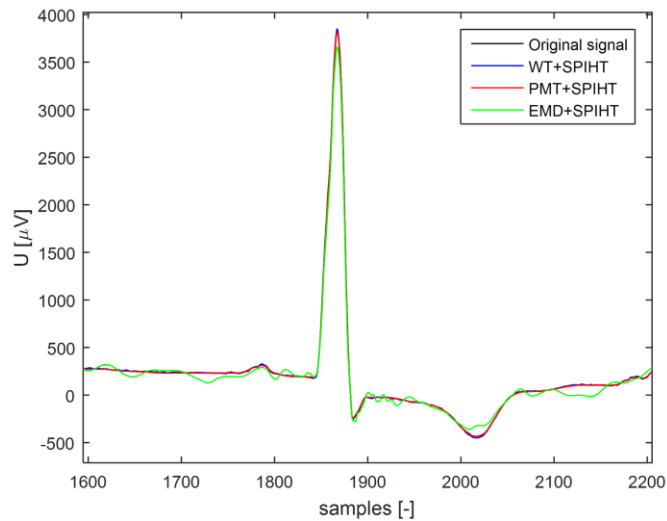


Fig. 4. Signal no. 117 compressed with the lowest distortion.

distortion, which meet the criteria. Therefore, the WT remains the most appropriate decomposition algorithm, which can be used with SPIHT.

ACKNOWLEDGMENT

This work was supported by grant project GAČR P102/12/2034.

REFERENCES

- [1] M. Sabarimalai Manikandan, and S. Dandapat, "Wavelet-based electrocardiogram signal compression methods and their performances: A prospective review," *Biomedical Signal Processing and Control*, vol. 14, pp. 73-107, November 2014.
- [2] The CSE Working Party, "Common standards for quantitative electrocardiography", 1990, CD-ROM version of the CSE database.
- [3] S. Dandapat, L. N. Sharma, and R. K. Tripathy, "Quantification of Diagnostic Information from Electrocardiogram Signal: A Review", *Advances in Communication and Computing*, vol. 347, pp. 17-39, 2015.
- [4] D. Salomon, "Data Compression: The Complete Reference", 4th ed., London: Springer, 2007.
- [5] A. Said, and W. A. Pearlman, "A new, fast, and efficient image codec based on set partitioning in hierarchical trees", *IEEE Transactions on Circuits and Systems for Video Technology*, vol. 6, no. 3, pp. 243-250, June 1996.
- [6] Z. Lu, D. Y. Kim, and W. A. Pearlman, "Wavelet compression of ECG signals by set partitioning in hierarchical trees algorithm", *IEEE Transactions on Biomedical Engineering*, vol. 47, no. 7, July 2000.

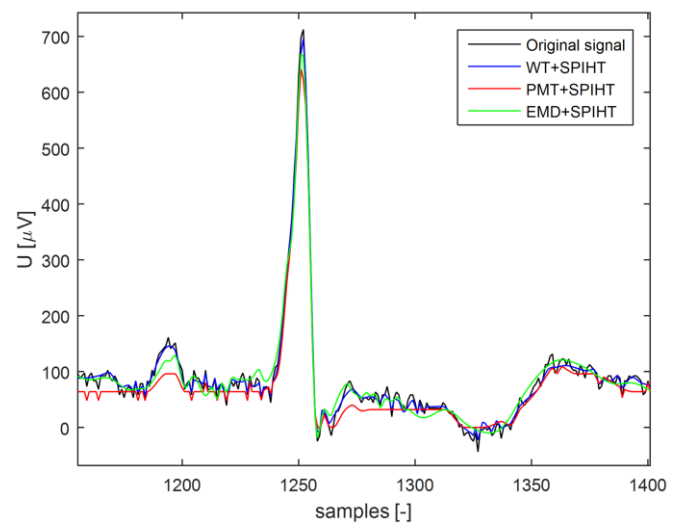


Fig. 5. Signal no. 20 compressed with the highest distortion.

- [7] J. Hrubeš, M. Vitek, and J. Kozumplík, "Possibilities of wavelet decomposition for SPIHT compression of ECG signals", *Biosignal Conference*, 2008.
- [8] M. Vitek, J. Hrubeš, and J. Kozumplík, "EKG KVANTUM", [software], 2009.
- [9] V. P. Melnik, I. Shmulevich, K. Egiazarian, and J. Astola, "Block-median pyramidal transform: Analysis and denoising applications", *IEEE Transactions on Signal Processing*, vol. 49, no. 2, pp. 364-372, February 2001.
- [10] J.-L. Starck, F. Murtagh, and M. Louys, "Astronomical Image Compression Using the Pyramidal Median Transform", *Astronomical Data Analysis Software and Systems IV*, ASP Conference Series, vol. 77, pp. 268-271, 1995.
- [11] N. E. Huang, Z. Shen, S. R. Long, M. C. Wu, H. H. Shih, Q. Zheng, N.-C. Yen, C. C. Tung, and H. H. Liu, "The empirical mode decomposition and the Hilbert spectrum for nonlinear and non-stationary time series analysis", *Proceedings of the royal society*, vol. 454, no. 1971, March 1998.
- [12] Y. H. Wang, C. H. Yeh, H. W. V. Young, K. Hu, and M. T. Lo, "On the computational complexity of the empirical mode decomposition algorithm", *Physica A: Statistical Mechanics and its Applications*, vol. 400, issue 15, pp. 159-167, 2014.
- [13] J. Hrubeš, M. Vitek, and J. Kozumplík, "Multipoint Validation of Decompressed ECG Signal", *Biosignal Conference*, pp. 138-142, 2010.
- [14] M. Sabarimalai Manikandan, and S. Dandapat, "Wavelet energy based diagnostic distortion measure for ECG", *Biomedical Signal Processing and Control*, vol. 2, pp. 80-96, April 2007.
- [15] M. S. Manikandan, and S. Dandapat, "An Effective Wavelet-Based Lossy Compression of Noisy ECG Signals", *TENCON*, pp. 2652-2657, 2008.

Lockless Shared Memory Based Multicore Communication Protocol

Marek Novak, Marian Cingel
 Department of Radio Electronics
 Faculty of Electrical Engineering and Communication
 Brno University of Technology
 Technicka 12
 616 00 Brno (Czech Republic)
 Email: xnovak0m@vutbr.cz

Abstract—The article describes a lockless shared memory-based multicore communication protocol. The technique addresses mainly asymmetric multiprocessor systems (AMP), which it was designed for. The benefits of the protocol inferred from its implementation are explained, especially the advantage of its lockless nature. The protocol is integrated into Linux Kernel and there exist multiple multicore microcontroller implementations such as RPMsg Lite or OpenAMP RPMsg.

Keywords—AMP, Multicore, RPMsg, RPMsg Lite, OpenAMP, Linux, Kernel, VirtIO

I. INTRODUCTION

In asymmetric multiprocessor systems, the most common technique for different cores to cooperate is to mutually share data. Either a dedicated hardware component is provided in the system, such as a First-In-First-Out (FIFO) buffer or, a shared memory addressable by all cores in the system and intercore interrupts are used. This paper aims the second approach which does not require any dedicated hardware to be introduced and is platform independent.

The protocol is divided into multiple layers. The physical layer is realized by intercore interrupts and the shared memory present on the system bus. The media access control layer is realized by a component called VirtIO. It defines both the way data is represented in the shared memory (Vring) and the sequence of actions to be taken to transmit and receive a message between two cores. The transport layer is defined by a component called Remote Processor Messaging (RPMsg). It uses the underlying components to provide a communication application interface to the rest of the software/firmware. This protocol is currently used in Linux Kernel to implement AMP (asymmetric multiprocessing) [3].

In the next section, the physical, media access control and transport layers' data objects are described. Following section explains the sequence of actions for message transaction between the cores.

II. LAYERS OF THE PROTOCOL

Figure 1 shows the layers of the protocol. In the boxes, there are names of the components belonging to a layer. The layers' name is on the right side of the figure.

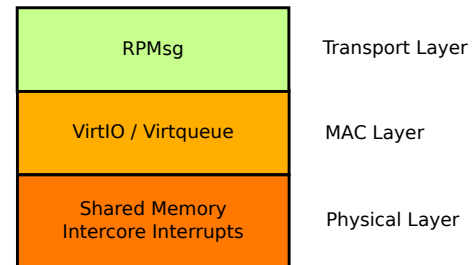


Fig. 1. Layered model of the protocol

A. Physical Layer

As mentioned, the physical layer is composed of two components - the shared memory and the intercore interrupts. The second one is however optional.

The provided shared memory needs to be accessible by all communicating processor cores in the system. Possible topologies are shown in Figure 2. The memory can be connected to a shared bus, which must provide an arbitration for bus accessing (such a bus would have at least two masters - the communicating cores). Another option is to use a dual-port memory accessible by both communicating cores.

When a communicating core wants to be notified when a message arrives, an intercore interrupt must be present between the sender and the receiver core. Alternatively, the core can poll the shared memory data structures to detect the arrival of new data. This solution is not optimal, but in a continuous communication, it can be more efficient than interrupt driven reception.

B. Media Access Control Layer

The media access control layer is implemented using VirtIO [1]. More specifically, it is defined by the Virtqueue component, which is a part of VirtIO.

The Virtqueue provides an application interface to interact with data object called Vring, which is stored in the shared memory. Vring is composed of three basic components - buffer descriptors' pool, "avail" ring buffer and "used" ring buffer as shown in Figure 3.

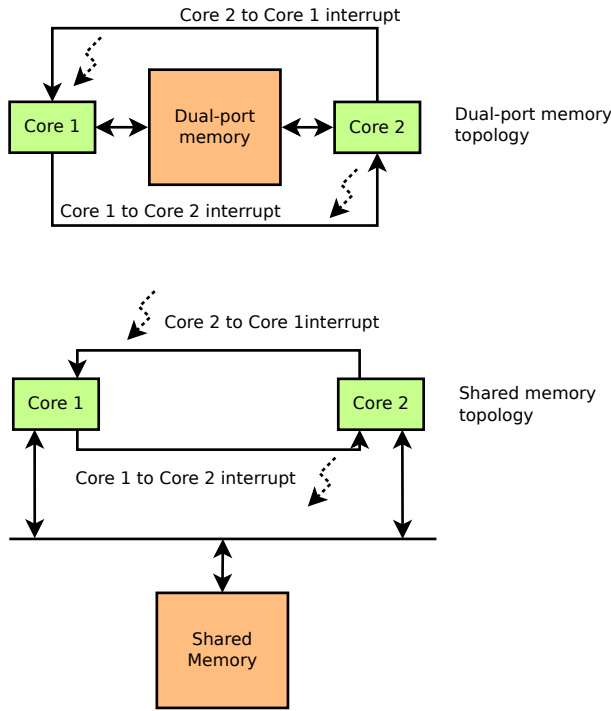


Fig. 2. Physical layer - possible implementations

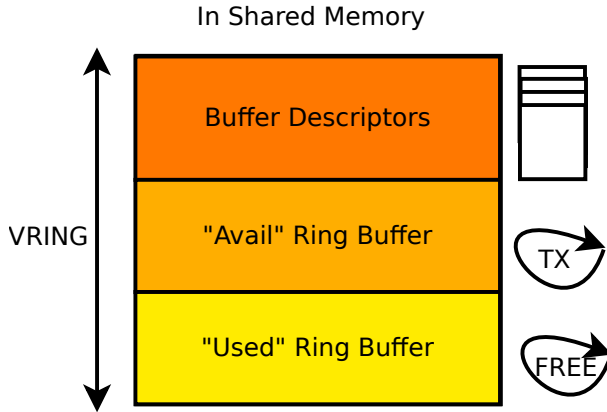


Fig. 3. Vring - bookkeeping structure for Virtqueue

Both mentioned ring buffers hold indexes to actual communication buffers, which are listed in the buffer descriptors' pool. This indirect addressing approach enables the communication buffers to be chained - a whole linked list of buffers can be transferred. In such a situation, the ring buffer contains only index of the first item in the linked list. Another important property is that the communication buffers can be input into the ring buffers in any desired order. This way an out-of-band communication can take place or multiple communication streams can be transferred independently.

Due to the complexity, detailed data structures are not provided in this paper. For a complete definition, please refer to source code of virtqueue [2].

C. Transport Layer

This layer is implemented by the Remote Processor Messaging (RPMMsg) protocol. It uses the Virtqueue interface and defines the roles of both communicating cores. RPMMsg is therefore a core-to-core protocol (as opposed to core-to-multicore approach). One core in the system is the "master" and another core is called "remote". The "master" manages the memory and can add new buffers to the buffer descriptors' pool.

The protocol does not require any intercore synchronization component, such as intercore mutex or intercore semaphore, since it adopts a single-writer-single-reader approach to the ring buffers in Vring. This way, a race condition cannot occur and still the ring buffers are used to communicate between two independent processor cores.

Thanks to the properties of Virtqueue, RPMMsg defines so-called endpoints. These are used to split multiple concurrent communication streams at the application level. They serve a similar purpose as ports in TCP (Transmission Control Protocol) or UDP (User Datagram Protocol) protocol. As the communication is core-to-core, there is no need for a network layer - a message sent by one core is automatically destined to the other one - due to behaviour of lower layer.

Each endpoint is denoted by its address which is a unique number in a core domain with the range of long integer (0 to 4294967295). It can be specified by the application or assigned dynamically by RPMMsg layer. The communication is achieved by sending messages between endpoints cross cores and each message can be delivered only to a single destination endpoint. There is no support for broadcasting-like behavior. When a message is received on an endpoint, a callback procedure is executed on the remote core. The actual handling of reception is implementation specific.

The message consists of application data and RPMMsg header which is added to the buffer transported by Virtqueue. It is shown in Figure 4. First two words are source (local) and destination (remote) endpoint addresses. Then there is a flags field, which is currently unused and the length of the payload. A reserved field is introduced to align the header to 16 bytes. It can be used only locally for buffer processing in the RPMMsg protocol implementation.

III. TRANSACTION OF DATA BETWEEN CORES

Having defined the memory layout and which interrupt should be used to trigger interrupt at the remote core, it is also needed to define the actual sequence of execution to accomplish a transfer of data. Figure 5 shows this.

Figure 5 does not show how "free" buffers initially get into the "used" ring buffer in case "master" is sending message to "remote". It neither shows how "free" buffers get into the "avail" ring buffer when the roles are swapped. One approach is to fill the master's "used" ring buffer and remote's "avail" ring buffer during the initialization of the RPMMsg communication stack. This is the only moment, when the fact that all ring buffers use single-writer-single-reader approach can be violated.

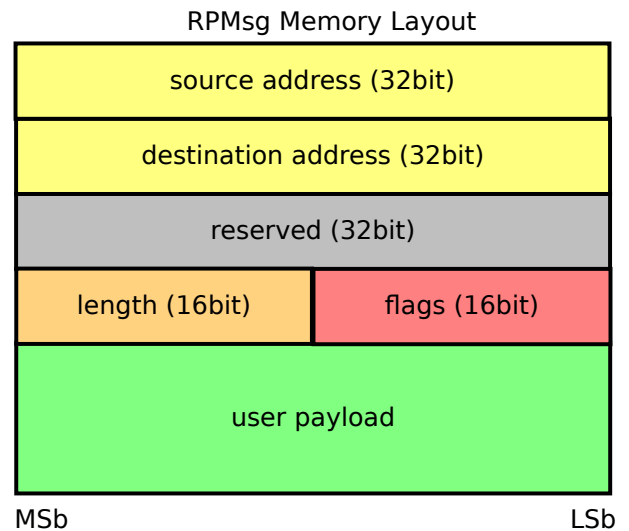
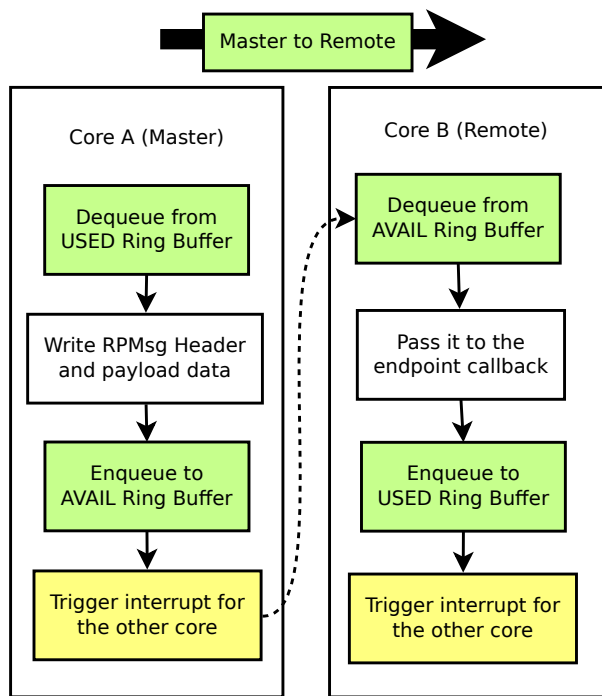


Fig. 4. RPMsg header layout

IV. CONCLUSION

In last years, the AMP is getting more and more marketing interest due to its natural properties caused by integrating and interconnecting cores with different aim to use. Security, high speed requests, complexity and simplicity together - all those aspects raise demands. And not just for hardware engineers. Without appropriate software, stable protocol and a standardized way to communicate between asymmetric cores, the whole technology is not ready for real use.

This article briefly introduced one possible solution for AMP software communication stack: The RPMsg protocol with its basic principles and capabilities which satisfies wide range of final application use-cases and last but not least, the lower layer - Virtio and its approach to deal with issues of shared resources using a lock free algorithm. Virtio has proven to be a solid ground for building high-level layers, especially in the field of para-virtualization, currently present in Linux kernel. We consider the presented technology (RPMsg and VirtIO) to be suitable for current requirements of AMP communication.

REFERENCES

- [1] IBM. Virtio: An I/O virtualization framework for Linux. 2010. Available from: <http://www.ibm.com/developerworks/library/l-virtio/>
- [2] OpenAMP. Virtqueue source code. 2016. Available from: <https://github.com/OpenAMP/open-amp/tree/master/lib/virtio>
- [3] RPMsg in Linux kernel. Available from <https://github.com/torvalds/linux/blob/master/Documentation/rpmsg.txt>

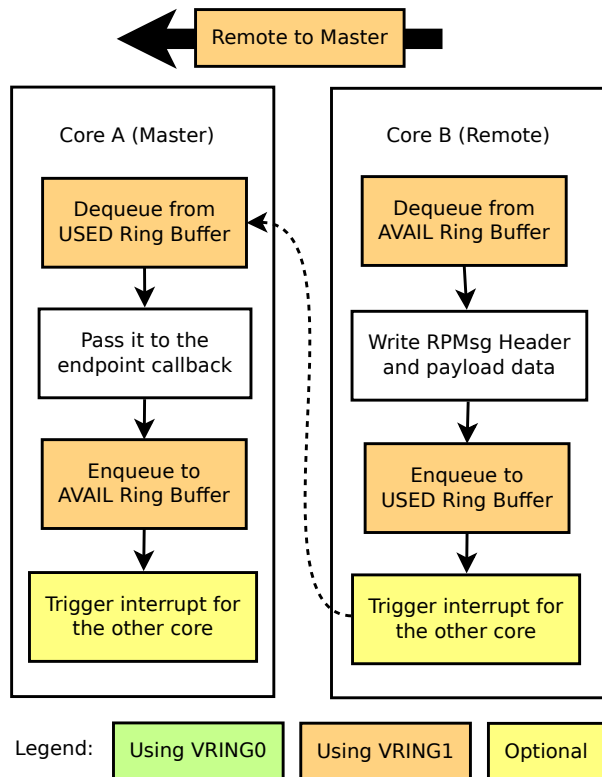


Fig. 5. Transmission sequence between "master" and "remote" and between "remote" and "master"

Automated Measuring System Used to Measure Input and Output Impedances of Current Amplifiers

Josef Polak, Jan Jerabek, Lukas Langhammer

Department of Telecommunications

Brno University of Technology

Brno, Czech Republic

Email: xpolak24@phd.feec.vutbr.cz, jerabek@feec.vutbr.cz, langhammer@phd.feec.vutbr.cz

Abstract—Measuring systems controllable by suitable software are referred to as automated measuring systems. Software environment used in this particular application of automated measuring system is Agilent VEE Pro 9.2. This software allows connecting of individual measuring devices (voltage source, current source, impedance analyzer, network analyzer, multimeter, etc.) using general purpose interface bus GPIB, for instance. The proposed automated measuring system is capable to measure AC impedances of current amplifiers, i.e. of current inputs and current outputs terminals and is finetuned for Digitally Adjustable Current Amplifier (DACA). The proposed measuring system can be easily adapted also for measurement of the impedance of individual inputs and outputs terminals of another active element.

Keywords—impedance; GPIB; measuring system; current amplifier; impedance analyzer

I. INTRODUCTION

Automated processes [1] (manufacturing, measuring, etc.) are carried out for the purposes of reducing the complexity and duration of the work. In some cases, it is not necessary to implement automation in manufacturing or measuring process (e.g. simple measurement of current taken from the battery). If we want to measure this current taken from the battery periodically, then the implementation of automated measurement controlled by a simple measuring program is appropriate. The proposed measuring program controls the measurement system and the operator (person controlling the measurement program) will receive the required results after the end of the measurement program or also partial results during the measurement. With automation, an operator can control the measurement remotely and moreover control more than one measurement at the same time.

The measuring system can be divided into three basic parts. Measuring devices (voltage sources, multimeters, analyzers, etc.), control computer with corresponding software and technology of interconnection of individual components, in our case using a general purpose interface bus GPIB [2].

The measuring system is proposed to measure the impedance of terminals of digitally controlled current amplifier, implemented as DACA_N chip [3], [4]. One integrated circuit DACA_N contains two current amplifiers DACA. Pinout and installation of DACA_N amplifier into the socket is shown in Figure 1 and Figure 2. More detailed

description of DACA_N is available in [3]. Individual current amplifiers DACA inside integrated circuit DACA_N are digitally controlled by six control pins (referred to as Gain_control in Fig. 1). IN+ and IN- are differential low impedance current inputs and OUT+ and OUT- are differential high impedance current outputs. Other terminals are not important for purposes of this paper, however, more detailed description of the connection and function is available in [3], [4].

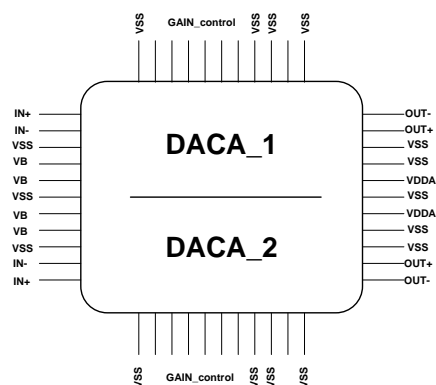


Fig. 1. Pinout of DACA_N in simplified form [3].

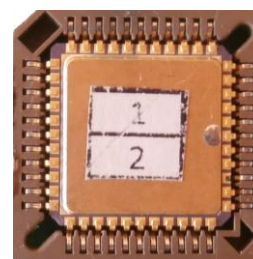


Fig. 2. Integrated circuit DACA_N inserted into the 44-pin PLCC socket.

II. PROPOSAL OF MEASURING SYSTEM FOR IMPEDANCE MEASUREMENTS

The measuring system shown in Figure 3 used for measuring the input and output impedances of the integrated circuit DACA contains three sources Agilent E3642 [5] for adjusting required gain (Gain_control of DACA), voltage source E3631A [6] providing supply voltage of the circuit and the impedance analyzer 4294A [7] with an impedance probe

42941A [8]. When input impedance is measured, it is necessary to connect adapter 16065C between the analyzer and probe. It provides separation of DC component from the input of impedance analyzer 4294A. Note that output impedance measurements are performed without the adapter 16065C.

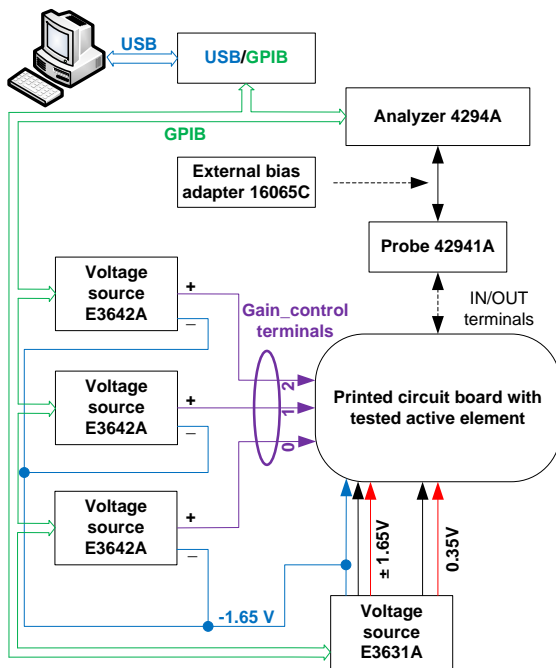


Fig. 3. Block diagram of measuring system for impedance measurements.

III. ALGORITHM PROPOSAL FOR IMPEDANCE MEASUREMENTS

A flow chart of the control program of the measuring system in case of the impedance measurement is illustrated in Fig. 4. At the beginning of the program, the required values of the gain of the DACA element, number of steps and other parameters of the analyzer are being set. After this setup, the measurement itself starts after 5 second delay because of stabilization of parameters of the circuit. The measuring process includes three mutually interconnected cycles (range of gain, the number of points of Trace A, number of points of Trace B). The range of gain consists of three parameters (From, Thru, Step). The number of points of Trace A (impedance measurement) and Trace B (phase measurement) only determines the required number of measurement points. The delay of 25 s is used to execute the measurement by the impedance analyzer.

Let us begin with the explanation of the cycle for number of measured points in case of Trace A. Parameter „Number of points” has to be set initially. The value of parameter P states the actual state of cycle (at the beginning of the cycle, the starting value of this parameter is $P = 1$). If a condition $1 \leq P \leq \text{“Number of points”}$ is valid, the data are saved to a file and a function $P = P + 1$ is made. The cycle continues till the validity of the above-stated condition. When this happens the program switches to the cycle of number of measurement points of Trace B. The principle of this cycle is exactly the same as in the previous case, only using a different counter (variable Q is used in this particular case).

The last cycle of the program is used to set individual gains. After entering the parameters, the validity of condition “From” $\leq A \leq$ “Thru” is being determined. If this condition is met, the gain is adjusted based on the current value of variable A . At the same time, the actual data labels are placed to the file. This condition can be considered to be the last one. If this condition is invalid, the program is terminated.

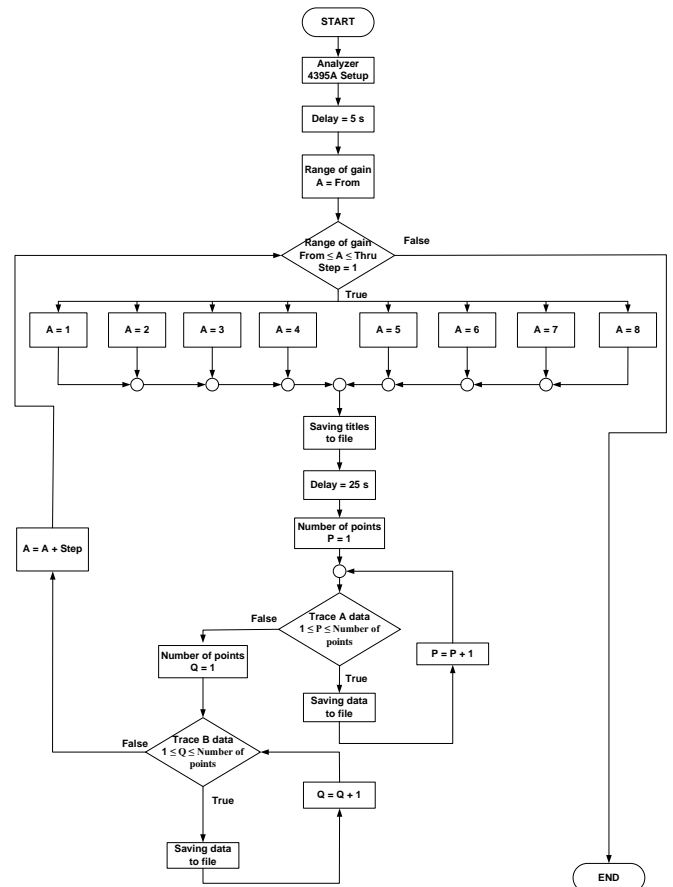


Fig. 4. The flowchart of the program for measurement of the input and output impedances of DACA element.

IV. THE PROPOSED PROGRAM FOR IMPEDANCE MEASUREMENTS

The proposed control panel for the impedance measurement is depicted in Figure 5. As can be seen the panel is divided into three parts, each with its own function.

The left part of the panel is used to set the devices before the start of actual measurement. There are buttons for setup and disconnection of the output voltage of the source E3631A used to supply active devices. Furthermore, the specification of the location where files for both channels (Trace A, Trace B) are supposed to be stored has to be set. Paths for storing measurement data from both channels in these files are placed in the middle of the control panel. When the paths of given files are specified, we can click on "Create new files" button which will create templates for storing measurement data.

The right part of the panel is used to calibrate the analyzer 4294A with attached impedance probe 42941A. Before the measurement itself, the calibration of the measuring workspace with connected impedance probe must be made.

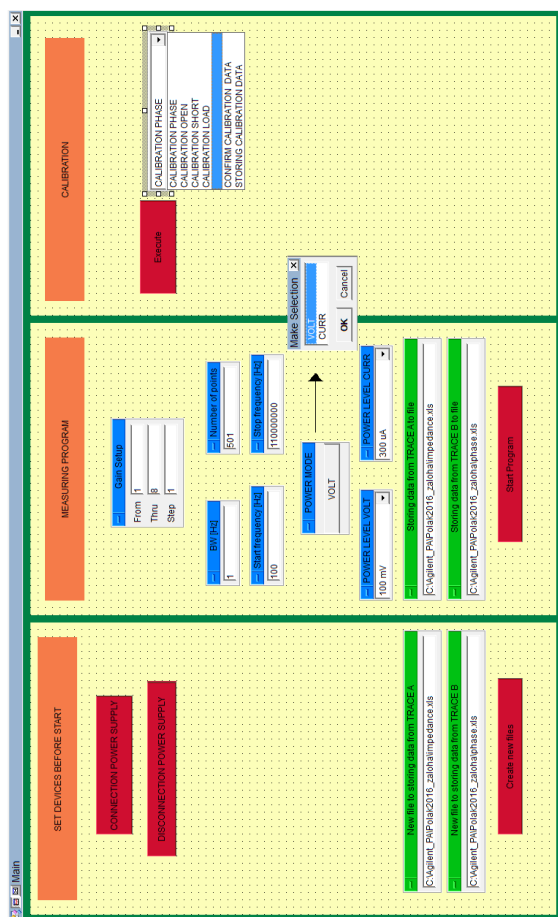


Fig. 5. Control panel of the proposed program.

This calibration consists of four phases. The most important is the last step of the calibration. We select the fourth item in the drop-down window. A resistance of 10 Ω must be screwed on the probe in case of the input-impedance calibration and resistance of 10 k Ω for the output-impedance calibration. We proceed to click on "execute" button on the control panel and monitor the calibration procedure on the display. After the completion of all four calibrations, we select "Confirm calibration data" item in the drop-down window and click on "Execute" button. The calibration is saved in the analyzer memory. It can be overwritten by another calibration.

Now we come to the description of the middle part of the panel for controlling the impedance measuring system. First, we set the desired range of gain along with setting parameters of analyzer. Here we select the voltage or current mode sourcing (VOLT, CURR) for the measurement of output or input impedance. After selecting the mode, it is necessary to choose the level of the voltage, current respectively. Now we have completed the initial setup. After connecting the probe to the input or output of DACA element, the program sequence "Start Program" can be started and measuring process can be followed on the screen of the analyzer. Figure 6 shows the development environment of proposed program. The control panel (Fig. 5) is used to control the proposed program by an operator (the person controlling measuring workplace). The

operator cannot change the function of the control program, the operator can only control the measuring system and set the parameters for individual measurements.

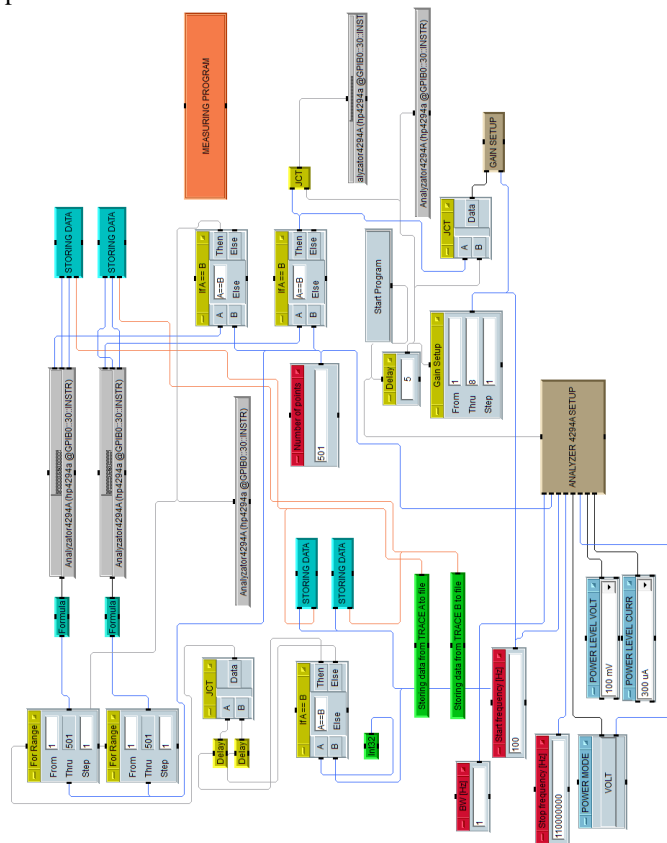


Fig. 6. Implementation of developed algorithm from Fig. 4 in the development environment of proposed program in Agilent Vee Pro 9.2.

V. THE RESULTS OF EXPERIMENTAL MEASUREMENTS CARRIED OUT BY THE PROPOSED PROGRAM

Experimental measurements of the input and output impedances of the current amplifier DACA were performed in case of four samples of DACA element. Particular methods of measurement are always dependent on measured input or output connected to the analyzer and also on setting of the analyzer to a current or voltage mode of sourcing. The following comparison of the measured values is made for the particular value of 500 μ A (current mode analyzer, input impedances) and 500 mV (voltage mode analyzer, output impedance). Curves of input impedances of individual measured amplifiers (referred to as 1, 2, 3, 4) are shown in Figure 7. Gain of current amplifiers is set to one. Legend of the graph in Figure 7 (1 IN+ for example) indicates a number of tested integrated circuit (DACA_1) and non-inverting or inverting input of tested current amplifier (I_{IN+} , I_{IN-}). Figure 8 illustrates curves of output impedances of individual measured amplifiers. Gain of the current amplifiers is again set to one. Legend of the graph in Figure 8 shows a number of individual current amplifier and inverting or non-inverting outputs (1OUT+ stands for 1st sample and OUT+ output, for instance).

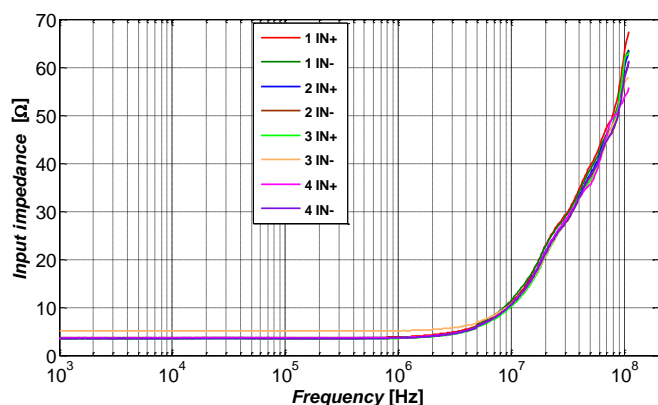


Fig. 7. Input impedance of four measured current amplifiers for current gain $A = 1$.

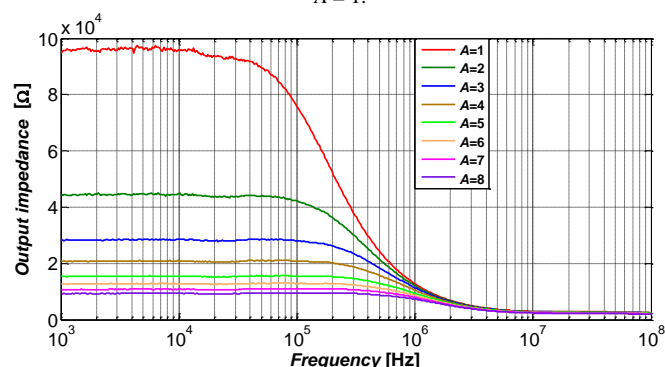


Fig. 8. Output impedance of DACA_1 OUT+ for individual values of gains.

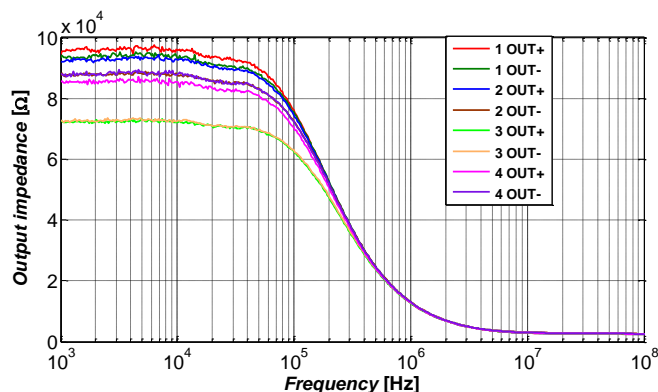


Fig. 9. Output impedance of four measured current amplifiers for current gain $A = 1$.

The DACA element has low impedance inputs and high impedance outputs. In Figure 7, the input impedance of tested amplifiers 1, 2, 4 is constant 3Ω up to frequency 1 kHz. The inverting input of amplifier 3 is slightly deviated from other tested amplifiers. The input impedance of this input is 5Ω up to frequency 1 kHz. The dependence of the output impedance OUT+ of current amplifier DACA_1 for each value of gain is shown in Figure 8. In Figure 9, the output impedance at lower frequencies is in the range from $74 \text{ k}\Omega$ to $96 \text{ k}\Omega$. Slight deviations between the outputs of the current amplifiers can be seen in the curves of the graph in Figure 8. Note that these deviations are caused by manufacturing process, nevertheless,

analysis of these deviations is not the main purpose of this paper.

VI. CONCLUSION

This paper presents the proposal of the measuring system which is adapted to measure input and output impedances of individual terminals of the current amplifier DACA. The proposed control program is presented in a form of a flowchart diagram and also in a form of a control panel used to control the measuring system by operator. The outputs of the control program are data files that are intended for further processing. The measurement of the input and output impedances is demonstrated for four samples of the DACA element. The measured data are processed in a form of graphs depicting a comparison of input and output impedances of the measured amplifiers. The proposed measuring system, including the proposed control program can be relatively easily adapted to measure the impedance of the terminals of any active element. The advantage of this program is that a person who is unfamiliar with Agilent VEE Pro 9.2 environment can operate the measuring system. Other advantage is the ability to control measuring workplace using remote desktop or for long-term measurements.

ACKNOWLEDGMENT

Research described in this paper was financed by the National Sustainability Program under grant LO1401. For the research, infrastructure of the SIX Center was used.

REFERENCES

- [1] SVARC, I. Základy Automatizace [online]. 2002 [cit. 2016-08-9]. Available from: <http://autnt.fme.vutbr.cz/svarc/ZakladyAutomatizace.pdf>
- [2] ROZTOCIL, J. Automatizované měřicí systémy se sběrnici GPIB [online]. 2009 [cit. 2016-08-9]. Available from: http://147.32.204.5/sites/default/files/vyuk/x38msp-IEEE488_SCPI_VISA.pdf
- [3] JERABEK, J., K. VRBA a I. KOUDAR. Prototyp obvodu dvojité digitálně říditelný proudový zesilovač (DACA). In: *Data Sheet* [online]. 2010. Available from: <http://www.utko.feec.vutbr.cz/~jerabekj/daca.pdf>
- [4] POLAK, J., L. LANGHAMMER a J. JERABEK. Behavioral modeling of Digitally Adjustable Current Amplifier. *International Journal of Advances in Telecommunications, Electrotechnics, Signals and Systems*. 2015, 4(1), 1-7. ISSN 1805- 5443.
- [5] AGILENT, Technologies. Agilent E3642A User's Guide. In: *Data sheet* [online]. 2000 [cit. 2016-08-9]. Available from: <http://cp.literature.agilent.com/litweb/pdf/E3640-90001.pdf>
- [6] AGILENT, Technologies. Agilent 3631A User's Guide. In: *Data sheet* [online]. 2007 [cit. 2016-08-9]. Available from: <http://cp.literature.agilent.com/litweb/pdf/E3631-90002.pdf>
- [7] AGILENT, Technologies. Agilent 4294A Analyzer Programming Manual. In: *Data sheet* [online]. 2012 [cit. 2016-08-10]. Available from: <http://cp.literature.agilent.com/litweb/pdf/04294-90061.pdf>
- [8] AGILENT, Technologies. Agilent 42941A Impedance Probe Kit Operation and Service manual. In: *Data sheet* [online]. 3. 1999 [cit. 2016-08-10]. Available from: <http://cp.literature.agilent.com/litweb/pdf/42941-90010.pdf>

Using UWB Impulse Radar System for Measuring of Wideband Antenna Parameters and Its Comparison

Ján Schneider, Daniel Novák, Ján Gamec
Dept. of Electronics and Multimedia Communications
Technical University of Košice
Košice, Slovakia
{jan.schneider; daniel.novak; jan.gamec}@tuke.sk

Abstract—The article presents non-standard method of the antenna measuring and compares it with conventional method of measurement. In this case, the use of ultra-wideband (UWB) impulse radar is considered to non-standard method. Relatively low cost measuring system, its calibration, verification and calculation methods of the required parameters (impulse response, return loss and radiation pattern) are presented in this paper. For the measurements was used self-designed Vivaldi antenna and commercially available wideband antennas. The paper compares reflection impulse response of Vivaldi antenna with other reflection impulse responses of commercial antennas and also paper compares experimental results obtained by UWB radar with the results obtained by measurements with vector network analyzer.

Keywords—UWB; radar; antenna measurement; Vivaldi antenna

I. INTRODUCTION

Ultra-wideband (UWB) technology or UWB radars, where UWB device is defined as any device operating in absolute bandwidth greater than 500 MHz or fractional bandwidth greater than 0.2 of central frequency [1] has recently become one of the most promising solutions for a variety of applications [2].

Strong potential of progressive ultra-wideband radar systems for motion sensing and imaging can be use in impedance spectroscopy to detection the presence of impurities in the liquid (for example: lactose in milk, wet granular materials, etc.) [3], in medicine to detect, non-invasively, the movements of the heart wall [4], in ground penetrating radar (GPR) systems to detecting and estimating buried pipes and cables [5], in through-wall measurements to human being detection, localization and tracking [6] and more. The UWB radar system can also be used in another way than mentioned above – UWB antenna measurement system.

The most important thing in any UWB radar system is one or more antennas, depending on the application. All UWB systems have specific demands on the electric properties of the antennas. Elementary electric properties of the antennas verified by the measurements are return loss and radiation pattern (polarization of electromagnetic field, gain). The above mentioned properties of the antenna are normally measured using a vector network analyzer in an anechoic chamber. The anechoic chamber is a very expensive measuring device which

needs a lot of space for measuring radiation pattern of the antenna in the near field or the far field.

Electric properties of the antenna could be measured using impulse UWB radar in addition to using anechoic chamber devices. The radar works by sending and receiving simple impulses. The received impulse responses are further processed and evaluated. From the impulse responses, the electric properties of the antenna, such as ringing, return loss and radiation pattern can be obtained. In the measurement of the UWB radar, it is also important to reach a plane wave i.e. the antenna is to be placed and measured in the far field. This implies that the antenna can be measured in the open air. UWB impulse radar provides a more compact and cheaper option for verification of the properties of the antenna.

The following sections present the UWB antennas used for measurements, UWB impulse radar measuring system, experimental results of measurements and the final conclusion.

II. MEASURING BY UWB IMPULSE RADAR

A. Measuring system

System for measuring return loss of the antenna uses reflection impulse responses. The system consists of a pulse generator, scope, measured antenna, microwave coupling elements and cables. Position of the scope window is selected according to the cable length (line a, line b, line c) to avoid any reflections from inhomogeneities and from the measurement configuration in the observed time interval. The time which electromagnetic wave needs to overcome distance between antenna and walls (floors etc.) and back to antenna is longer as the end of scope observation window. The pulse generator transmits a narrow pulse with peak amplitude $U \approx 30V/50\Omega$ and width of the pulse $t < 50ps$ to the antenna. The reflected signal is received from the antenna after adjusting the observation window of the scope according to the lengths of lines a, b and c. The whole principle of measuring using impulse UWB radar is shown in Fig. 1.

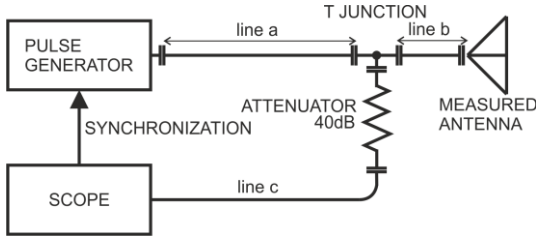


Fig. 1. Block diagram of reflection impulse responses measurement.

In the case of measuring the radiation pattern of the antenna the same equipment is used but in a different configuration. Transition impulse responses are used in this case.

The pulse from the generator is radiated by a reference antenna. The measured antenna is fixed to the turn table and receives radiated pulse at different angles. The received signal is sampled, recorded and displayed in the scope window and mathematically processed. The distance between the antennas must be greater than $10\lambda_{\max}$ to reach far fields conditions and guarantee for a plane wave. A block diagram of the radiation pattern measurement is given in Fig. 2.

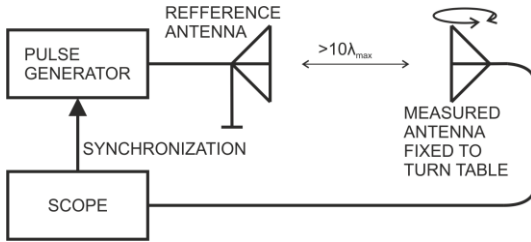


Fig. 2. Block diagram of transition impulse responses measurement.

B. Calibration and verification for return loss measurements

A calibration and adjustment of the measuring system is the most important thing for the accurate measurement of the UWB antennas. The shape and reference position of the excitation signal (in the scope window) entering the antenna were obtained by replacing the antenna with the calibration probe of the OPEN type. Probes of the LOAD and SHORT type were used for the procedural steps to calculate the return loss of the antenna.

The probe with resistance 18.75Ω was used to verify functionality of the measured system.

C. Return loss

Reflected impulse responses of the antenna and of the probes LOAD/SHORT were used to calculate return loss of the measured antenna.

If $v_A(n\Delta t)$ is the impulse response of the antenna, $v_L(n\Delta t)$ is the impulse response of the calibration probe LOAD and $v_S(n\Delta t)$ is the impulse response of the calibration probe SHORT, then reflection coefficient (no in dB) of the antenna is calculated from the following equation:

$$s_{11}(n\Delta\omega) = \frac{\mathbf{F}(v_A(n\Delta t) - v_L(n\Delta t))}{\mathbf{F}(-v_S(n\Delta t) - v_L(n\Delta t))}, \quad (1)$$

where \mathbf{F} is discrete Fourier transform operator and “./” is dot dividing.

Expression “ $v_A(n\Delta t) - v_L(n\Delta t)$ ” is to subtract the influence of the lines and of the entire system. It represents the reflected signal. Expression “ $-v_S(n\Delta t) - v_L(n\Delta t)$ ” is an incident signal after subtracting the impact of lines. The calibration probe of the SHORT type was used for the measurement instead of calibration probe OPEN. The SHORT probe reflects the wave with the opposite phase than the probe OPEN. Therefore, “ $v_L(n\Delta t)$ ” in the equation (1) is with a negative value.

Expression “ $-v_S(n\Delta t) - v_L(n\Delta t)$ ” is an incident wave. If the Fourier transforms of the incident and the reflected signal are put into ratio, then the function of frequency response of return loss is obtained.

Return loss in dB:

$$RL_{dB} = 20\log_{10}(s_{11}(n\Delta\omega)). \quad (2)$$

D. Radiation pattern

The main advantage of the block diagram in Fig.2 and of the method of measuring using UWB impulse radar is the possibility to eliminate the influence of multipath propagation of signals (i.e. walls, floor, etc.) and reflections from the environment. It is obtained by an appropriate adjustment of the measuring scope window. Impulses received from different angles of the measured antenna are used to obtain a radiation pattern. Every single impulse response is processed by FFT (Fast Fourier transform). The influence of noise in the results is depressed by smoothing. The processed signals for different steering angles are then divided by the value of the signal with appropriate angle of steering. In the final step, the processed signal is converted into dB scale.

III. ANTENNAS

For antenna measurements with UWB impulse radar and vector network analyzer was used four different types of the antennas. The first one is self-designed Vivaldi antenna. As the others were used commercially available antennas named below.

A. The Self designed Vivaldi antenna

The configuration of the developed Antipodal Vivaldi antenna is shown in Fig. 3. The top side is a signal layer connected to feeding line and bottom side is connected to the ground plane of the feeding line. The antenna is presented in [7]. It's printed on ARLON 600 substrate with relative permittivity $\epsilon_r=6.15$, tangent loss $\delta = 0.003$. The thickness of the substrate is $h = 1.575$ mm. Final dimensions of the antenna are 128×190 mm². The antenna works in frequency band from 0.81 GHz to 12 GHz with average gain 6.32 dBi, fractional bandwidth BW = 163% and low ringing factor.



Fig. 3. The Vivaldi antenna.

B. Commercial UWB antennas

For obtaining return loss of measured commercial antennas were used two methods – non-standard method by UWB radar and standard method by vector network analyzer. Experimental results of both measurements methods were compared below. Radiation pattern of the following commercial antennas were not measured.

- small bow-tie: GEOZONDAS AU – 1.0G4.5GR (1.0-4.5 GHz),
- large bow-tie: GEOZONDAS AU – 0.8G2.4G-B (0.8-2.4 GHz),
- Double ridged waveguide horn: RFspin DRH10 (0.74-10.5 GHz),

IV. EXPERIMENTAL RESULTS

This section presents measured results obtained by UWB radar and vector network analyzer. Firstly, reflection impulse response of Vivaldi antenna was compared with other reflection impulse responses of wideband commercial antennas. Impulse responses were obtained by UWB impulse radar. Next, from reflection impulse responses of all antennas were calculated return loss parameters. Then it is compared with the results obtained by vector network analyzer. Finally, the radiation pattern was measured by UWB radar and by VNA in anechoic chamber for the Vivaldi antenna only and results were compared too.

A. Measured results of reflected impulse responses

The measured results in the time domain of the Vivaldi antenna were compared with the other wideband commercial antennas and are given in Fig. 4 to Fig. 7. The scale of the exciting pulse in the obtained results (in figures) of the measurement was decreased (y scale of impulse was reduced).

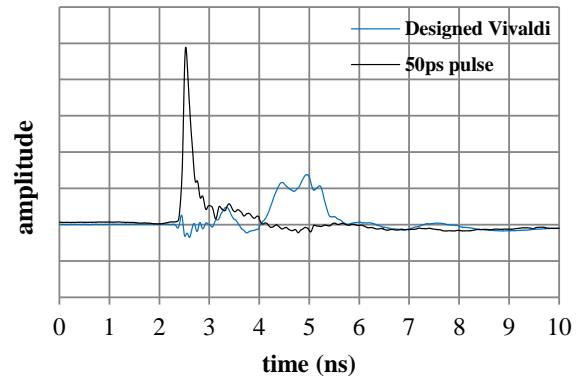


Fig. 4. Reflected response of the Vivaldi antenna on exciting pulse.

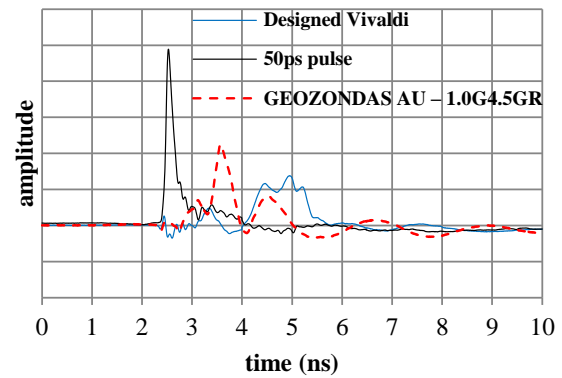


Fig. 5. Reflected response of the manufactured Vivaldi antenna compared with GEOZONDAS AU – 1.0G4.5GR.

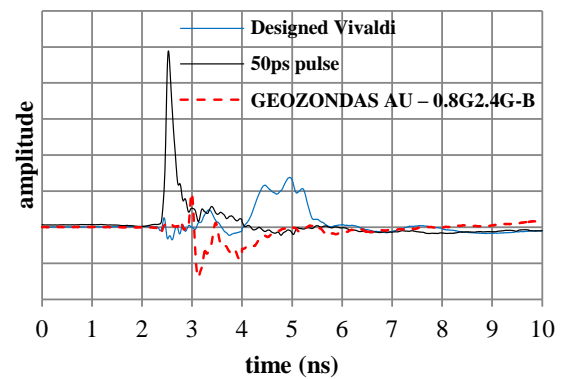


Fig. 6. Reflected response of the manufactured Vivaldi antenna compared with GEOZONDAS AU – 0.8G2.4G-B.

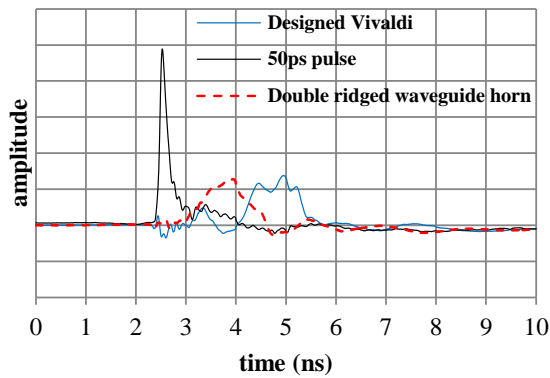


Fig. 7. Reflected response of the manufactured Vivaldi antenna compared with Double ridged waveguide horn.

The reflected impulse responses (Fig. 4 - Fig. 7) of the proposed Vivaldi antenna have satisfactory frequency character in the wide bandwidth applications. Positive feedback from measurements in the time domain is that antenna has a very low ringing in comparison with commercially available antennas. The result presented above predestinates the manufactured antenna for applications sensitive to changes in group delay receiving and transmitting signal – UWB radar systems.

B. Measured results of return loss

The return loss parameter was obtained by impulse response of the antenna according to chapter 2 part C and also obtained by VNA. Both measured results for every one antenna alone are depicted from Fig. 8 to Fig. 11. For The Vivaldi antenna are depicted simulated results of return loss (Fig.8).

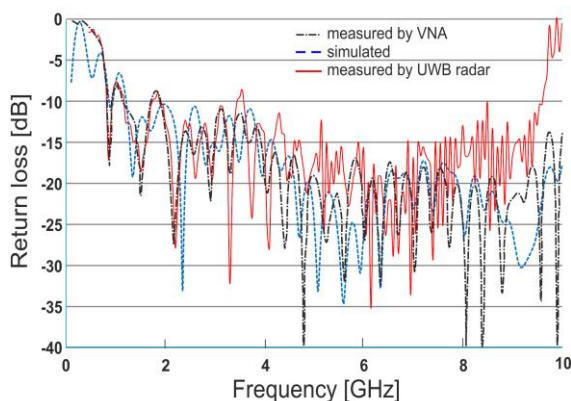


Fig. 8. Return loss of the Vivaldi antenna

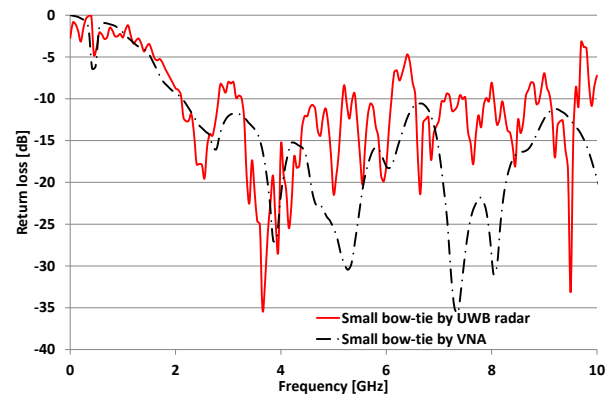


Fig. 9. Return loss of the small BOW-TIE antenna.

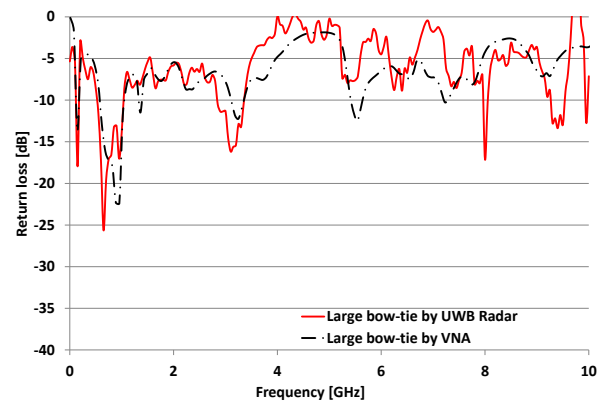


Fig. 10. Return loss of the large BOW-TIE antenna.

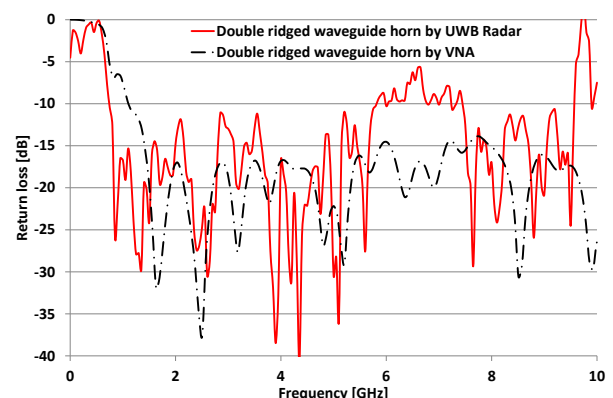


Fig. 11. Return loss of the Double ridged waveguide horn antenna.

From the results obtained (Fig. 8-Fig. 11), it is obvious that the results of measurements with the VNA and those from impulse responses (by UWB radar) show satisfactory match of results up to 5-6 GHz. The diversity of return loss over the mentioned frequency 5-6 GHz is observed. This gradual increase of diversity may be caused by noise and hardware bandwidth limitations of the pulse UWB radar.

C. Measured results of radiation pattern

The radiation patterns of the antenna are measured only for the Vivaldi antenna and are given in Fig. 12 and Fig. 13. Figures shows simulated radiation pattern, measured pattern by VNA in the anechoic chamber and experimental results of the radiation pattern obtained by UWB pulse radar. The third mentioned radiation pattern is measured only in H-plane and starts from -90° to 90° . Turn step of the analyzed antenna was 11.25° . All radiation patterns are for two different frequencies 2 GHz and 4 GHz.

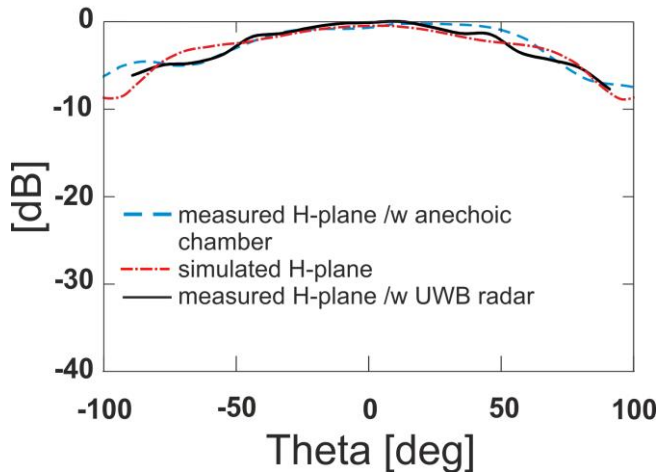


Fig. 12. Radiation pattern of the antenna at 2GHz.

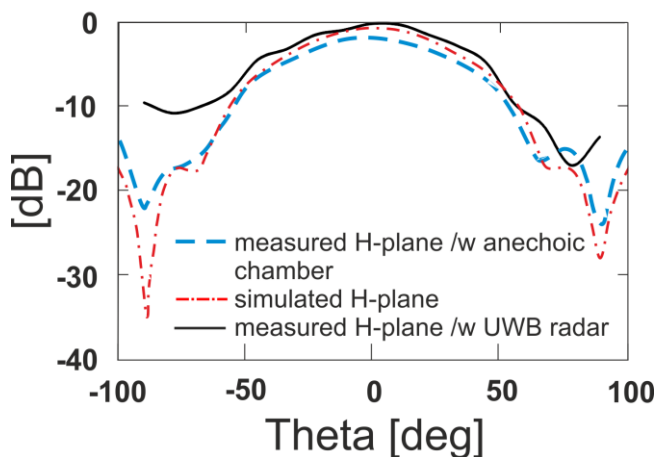


Fig. 13. Radiation pattern of the antenna at 4GHz.

The results for the Vivaldi antenna of the radiation pattern measured by the UWB radar are in good agreement with the simulated and measured (by VNA) results up to 6 GHz. The same mismatch as with return loss measurements is caused at the frequency 6 GHz.

V. CONCLUSION

For experimental measurements, an own manufactured Vivaldi antenna and few commercial wideband antennas were used.

The results obtained by UWB radar and their comparison with other results suggest a satisfactory estimation of parameters even with much cheaper and simpler technical equipment than measured with the vector network analyzer (VNA in the anechoic chamber – radiation pattern)

The reached results show in addition to the conventional methods of measurement (vector network analyzer) that the antenna can be measured with UWB impulse radar. It is obvious that return loss/radiation pattern obtained by UWB radar is in good agreement in comparison with other results to 6 GHz.

ACKNOWLEDGMENT

The research described in this paper was supported by Ministry of Education, science, research and sport of the Slovak Republic under grant KEGA - 062TUKE-4/2014 "Interactive Multiview Video Streaming for Supporting Education" and by Slovak Research and Development Agency under the contract No. APVV-0404-12.

REFERENCES

- [1] D. Kocur et al., "Short-range UWB radar: Surveillance robot equipment of the future", Systems, Man and Cybernetics (SMC), 2014 IEEE International Conference on, San Diego, CA, 2014, pp. 3767-3772.
- [2] P. Lukacs, A. Pietrikova, J. Potencki, G. Tomaszewski, "UWB antenna based on nanoparticles of silver on polyimide sub-strate," in Electronics Technology (ISSE), 2015 38th International Spring Seminar on , vol., no., pp.408-413, 6-10 May 2015.
- [3] M. Ziga, P. Galajda, S. Slovak and M. Kmec, "Determination of the quality of frying oil based on UWB impedance spectrometer", Radar Symposium (IRS), 2015 16th International, Dresden, 2015, pp. 955-960.
- [4] E. M. Staderini, "UWB radars in medicine", IEEE Aerospace and Electronic Systems Magazine, vol. 17, no. 1, pp. 13-18, Jan 2002.
- [5] W. A. Wahab, J. Jaafar, I. M. Yassin and M. R. Ibrahim, "Interpretation of Ground Penetrating Radar (GPR) image for detecting and estimating buried pipes and cables," Control System, Computing and Engineering (ICCSCE), 2013 IEEE International Conference on, Mindeb, 2013, pp. 361-364.
- [6] M. Švecová, D. Kocur and J. Kožej, "Target tracking algorithms for UWB radar network," 2016 26th International Conference Radioelektronika (RADIOELEKTRONIKA), Kosice, 2016, pp. 319-324.
- [7] Gamec, J.; Schneider J.; Gamcová M., "Vivaldi Antenna for UWB Sensor Networks," ELEKTRONIKA IR ELEKTROTECHNIKA, vol. ,no, pp,2016. Accepted for publication.

Detection of QRS Notching Using Continuous Wavelet Transform

Radovan Smíšek, Martin Vitek
 Department of Biomedical Engineering
 Brno University of Technology
 Brno, Czech Republic
 xsmise00@stud.feec.vutbr.cz, vitek@feec.vutbr.cz

Abstract—QRS notching is an indicator of myocardial ischemia, early repolarization and according to the new criteria also left bundle branch block (LBBB). Automatic detection of QRS notching is therefore highly desirable. The aim of this article is the automatic detection of QRS notching using a continuous wavelet transform (CWT). The Haar wavelet was used as the mother wavelet and the scales were chosen in the range from 6 to 70. For testing were used 123 signals from the CSE database (12 leads, 10 seconds duration, 500 Hz sampling frequency and 16 bits resolution). The automatic detection had the sensitivity of 88.07%, the specificity of 94.23% and the positive predictive value of 93.16%. The accuracy is 91.33%.

Keywords—QRS notching; continuous wavelet transform; ECG; early repolarization; true LBBB

I. INTRODUCTION

Electrocardiography (ECG) is a common cardiological examination method. QRS notching is a notch in the ECG signal within the QRS complex (see Fig. 1). Several currently researched cardiac pathologies are manifested in ECG by occurrence of QRS notching. These pathologies are myocardial ischemia, early repolarization and true LBBB.

Myocardial ischemia is manifested by the emergence of QRS notching located by the place of ischemia. The depth of the notch is evolving with the length of ischemia. [1, 2]

Early repolarization is manifested among others as the **end-QRS notching** (Fig. 1). This is a risk factor for the cardiovascular mortality. Many current automated systems can evaluate the presence of early repolarization, but most of them, consider only the presence of ST elevation regardless of QRS notching. [3, 4]

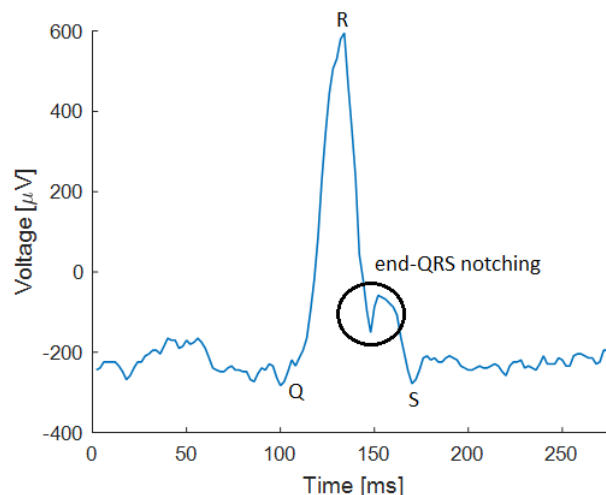


Fig. 1. End-QRS notching.

Predicting of patients eligible for cardiac resynchronization therapy is an important topic. Resynchronization therapy involves implanting biventricular pacemaker. It was found out that resynchronization therapy is particularly suitable for patients with LBBB but not for patients with right bundle branch block (RBBB). It was also discovered that the traditional approach to the diagnosis of LBBB is not sufficient and that one third of patients have incorrectly determined LBBB. Recommendations for determining LBBB were expanded (LBBB determined in accordance with these recommendations is called true LBBB). According to these recommendations, one of the indicators for implantation of biventricular pacemaker is presence of **mid-QRS notching** or slurring at least in two leads from leads V1, V2, V5, V6, I and aVL. [5, 6, 7, 8, 9]

Ambiguous and inconsistent definition of QRS notching is the problem of QRS notching detecting. [3, 4, 10] The QRS notching is usually detected in standard time domain [3, 5, 6, 10]. In the paper [1] has been proposed the possibility of the QRS notching detection using CWT. This method of detection has not been tested yet. Testing the possibilities of the QRS notching detection using CWT is the main contribution of this paper.

II. METHODS AND DATA

A. The used data

For testing of the detection QRS notching detection was used The Common Standards for Quantitative Electrocardiography (CSE) database. In this work, the 123 ECG records from the dataset 3 have been used. Two signals (67 and 70) containing stimulation peaks were dropped because the algorithm used for delineation of ECG signals [12] is not functional on such signals. It was used 12 standard leads. In a total was used 1476 signals (12*123). The length of each record is 10 seconds. All ECG records have been converted to microvolts. The sampling frequency is 500 Hz, the resolution is 16 bits and the quantization level is a less than 5 mV or equal. [11]

The information about the presence of QRS notching in ECG signals was determined by an expert on the analysis of ECG. The expert marked each signal 0/1, meaning the absence/presence of the QRS notching. The QRS notching was found in 697 signals, while 779 signals were identified as without of QRS notching.

B. Detection of notched QRS

Before the detection of the QRS notching it is necessary to detect the start and end of the QRS complexes. The algorithm proposed in [12] is used for detection of these points. The analyzed area is then expanded by 100 ms on both sides, because an inaccuracies caused by CWT occur at the edges of the signal.

The first step of the algorithm for the QRS notching detection is the transformation of the QRS complex using CWT. The Haar mother wavelet was used. The scale was chosen in the range from 6 to 70. The lower scale has already reacted with the present high-frequency noise. The notch itself is most evident in the scale range from 6 to 15. The higher frequency of a notch is, the more it is reflected by a smaller scale of the wavelet, and vice versa. A time-scale domain is the result of CWT. In the Fig. 2, there is the time-scale domain which belongs to the QRS complex with the end-QRS notching shown in Fig. 1. The area caused by the end-QRS notching is clearly visible here (the light green area at the top of the yellow area).

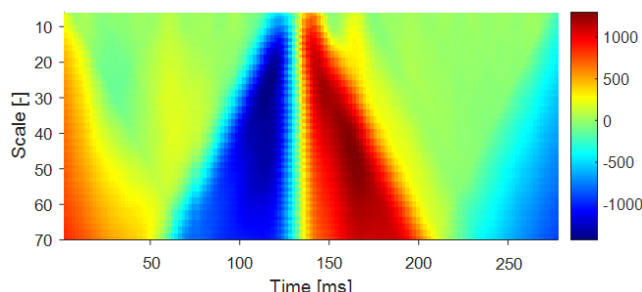


Fig. 2. The time-scale domain of the QRS complex with the end-QRS notching.

The second step is the transfer of the obtained image to a binary image. In this binary image, the ones represent the CWT coefficients in the range from -145 to 145. Other points

are marked by zero values. Selection of the points from this range ensures analysis of those points which have low CWT coefficients. The low CWT coefficients are selected because of the fact, that there is a transition between the increasing and decreasing part of the signal (transition between positive and negative CWT coefficients) - the notch may be present here. However, the low CWT coefficient also indicates a signal section without the high frequency components (the signal outside of the QRS complex). The resulting binary image is shown in Fig 3. There we can clearly see the area corresponding to the end-QRS notching (filled arc which is present in the scale 6-14 with the center at the time 155 ms).

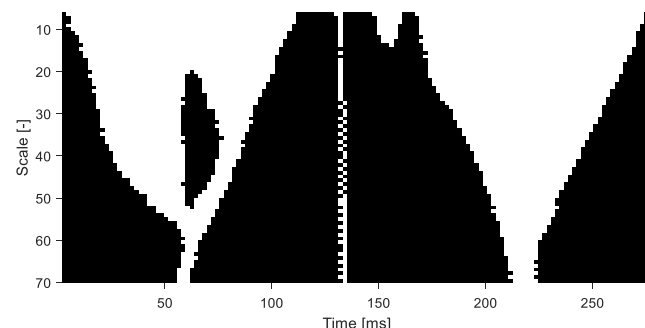


Fig. 3. Binary image created from a time-scale domain of QRS complex with end-QRS notching (ones are white points - CWT coefficients in the range from -145 to 145, zeros are black points - other CWT coefficients).

The next step is the distribution of the selected points (CWT coefficients in the range from -145 to 145) into groups. All points touching each other by side or corner are in a group. It is important that filled arc corresponding to the end-QRS notching has its own group. Points distributed to groups are shown in Fig. 4 (each group has a different color).

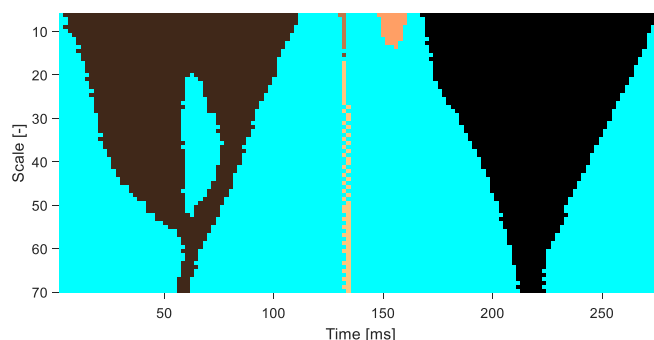


Fig. 4. Five groups which may correspond to the notch.

The thin line can be seen in the middle of Fig. 3 and Fig. 4. This line corresponds to the peak of the QRS complex. At this time, the positive part of the wavelet is at the end of the increasing part of the QRS complex and the negative part of the wavelet is at the starting point of decreasing part of the QRS complex. Therefore, the values at the starting point of the decreasing part of the QRS complex and the values at the end of the increasing part of the QRS complex are deducted. These values are usually similar, thus the low number is the result of their mutual subtraction (low CWT coefficient). This line should be present in the majority of the signals at all scales. When a discontinuity appears as in Fig. 3 and Fig. 4, it is

appropriate to put the whole line into one group, as it can be seen in Fig. 5.

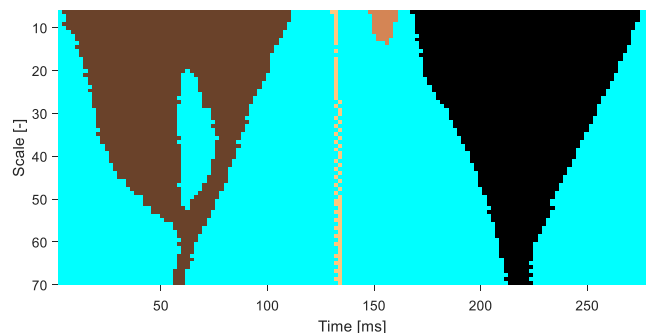


Fig. 5. The points belonging to the line corresponding to the peak of the QRS complex are put into the one group.

At some signals it may happen that filled arc corresponding to the end-QRS notching is associated with a region that already corresponds to the area outside of the QRS complex (see Fig. 6). In this case, the following rule is applied. If in one of the scales from 9 to 15 will be a temporary interruption of some group, then the group is split at the point of extreme. In the case referred in Fig. 6 there is present a black group around the scale 8 at the time of 164 ms, then disappears and finally this group again occurs. Therefore, the black group is divided into two parts at the point indicated in Fig. 6 with a red line. This rule is not applied in case that the groups are connected at a higher scale than the detected interruption.

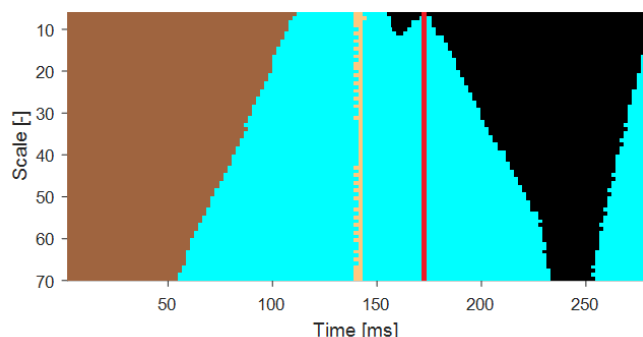


Fig. 6. Filled arc corresponding to the notch is connected with another group and it must be separated (the red line is the dividing line).

Finally, it is evaluated for each group, whether the group represents the QRS notching or not. Firstly, areas are removed if they have in the scale 6 more than 37 points. Then, the presence of the QRS notching is evaluated when the following conditions are met:

- at least single number one from the evaluated area is on the first and second line of the binary image (this corresponds to the scale 6 and 7),
- no number one from the evaluated area is present on the last two lines in a binary image (this corresponds to the scale 69 and 70),
- the sum of numbers one from the evaluated area on the first three lines (scale 6-8) must be greater than 7.

These conditions are set down on the grounds of the QRS notching is usually high frequency and not too deep. Therefore the QRS notching should be present mainly in the low scales. Conversely, because the QRS notching is usually not too wide, at large scales the CWT coefficients should be also large and thus marked by zero in a binary image.

The mid-QRS notching is an exception. The mid-QRS notching is present in the middle of the QRS and thus the low CWT coefficients are for the Haar wavelet in the large scales (CWT coefficients are between increasing and decreasing part of the QRS complex low for large scales as was explained above). In this case it is possible to determine the area as the notch even if that part of the area is located on the last two lines of the binary image. This is possible under the following conditions:

- the line of ones in a binary image is wide maximum of 2 points,
- the difference in the time of occurrence number one in a binary image in the scale 6 and in the scale 70 is not more than 8 points,
- the sum of numbers one within the evaluated area on the first three lines (scales 6-8) must be greater than 7.

All groups which do not meet the above described conditions are removed (see Fig. 7). If any group meets the conditions for the QRS notching, it is verified whether it is located inside the QRS complex (analyzed area is about 100 ms long on the right and on the left). If so, the QRS notching is indicated in place the remaining groups (see Fig. 8).

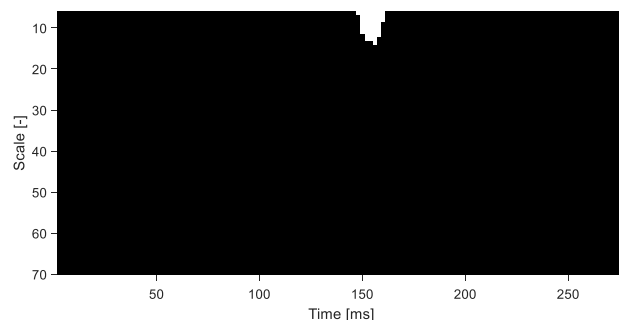


Fig. 7. The group that corresponds to notch is the only undeleted group.

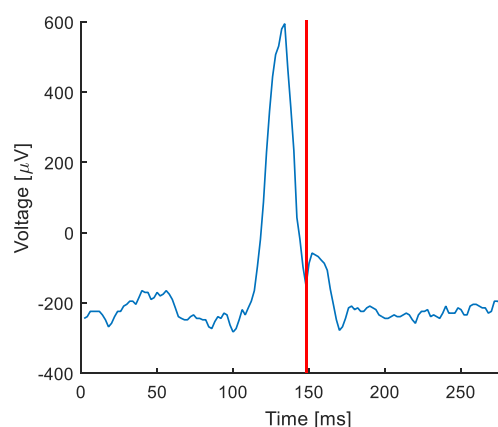


Fig. 8. Detected QRS notching (it is marked by a red line).

III. RESULTS AND DISCUSSION

This chapter describes the achieved accuracy of the QRS notching detection.

Accuracy of the QRS notching detection is described by: accuracy (Acc), sensitivity (Se), specificity (Sp) and positive predictive value (PV+). These variables are calculated as follows:

$$\text{Acc} = (\text{TP} + \text{TN}) / Y, \quad (1)$$

$$\text{Se} = \text{TP} / (\text{TP} + \text{FN}), \quad (2)$$

$$\text{Sp} = \text{TN} / (\text{TN} + \text{FP}), \quad (3)$$

$$\text{PV+} = \text{TP} / (\text{TP} + \text{FP}), \quad (4)$$

where TP (true positive) is the number of correctly detected QRS notching, TN (true negative) is the number of correctly marked signals without the QRS notching, FP (false positive) is the number of signals without the QRS notching with incorrectly detected QRS notching, FN (false negative) is the number of signals with a notch where a notch is not detected, Y is the number of all signals.

Achieved accuracy of the QRS notching detection is shown at the first line of Table I. The achieved sensitivity is 88.07%, specificity is 94.23% and positive predictive value is 93.16%. The achieved accuracy is 91.33%. From the results it is evident, that more times the situation arose, where a signal with the QRS notching is identified as a signal without the QRS notching than the opposite situation.

The results of this study can be compared with the previous studies. This comparison is shown in Table I. The column "Detected phenomenon" shows what was detected in the corresponding study (QRS notching, mid-QRS notching or end-QRS notching). In paper [3], there was detected simultaneously the QRS notching and slurring without differentiation. The sensitivity, specificity and positive predictive value achieved in this work are similar with other studies. In other studies, one of the parameters is usually higher and one lower than in this study. This means, that the results of the proposed algorithm are the middle way between the emphasis on high sensitivity or high specificity.

TABLE I. THE ACCURACY OF THE QRS NOTCHING DETECTION IN THIS AND OTHER STUDIES

Authors	Detected phenomenon	Se [%]	Sp [%]	PV+ [%]
This study	QRS notching	88.07	94.23	93.16
Xia [6]	QRS notching	87	96	-
Xia [6]	mid-QRS notching	95	85	-
Xia [10]	mid-QRS notching	74	100	94
Clark ^a [3]	end-QRS notching and slurring	90.5	96.5	87.9

^a. The QRS notching and slurring without differentiation were detected simultaneously.

IV. CONCLUSION

Algorithm for the QRS notching detection was proposed in this article. This is a significant indicator of several currently researched cardiac pathologies. The method used in this work was based on CWT. The Haar wavelet was used as the mother wavelet and the scales were chosen in the range from 6 to 70. QRS notching is most pronounced at the scales from 6 to 15. Detection of a notch in this manner has not been tested until now. For testing of the proposed algorithm were used 123 signals from the CSE database. The achieved results (Se 88.07%, Sp 94.23% and PV+ 93.16%) were compared with the results from scientific articles published in the last two years. The accuracy of the detection achieved in this study is comparable with those studies. It has been tested, that detection of the QRS notching using a CWT is possible. An ambiguous and inconsistent definition of QRS notching is obstacle for greater accuracy of automatic detection achievement in this and also in other studies.

ACKNOWLEDGMENT

This work was supported by grant project GAČR P102/12/2034.

REFERENCES

- [1] J. Sekora, I. Provazník, J. Kolářová, and M. Nováková, "A Wavelet Based Detection of Abnormal Intra-QRS Potentials," in Proceedings of the World Congress 2009 for Medical Physics and Biomedical Engineering, 2009.
- [2] J. Sekora, M. Nováková, and I. Provazník, "Behavior of Intra-QRS Potentials during Induced Ischemia in Isolated Guinea Pig Hearts," in BIOSIGNAL, 2010, pp. 447–450.
- [3] E. N. Clark, I. Katibi, and P. W. Macfarlane, "Automatic detection of end QRS notching or slurring," J. Electrocardiol., vol. 47, no. 2, pp. 151–154, 2014.
- [4] P. W. Macfarlane and E. N. Clark, "ECG measurements in end QRS notching and slurring," J. Electrocardiol., vol. 46, no. 5, pp. 385–389, 2013.
- [5] D. G. Strauss, R. H. Selvester, and G. S. Wagner, "Defining left bundle branch block in the era of cardiac resynchronization therapy," Am. J. Cardiol., vol. 107, no. 6, pp. 927–934, 2011.
- [6] X. Xia, A.-C. Ruwald, M. H. Ruwald, N. Ugoeke, B. Szepletowska, et al., "Automatic Diagnosis of Strict Left Bundle Branch Block from Standard 12-lead Electrocardiogram," in Computing in Cardiology, 2016, vol. 42, pp. 665–668.
- [7] M. H. Nikoo, A. Aslani, and M. V. Jorat, "LBBB: State-of-the-art criteria," Int. Cardiovasc. Res. J., vol. 7, no. 2, pp. 39–40, 2013.
- [8] Y. Tian, P. Zhang, X. Li, Y. Gao, T. Zhu, et al., "True complete left bundle branch block morphology strongly predicts good response to cardiac resynchronization therapy," Europace, vol. 15, no. 10, pp. 1499–1506, 2013.
- [9] D. G. Strauss, "Differentiation between left bundle branch block and left ventricular hypertrophy: Implications for cardiac resynchronization therapy," J. Electrocardiol., vol. 45, no. 6, pp. 635–639, 2012.
- [10] X. Xia, B. Wieslander, D. G. Strauss, G. S. Wagner, W. Zareba, et al., "Automatic QRS Selvester scoring system in patients with left bundle branch block," Europace, vol. 18, no. 2, pp. 308–314, 2015.
- [11] The CSE working party, *Common standards for quantitative electrocardiography*. 1990.
- [12] M. Vitek, "Automatic delineation of ECG signals," Brno University of Technology, 2010.

UAS Model Using WEBOTS Robot Simulator

Vadim Starý and Václav Křivánek
 Faculty of Military Technology, University of Defence
 Kounicova 65, Brno, Czech Republic
 vadim.starý@unob.cz, vaclav.krivanek@unob.cz

Abstract—The paper deals with the Unmanned Aerial System modelling in WEBOTS¹ robot simulator environment. Main purpose is to create initial conditions for further usage for project of UAS autonomous landing application. The model is composed of several elements: unmanned aerial vehicle, ground based control station and environment with physical behaviour. Virtual reality modelling language (VRML) was used for model parts description.

Keywords—UAV; UAS; WEBOTS; VRML; modelling; simulation

I. INTRODUCTION AND MOTIVATION

UAS is a term for the Uncrewed Aerial System which consists of the aerial part, the Unmanned Aerial Vehicle (UAV) and the ground based part. Many categories of UAS exist. This paper is focused on the most widespread category, the mini UAV (up to 20kg) based on copter design [1], [2]. As a reference UAV was chosen a quadcopter PHANTOM III from DJI Company. Parameters of this copter are in [3]. Visualization of UAV is based on PHANTOM III [4], but the model represents general quad-copter with different kinds of sensors.

The article describes a part of a long term research at the Department of Air Defence Systems at University of Defence [5], [6]. This research is mainly focused on detection, protection and defence against UAS and among others deals with their guidance systems for autonomous behaviour, *i.e.* autonomous landing application [7]. Basic idea for landing application is to modify current missile guiding systems and use them for UAS [8], [9]. As the appropriate one seems the usage of a laser beam guidance because of suppression of unwanted emission and confidentiality [10], [11]. The aim of this article is to describe the environment, conditions and basics of creation UAS model in WEBOTS robot simulator.

Graphic model of UAV was edited in 3D creation suite Blender and imported as a *.wrl* file, which is a standard file format of VRML 2.0 for representing 3D interactive vector graphics in WEBOTS simulator.

Because of the wide range of the project and for purpose of this article, several simplifications were made:

- UAV and ground post model visual simplification.
- Ideal and known external conditions.
- No UAV dynamics, limited communication.

II. WEBOTS AND MODEL PARTS

This part describes elementary philosophy and information about simulator and tools which were used.

A. WEBOTS Robot Simulator and VRML 2.0

WEBOTS is a commercial robot simulator developed by Cyberbotics company with cooperation with Swiss Federal Institute of Technology, Lausanne. It is used to model and simulate robots in 3D. A Webots simulation is composed of the items bellow, more details are described in [12].

- World file (*.wbt*) – includes environment and description of all entities based on VRML nodes structure.
- Controller file – it is a program to control and specify the behaviour of world entities. Control can be done by C, C++, Python, Java or Matlab controller code.
- Optional plugin for physics.

The general simulation schema on Fig. 1 illustrates the standards and supported file formats of entities, environment and controllers.

The structure of entities is based on nodes using VRML syntax. A lot of sensors, actuators and even robot platforms are available in WEBOTS from developer in default. All nodes, which were used, are described at each entity. As a controller was used C++ programming language code in *.cpp* file. WEBOTS has a built-in Application Programming Interface (API) with editor and compiler.

The structure of VRML nodes is hierarchical with inheritance relationship. Derived nodes are called “children”. Some nodes are abstract (not visible) and for 3D representation it is necessary to bound them with a 3D geometry object. For example:

Main node ROBOT

```

↪ Children TRANSFORM
    ↪ Children LIGHT_SENSOR
        ↪ Children SHAPE
    
```

All these sensors, nodes and parameters can be found in [13].

B. World & Environment

World is made of essential entities for the creation of the simulation. It consists of these nodes (set parameter values are in brackets):

- *WorldInfo* – contains meta information about the world, define gravitational acceleration (9.81 ms^{-2}),

¹Registered trademark, version WEBOTS PRO 8.4.0

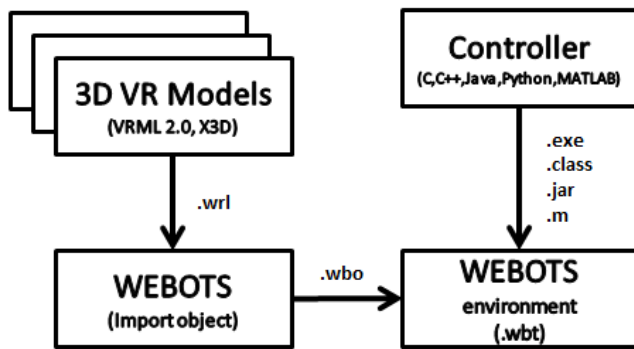


Figure 1. WEBOTS General Simulation Schema



Figure 2. UAV DJI Phantom III Model

parameters of Constraint Force Mixing (10^{-5}), Error Reduction Parameter (0.2), Basic Time Step (16 ms), Frames Per Second (60), GPS Coordinate System (local), North Direction (1, 0, 0)².

- *ViewPoint* – the node defines a specific location in the local coordinate system from which the user may observe the scene. Initial position (-1, 4, 18) for view on UAV.
- *Background* – the node defines the background used for rendering the 3D world. As a background were used textures of noon sunny weather.
- *DirectionalLight* – is a derived node of Light. In general it has two purposes. First is to graphically illuminate objects and second to determine quantity of light for light sensor. The Directional Light node defines a light source that illuminates along rays parallel to a given 3D vector. This type of light do not attenuate with distance. Ambient intensity (0), color (1, 1, 1)³ – white light, direction (0, 0, -1). Intensity (0.75).
- *DEF FLOOR Solid* – the node represents an object with physical properties. This node consists of “children” nodes – Transform and Shape, which describes the shape (plane), size (500 m × 300 m) and appearance (texture grass).

These are the basic entities, which create the world environment and provide the proper view of other objects. Rest of parameters are default.

C. UAV

Visualization is based on 3D graphics model of DJI Phantom (Fig. 2). The model consists of these nodes (set parameter values are in brackets):

DEF UAV Robot – the node is used as basis for building robots. This is a main node which includes basic parameters and children robot nodes.

- *Translation* – robot coordinates expressed as distances from the origin (0, 3.33, -21).

- *Controller* – name of the controller program that the simulator must use to control the robot *UAV_control.cpp*.

Children nodes:

- *DEF Body_1 Transform* – defines the visualization of the first part of the body and landing frame.
- *DEF Body_2 Transform* – defines the visualization of the second part of the body.
- *DEF Rotors Transform* – defines the visualization of rotors with propellers (propellers are also available as a unique entity).
- *DEF Camera Transform* – defines the visualization of the camera and includes camera entity to display the view from the UAV. Resolution is set as VGA (640 px × 480 px). Behavior of the camera is set in *UAV_control.cpp*.
- *DEF Motor_X Transform* – defines the visualization of motors 1 to 4.
- *Accelerometer* – the node which measures acceleration forces in three dimensions.
- *Emitter* – the node for communication (radio, serial or IR). Range (500 m). Aperture (-1) = 360°. Type (Radio). Channel (1). BaudRate (20 MBs⁻¹).
- *Receiver* – the node for communication (radio, serial or IR). Configured for the emitter above.
- *GPS* – the node representing model of GPS sensor.
- *Gyro* – the node representing gyroscope sensor.
- *Compass* – the node representing compass sensor.
- *LightSensor* – the node for light detection. It is used for detection of the laser beam from the ground post to get the control parameters for the project of assisted landing of UAV. It measures the irradiance of light in a given direction. It is created as the 10 × 10 × 10 cm cube.

According to the aim and the range of this article there are used only – *Camera* and *LightSensor*.

²*x, y, z* Cartesian coordinate system

³RGB form 0 to 1 (0 ÷ 100 %)

D. Ground Post

Ground post is represented by a simple graphic model, composed of elementary shapes. Its function is to track the UAV using camera and image processing and to emit the laser beam for landing procedure.

DEF Ground_base Robot – This is a main node which includes basic parameters and children robot nodes. *Ground_base_controller.cpp* is used as a controller.

Children nodes:

- *SpotLight* – the node emits light from a specific point in a specific direction with specific parameters. Position is in the origin of Cartesian coordinate system. Direction is toward to UAVs LightSensor. Color – white (1, 1, 1). CutOffAngle is equal to BeamWidth (0.002 m). See (1) and (2).
- *Camera* – includes camera entity to display the view from the ground post. Resolution is set as VGA (640 px × 480 px).
- *DistanceSensor* – the node represents laser range finder. Sensor position and direction is coupled with *SpotLight*. *LookupTable* is a parameter used for specifying the desired response curve and noise of the device. The table is set as linear with no noise. Maximum range is set up to 500 m. Aperture parameter for “laser” sensor type specifies the radius of the red spot (0.03 m).

$$\text{intensity}(\text{angle}) = \text{intensity}[(\cos(\text{angle}))^{\text{exp}}] \quad (1)$$

$$\text{exp} = \frac{0.5 \log 0.5}{\log[\cos(\text{beamWidth})]} \quad (2)$$

E. Supervisor & Controllers

Supervisor is a type of node, which represents a robot or a human to control the simulation. Robot control is currently provided manually by editing UAV position parameters. Controller files are described in section III.

III. SIMULATION AND MEASUREMENT

Fig. 3 shows the UAV, ground post models and view from their cameras in a physical environment. Green, red and blue axis represents the axis of Cartesian coordinate system (x , y , z). Red (green) axis is a laser beam from a distance sensor oriented toward the UAVs light sensor.

Fig. 4 shows the output from the distance sensor and represents the movement of UAV in distances from 23.05 m to 24.51 m. For the autonomous guidance over the laser beam is the most important light sensor. The function is shown on the Fig. 5, where is the light intensity depending on the time, where UAV is changing its distance. The result of rough measure of the laser beam elevation angle error according to the distance is shown in Tab. I. According to the data, an ideal laser beam of distance sensor with constant aperture has angle variances in y axis on distances from 10 m to 400 m approximately 0.6 to 0.04°. It may be assumed, that real laser

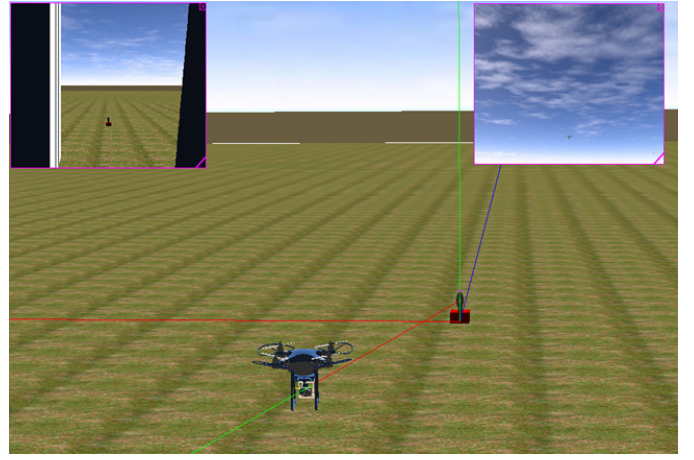


Figure 3. Simulation Layout

beam emitter will have aperture variable according to the distance, so it should be simulated and the current distance sensor model is not appropriate. The possible solution is to model a spot light as an emitter of the “laser beam”.

A. UAV_controller.cpp

This controller provides functionality of the sensors on the UAV (light sensor and camera). It includes *robot.h*, *light_sensor.h* and *camera.h* files which defines the default behavior. Time step is set to 64 ms.

B. Ground_post_controller.cpp

This controller provides functionality of the sensors and actuator on the ground post (distance sensor and camera). It

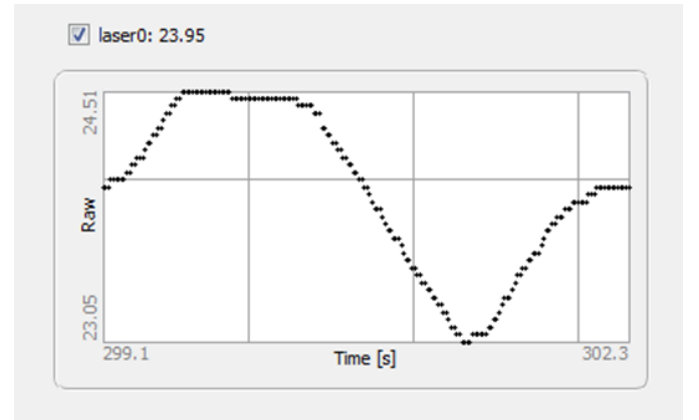


Figure 4. Laser Distance Sensor Output

Table I. ERROR OF ELEVATION ANGLE

z [m]	10	20	50	100	400
y_{min} [m]	1.85	3.16	7.09	13.64	52.94
y_{max} [m]	1.95	3.26	7.21	13.78	53.23
α_{min} [°]	10.72	9.13	8.18	7.86	7.63
α_{max} [°]	11.31	9.42	8.31	7.94	7.67
$\Delta\alpha$ [°]	0.59	0.29	0.14	0.08	0.04

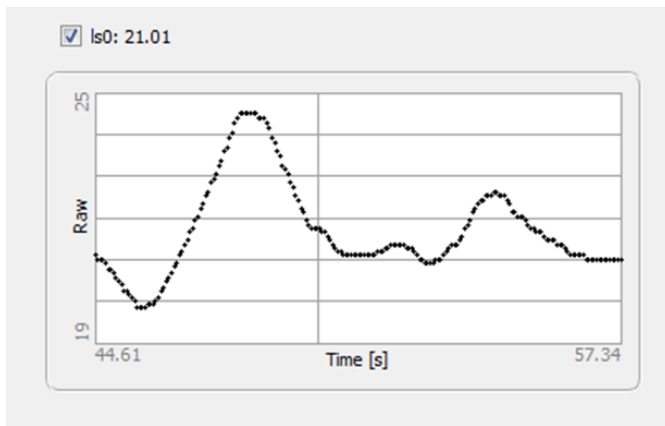


Figure 5. Light Sensor Output

includes *robot.h*, *distance_sensor.h* and *camera.h* files which defines the default behavior. Time step is set to 64 ms.

IV. CONCLUSION AND FUTURE WORK

This article describes particular solution for the project of guidance systems for autonomous landing application of UAS. Main task was to analyse the possibilities of the WEBOTS robot simulator and its suitability for this application. In general the WEBOTS simulator has all necessary parts for the entities creation. Main parts are – environment with physics, UAV with sensors and ground post with sensors. Functionality of the laser distance sensor and light sensor was tested. Laser beam from the laser sensor is not appropriate for the usage for guiding the UAV.

The next step of this project is to create more precise model of the UAV with dynamics, implement the control, extend the ground post sensor for the autonomous tracking of UAV using image processing algorithms and remove initial simplifications.

For example dynamics can be done as a nonlinear model with all degrees of freedom, linear model or their combination [14]. Other possibility is the nonlinear model with interaction with the simulated world physics (physics plugin) – model propellers and air, which is much more complex task and the WEBOTS has limited default capabilities [15].

Final step should be implementation of these findings into the real UAS and testing its behavior.

ACKNOWLEDGMENT

The work presented in this article has been supported by the Czech Republic Ministry of Defence (University of Defence development program “Research of sensor and control systems to achieve battlefield information superiority”).

REFERENCES

- [1] P. Fahlstrom and T. Gleason, *Introduction to UAV systems*. Chichester, UK: John Wiley & Sons, 2012.
- [2] P. Cermak and J. Martinu, “Component based design of mini uav,” in *Military Technologies (ICMT), 2015 International Conference on*, May 2015, pp. 1–5.
- [3] *Advanced User Phantom III Manual*, DJI company, Design Building, No.18 Gaoxin South 4th Ave, Nanshan District, Shenzhen, China, 2015, version 1.0.
- [4] V. Degryse. (2015, april) Dji phantom iii 3d model. [Online]. Available: <https://grabcad.com/library/my-dji-phantom-3-best-accessories-for-drones-1>
- [5] J. Farlík, M. Krátký, and J. Časar, “Detectability and jamming of small uavs by commercially available low-cost means,” in *2016 IEEE International Conference on Communications*. Military Technical Academy, Romania, 2016, pp. 121–124.
- [6] A. de La Bourdonnaye, R. Doskočil, V. Křivánek, and A. Štefek, “Practical experience with distance measurement based on the single visual camera,” *Advances in Military Technology*, vol. 7, no. 2, pp. 49–56, 2012.
- [7] R. Doskočil, V. Křivánek, A. Štefek, Y. T. Bergeon, and J. Motsch, “Uav assisted landing on moving ugv,” in *International Conference on Military Technology – ICMT 2015*, V. Křivánek, Ed. Brno: IEEE, University of Defence, May 2015, pp. 611–615.
- [8] S. Balakrishnan, A. Tsourdos, and B. White, *Advances in missile guidance, control, and estimation*. CRC Press, 2012.
- [9] J. Z. Ben-Asher and I. Yaesh, *Advances in missile guidance theory*. Amer Inst of Aeronautics, 1998, vol. 180.
- [10] J. V. Gomez and F. E. Sandnes, “Roboguidedog: Guiding blind users through physical environments with laser range scanners,” *Procedia Computer Science*, vol. 14, pp. 218–225, 2012.
- [11] P. Kutilek, V. Socha, P. Fitl, and P. Smrcka, “Evaluation of the adhesion strength using digital microscope and international standards,” *Proceedings of the 16th International Conference on Mechatronics, Mechatronika 2014*, pp. 519–525, 2014.
- [12] *Webots Reference Manual*, CYBERBOTICS co, Laussane, 2016, release 8.4.0.
- [13] *Webots User Guide*, CYBERBOTICS co, Laussane, 2016, release 8.4.0.
- [14] P. Fankhauser, S. Bouabdallah, S. Leutenegger, and R. Siegwart, “Modeling and decoupling control of the coax micro helicopter,” in *IEEE/RSJ International Conference on Intelligent Robots and Systems*, Deajeon, South Korea, 2011, pp. 2223–2228.
- [15] E. F. Calafell, “Coax flight simulator in webots,” Master’s thesis, ETH Zurich, Zurich, 2011.

Study of Wearable Antenna for 2.4 GHz ISM Frequency Band

Petr Vasina, Marek Jakubicek

Dept. of Radio Electronics
Brno University of Technology
Brno, Czech Republic

xvasin05@stud.feec.vutbr.cz, xjakub22@stud.feec.vutbr.cz

Abstract—This paper is focused on fabrication of wearable antennas and brief description of their essential properties. A numerical model of the patch antenna for the 2.4 GHz ISM frequency band is created using CST Microwave Studio. Further, the paper discusses the influence of human body and bending of the antenna on antenna parameters.

Keywords—wearable antenna; textile patch antenna; ISM band; off-body communication

I. INTRODUCTION

In the last decade, wearable antennas designed for application operates in proximity of human body have been rapidly developed. These antennas are designed for use in medical, industrial, military, aerospace or smart clothing, used in applications for the purpose of monitoring the health of the user, ensuring communication, attendance system or the endless possibilities of multimedia entertainment.

II. WEARABLE ANTENNAS

Wearable antennas are divided according to the type of communication (Off- Body Communication and On-Body Communication). For Off- Body antennas intended for use in proximity of human body is the ideal 180° radiation pattern in the perpendicular direction from the plane of the body because it cannot clearly determine the position of the second communication point located outside the body. In the case of On-Body Communication the communication points are located on the body the required directional characteristics are different according to the particular configuration (most commonly omnidirectional radiation) [1, 2]. Due to the nature of the human body, the effect of the human tissues and the possibility of mechanical bending structure should be investigated.

The choice of material (an electrically conductive layer and the substrate) and fabrication technology are the most important steps in the design of wearable antennas. This property is necessary for deformations in certain parts of the human body (e.g. the shoulder, arm, and knee) and for deformation caused by the movement of the user or the current status of the body. The bending must not influence electrical properties, especially deformation radiation characteristics, shift of resonance frequency or the impedance mismatching.



Fig. 1. Textile patch antenna manufactured on fleece.

The requirements of material are low weight, flexibility, resistance to deformation and a minimal extensibility [2]. Antenna parameters should not be changed even if the compression of material or humidity and temperature are changed.

A. Materials

Conductive materials are defined by a specific conductivity σ for separate fibers or by surface resistivity R_s for woven fabric. Electrical conductive layer on textiles can be generally ensured:

- electro-textile
- electrically conductive paint
- electrically conductive foil

Electro-textile is formed by using the improved metal-polymer fiber in combination with conventional materials or using individual conductive fibers. These substances are considered to be a suitable candidate for integration into clothing, electronic applications and usage on the body, because it is washable, mechanically robust and flexible [3].

Dielectric material has to ensure stability of electrical properties during the mechanical deformation, change in temperature or humidity of the surroundings. Inhomogeneous and often anisotropic characteristics do not ensure material reliability. Variable height and moisture absorption does not provide the stability of electrical properties of the antenna.

Examination of properties of textiles can be preceded by some phenomena and fabrics used for substrates.

Cotton is frequently used textile material as a substrate. In combination with e.g. synthetic polyester it becomes mechanically durable. The relative permittivity ϵ_r of textile substrates ranges from 1 to 2. As a material with a higher relative permittivity can be used foam which value of relative permittivity ϵ_r reach up to 4, depending on the type of material used. Foam substrates can be made e.g. of polyethylene in combination with other substance.

It is relatively difficult to provide stable electric properties of textiles. Changes in relative permittivity ϵ_r due to moisture can be partially prevented by impregnating materials or applying protective layers. However, it is necessary to investigate their influence on a whole structure.

B. Manufacture technology

Weaving technology is the process of making fabric. In principle it is a repeated crossing of longitudinal (Warp) and transverse (Weft) threads systems. In the simplest embodiment where the transverse and longitudinal fibers intersect in a ratio of 1:1, the system of longitudinal threads is attached and tensioned. In the first phase of the cycle, odd longitudinal fibers are lifted to form a space which is threaded through a transverse fiber. In the next step, even longitudinal threads are raised and the transverse threads are runs through back. This creates a woven pattern where the transverse fiber always passes through the entire width of the fabric. In another ratio woven pattern is always lifted a larger group of threads. For planar circuits, this technology is particularly suitable for forming larger surfaces. This technology is not very suitable for the production of very small elements.

Embroidery can be achieved by smaller, more flexible conductive elements. Lattice embroidery elements can imitate a larger area of the antenna structure and reduce production costs antenna. The chosen grid pattern embroidered is a compromise between the quantity of conductivity material and degradation of electrical properties.

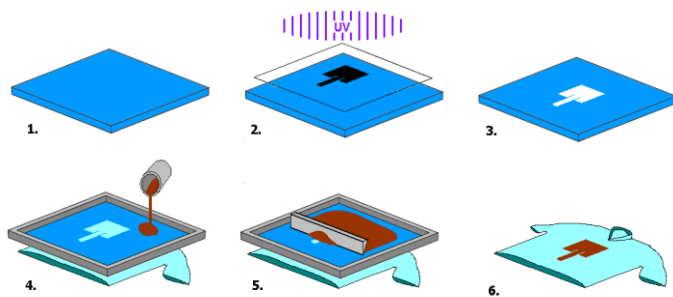


Fig. 2. The principle of etching foil.

For knitted elements it is necessary to expect larger losses taken by inhomogeneous surface, which will be reflected to a greater extent than with woven patterns. This is due to the meandering of the fiber bend. Using knitting conductive elements of the antenna, the antenna efficiency may decrease up to 50% compared to a standard antenna [4].



Fig. 3. The principle of etching foil.

Undoubtedly the most popular way of creating a theme for textile is screen printing. In a principle it is a paint application on the textile passage through a sieve having a defined density. The screen printing technique is shown in Fig. 2. When cleaning sieves after use, it is appropriate to proceed very carefully. When properly treated, a sieve can be used repeatedly in the tens or hundreds of printing processes.

Inkjet printing technology is reaching a very good resolution of the printed elements. The result and the print quality mainly depend on the size of the ink droplet and the spacing between the drops. In case of printing, in order to ensure electrical conductivity elements, these parameters are necessary. Small print density causes a discontinuity in the theme, which does not provide electrical conductivity. Conversely, too much print density would cause bad paint drying and subsequent blurred or smeared. Ink drop size is around 60 microns [5].

Plating technology consists of depositing thin metallic plates on the substrate. This is a very simple and inexpensive alternative that can be realized with minimal technical equipment. Production elements of a thin conductive layer can be done in several ways. The easiest way is to manually cut out the theme of the film directly, but at the cost of low accuracy and can thus be realized only by simple shapes theme. A more accurate, but still accessible way is to create a theme using etching in ferric chloride. The process is in principle not very different from the process of manufacturing a theme to the standard solid substrate. The process is illustrated in Fig. 3. Another possibility is to obtain theme using automated laser cutting, which will achieve more accurate dimensions but at a higher cost.

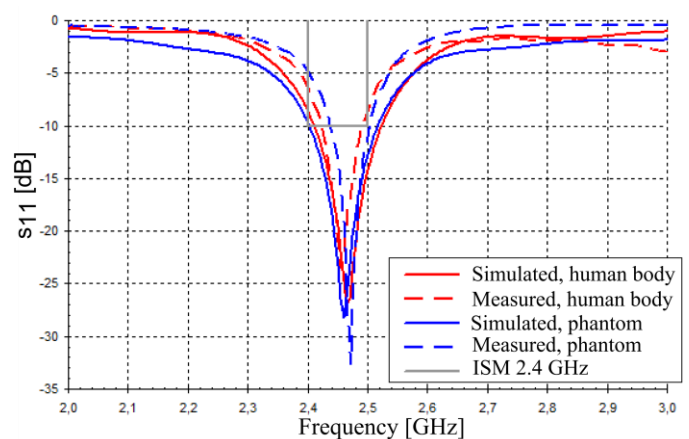


Fig. 4. Measured and simulated reflection coefficient of proposed antenna placed in proximity of human body.

III. EFFECT OF PROXIMITY OF HUMAN BODY

The patch antenna (Fig. 1) is manufactured on fleece (relative permittivity $\epsilon_r = 1.07$, textiles height $h = 3$ mm) substrate.

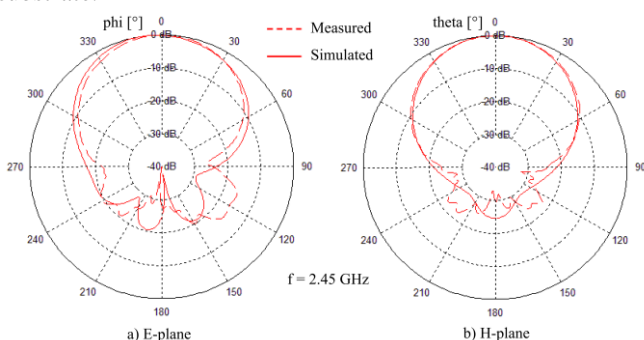


Fig. 5. Simulated and measured radiation pattern in E-plane and H-plane for antenna placed in free space.

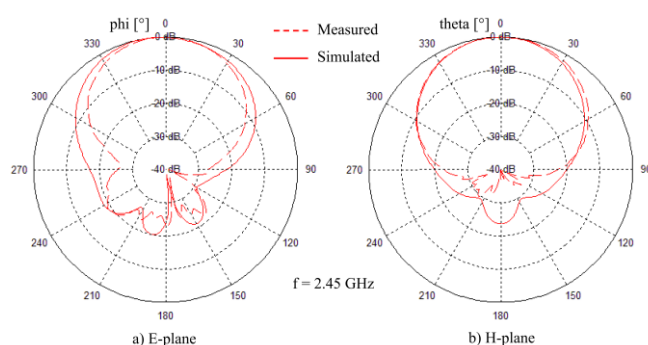


Fig. 6. Simulated and measured radiation pattern in E-plane and H-plane for antenna placed on the phantom.

During the first measurement antenna was located on the body in the upper third of the back. At this point, the shape of the body below the antenna closes to a perfectly flat surface and the measurement is influenced by other parts of the body. The second measurement is carried out on a phantom made of agar. The height of the phantom is $h_{PHA} = 20$ mm. The phantom has a specific properties at the frequency of 5.8 GHz, it has a defined relative permittivity $\epsilon_r = 48$ and a conductivity $\sigma = 8$ S / m.

The measured results of influence of human tissues on the reflection coefficient are depicted in Fig. 4. The simulation of the presence of the human body shows a slight increase in bandwidth which was confirmed by measurement. The radiation patterns in both orthogonal planes are shown in Figs. 5 and 6. Reflection coefficient and radiation pattern are affected by the proximity of human tissue at least through the ground plane patch antenna. The value of the measured gain differs from the simulated gain maximally about 1.5 dBi.

IV. EFFECT OF BENDING ANTENNA STRUCTURE

The results presented so far have been used for a flat motive model. This model represents the situation of the location of the antenna on the back, abdomen or chest. This section discusses the possibility of placement of the antenna

structure to the shoulder, arm, or leg. The surface of the antenna in the simulation replicates the surface of an imaginary cylinder oriented according to the x-axis or y-axis.

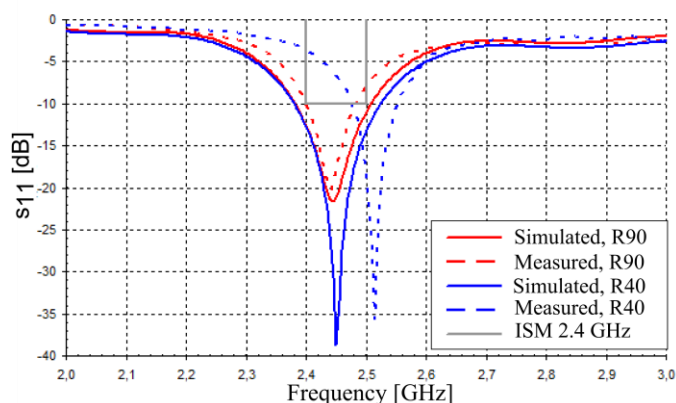


Fig. 7. Simulated and measured reflection coefficient of proposed antenna for concave bending along the y axis.

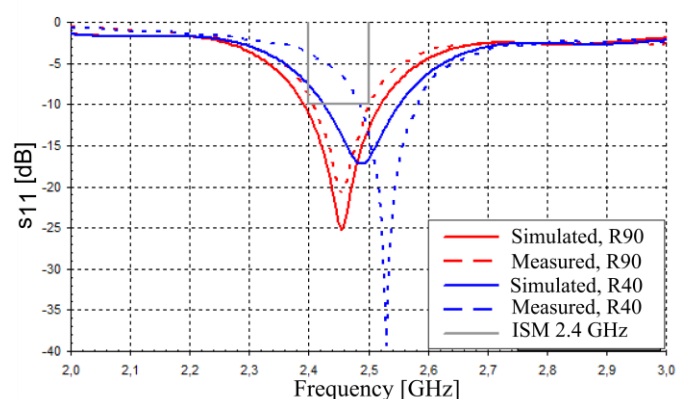


Fig. 8. Simulated and measured reflection coefficient of proposed antenna for concave bending along the x axis.

For simulation of bending under measurement without influence of a human body, antenna is bent into a reproducing surface of the auxiliary paper corpus. For the measurement of flexible features combined with the influence of the human body, the antenna has been placed on a body part with a curvature radius comparable simulated. The disadvantage of a copper foil is that it has a tendency to irreversible deformation at sharp bends. Comparison of results (Fig. 7 and Fig. 8) of numerical model with concave bend of radius $R = 40$ mm show more pronounced shift in resonant frequency (about 58 MHz) for bending in both axes (x-axis or y-axis).

Figs. 9 and 10 depicted results of measuring the flexibility on the human body. Measurement of bending radius $R = 40$ mm was realized on forearm in place where its circumference corresponds to this radius. Measurement of the radius $R = 90$ mm were made on the thigh and measurement of spherical cap of radius $R = 50$ mm were simulated on the shoulder. The measured results are compared with the simulation antenna model tissue according to [6]. Effect of the concave bend of the antenna located on the human tissue is similar to the previous case. Simultaneously, there is deterioration of the an-

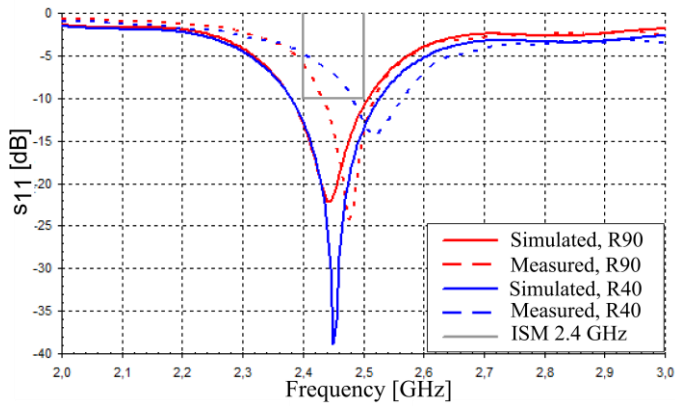


Fig. 9. Simulated and measured reflection coefficient of proposed antenna placed on the phantom for concave bending along the y axis.

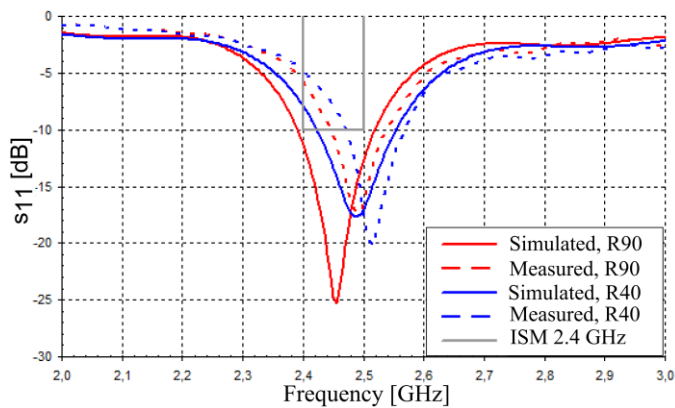


Fig. 10. Simulated and measured reflection coefficient of proposed antenna placed on the phantom for concave bending along the x axis.

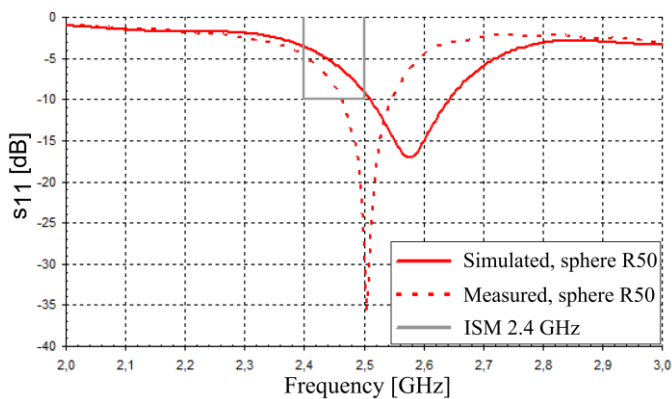


Fig. 11. Simulated and measured reflection coefficient of proposed antenna for bending to the surface of a sphere.

tenna impedance matching and in the worst case up -14 dB (Figs. 9 and 10).

The measured and simulated reflection coefficients of proposed antenna after placing antenna on the surface of a sphere are depicted in Fig. 11. The measured resonant frequency is about 70 MHz lower than the results of numerical model, but even this does not cover the entire 2.4 GHz ISM band.

V. CONCLUSIONS

In this paper the manufacturing technology and wearable patch antenna designed for the ISM frequency band 2.4 GHz on the textile material (fleece) have been described. The antenna has been implemented and measured for verified properties when placed near the body at the concave bending in the two main axes, and bending around a spherical cap. As already mentioned, the reflectance curves, directional characteristics and the gain are not significantly different when placing the antenna near the body. In the case of concave bending and bending around the spherical cap there is a shift of the resonant frequency and the degradation of impedance matching of the antenna occurs.

ACKNOWLEDGMENT (Heading 5)

The presented research was supported by the Czech Grant Agency project no. P102/12/1274, by the Czech Ministry of Education in frame of National Sustainability Program under grant LO1401, and by the Internal Grant Agency of Brno University of Technology project no. FEKT-S-14-2483. The research is the part of the COST Action IC1301 which is financially supported by the grant of the Czech Ministry of Education no. LD14057. For research, infrastructure of the SIX Center was used.

REFERENCES

- [1] KHAN, M. M.; MAGANI, M.; RAHMAN, A.; PARINI, C. A Dual Band Planar Inverted F Antenna for Body-centric Wireless Communications. *3rd Annual Seminar on Passive RF and Microwave Components*. March 2012, pp 57 – 64.
- [2] HALL, P. S.; YANG HAO. Antennas and Propagation for Body-centric Wireless Communications. 2nd ed. Boston: Artech House, 2012, XIII, 387 s. antenna and propagation series. ISBN 978-1-60807-376-4.
- [3] KUHN, H., CHILD A. a REYNOLDS J.R. Electrically conductive textiles. *Handbook of conducting polymers*. 1998, s. 993-1013. DOI: 0-8247-0050-3.
- [4] ANTAR, Yahia, Debatosh GUHA. Microstrip and printed antennas: new trends, techniques, and applications. DOI: 9780470681923.
- [5] LI, Yi, Russel TORAH, Steve BEEBY, John TUDOR, S. KIM, B. S. COOK, J. R. COOPER, M. M. TENTZERIS. An all-inkjet printed flexible capacitor on a textile using a new poly (4-vinylphenol) dielectric ink for wearable applications. *2012 IEEE Sensors*. 2012, s. 71-90. DOI: 10.2495/978-1-84564-986-9/004.
- [6] Foundation for Research on Information Technologies in Society: Interactive tissue frequency chart. [online]. [ref. 2014-12-13]. Available from: <http://www.itis.ethz.ch/virtualpopulation/tissueproperties/database/tissue-frequency-chart/>.

Analysis of Microstrip Line Relative Permittivity Measurement

Jan Vélím, Michal Mrnka

Department of Radio Electronics, Brno University of Technology

Email: velim@phd.feec.vutbr.cz

Abstract—The paper describes a methodology how to measure the relative permittivity by a microstrip line. The relative permittivity is calculated from measured scattering parameters. The results are corrected to achieve the more precisely values.

I. INTRODUCTION

The transmission line method is used for measurement of the permittivity in many articles e.g [1], [2]. This method has the advantage of broadband measurements compared with a resonant techniques. In spite of that the resonant technique has narrow band it is more popular for its accuracy, moreover numerical models are used for evaluation of the relative permittivity that means that no analytical equations are necessary to include. The results are achieved by optimization techniques and comparison between measured data and simulated data. In this article is shown that analytical processing does not bring additional errors only, but can contribute to the reduction of errors and smoothing of the results.

The next section explain the methodology how to get the value of the relative permittivity of a material which serves as dielectric layer in a microstrip line structure. The third section presents the source of inaccuracies and their removal.

II. MEASUREMENT METHODOLOGY

There is necessary to have two samples of microstrip lines with different length (Fig. 1) for measurement of a relative permittivity by the transmission line method. We get values of scattering parameters for the shorter microstrip line S_T and for the longer microstrip line S_L through the vector network analyzer (VNA). There is no need of any calibration of the VNA because the precise value of the transmission coefficient T of the segment (15 mm long) is calculated from the measured values S_L and S_T . Because of mathematical operations in next steps it is more useful to transform matrices of the scattering parameters in to transmission matrices T_L and T_T by equations [3]:

$$T_{11} = \frac{1}{S_{21}}, \quad (1)$$

$$T_{12} = -\frac{S_{22}}{S_{21}}, \quad (2)$$

$$T_{21} = \frac{S_{11}}{S_{21}}, \quad (3)$$

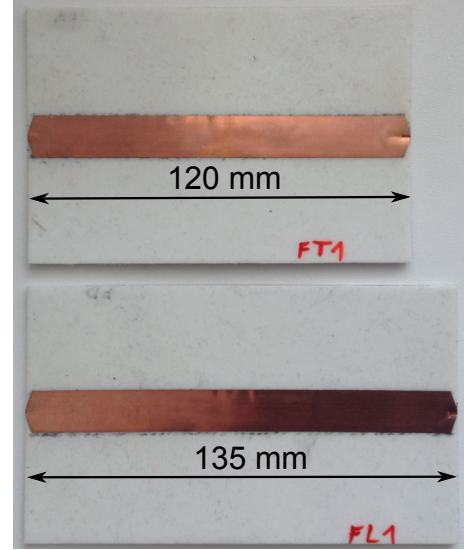


Fig. 1. Measured samples of the microstrip lines.

$$T_{22} = S_{12} - \frac{S_{11}S_{22}}{S_{21}}, \quad (4)$$

where T_{11} , T_{12} , T_{21} , T_{22} are coefficients of the transmission matrices and S_{11} , S_{12} , S_{21} , S_{22} are coefficients of the scattering matrices.

The transmission coefficient of the 15 mm long segment T is calculated by function "eig()" how is presented in [4]. The input arguments are the transmissions matrices and the outputs are eigen values which correspond with transmission coefficient (5):

$$[T] = \text{eig}(T_L T_T^{-1}) = \begin{pmatrix} e^{-\gamma l_s} \\ e^{\gamma l_s} \end{pmatrix}, \quad (5)$$

where l_s represents the length of the segment of the microstrip line and γ is the propagation constant. This complex number $\gamma = \alpha + j\beta$ is evaluated by equation (6). The α represents attenuation and β represents phase constant of the electromagnetic waves in the structure.

$$\gamma = -\frac{\ln(T)}{l_s}. \quad (6)$$

As proved by equation 7, only imaginary part of the propagation constant has influence to the value of the relative

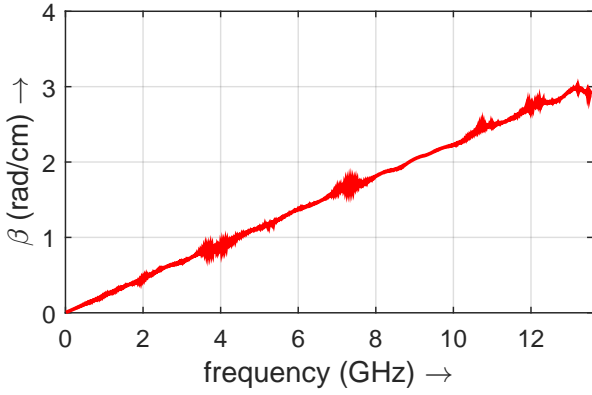


Fig. 2. Measured phase constant of the segment of the microstrip line.

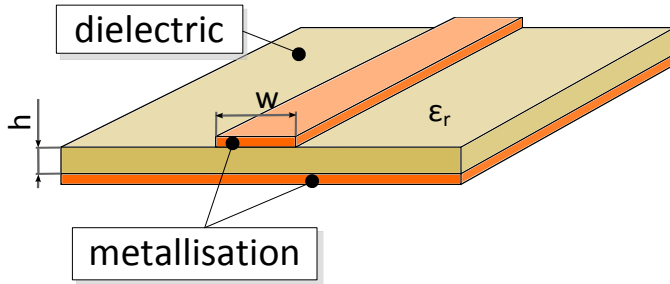


Fig. 3. Measured phase constant of the segment of the microstrip line.

permittivity. This equation can be used only in cases where a transversal electromagnetic (TEM) mode or a quasi-TEM mode propagate in the structure [1]. The curve of the phase constant is depicted in Fig. 2.

From the generally known physical laws it is known that wavelength of electromagnetic waves become shorter when environment has higher relative permittivity. Therefore it is possible to derive equation (7) which calculate relative permittivity from values of the phase constant β , speed of light in vacuum c_0 and the angular frequency ω ,

$$\epsilon_{r_{eff}} = \left(\frac{c_0}{\omega} \beta \right)^2. \quad (7)$$

The output of the equation (7) is not relative permittivity of the dielectric only but the relative effective permittivity of the whole microstrip line structure (Fig. 3). Hence the conformal mapping method is exploited for enumeration of the relative permittivity of the tested dielectric material (8) [5]. A FoamClad with high 2.54 mm, relative permittivity 1.2 and loss tangent 0.002 is used as tested material.

$$\epsilon_r = \frac{\epsilon_{r_{eff}} - e}{1 - e}, \quad (8)$$

where,

$$e = \frac{\ln(6.28(\frac{w}{2h} + 0.85))}{\frac{2w}{h} + \frac{2}{\pi} \ln(17.08(\frac{w}{2h} + 0.85))},$$

where w is width of conductive line on the top of the microstrip line and h is high of the dielectril layer (Fig. 3).

III. ACCURACY IMPROVEMENTS

The results of the aforementioned procedure which calculates the relative permittivity is depicted in Fig. 4 by red line. As shown, the individual samples of measured values are affected by inaccuracies from measurement and rounding. The most simple solution how to improve the results is to interpolate the samples (Fig. 4 - black dashed line). Now the question is whether this is sufficient. The true is that the result can be improved further. The key is in the removing errors sooner, in a place where it is easier to detect them. If we look at the phase constant chart (Fig. 2), we can see the ripple that does not correspond with physical properties of the FoamClad. That is accordingly more suitable to approximate phase constant by a straight line. This approximation unfortunately brings inaccuracies in low frequency part. That is because the straight line does not direct in to the coordinate origin (Fig. 5 - blue line). From the physical laws it is clear that beta has to start at coordinate origin therefore the interpolated line is redirected in to it (Fig. 5 - blue dashed line). Above mentioned adjustment brings significant improvement of the values of the relative permittivity (Fig. 4 - blue dashed line).

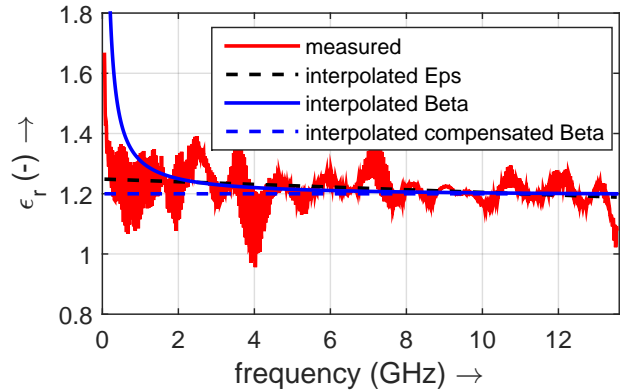


Fig. 4. The relative permittivity of the FoamClad.

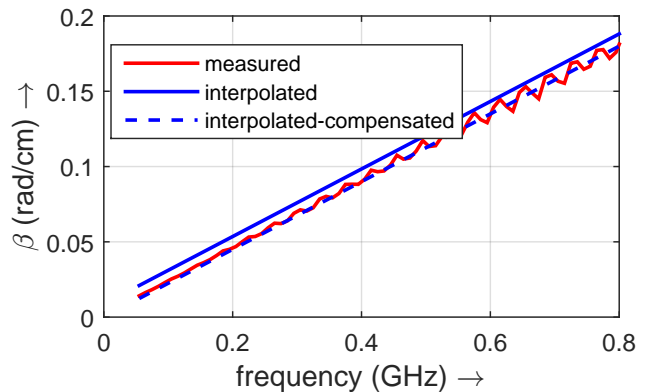


Fig. 5. The detailed view at the phase constant of the FoamClad.

IV. CONCLUSION

The article proves that transmission line method is suitable technique for the broadband measurement of a relative permittivity. The microstrip line can be used up to 13.6 GHz. Using a corrections, which are based on physical knowledge, causes the more accurate results. The significant improvement was achieved especially in the lower parts of the frequency band as shown in Fig. 4.

ACKNOWLEDGMENT

Research described in this paper was financially supported by the Czech Science Foundation under grant no. P102/12/1274. Research is a part of the COST Action IC1301 supported by the grant LD14057 of the Czech Ministry of Education. The presented research was supported by the Internal Grant Agency of Brno University of Technology project

no. FEKT-s-14-2483. For research, infrastructure of the SIX Center was used.

REFERENCES

- [1] P. Seiler, B. Klein and D. Plettemeier, "Broadband characterization of planar transmission line substrate permittivity up to 67 GHz," *Antennas and Propagation (ISAP)*, 2014 International Symposium on, Kaohsiung, 2014, pp. 373-374.
- [2] S. F. Barot and J. T. Bernhard, "Permittivity measurement of layered media using a microstrip test bed," 2008 IEEE Antennas and Propagation Society International Symposium, San Diego, CA, 2008, pp. 1-4.
- [3] Radmanesh, M. M., *RF & Microwave Design Essentials: Engineering Design and Analysis from DC to Microwaves*, AuthorHouse, 2007.
- [4] Y. Rolain, A. Barel, F. Gubbels and W. van Moer, "Microwave permittivity measurement of polymers by deposition on a coplanar wave guide," *Instrumentation and Measurement Technology Conference*, 2004. IMTC 04. Proceedings of the 21st IEEE, 2004, pp. 333-338 Vol.1.
- [5] SVAČINA, J.: Řešení mikrovlnných planárních struktur metodou konformního zobrazení. Akademické nakladatelství CERN, 2006

System Impulse Response Measurement Using M-sequences in the Presence of Non-linearities

Josef Vychodil

Department of Radio Electronics

Brno University of Technology

Technická 3082/12, 616 00 Brno, Czech Republic

Email: vychodil@phd.feec.vutbr.cz

Abstract—The m-sequence cross-correlation method is a powerful approach for obtaining a linear system impulse response estimate. However, when the system under test exhibits non-linear behaviour, the obtained estimate contains some artefacts, which are not part of the linear system impulse response. This paper describes the origin of these artefacts and how they arise.

I. INTRODUCTION

The m-sequence cross-correlation method is a widely used approach for measuring impulse responses of linear systems. For example, it is used in many time domain channel sounders, like it was shown in [1] or [2].

The method is usually performed as follows. A seamless repeating m-sequence is fed to the input of the system. The output of the system is then sampled and a correlation operation (usually performed using Fast Fourier Transform (FFT) for faster computation) between the output and the original m-sequence is computed. Because the auto-correlation function of a m-sequence can be approximated as ideal impulse function, the result is an estimate of the channel impulse response.

However, real (not only) electronic devices like amplifiers, mixers, etc. exhibit at least weak non-linear behavior. When the measured system is non-linear, the resulting estimate of the channel impulse response contains artefacts, which are not part of the linear impulse response.

II. LINEAR CASE

The input-output relationship of a linear time invariant system can be expressed as

$$y(t) = \int_0^{\infty} g_1(\tau_1) u(t - \tau_1) d\tau_1, \quad (1)$$

where $u(t)$ is the input of the system, $y(t)$ is the output and $g_1(\tau_1)$ is the system's impulse response.

From now, consider the input signal $u(t)$ as a seamless repeating m-sequence with number of chips N , period of T and duration of one chip Δt . The cross-correlation between the input $u(t)$ and output $y(t)$ can be expressed as [3]

$$R_{uy}(\tau) = \overline{u(t - \tau)y(t)} \quad (2)$$

where $\overline{}$ means time (t) average over one period (T) of the signal. When considering the system described by Eq. 1,

the cross-correlation becomes

$$\begin{aligned} R_{uy}(\tau) &= \overline{u(t - \tau)y(t)} \\ &= u(t - \tau) \int_0^{\infty} g_1(\tau_1) u(t - \tau_1) d\tau_1 \\ &= \int_0^{\infty} g_1(\tau_1) \overline{u(t - \tau)u(t - \tau_1)} d\tau_1 \\ &= \int_0^{\infty} g_1(\tau_1) R_{uu}(\tau, \tau_1) d\tau_1, \end{aligned} \quad (3)$$

where $R_{uu}(\tau, \tau_1)$ is the second moment of the input m-sequence $u(t)$ [3], which can be expressed as

$$R_{uu}(\tau, \tau_1) = \overline{u(t - \tau)u(t - \tau_1)} = \begin{cases} 1 & \text{if } \tau = \tau_1 \\ -\frac{1}{N} & \text{if } \tau \neq \tau_1, \end{cases} \quad (4)$$

Equation 3 then becomes

$$R_{uy}(\tau) \simeq \Delta t g_1(\tau), \quad (5)$$

which corresponds to the conventional system impulse response measurements utilizing m-sequences.

III. NON-LINEAR CASE

When the system is weakly non-linear, its input-output relation can be expressed using the Volterra series expansion, which is generalization of the system impulse response and the Taylor series, as

$$\begin{aligned} y(t) &= \int_0^{\infty} g_1(\tau_1) u(t - \tau_1) d\tau_1 \\ &+ \int_0^{\infty} \int_0^{\infty} g_2(\tau_1, \tau_2) u(t - \tau_1) u(t - \tau_2) d\tau_1 d\tau_2 \\ &+ \int_0^{\infty} \int_0^{\infty} \int_0^{\infty} g_3(\tau_1, \tau_2, \tau_3) u(t - \tau_1) u(t - \tau_2) u(t - \tau_3) d\tau_1 d\tau_2 d\tau_3 \\ &+ \dots \\ &+ \int_0^{\infty} \dots \int_0^{\infty} g_i(\tau_1, \dots, \tau_i) u(t - \tau_1) \dots u(t - \tau_i) d\tau_1 \dots d\tau_i \end{aligned} \quad (6)$$

or in shorter form as

$$y(t) = \sum_{i=1}^{\infty} \int_0^{\infty} \dots \int_0^{\infty} g_i(\tau_1, \dots, \tau_i) u(t-\tau_1) \dots u(t-\tau_i) d\tau_1 \dots d\tau_i, \quad (7)$$

where $u(t)$ is the input to the system, $y(t)$ is the output of the system and $g_i(\tau_1, \dots, \tau_i)$ is the i -th order Volterra kernel, which can be viewed as higher order impulse response of the system. Please note that if the system is linear, only the first order Volterra kernel $g_1(\tau_1)$ (first term of Eq. 6) is non zero. The equation then reduces to ordinary convolution, where $g_1(\tau_1)$ is the linear impulse response, e.g. the equation becomes Eq. 1.

Now, let's introduce one of the properties of m-sequences, the so-called shift and add property [4]. When we take any m-sequence and multiply it by the same but shifted sequence, we obtain the same sequence, but with different time shift. For example, with a sequence $u[n]$ with length of 15 chips

$$\begin{aligned} u[n] &= [\circ \circ \circ \circ \bullet \circ \bullet \circ \circ \bullet \bullet \circ \bullet \bullet \bullet] \\ \cdot u[n-1] &= [\bullet \circ \circ \circ \circ \bullet \circ \bullet \circ \circ \bullet \bullet \circ \bullet \bullet \bullet] \\ = u[n-4] &= [\circ \bullet \bullet \bullet \circ \circ \circ \circ \bullet \circ \bullet \circ \circ \bullet \bullet], \end{aligned} \quad (8)$$

where the -1 and 1 numbers are for better illustration represented by \circ and \bullet symbols, respectively, it can be clearly seen that the original sequence multiplied by the same sequence but shifted by one chip to the right equals the same sequence but shifted by 4 chips to the right. The shifts are unique for every m-sequence and can be determined from the generating polynomial of the m-sequence.

Equation 4 can be generalized to the i -th moment of $u(t)$ as

$$\begin{aligned} R_{uu\dots u}(\tau, \tau_1, \dots, \tau_i) &= \overline{u(t-\tau)u(t-\tau_1)\dots u(t-\tau_i)} \\ &= \begin{cases} 1 & \text{under certain values of } \tau, \tau_1, \dots, \tau_i \\ -\frac{1}{N} & \text{otherwise.} \end{cases} \end{aligned} \quad (9)$$

The crosscorrelation between the input $u(t)$ and the output $y(t)$ using 3, 7 and 9 can be rewritten as [5]

$$\begin{aligned} R_{uy}(\tau) &= \overline{u(t-\tau)y(t)} \\ &= \overline{u(t-\tau) \sum_{i=1}^{\infty} \int_0^{\infty} \dots \int_0^{\infty} g_i(\tau_1, \dots, \tau_i) \cdot u(t-\tau_1) \dots u(t-\tau_i) d\tau_1 \dots d\tau_i} \\ &= \sum_{i=1}^{\infty} \int_0^{\infty} \dots \int_0^{\infty} g_i(\tau_1, \dots, \tau_i) \cdot \overline{u(t-\tau)u(t-\tau_1)\dots u(t-\tau_i)} d\tau_1 \dots d\tau_i \\ &= \sum_{i=1}^{\infty} \int_0^{\infty} \dots \int_0^{\infty} g_i(\tau_1, \dots, \tau_i) \cdot R_{uu\dots u}(\tau, \tau_1, \dots, \tau_i) d\tau_1 \dots d\tau_i, \end{aligned} \quad (10)$$

which can be approximated, when neglecting 4th and higher

order kernels as

$$\begin{aligned} R_{uy}(\tau) &\simeq \Delta t g_1(\tau) + F_3(\tau) \\ &+ 2! \sum_{j=1}^{m_2} (\Delta t)^2 g_2(\tau - k_{21}^{(j)} \Delta t, \tau - k_{22}^{(j)} \Delta t) \\ &+ 3! \sum_{j=1}^{m_3} (\Delta t)^3 g_3(\tau - k_{31}^{(j)} \Delta t, \tau - k_{32}^{(j)} \Delta t, \tau - k_{33}^{(j)} \Delta t), \end{aligned} \quad (11)$$

where the integers $k_{ir}^{(j)}$ ($1 \leq r \leq i$) are the unique shift coefficients of the m-sequence, m_i is the count of the sets of numbers $k_{ir}^{(j)}$. We can observe that the cross-correlation now contains the first order kernel (linear impulse response) and also shifted cross sections of higher order kernels. The term $F_3(\tau)$ is the sum of the third order Volterra kernels, which have one or more parameters the same and equals to

$$F_3(\tau) = (\Delta t)^3 g_3(\tau, \tau, \tau) + 3(\Delta t)^3 \sum_{q=1}^{m_1} g_3(\tau, q, q). \quad (12)$$

A. Unobservable and overlapped kernels

As can be seen from Eq. 11 and Eq. 12 there are several parts of Volterra kernels, which are not directly observable or are overlapped with other kernels.

In the concrete, we cannot observe any second order Volterra kernel, which have equal parameter, e.g. $g_2(q, q)$. This is because when the binary m-sequence is multiplied by the same m-sequence, the result is a constant 1, e.g. $u(t) \cdot u(t) = 1$ [6]. This can be generalized for all even order kernels, but in the scope of this work only kernels up to third order are considered.

From Eq. 12 we can see that any third order Volterra kernel, which have one or more parameters the same, overlap with the first order kernel. The explanation is as follows: $u(t) \cdot u(t) \cdot u(t) = u(t)$ or more generally $u(t) \cdot u(t-\tau) \cdot u(t-\tau) = u(t)$. This property can also be generalized for all odd order kernels.

IV. EXAMPLES

This section gives some examples of the described principles. Those examples were carried out using computer simulation. Consider one of the simplest non-linear system, the so-called Wiener model.

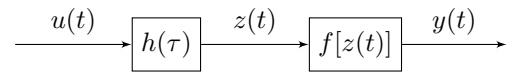


Fig. 1. Wiener type non-linear model.

This model consists of cascade of a linear memory block, which can be characterized by its impulse response $h(\tau)$, and a static (memory-less) non-linearity, which can be modeled by a (possibly truncated) polynomial, e.g.

$$y(t) = c_1 z(t) + c_2 z^2(t) + c_3 z^3(t), \quad (13)$$

when considering non-linearities only up to third order.

The i -th order Volterra kernel of this system is then [7]

$$g_i(\tau_1, \dots, \tau_i) = c_i h(\tau_1) \dots h(\tau_i). \quad (14)$$

First consider the case without the non-linear block, which can be viewed as if only the coefficient $c_1 = 1$ of the non-linear block is non-zero. For example let the $h(\tau)$ be a right triangle shaped function with base length of 10 samples, height 1 and lag of 500 samples for better illustration. All other values of $h(\tau)$ are zero. The original impulse response function and the one measured using m-sequence of length 2047 chips is shown on Fig. 2.

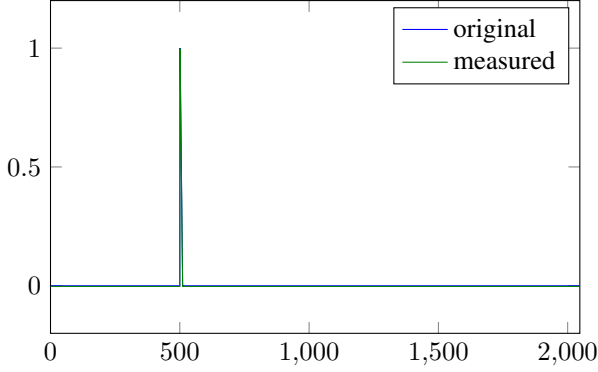


Fig. 2. Original and measured impulse response function.

It shows a good agreement, with minor error, which is caused by the fact, that the values of the auto-correlation function of the m-sequence outside the correlation peak are not exactly zero, but $1/N$.

Now, consider the Wiener model on Fig. 1 with coefficients $c_1 = 1$ and $c_2 = 0.1$, others zero. The result is depicted on Fig. 3.

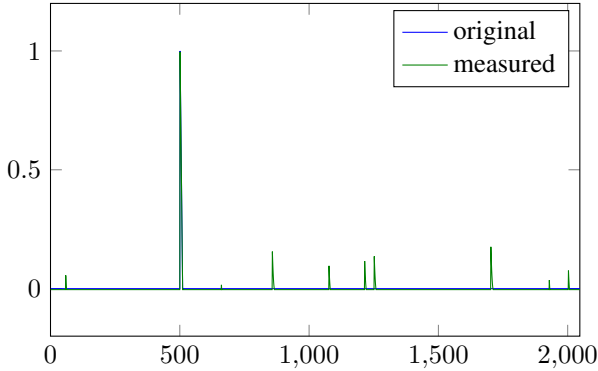


Fig. 3. Original and measured impulse response function in presence of second order non-linearity.

It can be clearly seen, that the linear part (impulse response) remains unaffected by second (or even in general) order distortion. The cross-correlation now contains also the cross-sections of second order Volterra kernels. There are 9 of them, the part with equal parameters ($g_2(q, q)$) is unobservable.

For better illustration, Fig. 4 depicts the same situation, but the used m-sequence has been generated using different generating polynomial. The number of chips remains the same.

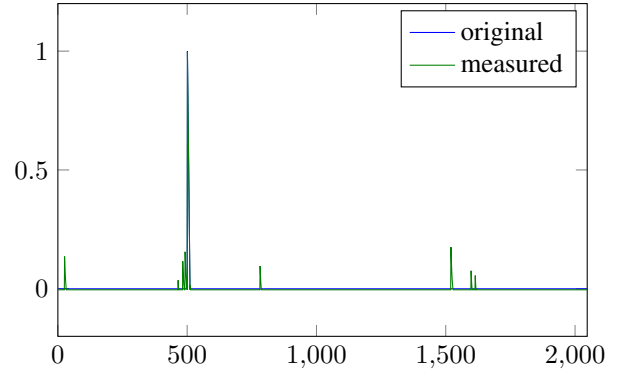


Fig. 4. Original and measured impulse response function in presence of second order non-linearity. Different m-sequence used.

It can be seen that the cross-sections of the second order Volterra kernels are at different positions, possibly overlapping with each other or with the linear impulse response.

Now consider the coefficients of non-linear part $c_1 = 1$ and $c_3 = 0.08$, others zero. The result can be seen on Fig. 5.

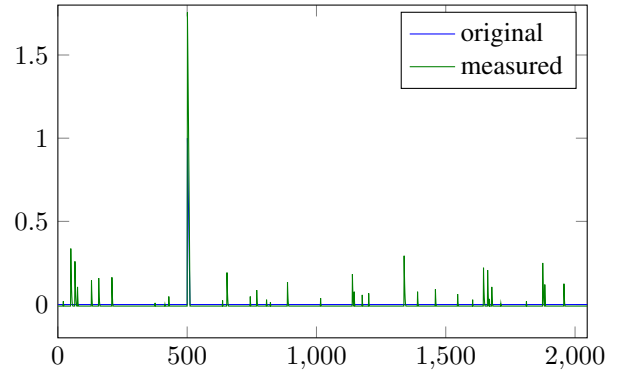


Fig. 5. Original and measured impulse response function in presence of third order non-linearity.

It can be clearly seen that the third (or odd in general) order Volterra kernels now overlaps and affects the linear impulse response, as was discussed earlier. The resulting cross-correlation function also contains more cross-sections of the three dimensional Volterra kernel.

Last example depicted on Fig. 6 shows that the result gets complicated as the number of non-zero elements of $h(\tau)$ grows. The length of the base of the triangle in $h(\tau)$ is now 50 samples. The coefficients of non-linear block are $c_1 = 1$, $c_2 = 0.1$ and $c_3 = 0.08$.

Many overlapped Volterra kernels cross-section can be seen in the result and also the linear impulse response is more affected (distorted).

V. CONCLUSION

The mechanism of the origin of the artefacts, appearing when measuring (weakly) non-linear system using m-sequence correlation method was described in detail. Some practical examples were given, showing the behaviour when applying

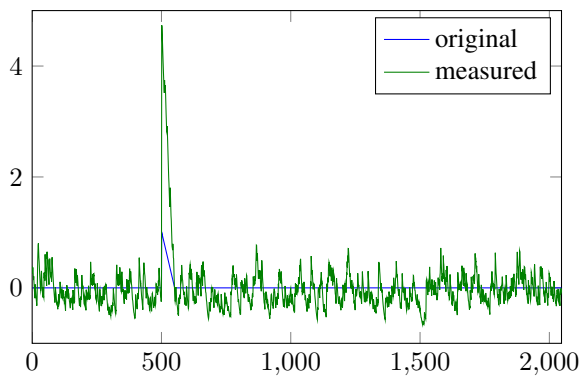


Fig. 6. Original and measured impulse response function for $h(\tau)$ with 50 non-zero elements in presence of second and third order non-linearity.

the method to one of the simplest non-linear system, the Wiener type non-linear model.

Future work will cover examining the possibility of recovering the linear impulse response of the system from one or multiple m-sequence cross-correlation measurements, or even utilizing the m-sequence cross-correlation method for non-linear system identification.

ACKNOWLEDGMENT

This work was supported by the Czech Science Foundation project No. 13-38735S Research into wireless channels for intra-vehicle communication and positioning, and was performed in laboratories supported by the SIX project, No. CZ.1.05/2.1.00/03.0072, the operational program Research and Development for Innovation. Research described in this paper was financed by Czech Ministry of Education in frame of National Sustainability Program under grant LO1401. For research, infrastructure of the SIX Center was used.

REFERENCES

- [1] R. Zetik, M. Kmec, J. Sachs, and R. S. Thoma, "Real-time mimo channel sounder for emulation of distributed ultrawideband systems," *International Journal of Antennas and Propagation*, vol. 2014, p. 16, 2014. [Online]. Available: <http://dx.doi.org/10.1155/2014/317683>
- [2] A. Durantini, W. Ciccognani, and D. Cassioli, "UWB propagation measurements by PN-sequence channel sounding," in *Communications, 2004 IEEE International Conference on*, vol. 6, June 2004, pp. 3414–3418 Vol.6.
- [3] H. Harada, Y. Toyozawa, M. Shigaki, H. Kashiwagi, and T. Yamaguchi, "Identification of nonlinear parameters by using m-sequence and harmonic probing method," *Journal of System Design and Dynamics*, vol. 2, no. 1, pp. 209–217, 2008.
- [4] Y. Lin, "Shift and add property of m-sequences and its application to channel characterisation of digital magnetic recording," *IEE Proceedings - Communications*, vol. 142, no. 3, pp. 135–140, Jun 1995.
- [5] H. Tsukino, H. Harada, Y. Toyozawa, H. Kashiwagi, and R. Ohtsubo, "Identification of nonlinear parameters by using low-pass filtered M-sequence," in *ICCAS-SICE, 2009*, Aug 2009, pp. 4512–4515.
- [6] E. Nishiyama, "Identification of first order volterra kernels of m-sequence correlation method for nonlinear system," in *Control, Automation and Systems, 2007. ICCAS '07. International Conference on*, Oct 2007, pp. 939–942.
- [7] V. Kekatos, D. Angelosante, and G. B. Giannakis, "Sparsity-aware estimation of nonlinear volterra kernels," in *Computational Advances in Multi-Sensor Adaptive Processing (CAMSAP), 2009 3rd IEEE International Workshop on*, Dec 2009, pp. 129–132.

When the Numbers Speak - Hidden Statistics of a Crowdsourced QoE Study

Ondrej Zach, Eva Klejmová

Dept. of Radio Electronics

Brno University of Technology

Technická 12, 602 00 Brno, Czech Republic

Email: ondrej.zach@phd.feec.vutbr.cz, klejmov@phd.feec.vutbr.cz

Abstract—Presented paper deals with a crowdsourcing-based Quality of Experience study. Using crowdsourcing for QoE evaluation has become very popular, however, the gathered data need to be processed carefully. In this work, we try to take a different look on the data gathered and possibly present some interesting aspects regarding the users and their behavior.

I. INTRODUCTION

Crowdsourcing has become a very convenient tool in the field of Quality of Experience (QoE). Conventional QoE studies need to be run according to variety of conditions in a controlled environment (ambient light, viewing distance, etc.). Such a study brings good insight in the quality of tested multimedia content as perceived by the viewers. However, running a conventional study has high demands on resources, both material and financial. On the other hand, running a crowd-sourced study may bring results faster and with a fraction of the costs compared to a laboratory-based testing. Nevertheless, a crowdsourced QoE study has to be designed carefully based on the expected participants, their equipment etc.

The challenges the researcher has to deal with are mainly focused on the final processing of the gathered data. As the participants are working on the given task in an uncontrolled environment (usually at their homes and using their own computer), the task has to be designed with emphasis on monitoring of the users action. In home environment, it is very easy for the participant to cheat and not to answer properly. These issues are well addressed in [1], [2]. As the unreliable users usually choose their answers randomly, such a behavior has to be detected and corresponding results then omitted from the final processing of the gathered data.

The focus of the paper is to analyze the "hidden information" from a crowdsourcing QoE study to address the possible issues e.g. regarding crowd selection, which might be beneficial for future research.

The rest of the paper is divided as follows. Section 2 describes the studies during which we gathered the data we use. In Section 3 we take a closer look at different issues, that can be found in the processed results and the last Section concludes.

II. THE STUDY

For purposes of this paper, we ran several crowdsourcing-based QoE studies previously published in [3], [4]. However, in

this work we offer a different approach to gathered data and try to look at the results from a different perspective. The research published in [4] is focused on a comparison of Advanced Video Coding (AVC) and High Efficiency Video Coding (HEVC) coded video content. An innovative feature of the study was an adaptive approach to allocation of the sequences to the users. The sequences to be played to the next participant were chosen according to the length of the confidence interval (CI) of the previously gathered quality scores of that respective sequence. Such an approach may lead to faster convergence of the scores to values with lower CIs. In [3] we evaluate the performance of the adaptive approach compared to conventional random or pseudo-random approach. For this study, we used AVC coded content only. We also try to suggest the best approach to content and quality level selection based on criteria of better statistical properties of the results (e.g. CI length, distribution etc.).

The video database created for the studies consisted of 5 different contents, each encoded to 5 different bitrate levels. This results in 25 different AVC encoded processed video sequences (PVS) and 25 HEVC encoded PVSs. These PVSs were then used for the crowdsourced studies. The length of each sequence was adjusted to 10 s. The study was run using a web-based application similar to [5]. The framework included wide variety of features to monitor user's activity and to detect possible cheating. For example, a set of simple user question is presented to the participant twice, at the beginning and at the end of the test, with different order of the answers. If the user answered some of these question differently, his ratings were marked as inconsistent. Also, the framework could monitor if the user switched to another tab of the web browser etc. The participants watched five PVSs with different content each. The study was available as a micro job on the Microworkers¹ crowdsourcing platform. Every user could participate and was rewarded with 0.30\$ upon completion of the test.

III. PROCESSING OF THE RESULTS

During the run of the study, we gathered wide variety of information from the participants. The framework itself monitored the behavior of the users (e.g. cheating, not focusing on the test properly) and information about equipment they use (used web browser, screen resolution, download speed etc.). Other information needed users' input, e.g. participants' sex, age, education, occupation, nationality and using of web-based

¹<https://microworkers.com>

video services. In following Section, we analyze some of these hidden aspects of the study.

A. Users' demography

Alltogether, the test was finished 1392 times. The study was divided in several runs, hence, this number does not need to represent the number of the participants as the user (identified by his unique mwID) could participate in all of the runs without any limitation. After omitting the repeating mwIDs, we had 672 unique users. These users came from 78 different countries, mainly from Bangladesh. More detailed information about the origin of the participants can be seen in Fig. 1. Quite surprisingly, among the countries with high share of participants is Belgium, which is, unlike the others, a well developed country.

Representation of countries in test

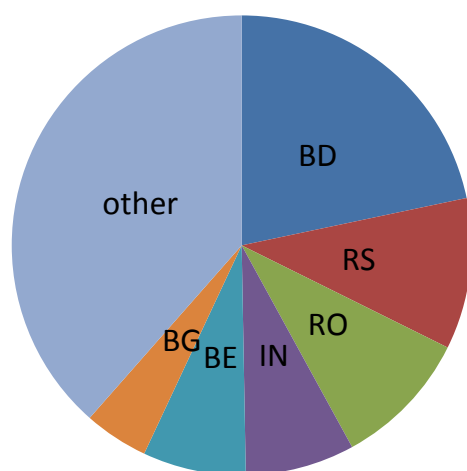


Fig. 1: Representation of participants' countries.

Another interesting finding might be the share of internet browser in the crowdsourcing society. Also in this case, the answer was quite surprising. More than 65% of the users used Google Chrome. The Windows' built-in Microsoft Internet Explorer was identified only in 4 cases. The situation can be seen in Fig. 2. The figure depicts only the type of the browser and not its specific version. As an The knowledge of the most often used browser can help the researcher in designing the study in the terms of features of the browser the research can use.

B. Cheating behavior

As already mentioned, the test's framework could monitor cheating-like behavior. The users were asked simple questions regarding the content of just presented sequence. If the user did not answer properly, his all ratings were neglected. This was detected in 52 cases. Other participants tried to switch to another browser tab during the playback. This was also monitored. If such an event occurred, the user was firstly asked to focus properly on the task and was offer to re-play the sequence. If he tried again to switch to another tab, his ratings were removed from further processing of the results. To sum

Browser share

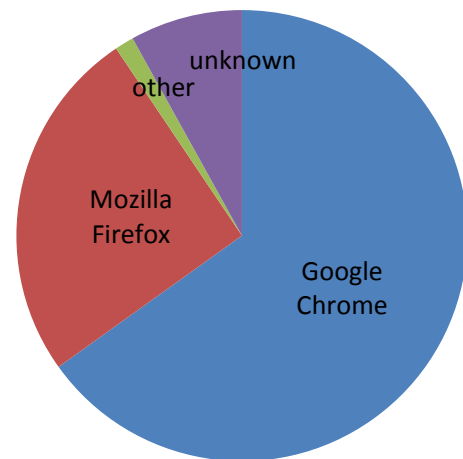


Fig. 2: Browser share.

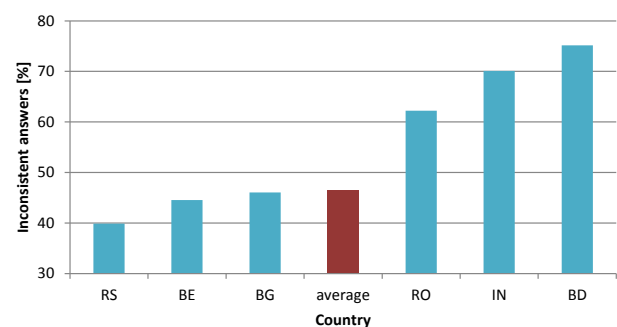


Fig. 3: Percentage of unreliable users among countries.

up, only about 44 % of the completed tests were finished without any disruption or attempts to cheat.

As each user has to be paid for completion of the task, identifying the groups of unreliable users may bring benefits for further studies. Hence, we asked the question, if there is a relation between nationality of the users and the percentage of inconsistent answer. In Fig. 3 the percentage of unreliable users among the users' countries is presented. We can see a surprisingly high value of unreliability of the users who claimed to come from Bangladesh. The value is about 75 %, which far beyond the average. If we try to express this in the way of costs, this means, that from 90\$ spent on bangladeshi users, only 22\$ were converted to usable results.

Other countries with unreliability rate above the average were India (70%) and Romania (62%). All this are countries with low quality of living, which may be interpreted in such a way, that the users earn their monthly income as crowdworkers and try to complete as many tasks as possible in short time, without regards to correctness of the results. Therefore, when designing a crowdsourcing study, the choosing of the right "crowd" should be one of the essential questions.

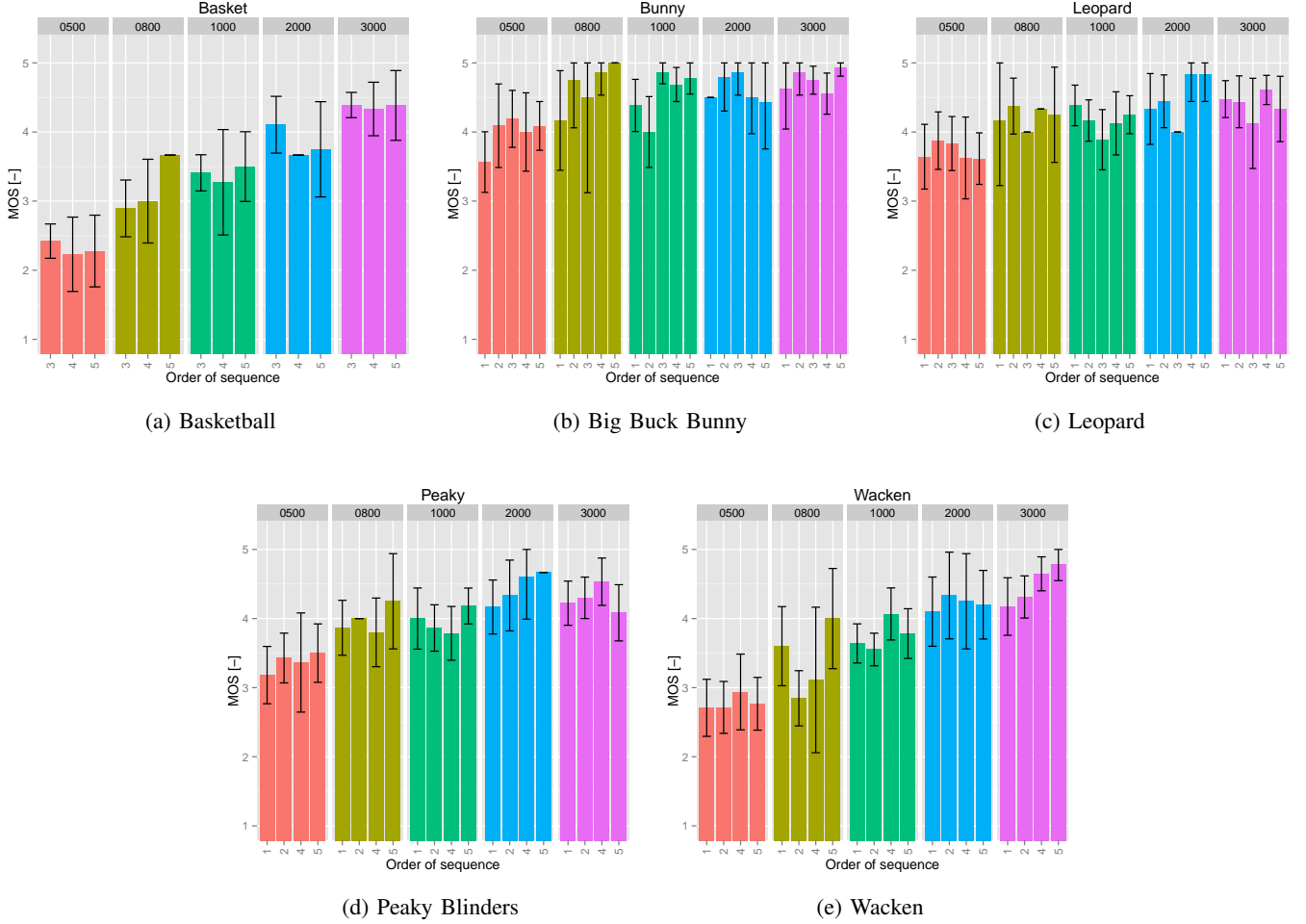


Fig. 4: Influence of PVS order on the MOS.

C. Sequence order issues

A typical QoE study implements random or pseudo-random selection of the presented sequences. Therefore, we asked the question, if the order of the sequences we used did affect the final ratings given by the users. The situation for our PVSs is depicted in Fig. 4. Each graph represents different content, the color represent the bitrate used to encode the sequence and horizontal and vertical axis show order of the sequence and resulting MOS, respectively. For simplifying the figures, only ratings of AVC coded sequences are considered.

It can be seen, that in most cases, the confidence intervals of respective PVSs overlap and therefore the influence of the sequence order can not be regarded as significant. However, a trend of rating the sequences presented to the viewer on 4th or 5th place with higher values of the perceived quality can be observed.

IV. CONCLUSION

In this paper, we tried to analyze the results of a crowdsourcing QoE study from a different perspective. Our findings can help with designing further studies. We identified several issues, e.g. the nationality of the participants, which should

be taken into account to improve the successfulness of such a study.

ACKNOWLEDGMENT

This paper was supported by the BUT project no. FEKT-S-14-2177. The described research was performed in laboratories supported by the SIX project; no. CZ.1.05/2.1.00/03.0072, the operational program Research and Development for Innovation. Research described in this paper was financed by Czech Ministry of Education in frame of National Sustainability Program under grant LO1401. For research, infrastructure of the SIX Center was used.

REFERENCES

- [1] HOSSFELD, Tobias, Christian KEIMEL, Matthias HIRTH, Bruno GARDLO, Julian HABIGT, Klaus DIEPOLD and Phuoc TRAN-GIA. Best Practices for QoE Crowdstesting: QoE Assessment With Crowdsourcing. *IEEE Transactions on Multimedia*. 2014, **16**(2), 541-558. DOI: 10.1109/TMM.2013.2291663.
- [2] ANEGEKUH, Louis, Lingfen SUN a Emmanuel IFEACHOR. A screening methodology for crowdsourcing video QoE evaluation. *2014 IEEE Global Communications Conference*. IEEE, 2014, , 1152-1157. DOI: 10.1109/GLOCOM.2014.7036964.

- [3] SEUFERT, Michael, Ondrej ZACH, Tobias HOSSFELD, Martin SLANINA and Phuoc TRAN-GIA. Impact of test condition selection in adaptive crowdsourcing studies on subjective quality. *2016 Eighth International Conference on Quality of Multimedia Experience (QoMEX)*. IEEE, 2016, , 1-6. DOI: 10.1109/QoMEX.2016.7498939.
- [4] ZACH, O. Let the Crowd Be Heard - A Crowdsourcing- based Study on Video Coding. *Proceedings of the 22nd Conference STUDENT EEICT 2016*. Brno: Vysok uen technick v Brn, Fakulta elektrotechniky a komunikanch technologi, 2016. p. 390-394.
- [5] HOSSFELD, Tobias, Michael SEUFERT, Matthias HIRTH, Thomas ZINNER, Phuoc TRAN-GIA and Raimund SCHATZ. Quantification of YouTube QoE via Crowdsourcing. *2011 IEEE International Symposium on Multimedia*. IEEE, 2011, , 494-499. DOI: 10.1109/ISM.2011.87.